DEUTSCHES ELEKTRONEN-SYNCHROTRON DESY

DESY 82-011
March 1982

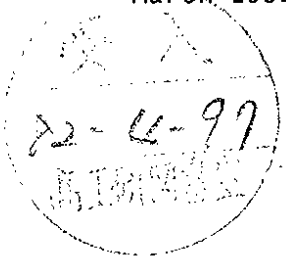

RECENT RESULTS IN ELECTRON-POSITRON AND LEPTON-HADRON INTERACTIONS

by

K.H. Mess

Deutsches Elektronen-Synchrotron DESY, Hamburg

B.H. Wiik

II. Institut für Experimentalphysik der Universität Hamburg

NOTKESTRASSE 85 · 2 HAMBURG 52

To be sure that your preprints are promptly included in the HIGH ENERGY PHYSICS INDEX , send them to the following address (if possible by air mail) :

DESY
Bibliothek
Notkestrasse 85
2 Hamburg 52
Germany

DESY 82-011
March 1982

RECENT RESULTS IN ELECTRON-POSITRON AND LEPTON-HADRON INTERACTIONS

K.H.Mess

Deutsches Elektronen-Synchrotron DESY, Notkestrasse 85,

2000 Hamburg 52 - Germany

B.H.Wiik

II. Institut für Experimentalphysik, Universität Hamburg, Luruper Chaussee 149,

2000 Hamburg 50 - Germany

Abbreviated title: ELECTRON-POSITRON AND LEPTON-HADRON INTERACTIONS

Content:

1. Introduction

During the past two decades, theory and experiments have conspired to produce a cohesive and simple picture of nature. At least down to distances of 10^{-16} cm matter is made of pointlike constituents leptons and quarks. The leptons have electromagnetic and weak interactions and are directly observed as free particles. The quarks have colour and participate in the strong interaction. So far only colour singlets - i.e. hadrons composed of two or three quarks - have been observed in abundance. This observation has led to the hypothesis that the quarks are confined and do not appear as free particles.

The forces, strong, electromagnetic and weak are predicted to arise from the exchange of gauge bosons. Based on low energy experiments, there is now a general belief that the electromagnetic and the weak interactions are unified to a electroweak interaction on a mass scale of 100 GeV. Furthermore, there are ample speculations that the strong and electroweak forces are also unified on a mass scale of 10^{15} GeV/c^2. Heroic attempts are being made to incorporate gravitation into this picture to create a truly unified theory.

Deep inelastic lepton-hadron or electron-positron annihilation experiments have contributed much to bring this picture into focus. The existence of quasi-free pointlike constituents in the nucleon was first discovered in lepton-nucleon scattering and well defined jets of hadrons resulting from the fragmentation of quarks were observed in e^+e^- annihilation at high energies. Hadrons reflecting the existence of new quarks have been detected in e^+e^- annihilation and both types of experiments have contributed much to the determination of quark properties. A new sequential lepton, the τ has been found and its properties determined in e^+e^- annihilation.

Neutrino experiments first revealed the existence of neutral weak currents and their continuation has determined much of the low q^2 properties of this new interaction.

The existence of gluons, the carrier of the strong interaction was first inferred from deep inelastic lepton-hadron experiments and the gluons were directly observed in three-jet events in e^+e^- annihilation.

Simplicity is one of the reasons why measurements of e^+e^- annihilation and deep inelastic lepton-hadron interactions have been successful. In e^+e^- annihilation the neutral timelike current - electromagnetic or weak - couples directly to the basic constituents. The current with $J^{PC} = 1^{--}$ can also produce particles with the same quantum numbers. In deep inelastic lepton-hadron interactions the lepton interacts directly with the quarks in the nucleon via neutral and charged spacelike currents.

These lectures will start with a few remarks on detectors and beams used to study e^+e^- annihilation and deep inelastic lepton-nucleon interactions. The main part of the lectures will discuss recent results obtained from a study of these processes including a discussion on the result of recent particle searches. The picture which emerges from these data is consistant with what has become known as the standard model. However, it is important to bear in mind that the experiments so far have only investigated masses which are small compared to 100 GeV/c^2, the characteristic mass of the weak interaction. The new generation of e^+e^- and ep collider will allow us to extend these measurements into a mass range above 100 GeV/c^2, and thus provide answers to many of the questions confronting the standard model.

2. The Experiments

2.1 Experiments at electron-positron colliding rings

2.1.1 The colliders

The art of colliding electrons and positrons has developed very rapidly. In only 20 years the field has progressed from the first model machine[1] with a circumference of 4.5 m to the present LEP project[2] with a circumference of 27.4 km.

The storage ring PETRA[3] at DESY is shown in Fig. 2.1 as an example of a high energy e^+e^- machine. PETRA consists of a single ring made of eight 45^o bends joined by eight straight sections, four 108 m long and four 68.4 m long. The total circumference is 2.3 km. Two bunches of electrons and positrons each are injected and travel around the ring in opposite directions guided by a system of dipole, quadrupole and sextupole magnets. The bunches cross in the middle of four straight sections and are here focussed down to a small cross section by two pairs of quadrupoles located

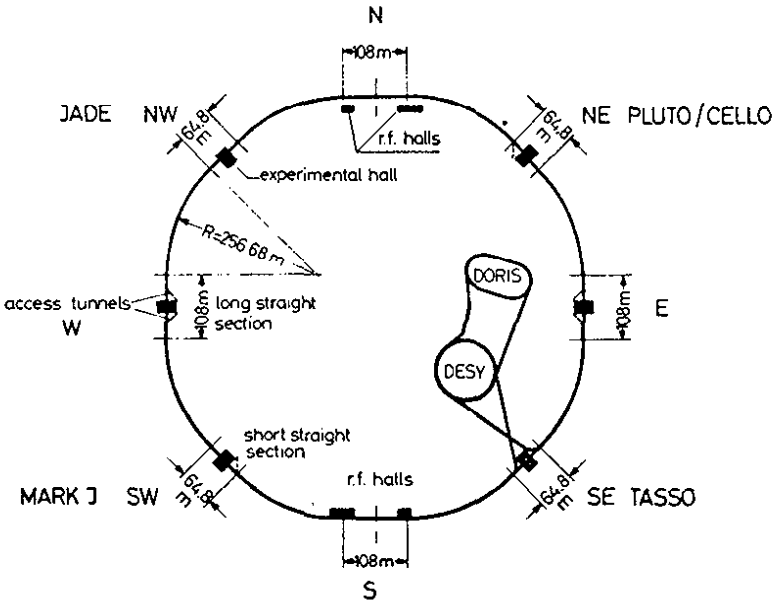

Fig. 2.1 - Layout of the e^+e^- collider PETRA

symmetrically with respect to the interaction point. The distance between the quadrupol pairs is a compromise between the free length needed to mount an experiment and the peak luminosity. At PETRA the free length has been reduced[4] from 15.0 m to 9.0 m leading to an increase in the luminosity by a factor of three to 1.7×10^{31} $cm^{-2}sec^{-1}$. Similar changes have also been carried out at CESR in Cornell and at PEP at Stanford with encouraging results.

An electron with energy E_o travelling around a ring with a bending radius ρ radiates an energy eU_o per turn.

$$2.1 \qquad eU_o = 88.5 \times 10^{-6} \left(\frac{m}{GeV^3}\right) \cdot \frac{E_o^4}{\rho}$$

Thus a 19 GeV electron in PETRA radiates on the average 58.5 MeV per turn. This energy loss is made up by the energy gain in the r.f. cavities located in the long straight sections. Due to synchrotron radiation the beam dimensions are Gaussian distributed. A bunch at the interaction point at 16 GeV is typically 0.12 mm high (σ_y), 0.5 mm wide (σ_x) and 20 mm long (σ_e) and contains on the order of $2 \cdot 10^{11}$ electrons.

As we will discuss below the cross section for hadron production in the continuum is very small and decreases with the square of the energy. It therefore becomes increasingly important to maximize the luminosity.

The luminosity in an e^+e^- colliding ring[5,6] is given by:

$$2.2 \qquad L = \frac{(n^2)\ B\ f}{4\pi\ \sigma_x^*\sigma_y^*} = \frac{i^2}{4\pi\ \sigma_x^*\sigma_y^* \cdot B\ f \cdot e^2}$$

n is the number of particles per bunch, B the number of bunches per beam and f the revolution frequency. σ_x^* and σ_y^* are the horizontal and vertical rms beam sizes at the interaction point defining an effective beam cross section $F = 4\pi\ \sigma_x^*\sigma_y^*$. The circulating current in each beam is given by $i = e\ n\ f\ B$.

High luminosities can only be achieved by maximizing n. However, when the bunches cross they interact electromagnetically and the ultimate limit on the number of particles in a bunch is reached when its partner is lost due to this interaction. This beam-beam interaction is parameterized by the tune shift ΔQ with

$$2.3 \qquad \Delta Q_x = \frac{r_e}{2\pi\gamma} \frac{n \beta_x^*}{(\sigma_x^* + \sigma_y^*) \sigma_x^*}$$

Here $r_e = 2.82 \cdot 10^{-13}$ cm is the classical electron radius and $\gamma = E/m_e$. It has been found at the high energy e^+e^- machines that ΔQ must be less than 0.03 to ensure stable operation. Therefore to maximize n the value of the amplitude function β^* at the interaction point must be minimized. The ultimate limit is presumably reached when β^* is comparable to the bunch length, i.e. a few cm. However, a practical limit for existing machines with the detectors already in place is imposed by β_{max}, the largest allowed value of the amplitude function at the quadrupoles adjacent to the interaction region. Roughly speaking β_{max} should not exceed 500 - 1000 m. However, since β increases as $\beta(s) = \beta^* + s^2/\beta^*$ with the distance s from the interaction region, this implies that these quadrupoles must be moved towards the interaction point - i.e. the free region available to experiments must be reduced.

So far electron-positron colliders have operated efficiently only over a rather narrow energy range centered near the peak energy. A typical luminosity curve is sketched in Fig. 2.2. The rms beam size σ is given by $\sigma = \sqrt{\epsilon\beta}$ where ϵ is the beam emittance and β the value of the amplitude function at a particular location. In electron machines ϵ is not a constant but rather determined by the synchrotron radiation and the focussing strength of the lattice and grows, for constant β-values, with the energy squared.

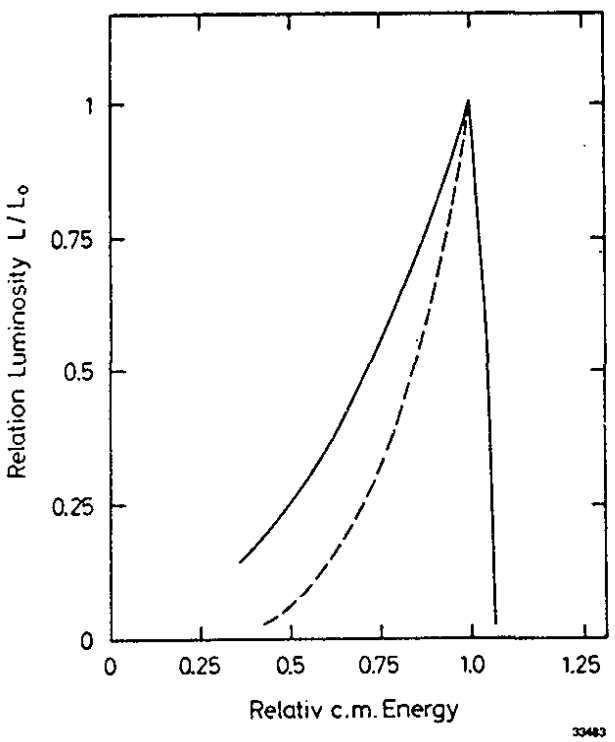

Fig. 2.2
Characteristic energy dependence of e^+e^- luminosity. The solid line represents the luminosity achieved by optimizing the emittance at each energy. The dashed line represents the luminosity for a constant optic.

From eqns 2.2 and 2.3 it then follows that the luminosity for constant β will increase as E^4 until a maximum energy E_{max} given by the available r.f. power is reached. According to eq. 2.1 the energy loss per turn increases as E^4 such that the r.f. power needed to produce the necessary energy gain per turn grows proportional to E^8. The available r.f. power is increasingly used to establish the accelerating field and the corresponding reduction in circulating current leads to a very rapid drop in luminosity above E_{max}.
The luminosity at lower energies can be increased above the E^4 dependence by increasing the beam emittance and hence the beam size. The emittance can be varied by either changing the focussing strength of the lattice (variable optics) or by the use of wiggler magnets. In this case the luminosity may vary as E^2. At high energies, where the r.f. power is the limiting factor, the luminosity may be increased by reducing the emittance - i.e. by increasing the focussing strength of the lattice.

The data on e^+e^- annihilation discussed below are from experiments performed at SPEAR and PEP at SLAC, DORIS and PETRA at DESY and CESR at Cornell. The start up dates of these accelerators and the nominal center of mass range are listed in Table 2.1.

Table 2.1

Ring	Start of operation	Center of mass energies (GeV)	Max.luminosity achieved $_{cm}^{-2}{}_{s}^{-1}$	Interaction regions
SPEAR, SLAC	1973	3 - 8	$1 \cdot 10^{31}$	2
DORIS, DESY	1974	3 - 10.5 (12)	$3.5 \cdot 10^{30}$	2
PETRA, DESY	1978	10 - 36.8 (45)	$1.7 \cdot 10^{31}$	4
CESR, Cornell	1979	8 - 16	$1 \cdot 10^{31}$	2
PEP, SLAC	1980	10 - 30	$7 \cdot 10^{30}$	6

Center of mass energies up to 12 GeV will be available at DORIS starting May 1982. The energy in PETRA will be increased in steps, 40.5 GeV will be available in the autum of 1982 and 45 GeV in 1983.

2.1.2 The experiments

Before we discuss the detectors it might be useful to recall the basic features of e^+e^- interactions.

In lowest order e^+e^- annihilate to a timelike current, electromagnetic or weak which couples directly[7-10] to the basic fermions as shown in Fig. 2.3. At the small distances involved in present e^+e^- experiments the quarks behave like free particles and quark and lepton pairproduction have therefore similar cross sections and angular distributions. At present energies the

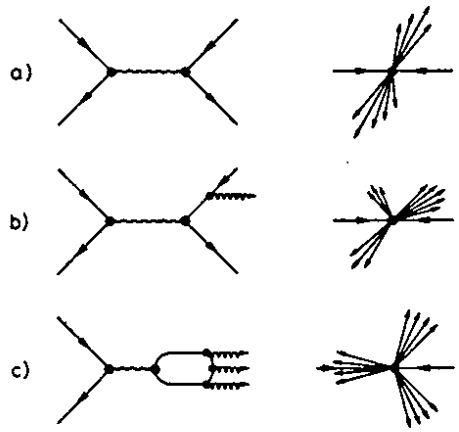

Fig. 2.3
Feynman graphs and topologies for α^2 processes in e^+e^- annihilation
a) $e^+e^- \rightarrow q\bar{q}$
b) $e^+e^- \rightarrow q\bar{q}g$
c) $e^+e^- \rightarrow 1^{--} \rightarrow ggg$

electromagnetic current dominates and the cross section for muon pairproduction is given by:

$$\sigma(e^+e^- \rightarrow \mu^+\mu^-) = \sigma_{\mu\mu} = 4\pi\alpha^2/3s = 86.8/s \text{ nb GeV}^2$$

where s is the c.m. energy squared.

The total cross section for hadron production is proportional to $\sigma_{\mu\mu}$ and the constant of proportionality R is given by:

$$2.4 \qquad R = \frac{(e^+e^- \rightarrow q\bar{q} \rightarrow \text{hadrons})}{\sigma_{\mu\mu}} = 3 \cdot \sum_i (e_i/e)^2 .$$

The sum is over all liberated quark flavours and the factor of 3 accounts for colour.

As the quarks start to move apart the confining force increases and new quark pairs are created from the vacuum. At distances on the order of 10^{-13} cm the quarks combine into colourless hadrons resulting in two acolinear hadron jets along the direction of the original quarks (Fig. 2.3a). At a center of mass energy of 36 GeV each jet on the average consists of 6 - 7 charged particles within a cone of an opening angle of 34^o. Roughly 65% of the total energy is carried off by charged particles. The angular distribution of the hadron jets with respect to the beam axis is $1 + \cos^2\theta$ reflecting the spin 1/2 nature of the quarks.

The outgoing quark may also radiate[11] a gluon[12] at a large angle resulting in three well separated hadron jets as indicated in Fig. 2.3 b.

The timelike current also couples directly to vector mesons as shown in Fig. 2.3 c. Below the threshold for new flavour production, these resonances are narrow and they decay[13] according to QCD[14] with three gluons in the intermediate state resulting in three jet events (Fig. 2.3 c). Hidden flavour states with even charge conjugation can be populated by photon emission from the vector states.

A new class of processes[15,16] depicted in Fig. 2.4a, b, occur to fourth order in α. The virtual photon cloud accompanying the electrons interacts directly $e^+e^- \to \gamma^*\gamma^* e^+e^- \to$ hadrons e^+e^-. This spacelike interaction can be divided in two groups depending whether the photon reveal its hadronlike or pointlike character. In the first case the photons convert into vector mesons which interact to produce a final state similar to that observed in hadron-hadron collisions, where the final state hadrons in general emerge with low transverse momenta with respect to the beam axis. A rough estimate of the $\sigma(\gamma\gamma \to \text{hadrons})$ using factorization yields

$$\sigma(\gamma\gamma \to \text{hadrons}) = (\sigma_{\gamma p})^2 / \sigma_{pp} \simeq 300 \text{ nb}$$

In the pointlike piece the photon couples directly to the quarks which fragments into hadron jets. The hadrons are distributed[17] roughly as $1/p_T^4$ with respect to the beam axis.

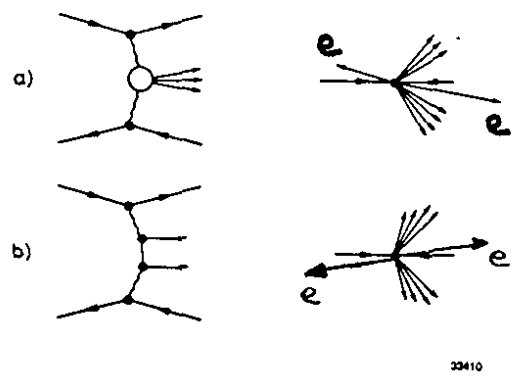

Fig. 2.4
Feynman graphs and topologies for some α^4 processes in e^+e^- interactions
a) $e^+e^- \to$ hadrons e^+e^-
b) $e^+e^- \to q\bar{q}\, e^+e^-$

The physics which can be investigated with an e^+e^- machine is therefore both rich and varied and this results in conflicting demands on the detector. Some of the factors which influence the detector design can be summarized as follows.

The total cross section is low resulting in some 100 annihilation events per day for an integrated luminosity of 400 nb^{-1} at 36 GeV. The detector should therefore cover a large solid angle. All annihilation events are accepted and the trigger is used only to reduce the beam gas background to an acceptable level. Since the annihilation physics is independent of angle there is no special incentive to cover the difficult region very close to the beam.

In the continuum the hadrons in general appear in well defined jets. The aim is to reconstruct the physics on the parton level from the particles in the jet. To this end charged particles and photons travelling close together must be measured and identified. Good electron (muon) identification within a jet is valuable to select either new physics or weak decays of heavy flavours. For onium spectroscopy the photon calorimeter must be able to measure low energy photons with good resolution.

Two photon physics imposes additional constraints on the detector. The energy and the Q^2 of the virtual photon can be determined from a measurement of the angle and the energy of the scattered electrons. This requires an electron detector which extends down to small angles with respect to the beam line. However, electrons radiating nearly real photons will escape down the beam tube. In this case the c.m. energy must be determined from a measurement of the final state particles. It is then important that the detector covers extreme forward and backward angles to catch particles which travel close to the beam line.

To see how these requirements are met we will discuss two different types of detectors, the JADE detector[18] as a representative of detectors based on a solenoidal field and the Crystal Ball[19], a non magnetic detector designed to measure photons with high resolution.

The main component of the JADE detector shown in Fig. 2.5 is a normal conducting solenoid which creates a longitudinal magnetic field of 0.5 T parallel to the beam axis. The coil is 3.5 m long with a diameter of 2 m.

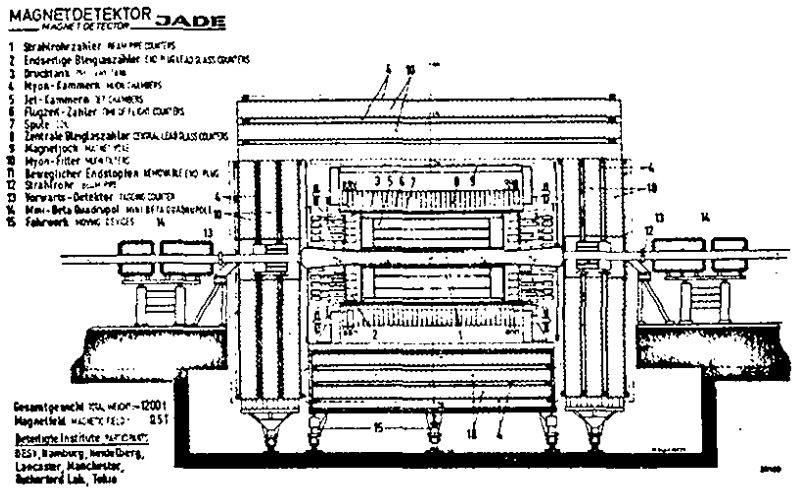

Fig. 2.5
The JADE detector at PETRA

Particle tracking is done using a drift chamber with a total of 48 coordinate space points along each trajectory: The azimuthal coordinate r and ϕ are measured to 160 μ using the drift information and the axial coordinate is measured by charge division to 1.6 cm. The double track resolution is 7 mm. In addition dE/dx information is available at each coordinate point. The chamber is 2.36 m long with an inner radius of 21 cm and an outer radius of 79 cm. A lead glass detector consisting of 2688 separate blocks is mounted outside the cylindrical part of the solenoid. The endcaps are covered by 2 x 96 counters. The whole detector is surrounded by a segmented muon detector made of a steel concrete absorber interleaved

with driftchambers. The region close to the beam is covered by counters used to determine the luminosity via a measurement of small angle Bhabha scattering or to measure the energy and direction of electrons in $e^+e^- \to X\, e^+e^-$.

The Crystal Ball detector[19] depicted in Fig. 2.6 is a non magnetic detector optimized for photon detection. Tracks emerging from the interaction region are detected by a set of proportional and magnetic chambers which measure charge over 94% in 4π and tracks over 71% in 4π defined by the last chamber. The chambers are surrounded by the main component of the detector, a 16 r.l. thick shell of NaI (Tl) which is subdivided into 672 units and stacked as a geodesic dome. The crystals are hermetically

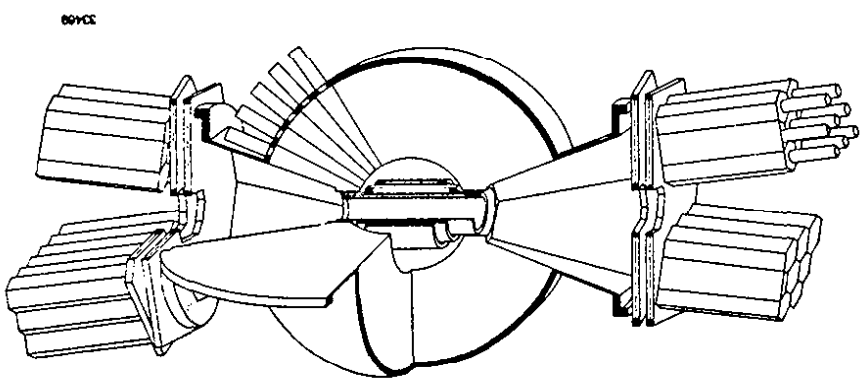

Fig. 2.6
The Crystal Ball detector at SPEAR

sealed in two hemispheres. These are normally in contact but might be moved apart to access the inner detector. The end cap detectors are made of planar magnetostrictive spark chambers followed by 51 cm long hexagonal NaI (Tl) crystalls. Muon detectors made of iron interleaved with proportional tubes, cover 15% of 4π and are centered at 90^o.

The energy of photons and electrons is measured with an resolution of $\sigma = 0.028 \cdot E^{3/4}$ GeV and the angle of the photon is determined to about 2.0^0. These properties of the Crystal Ball have led to the discovery of both the η_c and η_c' in the presence of a high background.

2.2 Beams and detectors in deep inelastic lepton-hadron interactions

2.2.1 Neutrino-experiments

The basic processes which can be studied[20] in neutrino-nucleon interactions are indicated in Fig. 2.7a and b. The incoming neutrino interacts with the quarks in the target via a charged or neutral current. In the case of charged current interactions the final state consists of a high energy muon, a hadron jet resulting from the fragmentation of the struck quark and hadrons from the target fragmentation. The jet and the target fragmentation are not separated at present energies. In the case of the neutral current interaction the muon is replaced by a neutrino which escapes the detector and a hadronic state similar to the one observed in charged current interaction.

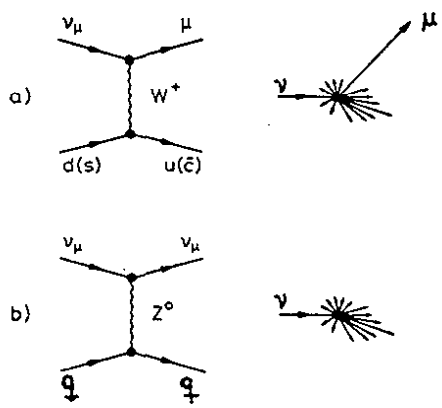

Fig. 2.7
Feynman graphs and topologies for neutrino-quark interactions
a) $\nu_\mu q \rightarrow \mu\, q'$
b) $\nu_\mu q \rightarrow \nu_\mu\, q'$

The two processes can be distinguished by the appearence or nonappearence of a high energy muon in the final state. Every high energy neutrino detector must therefore be capable of identifying high energy muons. In the case of the charged current interaction Q^2 and ν of the process are determined - if the energy of the incident neutrino is known -

by measuring the energy and the angle of the outgoing muon. In a neutral current event these quantities must be determined from a measurement of the final state hadrons. Hence it's important to measure the momentum and the production angles of both the muon and the hadrons in the event.

The total cross section, at present energies[21], for charged current interactions are given by $\sigma(\nu_\mu N \to \mu^- X) = 0.6 \times 10^{-38} E_\nu \cdot cm^{-2}$ for an incident neutrino beam and by $\sigma(\bar{\nu}_\mu N \to \mu^+ X) = 0.28 \times 10^{-38} E_\nu \cdot cm^{-2}$ for an incident antineutrino beam. These are very small cross sections and it requires both a high intensity neutrino beam and a large target mass to carry out detailed measurements of these processes.

The neutrino beams at high energy accelerators are tertiary beams resulting from the decay of secondary charged pions and kaons:

$$\pi^\pm \to \mu^+(\mu^-) + \bar{\nu}\ (\nu)$$
$$K^\pm \to \mu^+(\mu^-) + \bar{\nu}\ (\nu)$$

The twobody decay results in a neutrino spectrum which is flat up to the maximum energy which is given by $E_\pi(1 - m_\mu^2/m_\pi^2)$, respectively $E_K(1 - m_\mu^2/m_K^2)$. If the energy of the parent pion or kaon is known then it is sufficient to measure the angle of the neutrino to determine its energy. The neutrino beams originating from these twobody decays are contaminated on the few percent level by neutrinos from the decays

$$K^0 \to e\ \pi \nu_e \quad \text{and} \quad K \to \mu\ \pi\ \nu_\mu \ .$$

The neutrino beam line at the CERN SPS is shown schematically in Fig. 2.8. The primary proton beam is focussed on to a production target. The secondary hadrons emerging from the target are sign selected, their momenta are defined by a focussing device, and they are passed through a long decay

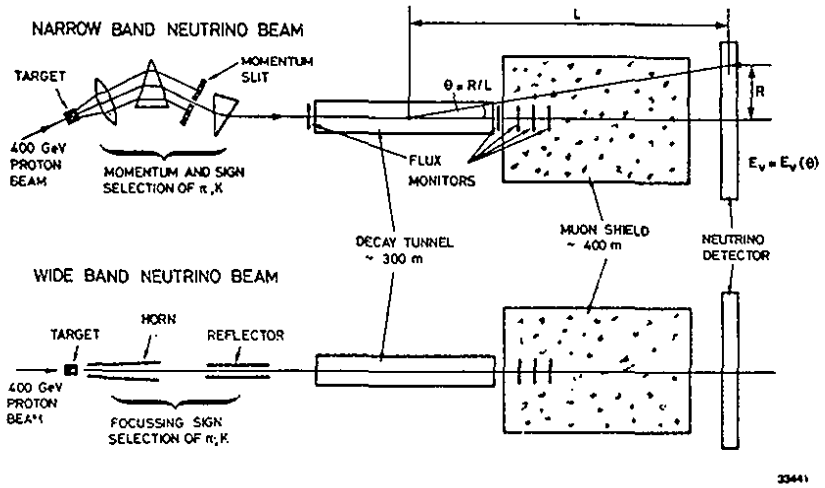

Fig. 2.8
Schematic layout of the CERN SPS neutrino beam line

region. At the end of the decay region the particles enter a massive 400 m long iron shield which absorbs remaining hadrons and muons. The length of the shield is set by the requirement that all decay muons are absorbed, this requires roughly 0.5 m of iron per GeV of muon energy. Detectors to monitor the neutrino flux are installed in the shield.

The energy spectrum of the broad band neutrino beam resulting from the decay of a hadron without well defined momenta is shown in Fig. 2.9.

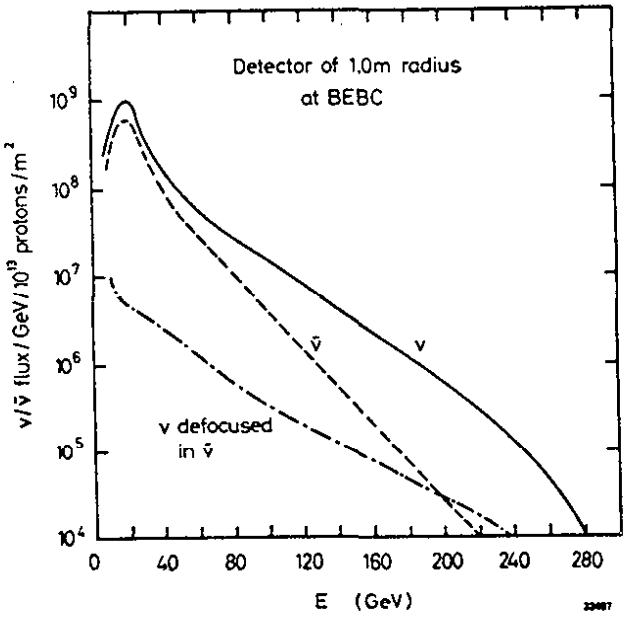

Fig. 2.9
The neutrino broad band energy spectrum

The flux of neutrinos and antineutrinos are given per GeV and m^2 for 10^{13} incident protons. The flux is measured with a 1 m radius detector at the position of BEBC. The spectrum is peaked around 20 GeV with a rapid, nearly exponential fall off towards larger energies. The neutrino flux near the endpoint energy is much higher than the antineutrino flux. This simply reflects the prepondereance of positively charged particles at high relative momenta. The rapid fall off with energy is one of the problems associated with a precise determination of the flux. The flux is monitored by both measuring the hadron beam and by observing the muons.

The intensity of the broad band beam is high but the neutrino energy is not known. The neutrino energy can be determined by momentum selecting the hadrons ("narrow band beam") and measuring the emission angle of the neutrino. The latter information is obtained by measuring the transverse distance from the beam center line to the event vertex. The neutrino energy as determined from a measurement by the CDHS detector of the final state particles is plotted versus the impact radius in Fig. 2.10. The upper band corresponding to $K \to \mu\bar{\nu}_\mu$ decays and the lower band resulting from $\pi \to \mu\ \bar{\nu}_\mu$ decays are clearly seen. The knowledge of the neutrino energy leads typically to a loss in flux by a factor 100.

The small cross section, the large size of the incident beam and the necessity to identify the muon and if possible measure its energy and angle makes it necessary to combine the target and the detector into a single unit. Examples of such devices are bubble chambers and calorimeter type electronic detectors.

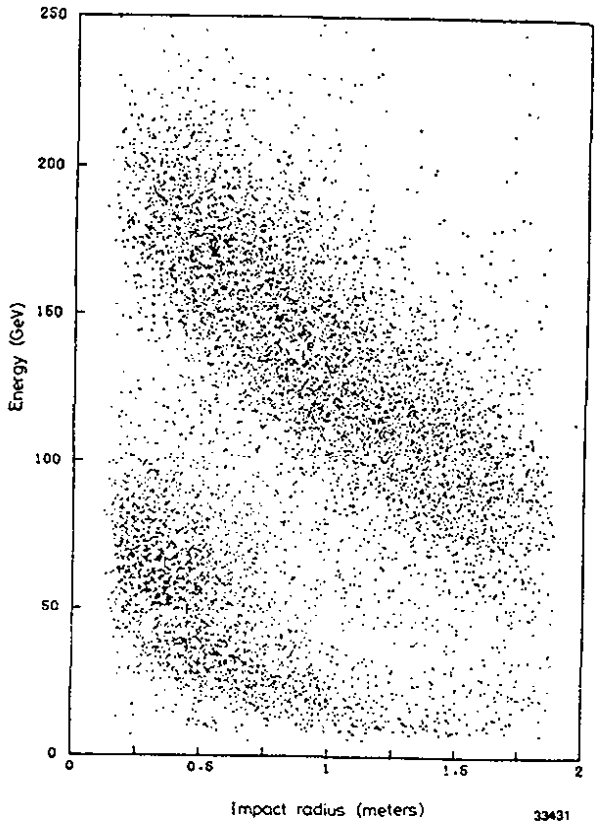

Fig. 2.10

Neutrino energy plotted versus the impact radius; the data are from CERN SPS narrow band neutrino beam

The bubble chambers offer high granularity, and can be filled both with light and heavy fluids. The draw back of a bubble chamber is its comparativly low mass. The big European bubble chamber BEBC[22] has a total volume of 32 m^3 and a fiducial volume of 10 - 20 m^3. It is surrounded by superconducting magnets producing a field of 3 Tesla. The chamber can be filled with hydrogen, deuterium or neon. Data have also been taken with a hydrogen target (TST) surrounded by liquid neon, attempting to combine the advantages of both fluids. Downstream, the chamber is followed by electronic detectors.

The second group of detectors is finely sampling hadron calorimeters of enormous dimensions. The CDHS [23] (CERN-Dortmund-Heidelberg-Saclay) detector is the first one shown in Fig. 2.11. The detector is modular, made of 19 magnetic torroids, each 3.75 m in diameter, weighing 65 tons. Each of the 7 units is subdivided into 15 five cm thick ironplates interleaved with scintillation counters. The remaining

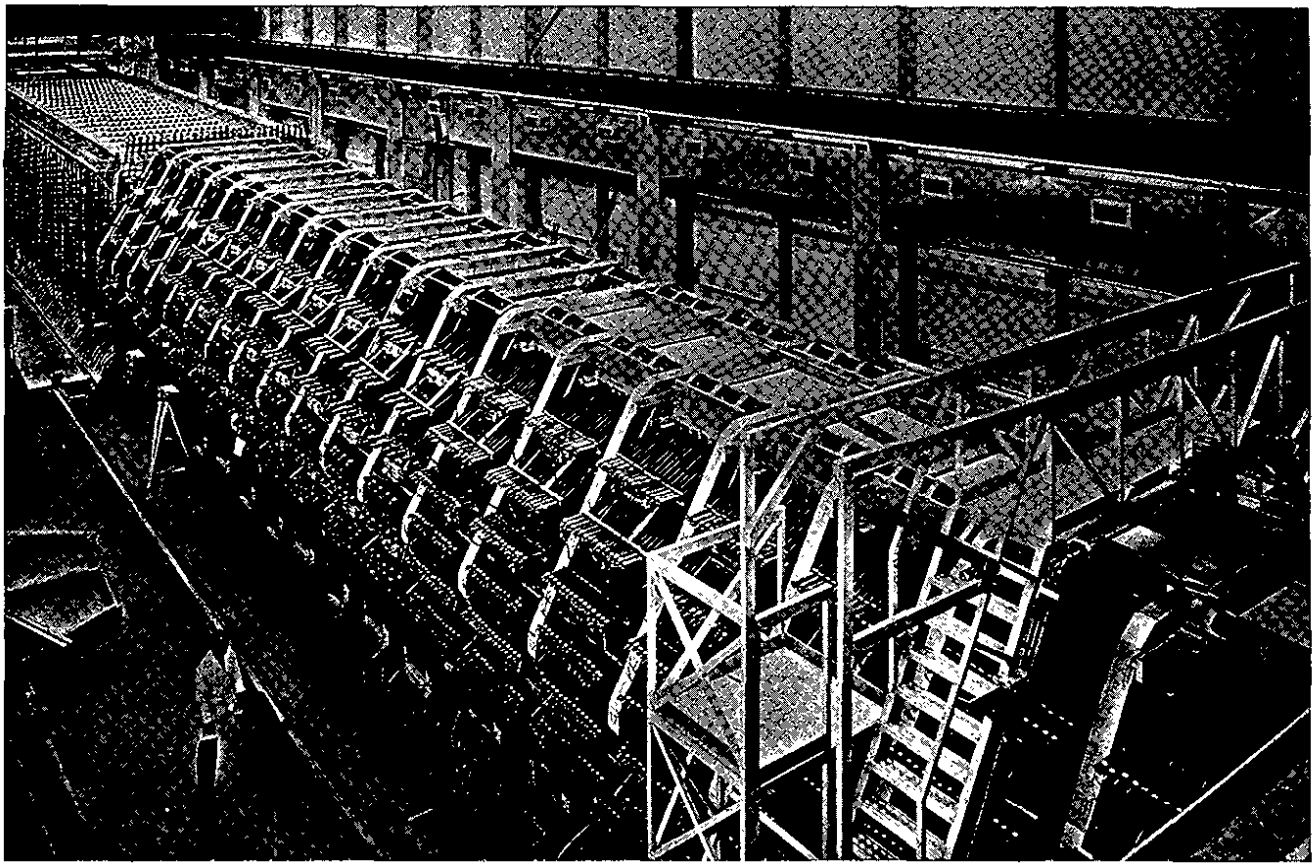

Fig. 2.11 - View into the CERN neutrino hall. The detector consisting of iron toroids and hexagonal driftchambers is the CDHS detector. The CHARM detector (square cross section) follows directly behind.

12 units are each made of five 15 cm thick ironplates and scintillators. The iron plates are magnetized by means of two vertical coils which produce an average field of 1.65 T in the plates. Three sets of drift wires are installed between each module to measure tracks. The detector has a fiducial good resolution mass of 400 tons and an additional 800 tons with poorer resolution.

The CHARM[24] (CERN-Hamburg-Amsterdam-Rome-Moscow) detector shown as the second one in Fig. 2.11 is a finely grained calorimeter capable of measuring the energy and direction of hadronic showers. Its primary goal is to investigate neutral current events.

The detector consists of 80 sheets of 80 mm thick marble 3 x 3 m^2 square. The sheets are surrounded by a picture frame magnet used to determine the charge sign of muons produced in charged current events.

2.2.2 Charged lepton experiments

The basic process which can be measured in muon (electron) nucleon interactions is shown in Fig. 2.12. In fact it was the famous deep inelastic electron-nucleon scattering experiments[25] at SLAC which gave the first direct evidence for pointlike constituents in the nucleon.

The incoming lepton interacts with a quark in the target by the exchange of a photon or a neutral weak boson (Z_o). The cross section at present energies is dominated by one photon exchange. The final state consists of a muon (electron) and as

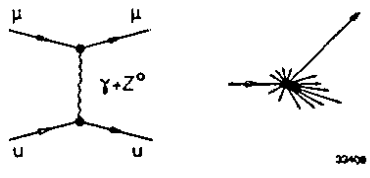

Fig. 2.12 - Feynman graph and topology for μ (e) q → μ' (e') q

in charged current interactions,of two hadron jets, one from the struck quark and the other from the target fragments. The jets are not separated at present energies. Clearly it is easier to reconstruct deep inelastic muon hadron events than neutrino hadron events since the former have charged leptons both in the initial and the final state. However, muon-hadron events have larger radiative corrections and the cross section is supressed by the photon propagator at large values of Q^2. The lepton may also interact with the quark via the charged weak current $\mu N \rightarrow \nu X$. The resulting cross section is very small at present energies and the events are more difficult to reconstruct due to the neutrino in the final state. Data on this process have not been reported.

The SLAC linear accelerator delivers a well defined high intensity beam of about 10^{14} electrons per second. The maximum energy has been increased to 33 GeV by shortening[26] the r.f. pulse length and increasing the peak power ((SLED). It is planned to increase the energy to 50 GeV and beyond using this scheme.

The decay of kaons and pions into muons and neutrinos is the source of the high energy tertiary muon beams at high energy proton machines. While at FNAL both decay products are used simultanously by bending the muons away from the neutrino beam, at CERN a special muon beam has been built. It consists of four parts. The front end accepts parent pions and kaons within an energy-dependent solid angle of 10 - 20 μsr in the forward direction and separates off the unused primary protons. A momentum band of

$\Delta p/P(\pi,K) \leq + 10\%$ is accepted by the second part, a FODO decay channel. This 600 m long channel consists of a regular array of large aperture quadrupoles, alternatively focussing and defocussing. The channel confine with small losses both the parent pions and kaons and also the decay muons. The third part, a hadron absorber, removes most of the pions and kaons remaining at the end of the decay channel. It consists of 10 m beryllium located at a focus within the aperture of the momentum selecting magents. Finally a back end consisting of two vertical bends and a 250 m FODO array selects the muons and transports them to the experiments. The effective momentum band is $\Delta p/p \simeq 5\%$. Per primary proton of 400 GeV incident on the production target $3.8 \cdot 10^{-5}$ positively charged muons with a momentum of 120 GeV/c are delivered to the experiment. The numbers for positively charged muons with momenta of 200 and 280 GeV/c are 1.4×10^{-5} and 1.8×10^{-6} respectively. For negative muons the fluxes are lower by a factor 2.5 - 5.

It is difficult to define the size of the muon beam due to the high penetration power of muons and special care has to be taken to avoid or at least detect halo muons. All detectors therefore start with a wall of veto counters to reject muons outside the acceptance. As a target, hydrogen, deuterium, carbon and iron has been used by the various experiments. The final state particles are measured by a magnetic spectrometer. Since the muon-nucleon cross section varies like $1/Q^4$ (with $Q^2 \approx 4\ EE'\ \sin^2\theta/2$), it is essential to measure the energies and directions of the in- and outgoing muons with similar precision. The detector of the EMC [27], shown in Fig. 2.13, is a good example for a high resolution muon scattering detector.

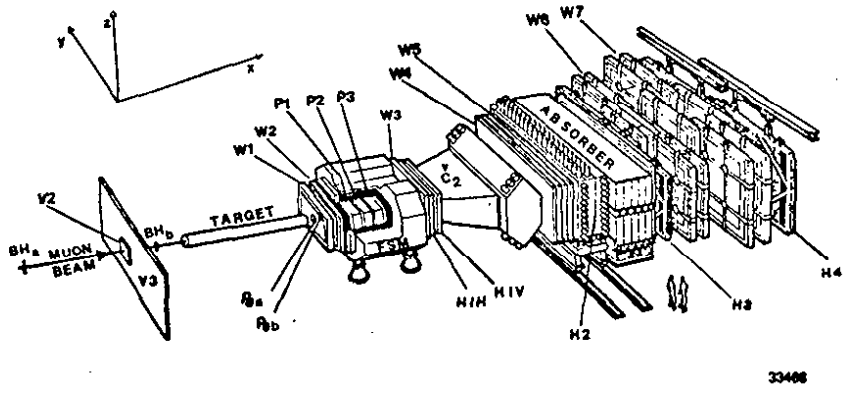

Fig. 2.13 - The detector used by the European Muon Collaboration EMC to measure deep inelastic muon interactions

To achieve the desired resolution in Q^2 and ν, the spectrometer consists of sets of driftchambers ($W_{1,2}$) installed in front and ($W_{3,4,5}$) installed at the back of a large aperture dipole magnet (FSM). The tracking through the magnetic field is done with proportional chambers ($P_{1,2,3}$). The large distances between the drift chambers and their good spacial resolution result in a momentum resolution of $\Delta p/p \simeq 10^{-4}$ p GeV/c at 5 Tm.

A multicell Cerenkov counter C_2 is used for particle separation in a limited momentum range. Thus muons are identified as tracks in the drift chambers W_6 and W_7 linking with one of the tracks in $W_{4,5}$.

A lead, iron, scintillator calorimeter with a depth of 5 interaction length is used to measure neutral particles. The calorimeter together with a 10 interaction-length deep iron block is used to remove the hadrons. While the EMC detector like the CHIO[28] (Chicago-Harvard-Illinois-Oxford) is designed as a general purpose detector, the BCDMS[29] (Bologna-Cern-Dubna-München-Saclay) detector is designed as a high statistics experiment. It is basicly a single arm spectrometer for the muons. It consists of a 55 m long magnetized iron torus with a 40 m carbon target in the central hole. Proportional chambers and scintillator hodoscopes measure the muon tracks. To be identified as a muon, it has to transverse at least 5.28 m of iron. This requirement introduces a cutoff in Q^2 ($Q^2 > 20$ GeV$^2/c^2$ at $E_\mu = 120$ GeV).

3. The Structure of the Electromagnetic and Weak Interactions

3.1 The standard model

The standard model is for the neutral current [30] based on the group $G = SU(2) \times U(1)$ and on a V-A interaction[31] for the charged current. The group SU(2) contains two massless gauge bosons $W^{\pm}$ and W^0 with coupling constant g and U(1) the massless gauge boson B^0 with coupling constant g'. The coupling constants are related to the electric charge:

$$3.1 \qquad e^{-2} = g^{-2} + g'^{-2} \; .$$

The gauge symmetry must be spontanously broken in order for the theory to be renormalizable. There is at present no consensus how this is achieved. In the standard model the symmetry is broken by introducing I = 1/2 scalar Higgs fields[32]. In this case we get massive $W^{\pm}$ bosons which mediate the charged weak current corresponding to the weak isospin raising and lowering operators $T_{\pm}$. The massless B^0, W^0 mix and we obtain two new bosons:

$$3.2 \qquad \begin{aligned} Z^0_\mu &= \cos\theta_W \, W^0_\mu - \sin\theta_W \cdot B^0_\mu \\ A_\mu &= \sin\theta_W \, W^0_\mu + \cos\theta_W \, B^0_\mu \; . \end{aligned}$$

The A_μ remains massless and can be identified with the photon coupled to the electric charge. The Z^0, however, will acquire a mass. In the standard model with I = 1/2 Higgs fields the Z^0 and the $W^{\pm}$ mass are related:

$$3.3 \qquad \rho = \frac{m^2_{W^{\pm}}}{m^2_{Z^0} \cdot \cos^2\theta_W} = 1$$

The Z^0_μ is coupled to a neutral current J^0_μ which is a mixture of the weak isospin current and the electromagnetic current:

$$3.4 \qquad J^0_\mu = J^3_\mu - 2\sin^2\theta_W \cdot J^{e.m.}_\mu$$

The mixing angle θ_W is a free parameter defined by $tg\theta_W = g'/g$. With this definition Eq. 3.1 becomes

3.5 $$e = g \cdot \sin\theta_W$$

At low values of q^2 the effective strength of the charged current interactions is given by

3.6 $$G_F / \sqrt{2} = g^2/8m_W^2$$

The $W^{\pm}$ mass and the Z^o mass can be expressed in terms of a single parameter $\sin^2\theta_W$ using equations 3.3, 3.5 and 3.6:

3.7 $$m_W = \frac{37.4 \text{ GeV}}{\sin\theta_W} \quad \text{and}$$

$$m_{Z^o} = \frac{37.4 \text{ GeV}}{\sin\theta_W \cdot \cos\theta_W} \quad .$$

To complete the model the transformation properties of leptons and quarks under SU(2) x U(1) must be specified.

In the standard model all fermions are arranged in left-handed weak isospin doublets:

3.8 $$\begin{pmatrix} \nu_e \\ e \end{pmatrix}_L \quad \begin{pmatrix} \nu_\mu \\ \mu \end{pmatrix}_L \quad \begin{pmatrix} \nu_\tau \\ \tau \end{pmatrix}_L$$

$$\begin{pmatrix} u \\ d' \end{pmatrix}_L \quad \begin{pmatrix} c \\ s' \end{pmatrix}_L \quad \begin{pmatrix} ? \\ b' \end{pmatrix}_L$$

and in right handed singlets. The fermions in the first two generations have all been found, whereas the last generation is still incomplete.

Measurements from PETRA show that the mass of the top quark - if it exists - must be above 18 GeV and the tau neutrino has not yet been observed directly.

The weak effective Lagrangian at low energies can be written as:

$$3.9 \qquad L_{eff} = \frac{G_F}{\sqrt{2}} \left(J^+_\mu J^+_\mu + J^0_\mu J^0_\mu \right) .$$

The lepton charged current is given by the doublet structure:

$$3.10 \qquad \nu_\ell \frac{1}{2} (1 - \gamma_5) \ell \qquad \text{with } \ell = e, \mu, \tau.$$

The quark charged current can be written as:

$$3.11 \qquad J^+_\mu = (\bar{u}, \bar{c}, \bar{t})\, \gamma_\mu \frac{1}{2} (1 - \gamma_5) \begin{pmatrix} d' \\ s' \\ b' \end{pmatrix}$$

It is generally assumed that the d', s' and b' quarks in the weak isospin doublets are related to the d, s and b quarks observed in the strong interactions by the Kobayashi-Maskawa matrix[33] analogous to the Cabibbo mixing in the four quark system

$$\begin{pmatrix} d' \\ s' \\ b' \end{pmatrix} = U \begin{pmatrix} d \\ s \\ b \end{pmatrix}$$

The mixing matrix U can be written in the form:

$$3.12 \qquad U = \begin{pmatrix} c_1 & -s_1 c_3 & -s_1 s_3 \\ s_1 c_2 & c_1 c_2 c_3 - s_2 s_3 e^{i\delta} & c_1 c_2 s_3 + s_2 c_3 e^{i\delta} \\ s_1 s_2 & c_1 s_2 c_3 + c_2 s_3 e^{i\delta} & c_1 s_2 s_3 - c_2 c_3 e^{i\delta} \end{pmatrix}$$

c_i and s_i are abreviations for $\cos\theta_i$ and $\sin\theta_i$, the generalized Cabibbo angles and δ is a complex phase which permits time violation.

The neutral current was defined in eq. 3.4. The axial g_A and vector g_V coupling of the fermions to the neutral current are then given by:

$$3.13 \qquad g_A = I_L^3$$
$$g_V = I_L^3 - 2Q \cdot \sin^2\theta_W$$

where Q is the charge and I_L^3 the third component of weak isospin (eq. 3.8). They are explicitly listed in Table 3.1 for the various fermions.

Table 3.1 - *Fermion neutral current coupling constants*

Fermion	g_A	g_V
ν_e, ν_μ, ν_τ	1/2	1/2
e, μ, τ	-1/2	$-1/2 + 2\sin^2\theta_W$
u, c, t	1/2	$1/2 - 4/3\sin^2\theta_W$
d', s', b'	-1/2	$-1/2 + 2/3\sin^2\theta_W$

A fit to the available data[34] gives $\sin^2\theta_W = 0.224$. The vector coupling constant of the neutral current to a charged lepton is therefore rather small.

3.2 Test of QED

QED predictions are based on the validity of Maxwell equations and on the assumption that leptons are pointlike objects without excited states. With e^+e^- machines these assumptions can be tested[35] at very small distances in a clean environment with only small and well defined corrections due to the strong interactions.

The Feynman graphs for Bhabha scattering, lepton pair production and two photon annihilation are shown in Fig. 3.1 and the differential cross sections for these processes at 31.6 in c.m. is plotted versus scattering angle in Fig. 3.2. All the cross sections scale with energy as 1/s with $s = (2E_{beam})^2$.

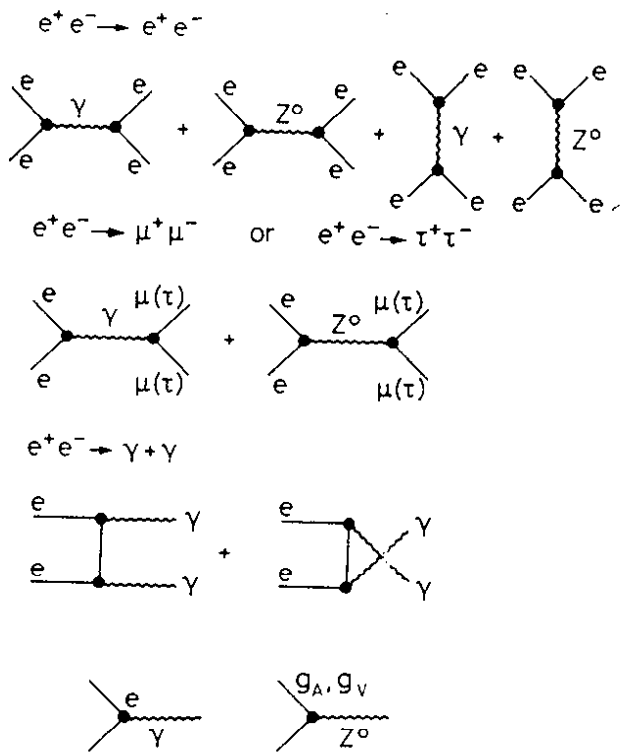

Fig. 3.1
The Feynman graphs for:
a) $e^+e^- \to e^+e^-$
b) $e^+e^- \to \mu^+\mu^-$ $(\tau^+\tau^-)$
c) $e^+e^- \to \gamma\,\gamma$

The interference of the weak and the electromagnetic currents leads to observable effects at the highest PETRA and PEP energies both in Bhabha scattering and in the forward-backward asymmetry in muon pair production. We will return to these effects after the discussion on QED limits.

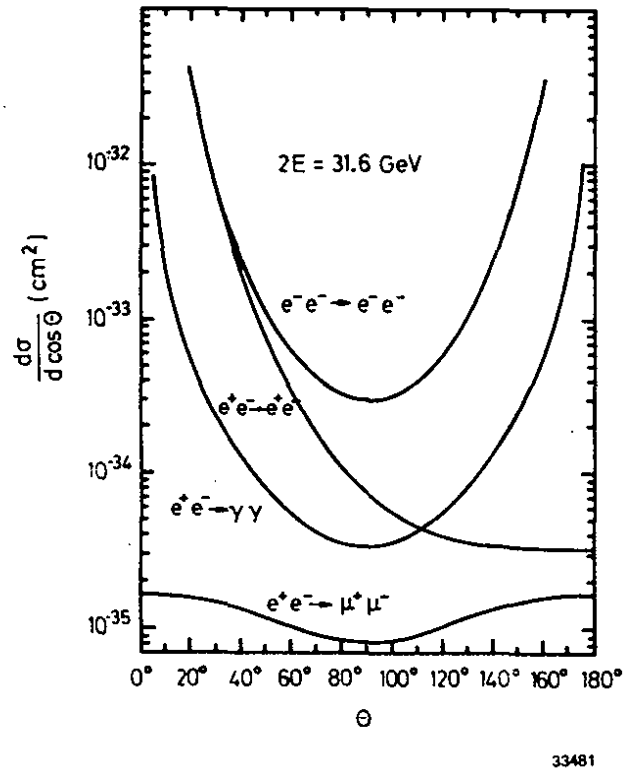

Fig. 3.2
Differential cross sections for two body QED reactions.

The standard procedure which is used to compare data with the QED predictions can be summarized as follows:

1) The data are corrected for weak effects assuming the Glashow-Salam-Weinberg model[30] with the standard values for $\sin^2\theta_W$. These corrections are small and in most cases negligible at present energies.

2) The measured cross section $d\sigma / d\Omega$ is corrected for radiative effects δ_R and effects due to the hadronic vacuum polarisation δ_H.

3.14 $$\frac{d\sigma}{d\Omega} = \frac{d\sigma_{QED}}{d\Omega}(1 + \delta_R + \delta_H).$$

3) The corrected cross section is compared to the QED predicted cross section and deviations are parametrized in terms of formfactors. The formfactors used for Bhabha scattering and lepton pair production can be written as:

$$F_s(q^2) = 1 \mp \frac{q^2}{q^2 - \Lambda_{s\pm}^2} \qquad 3.15$$

$$F_t(q^2) = 1 \mp \frac{s}{s - \Lambda_{t\pm}^2}$$

where F_s and F_t are respectively the formfactors for spacelike and timelike momentum transfers squared.

The differential cross section for $e^+e^- \to e^+e^-$ as measured by the various PETRA groups and normalized to the QED cross section are plotted[35] in Fig. 3.3 versus scattering angle. The data have been corrected for radiative effects and hadronic vacuum polarization but not for electroweak effects.

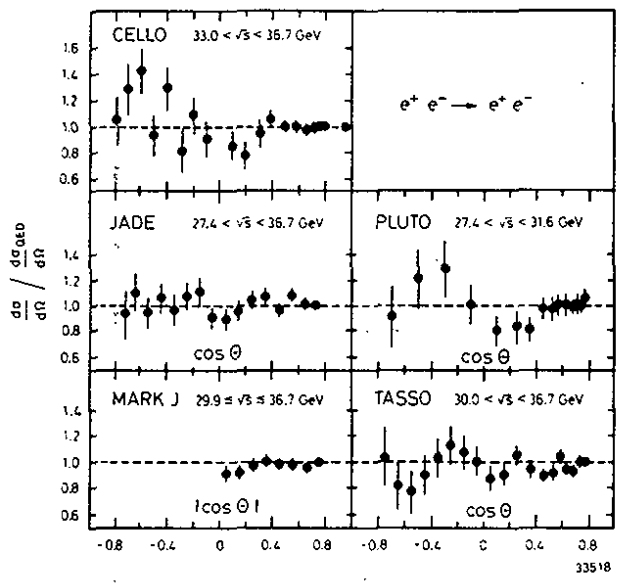

Fig. 3.3

Differential cross section for $e^+e^- \to e^+e^-$ divided by the QED prediction

The total cross sections for muon and tau pairproduction as measured by the PETRA groups are plotted[36] in Fig. 3.4 and Fig. 3.5 versus c.m. energy.

The data are in good agreement with the QED predictions shown as solid lines.

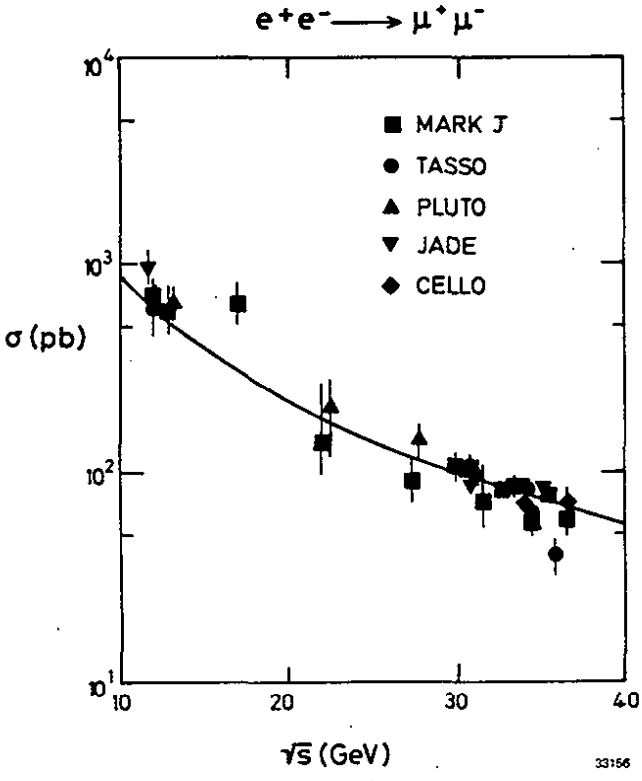

Fig. 3.4

The total cross section measured by the PETRA groups for muon pair production plotted versus c.m. energy. The solid line shows the QED prediction.

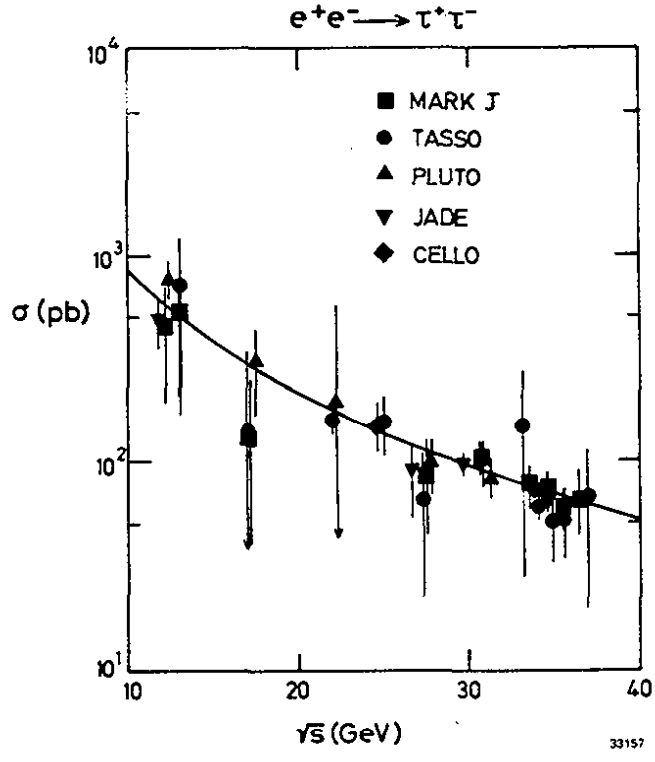

Fig. 3.5

The total cross section measured by the PETRA groups for tau pair production plotted versus c.m. energy. The solid line shows QED prediction.

The two photon annihilation process $e^+e^- \to \gamma\gamma$ proceeds by electron exchange in the t-channel. This reaction is unique among twobody QED reactions in that weak effects do not contribute to lowest order. The observed cross section is related to the QED cross section by

$$\frac{d\sigma}{d\Omega} = \frac{d\sigma}{d\Omega}_{QED} (1 + \delta_R + \delta_H + \delta_\Lambda)$$

where a breakdown of QED is parametrized by $\delta_\Lambda(s,\theta)$. Two possible breakdown mechanisms have been considered, the seagull term and the exchange of a heavy electron with coupling strength e and mass m. For the seagull term:

$$3.16 \quad \delta_\Lambda(s,\theta) = \pm \frac{s^2}{2\Lambda_\pm^4} \frac{\sin^4\theta}{1+\cos^2\theta}$$

and for the exchange of a heavy electron

$$3.17 \quad \delta_\Lambda(s,\theta) = \frac{s^2}{2\Lambda^4} \sin^2\theta \,.$$

The measured cross sections normalized to the QED prediction are plotted in Fig. 3.6. The data agree well with the QED prediction.

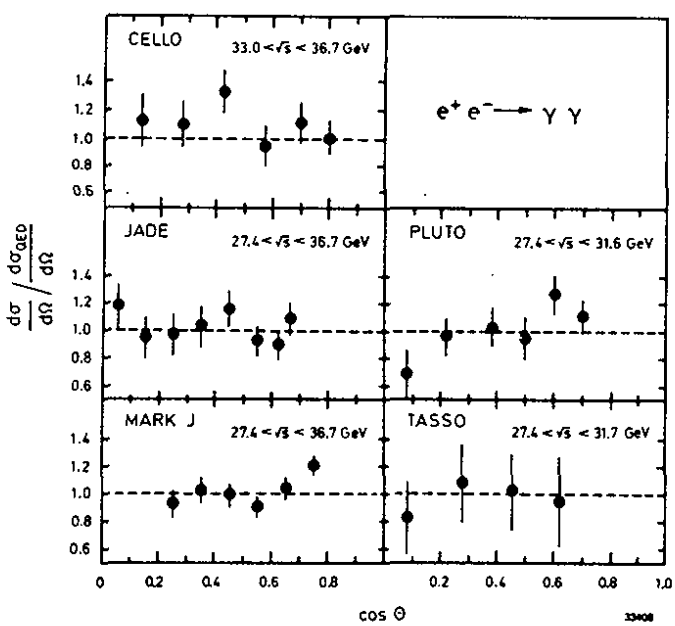

Fig. 3.6

The cross section for $e^+e^- \to \gamma\gamma$ measured by the PETRA groups normalized to the QED prediction.

Twobody QED reactions have been measured[37] by the MAC and by the MARK II Collaborations at PEP and also the data obtained by these groups are in agreement with QED.

The lower limits on the formfactor Λ extracted from a comparison between the data and the QED predictions are listed in Table 3.2. Equation 3.16 was

used in the case of $e^+e^- \to \gamma\gamma$. These data show that QED is valid down to distances of 10^{-16} cm and exclude a heavy electron with mass less than about 50 GeV and with a coupling strength e.

Table 3.2 - QED parameters: 95% confidence lower limits in GeV

Experiment	$e^+e^- \to e^+e^-$		$\mu^+\mu^-$		$\tau^+\tau^-$		$\gamma\gamma$	
	Λ_+	Λ_-	Λ_+	Λ_-	Λ_+	Λ_-	Λ_+	Λ_-
CELLO	83	155			139	120	43	48
JADE	112	106	142	126	111	93	47	44
MARK J	128	161	194	153	126	116	55	38
PLUTO	80	234	107	101	79	63	46	-
TASSO	140	296	127	136	104	189	34	42
MARK II							50	41

3.3 The neutral weak current in purely leptonic interactions

Neutrino-electron scattering gives information on the neutral weak interaction in a purely leptonic system. This current and its interference with the electromagnetic current have also been studied in $e^+e^- \to e^+e^-$, $e^+e^- \to \mu^+\mu^-$ and $e^+e^- \to \tau^+\tau^-$. The experimental results are discussed in this section.

3.3.1 Neutrino electron scattering

In principle four neutrino electron scattering processes are possible:

$$\begin{aligned} &\text{a)}\ \nu_e e^- \to \nu_e e^- \\ &\text{b)}\ \bar{\nu}_e e \to \bar{\nu}_e e^- \\ &\text{c)}\ \nu_\mu e^- \to \nu_\mu e^- \\ &\text{d)}\ \bar{\nu}_\mu e^- \to \bar{\nu}_\mu e^- \ . \end{aligned} \qquad 3.18$$

The processes (a) and (b) can occur through charged and neutral current interactions. The interference between these interactions gives information on possible scalar (S), pseudoscalar (P) and tensor (T) contributions to the neutral current amplitudes in addition to the vector (V) and axialvector (A) part. The cross sections[38] can be related to the V, A, S, P, T coupling constants:

3.19 $$\frac{d\sigma}{dy}(\nu_i e \to \nu_i e) = \frac{G^2 m_e E_\nu}{2\pi}[A_i + 2B_i(1-y) + C_i(1-y)^2]$$

where $i = \mu$ or e, and $y = \nu/\nu_{max}$.

3.20 $$A_\mu = (g_V^e + g_A^e)^2 + \left(\frac{C_S + C_P}{4}\right)^2 + \left(\frac{C_S - C_P - 4C_T}{4}\right)^2$$

$$B_\mu = B_e = C_T^2 - \left(\frac{C_S + C_P}{4}\right)^2 - \left(\frac{C_S - C_P}{4}\right)^2$$

$$C_\mu = C_e = (g_V^e - g_A^e)^2 + \left(\frac{C_S + C_P}{4}\right)^2 + \left(\frac{C_S - C_P + 4C_T}{4}\right)^2$$

$$A_e = \underset{\text{NC}}{A_\mu} + \underset{\text{CC}}{4} + \underset{\text{Interference}}{4(g_V^e + g_A^e)^2}$$

Neglecting S, P and T terms the total cross sections are (eq. 3.21):

3.21

$$\sigma(\nu_e e^-) = \frac{G^2 m_e E_\nu}{2\pi}(g_V^e + g_A^e + 2)^2 + 1/3\,(g_V^2 - g_A^2)^2 - \frac{m_e}{2E_\nu}[(g_V^e+1)^2 - (g_A^2+1)^2]$$

$$\sigma(\bar{\nu}_e e^-) = \frac{G^2 m_e E_\nu}{2\pi}\{(g_V^e - g_A^e) + 1/3(g_V^e + g_A^e + 2)^2 - \frac{m_e}{2E_\nu}[(g_V^e+1)^2 - (g_A^2+1)^2]\}$$

$$\sigma(\nu_\mu e^-) = \frac{G^2 m_e E_\nu}{2\pi}\{(g_V^e + g_A^e) + 1/3\,(g_V^e - g_A^e)^2 - \frac{m_e}{2E_\nu}[g_V^{e^2} - g_A^{e^2}]\}$$

$$\sigma(\bar{\nu}_\mu e^-) = \frac{G^2 m_e E_\nu}{2\pi}(g_V^e - g_A^e)^2 + 1/3\,(g_V^e + g_A^e)^2 - \frac{m_e}{2E_\nu}[g_V^{e^2} - g_A^{e^2}]$$

These equations describe four ellipses in a g_V^e - g_A^e plane which intersect in two points. Due to the small mass of the electron the cross sections are very small and high neutrino fluxes are needed to carry out the experiments.

There are no data on (a) since sufficiently high ν_e fluxes are not available. The reaction (b) has been measured[39] at a 1800 MW fission reactor with a flux of 2.2×10^{13} $\bar{\nu}_e/cm^2/s$. The main backgrounds are caused by inverse β decay ($\bar{\nu}_e\ p \rightarrow e^+ n$) and reactions induced by neutrons and photons. The inverse β-decay was identified and rejected by the e^+ annihilation and neutron capture. The latter processes were determined by varying the shielding and found to contribute less than 10%. A signal of 5.9 ± 1.4 events/day with $1.5 < E_e < 3.0$ MeV remained. The statistic is too poor to allow a definite conclusion on the interference term, but a destructive interference is slightly preferred[38]. The data confine the allowed g_A^e - g_V^e values to an ellipsoidal band as shown in Fig. 3.7.

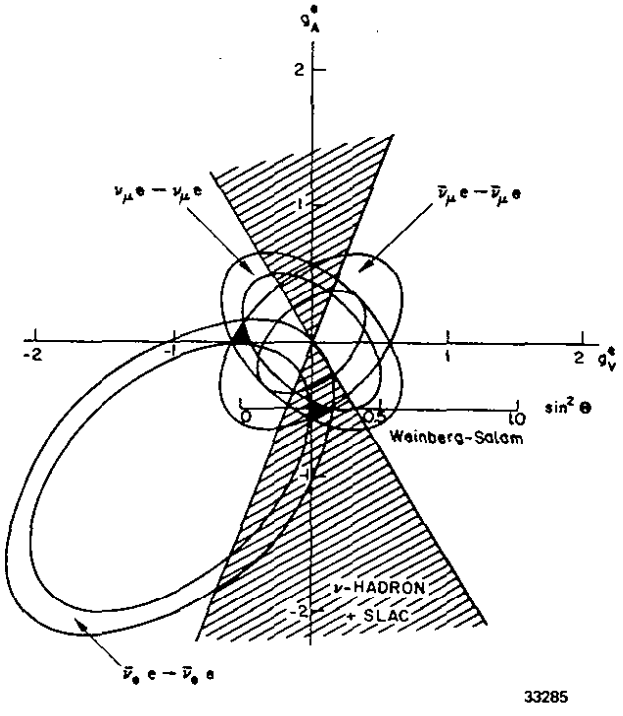

Fig. 3.7
Regions in the g_A^e, g_V^e plane allowed by the data for $\bar{\nu}_e\ e \rightarrow \bar{\nu}_e\ e$, $\nu_\mu\ e \rightarrow \nu_\mu\ e$ and $\bar{\nu}_e\ e \rightarrow \bar{\nu}_e\ e$. The ellipsodal bands are the 60% confidence limits.

The reactions (c) and (d) have been studied in high energy neutrino and antineutrino beams. The observation of $\bar{\nu}_\mu e \to \bar{\nu}_\mu e$ was in fact the first evidence for a neutral weak current. The discovery was made in the heavy liquid bubble chamber Gargamelle[40] at the CERN PS. Subsequently this reaction (d) and the reaction $\nu_\mu \to \nu_\mu e$ were investigated with Bubble chambers[41-46], visual spark chambers[47] and electronic detectors[48,49].

The world-averaged cross sections for neutrino lepton scattering are summarized in Table 3.3.

Table 3.3 - $\nu_\mu e^-$ and $\bar{\nu}_\mu e^-$ cross sections

Process	σ/E 10^{-42} cm^2/GeV	$\sin^2\theta_W$
$\nu_\mu e^- \to \nu_\mu e^-$	1.5 ± 0.3	$0.24 \pm {}^{0.06}_{0.04}$
$\bar{\nu}_\mu e^- \to \bar{\nu}_\mu e^-$	1.3 ± 0.6	$0.23 \pm {}^{0.09}_{0.23}$

The new results of the CHARM experiment[49] on the antineutrino cross section are not included in the above average. Fig. 3.8 shows the rate of observed events with an electron shower and no visible hadron in the final state as a function of $E^2\theta^2$(square of the momentum transfer). The (72 ± 16) $\bar{\nu}_\mu$ e events of this experiment with $q^2 = E^2\theta^2 < 0.12$ GeV^2 correspond to

$$\sigma/E = (1.7 \pm 0.33) \times 10^{-42} \text{ cm}^2/\text{GeV}$$

or in the GWS model

$$\sin^2\theta_W = 0.29 \pm 0.05.$$

The combined neutrino electron scattering data (Fig. 3.6) restrict the possible g_A^e, g_V^e values to the overlap-regions of three elliptical bands. Two possible solutions are left. The axial dominant solution has been fitted to

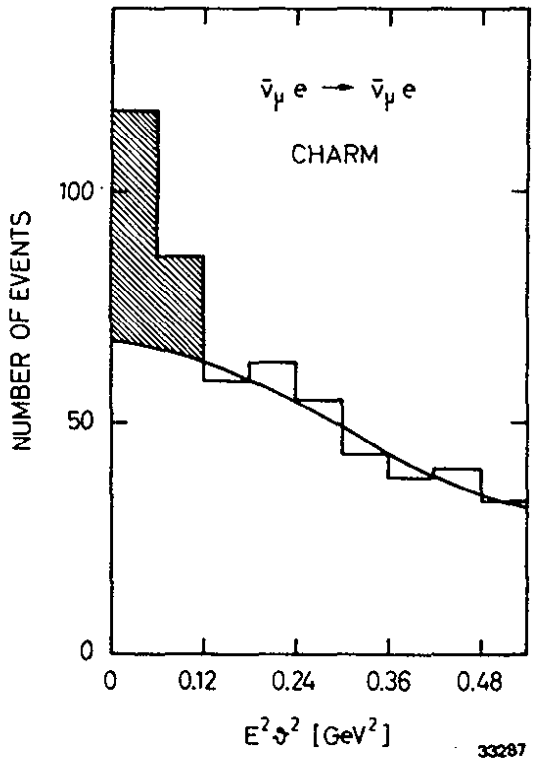

Fig. 3.8
Number of candidate events for $\bar{\nu}_\mu e \rightarrow \bar{\nu}_\mu e$ observed by the CHARM Collaboration plotted versus $E^2\theta^2$.

$$g_A^e = -0.52 \pm 0.06$$

$$g_V^e = 0.06 \pm 0.08$$

The second possible solution gives:

$$g_A^e = 0.06 \pm 0.08$$

$$g_V^e = -0.52 \pm 0.06$$

Data on either neutrino-quark and electron-quark scattering or from the e^+e^- storage rings are needed to resolve the ambiguity. The data from e^+e^- reactions are now sufficiently precise to observe weak electromagnetic interference effects such that a unique solution can be found using only leptonic data. This solution is excellent agreement with the Glashow-Weinberg-Salam model which predicts for $\sin^2\theta_W = 0.23$ the values $g_A^e = -0.5$ and $g_V^e = 0.04$.

3.3.2 Electroweak effects in e^+e^- annihilation

Including the neutral weak current will change [50] the normalized QED cross section for muon and tau pair production by ΔR and lead to a forward-backward charge asymmetry A in the final state.

At present PETRA and PEP energies the change in the normalized cross section

$$\Delta R = \frac{\sigma(\gamma + Z^0) - \sigma(\gamma)}{\sigma(\gamma)}$$

is given by:

$$3.22 \qquad \Delta R = -\left(\frac{G_F}{2\sqrt{2}\pi\alpha}\right)\frac{2s\, g_V^2}{(s/m_Z^2-1)} + \left(\frac{G_F}{2\sqrt{2}\pi\alpha}\right)^2 \frac{s^2(g_A^2+g_V^2)}{(s/m_Z^2-1)^2}$$

The forward-backward charge asymmetry is defined as:

$$A = \frac{\frac{d\sigma}{d\Omega}(\theta < 90^0) - \frac{d\sigma}{d\Omega}(\theta > 90^0)}{\frac{d\sigma}{d\Omega}(\theta < 90^0) + \frac{d\sigma}{d\Omega}(\theta > 90^0)}$$

A negative asymmetry results from an excess of negative muons along the initial e^+ direction. The asymmetry integrated over 4π, can be written at present energies as:

$$3.23 \qquad A_{\mu\mu} = \frac{3}{2}\left(\frac{G_F}{2\sqrt{2}\pi\alpha}\right)\cdot\frac{s\cdot g_A^2}{(s/m_Z^2-1)}$$

These quantities are plotted in Fig. 3.9 as a function of $s = (2E)^2$ for m_Z = 93 GeV and $\sin^2\theta_W$ = 0.23. Note that the Z^0 mass is increased from 89 GeV to 93 GeV by radiative corrections. At $\sqrt{s}$ = 35 GeV the model pre-

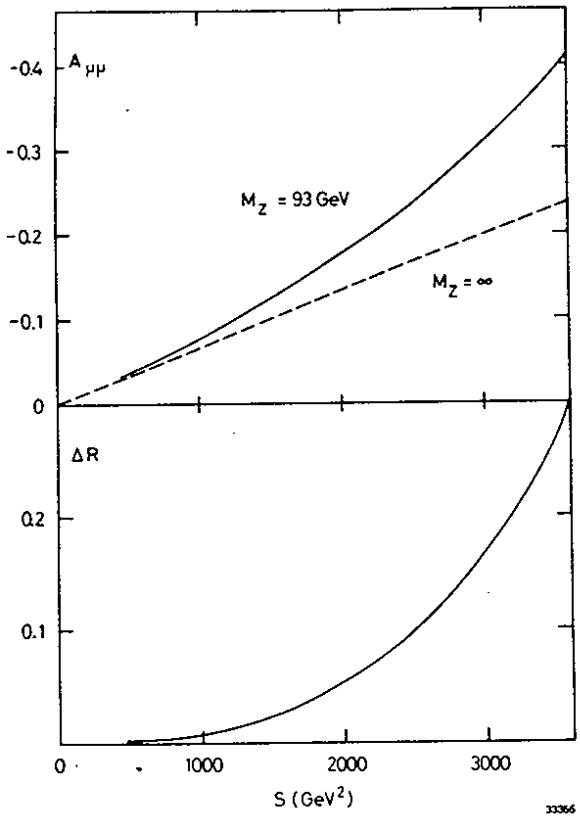

Fig. 3.9
Muon pair production in the Salam-Weinberg model evaluated for $\sin^2\theta_W = 0.23$
a) the forward-backward asymmetry plotted versus energy for $M_Z = 93$ GeV and $M_Z = \infty$
b) change in the cross section normalized to the QED cross section $\Delta R = [\sigma(\gamma+Z^0)-\sigma(\gamma)]/\sigma(\gamma)$.

dicts an asymmetry $A_{\mu\mu} = -9.6\%$ of which some 1.5% is due to the finite mass of the Z^0. ΔR is about 1.5% at 35 GeV and this results from the finite Z^0 mass. At 45 GeV, the highest PETRA energy with conventional cavities, it should be possible to determine the Z^0 mass by combining the total cross section and the asymmetry data. Mass effects can easily be measured at 60 GeV, an energy possible with superconducting cavities in PETRA.

The observed asymmetry must be corrected for radiative effects[51,52]. Some of the higher order QED diagrams produce muon pairs with even C and they interfer with the diagrams which lead to muon pairs with odd C to produce a positive charge asymmetry. The size of this asymmetry depends on the c.m. energy and on the experimental cuts which are used to select the data, i.e. minimum muon energy E_μ, the maximum value of the acollinearity angle ξ, and the acceptance in production angle θ. For typical conditions like $\xi \leq 20^0$, $E_\mu \geq 0.5\, E_{beam}$ and $|\cos\theta| < 0.8$ this asymmetry is +1.5% at $\sqrt{s}$ = 35 GeV. It is thus smaller than the asymmetry caused by the electroweak interference term and of opposite sign. All the data presented below have been radiatively corrected.

The angular distribution of the muons measured[53] by the JADE group at high energies is plotted in Fig. 3.10. The dotted line indicates the $1 + \cos^2\theta$ distribution for a pure electromagnetic current, the solid line shows the expected angular distribution including weak effects.

The value of the asymmetry extracted from these data is shown in Table 3.4 together with values[36] obtained by other PETRA groups.

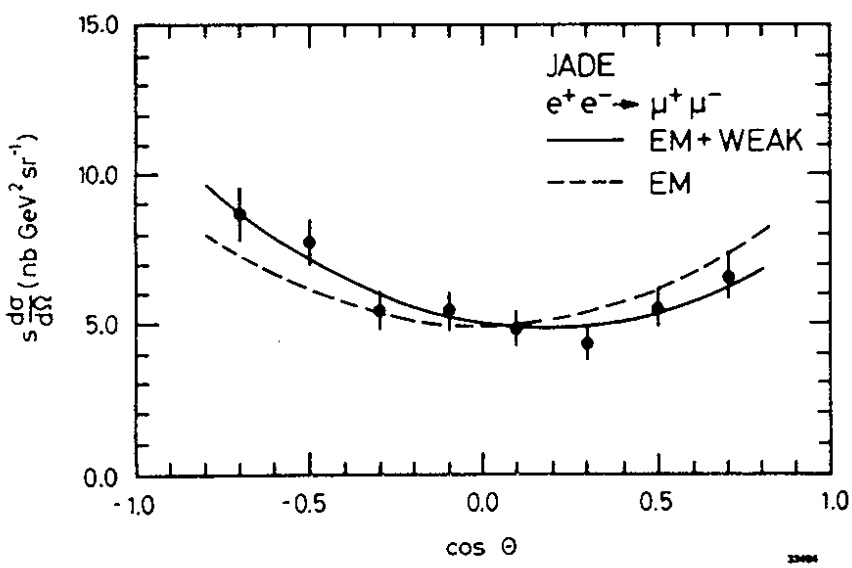

Fig. 3.10
The angular distribution in $e^+e^- \to \mu^+\mu^-$ as measured by the JADE Collaboration at c.m. energies and 35 GeV.

Table 3.4 - Charge asymmetry in muon and tau pairproduction

		JADE	MARK J	PLUTO	TASSO
$A_{\mu\mu}$	measured	-11 ± 4	-3 ± 4	7 ± 10	-11.3 ± 5
	predicted	-7.8	-7.1	-5.8	-8.7
$A_{\tau\tau}$	measured	-	-6 ± 11	-	0 ± 11
	predicted		-5		-7

The value quoted by TASSO was obtained by extrapolation to $|\cos\theta| \leq 1$. For the other experiments the asymmetry integrated over the detector acceptance, typically $|\cos\theta| < 0.8$ is given.

The systematic uncertainties are quite small and the data from the various groups can be combined. The resulting asymmetry [36] is $A_{\mu\mu} = -7.7 \pm 2.4\%$ with a χ^2 of 3.6 for 3 degrees of freedom. The result is in good agreement with the -7.8% predicted by the standard model and it yields

$$|g_A^e| = 0.5 \,{}^{+\,0.07}_{-\,0.09} .$$

This is the first evidence for a weak neutral current contribution in e^+e^- annihilation.

At PEP the muon asymmetry has been measured [37] by the MAC and the MARK II Collaboration at $\sqrt{s} = 29$ GeV. MAC finds $A_{\mu\mu} = (-0.9 \pm 5.2 \pm 1.5)\%$ and MARK II $A_{\mu\mu} = (-4.0 \pm 3.5)\%$.

The Bhabha data can now be used to set limits on $\sin^2\theta_W$. The difference between the observed cross section for Bhabha scattering and the QED prediction as measured by the MARK J Collaboration for center-of-mass energies between 14 GeV and 37 GeV is plotted versus $\cos\theta$ in Fig. 3.11. Only scattering angles between 0^o and 90^o can be measured since the charge sign of the outgoing lepton is not determined. The solid lines indicate the predictions based on the GWS model with $\sin^2\theta_W = 0.23$.

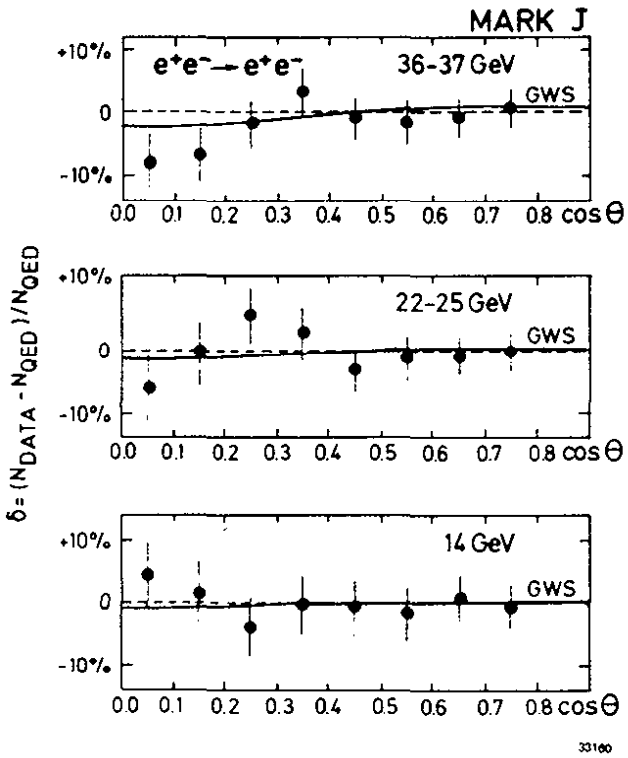

Fig. 3.11
The difference between the cross section for $e^+e^- \to e^+e^-$ as measured by the MARK J Collaboration and the QED prediction normalized to the QED prediction and plotted versus scattering angle.

The ratio of the experimental cross section to the QED cross section at a center of mass energy of 35 GeV is plotted versus $\cos\theta$ in Fig. 3.12. The data, obtained by the TASSO Collaboration are also compared with the standard theory for various values of $\sin^2\theta_W$. Although the present data are not yet sufficient to give a precise value of $\sin^2\theta_W$, they do limit the value of $\sin^2\theta_W$. Using all the available information the various groups have extracted the values for $\sin^2\theta_W$. These values are listed in Table 3.5.

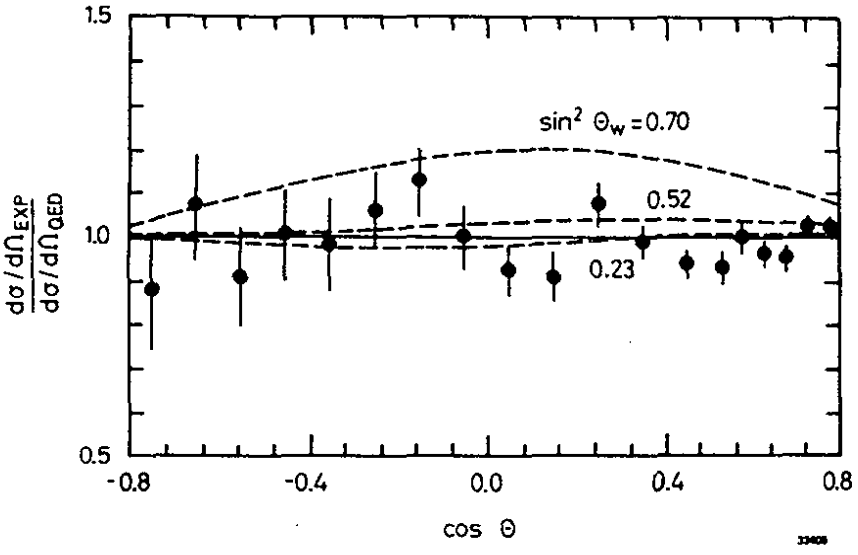

Fig. 3.12
The ratio of the measured cross section for $e^+e^- \to e^+e^-$ normalized to the QED cross section plotted versus cosθ. Predictions for the GWS model for various values of $\sin^2\theta_W$ are shown.

Table 3.5 - Values of $\sin^2\theta_W$ for purely leptonic reactions

Group	$\sin^2\theta_W$	input
CELLO	$0.22 \,^{+\,0.15}_{-\,0.10}$	e^+e^-, $\tau^+\tau^-$, $A_{\tau\tau}$
JADE	0.25 ± 0.15	e^+e^-, $\mu^+\mu^-$, $A_{\mu\mu}$
MARK J	0.25 ± 0.11	e^+e^-, $\mu^+\mu^-$, $\tau^+\tau^-$, $A_{\mu\mu}$
PLUTO	0.23 ± 0.17	e^+e^-, $\mu^+\mu^-$
TASSO	0.25 ± 0.10	e^+e^-, $\mu^+\mu^-$, $A_{\mu\mu}$
MAC	0.24 ± 0.16	e^+e^-
MARK II	$0.36 \,^{+\,0.09}_{-\,0.21}$	e^+e^-, $\mu^+\mu^-$

The 95% C.L. boundaries in a g_V, g_A plane as measured by the PETRA groups are shown in Fig. 3.13. They describe two well separated regions centered at $g_A = \pm 1/2$. If these data are combined with the elastic neutrino electron scattering data discussed above and replotted in Fig. 3.13 then we find a unique solution consistent with the assignment made in the GWS model, i.e. the axial coupling of the charged lepton is $g_A = -1/2$.

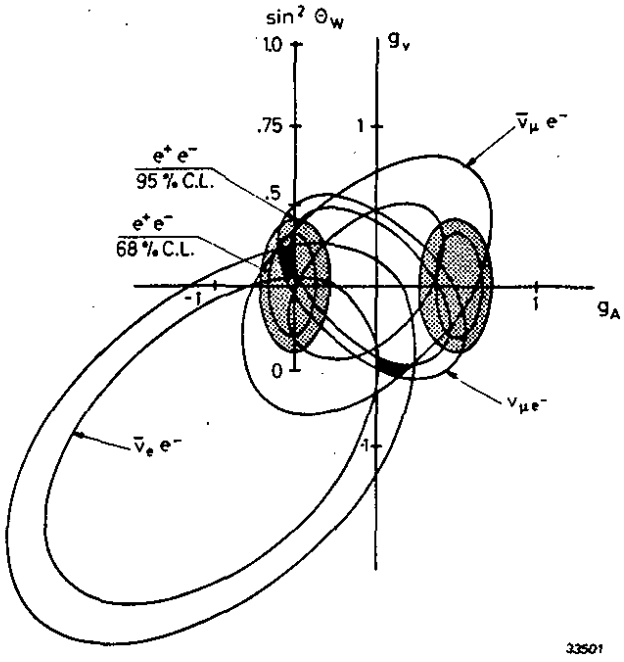

Fig. 3.13 - The 95% confidence limits for g_A and g_V as determined by combined PETRA data and compared to the 68% confidence limits extracted from the elastic neutrino-electron scattering data.

It is possible to construct models[54,55] which reproduce the low energy data but which have a much richer spectrum of vector bosons. In particular it has been pointed out that the low energy data can be reproduced in a model with an effective Lagrangian:

$$3.24 \quad \hat{L}_{eff} = L_{eff} + C \cdot \frac{4 \cdot G}{\sqrt{2}} (J._{e.m.})^2$$

In this class of models the vector coupling is modified to

$$3.25 \quad g_V^2 = \left(\frac{1}{2} - 2 \sin^2\theta_W \right)^2 + 4\,C$$

and g_V, g_A and g_A^2 remain unchanged.

The various groups working at PETRA have derived upper limits[36] on the value of C using the Bhabha scattering and the muon pair production data as an input.

Table 3.6 - 95% confidence upper limits on C

Group	Limit
CELLO	< 0.032
JADE	< 0.039
MARK J	< 0.027
PLUTO	< 0.06
TASSO	< 0.03

There are various ways to realize such models. For example[56] SU(2) x U(1) x U'(1) will have only one charged but two neutral vector bosons. In this case

3.26 $$C = \cos^4\theta_w \, (m_z^2/m_1^2 - 1) \, (1 - m_z^2/m_2^2) \, .$$

In this equation m_z is the mass of the Z^o in the standard SU(2) x U(1) model and m_1 and m_2 are the masses of two neutral bosons in the extended model.

It is also possible to construct a model with SU(2) x SU'(2) x U(1). Such a model[57] will have two charged and two neutral vector bosons, and in this case the $\cos^4\theta_w$ is replaced by $\sin^4\theta_w$. The limit on C can therefore be translated into limits on m_1 and m_2 using the expressions given above. The results are plotted in Fig. 3.14 for $C \leq 0.027$ (MARK J).

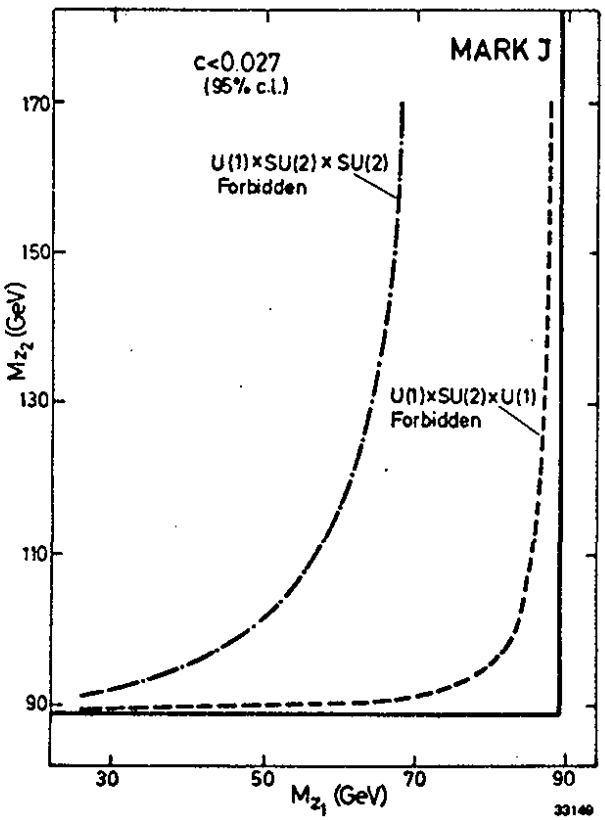

Fig. 3.14

Limits on the mass of neutral vector bosons.

3.4 The neutral weak current in mixed lepton-quark interactions

3.4.1 Neutral current neutrino quark interactions

Neutrino hadron interactions, inclusive, semi-inclusive and exclusive, determine[34,58,59] the neutral-current couplings to the light quarks u and d, also the first results on the neutral-current couplings to s and c quarks have been extracted from these data. As will be explained in chapter 9, the cross section for charged and neutral current neutrino interactions with an isoscalar target can be written as (eq. 3.27):

$$\frac{d\sigma^{CC}}{dy}(\nu N) = \frac{G^2 M_N E_\nu}{\pi}(Q + \bar{Q}(1-y)^2)$$

$$\frac{d\sigma^{CC}}{dy}(\bar{\nu} N) = \frac{G^2 M_N E_\nu}{\pi}(\bar{Q} + Q(1-y)^2)$$

$$\frac{d\sigma^{NC}}{dy}(\nu N) = \frac{G^2 M_N E_\nu}{\pi}\{[u_L^2 + d_L^2][Q + \bar{Q}(1-y)^2] + [u_R^2 + d_R^2][\bar{Q} + Q(1-y)^2]\}$$

$$\frac{d\sigma^{NC}}{dy}(\bar{\nu} N) = \frac{G^2 M_N E_\nu}{\pi}\{[u_L^2 + d_L^2][\bar{Q} + Q(1-y)^2] + [u_R^2 + d_R^2][Q + \bar{Q}(1-y)^2]\}$$

The contributions from the strange and the charmed sea are neglected, $y = E_{had}/E_\nu$ is the inelasticity. Q and $\bar{Q}$ are respectively the total quark and antiquark content, u_L, d_L, u_R and d_R are the chiral coupling constants of the neutral current to respectively u and d quarks assuming vector (V) and/or acial vector (A) couplings only.

The chiral coupling constants are related to the vector- and axial vector couplings by the simple relations:

3.28
$$g_A^u = u_L - u_R \qquad g_V^u = u_L + u_R$$
$$g_A^d = d_L - d_R \qquad g_V^d = d_L + d_R$$

The chiral coupling in the GWS model is related to the weak mixing angle θ_w as follows:

3.29
$$u_L^2 = \frac{1}{4} - \frac{2}{3}\sin^2\theta_w + \frac{4}{9}\sin^4\theta_w$$
$$d_L^2 = \frac{1}{4} - \frac{1}{3}\sin^2\theta_w + \frac{1}{9}\sin^4\theta_w$$
$$u_R^2 = \frac{4}{9}\sin^4\theta_w$$
$$d_R^2 = \frac{1}{9}\sin^4\theta_w$$

It is sometimes convenient to use Sakurais notation[60]:

$$
\begin{aligned}
u_L &= \tfrac{1}{4}(\alpha + \beta + \gamma + \delta) \\
U_R &= \tfrac{1}{4}(\alpha - \beta + \gamma - \delta) \\
d_L &= \tfrac{1}{4}(-\alpha - \beta + \gamma + \delta) \\
d_R &= \tfrac{1}{4}(-\alpha + \beta + \gamma - \delta)
\end{aligned}
\qquad 3.30
$$

If we assume that the neutral weak current does not change isospin by more than one unit, in analogy to the electromagnetic and the charged weak currents, then α, β, γ and δ have a very simple interpretation. In this case α represents the isovector vector, β the isovector axialvector, γ the isoscalar vector and δ the isoscalar axialvector fraction of the hadronic neutral current.

By adding or subtracting the NC cross sections (eq. 3.29) and normalizing to the CC cross sections one arrives at:

$$
3.31 \qquad R_+ = \frac{\sigma_{NC}(\nu N) + \sigma_{NC}(\bar{\nu} N)}{\sigma_{CC}(\nu N) + \sigma_{CC}(\bar{\nu} N)} = u_L^2 + d_L^2 + u_R^2 + d_R^2 + \text{corrections}
$$

$$
3.32 \qquad R_- = \frac{\sigma_{NC}(\nu N) - \sigma_{NC}(\bar{\nu} N)}{\sigma_{CC}(\nu N) - \sigma_{CC}(\bar{\nu} N)} = u_L^2 + d_L^2 - u_R^2 - d_R^2 + \text{corrections} .
$$

Equation 3.31 describes the total strength of the neutral current coupling, whereas equation 3.32 measures the VA interference.

If both right handed couplings, u_R and d_R, are zero, the interaction is pure V-A and accordingly pure V + A if the left handed couplings vanish. Pure V or A couplings require $u_L = u_R$ and $d_L = d_R$.

By defining $R_\nu = \dfrac{\sigma_{NC}(\nu N)}{\sigma_{CC}(\nu N)}$, $R_{\bar{\nu}} = \dfrac{\sigma_{NC}(\bar{\nu} N)}{\sigma_{CC}(\bar{\nu} N)}$

and $r = \frac{\sigma_{CC}(\bar{\nu}N)}{\sigma_{CC}(\nu N)}$, equations 3.31 and 3.32 can be combined to:

3.33 $$u_L^2 + d_L^2 = \frac{R_\nu - r^2 R_{\bar{\nu}}}{1 - r^2} + \text{corrections}$$

3.34 $$u_R^2 + d_R^2 = \frac{r(R_{\bar{\nu}} - R_\nu)}{1 - r^2} + \text{corrections} .$$

In the context of the GWS model equation 3.32 reduces to the well known Paschos-Wolfenstein relation[62]:

3.32 $$\frac{R_\nu - R_{\bar{\nu}}}{1 - r} = \frac{\sigma_{NC}(\nu N) - \sigma_{NC}(\bar{\nu}N)}{\sigma_{CC}(\nu N) - \sigma_{CC}(\bar{\nu}N)} = 1/2\ (1 - 2\sin^2\theta_w) + \text{corrections}$$

Recent data from CDHS[62], CHARM[63] and CITFRR[64] are summarized in table 3.7.

Similar results have been reported from earlier experiments. Clearly, the neutral current interactions are predominantly V-A but with an admixture of V+A, since $u_R = d_R = 0$ is ruled out.

Table 3.7 - Recent data on hadronic weak neutral current interactions

	CDHS	CHARM	CITFRR
R_ν	0.307 ± 0.008	0.320 ± 0.010	
$R_{\bar{\nu}}$	0.373 ± 0.025	0.377 ± 0.020	
r		0.498 ± 0.019	
R_+			0.330 ± 0.017
R_-			0.254 ± 0.037
$\sin^2\theta_w$	0.228 ± 0.018	0.230 ± 0.023	0.243 ± 0.015
$\lvert u_L\rvert^2+\lvert d_L\rvert^2$	0.300 ± 0.015	0.305 ± 0.013	0.292 ± 0.020
$\lvert u_R\rvert^2+\lvert d_R\rvert^2$	0.024 ± 0.008	0.036 ± 0.013	0.038 ± 0.020

To obtain more information on u_L, u_R, d_L and d_R one has to measure deep inelastic scattering on protons and neutrons or semi inclusive reactions. Ignoring the sea the NC/CC cross section ratios on protons and neutrons can be written as

3.36 $$R_p = \sigma^{NC}(\nu p) \,/\, \sigma^{CC}(\nu p) = 2\, u_L^{\,2} + d_L^{\,2} + \text{corrections}$$

3.37 $$R_n = \sigma^{NC}(\bar{\nu} N) \,/\, \sigma^{CC}(\nu N) = 2\, d_L^{\,2} + u_L^{\,2} + \text{corrections}$$

This determines the dominant left handed couplings up to a sign. The IMSTT - Illinois-Maryland-Stony Brook-Tohoku-Tufts-Collaboration obtains the following values[65] from a measurement of neutrino deuteron interactions in a bubble chamber:

$$R_p = 0.47 \pm 0.05$$
$$R_n = 0.22 \pm 0.02$$
$$R_\nu = 0.30 \pm 0.02$$

and derives

$$u_L^2 = 0.19 \pm 0.07$$
$$d_L^2 = 0.11 \pm 0.03$$

in reasonable agreement with previous results [66-70] and with the preliminary result of the BEBC-TST Collaboration [71]:

$$R_p = 0.530 \pm 0.045 \pm 0.030 \,.$$

The right handed couplings can be obtained from semiinclusive π^+, π^- production on isoscalar targets (the left handed couplings too) but the above described method gives more precise results.

The charged current interaction $\nu_\mu + d \to \mu^- + u$ on a valence d quark produces a u quark which subsequently fragments into charged pions with the probability D_u^+ and D_u^-. The number of observed pions coming from this primary process (i.e. with a high fractional energy $z = E_\pi/E_{had}$) is therefore proportional to D_u. The ratios of energetic positively and negatively charged pions resulting from (ν d) or ($\bar{\nu}$ u) interactions are related by

$$3.38 \qquad \left.\frac{N_\pi^+}{N_\pi^-}\right|_{\nu\to\mu} = \left.\frac{N_\pi^-}{N_\pi^+}\right|_{\bar{\nu}\to\mu} = \frac{D_u^{\pi^+}}{D_u^{\pi^-}} = \frac{D_d^{\pi^-}}{D_d^{\pi^+}}$$

For the neutral current reactions[72,73,74], both quark helicities are involved, the right handed being only $\frac{1}{3}$ as effective since $\int_0^1 (1-y)^2\, dy = \frac{1}{3}$. In an isoscalar target the π^+/π^- ratios are (3.39):

$$3.39 \qquad \left(\frac{N_\pi^+}{N_\pi^-}\right)_{\nu\to\nu} = \frac{[u_L^2 + \frac{1}{3}u_R^2]\, D_u^{\pi^+} + [d_L^2 + \frac{1}{3}d_R^2]\, D_u^{\pi^-}}{[u_L^2 + \frac{1}{3}u_R^2]\, D_u^{\pi^-} + [d_L^2 + \frac{1}{3}d_R^2]\, D_u^{\pi^+}}$$

$$\left(\frac{N_\pi^+}{N_\pi^-}\right)_{\bar{\nu}\to\bar{\nu}} = \frac{[u_R^2 + \frac{1}{3}u_L^2]\, D_u^{\pi^+} + [d_R^2 + \frac{1}{3}d_L^2]\, D_u^{\pi^-}}{[u_R^2 + \frac{1}{3}u_L^2]\, D_u^{\pi^-} + [d_R^2 + \frac{1}{3}d_L^2]\, D_u^{\pi^+}}$$

Experimentally[75] these ratios are

$$\left(\frac{N_\pi^+}{N_\pi^-}\right)_{\nu\to\nu} = 0.77 \pm 0.14$$

$$\left(\frac{N_\pi^+}{N_\pi^-}\right)_{\bar{\nu}\to\bar{\nu}} = 1.64 \pm 0.37$$

yielding[74]

$$u_R^2 = 0.03 \pm 0.015$$

$$u_R^2 = 0.00 \pm 0.015\ .$$

So far, the experiments allow a unique determination of the squares of the coupling constants, in particular d_R^2 is very small. Ignoring d_R^2 and defining the sign of u_L to be positive, the signs of the two products $u_L \cdot d_L$ and $u_L \cdot u_R$ have still to be determined. These products can be written in terms of the model independent notation[58]:

3.40
$$u_L \cdot d_L = \frac{1}{8}(-(\alpha+\beta)^2 + (\gamma+\delta)^2)$$
$$u_L \cdot u_R = \frac{1}{8}((\alpha+\gamma)^2 - (\beta+\delta)^2).$$

$u_L \cdot d_L < 0$ would be indicated by a strong isospin changing component in the hadronic neutral current; α and β are the isovector ($|\Delta I| = 1$) parts, likewise $u_L \cdot u_R < 0$ means a dominantly axial vector current (β and δ dominant).

The GGM Collaboration[76] observed a strong enhancement at the Δ in the reaction

$$\nu\, p \to \nu + p + \pi^0$$

which indicates a large isovector ($|\Delta I| = 1$) component in the neutral current i.e. $(\alpha+\beta)$ is dominant and $u_L \cdot d_L < 0$.

The neutrino disintegration of the deuteron[77] $\bar{\nu}_e + D \to \bar{\nu}_e + n + p$ is a pure isovector-axialvector (Gamov-Teller) transition near threshold. The $^3S_1(I=0)$ D-state goes into the $^1S_0(I=1)$ n-p state. This means that the transition is sensitive only to β.

Experimentally[77] one finds $|\beta| = 0.9 \pm 0.1$. Using the above data, the sign ambiguity of $u_L \cdot u_R$ can be transformed into two predictions for $|\beta|$

$$|\beta|_{\text{predicted}} = \begin{array}{ll} 0.92 \pm 0.14 & |\beta| \text{ large} = \text{axial vector dominant} \\ 0.58 \pm 0.14 & |\beta| \text{ small} = \text{vector dominant}. \end{array}$$

Clearly the solution $u_L \cdot u_R < 0$ is preferred.

Kim et al[34] have made a fit to all data available in 1980 arriving at the following values for the chiral coupling constants:

$$u_L = 0.340 \pm 0.033 \quad (0.347)$$
$$d_L = -0.424 \pm 0.026 \quad (-0.423)$$
$$u_R = -0.179 \pm 0.019 \quad (-0.153)$$
$$d_R = -0.017 \pm 0.058 \quad (0.077).$$

The numbers in brackets are the predictions of the GWS model for $\sin^2\theta_W = 0.23$.

Within the standard model the neutral current coupling to the quarks depends only on the charge and is independent[78] of the generation. Two experiments have reported measurements of the couplings to quarks belonging to higher generations.

The differential cross section for deep inelastic neutrino and anti-neutrino scattering on an isoscalar target can be written[79], with the assumption that the weak currents contain only V and A parts, as:

3.41

$$(d\sigma/dy)_{\nu\to\mu^-} = B\,[(1-\alpha^{\nu}) + \alpha^{\nu}(1-y)^2]$$
$$(d\sigma/dy)_{\bar{\nu}\to\mu^+} = B\,[(\alpha^{\bar{\nu}} + (1-\alpha^{\bar{\nu}})(1-y)^2]$$
$$(d\sigma/dy)\,(\bar{\nu}) \to (\bar{\nu}) = B\{(u^2_{L(R)} + d^2_{L(R)})\,[(1-\alpha^{\bar{\nu}}) + \alpha^{\nu}(1-y)^2]$$
$$+ (u^2_{R(L)} + d^2_{R(L)})[\alpha^{\nu} + (1-\alpha^{\bar{\nu}})(1-y)^2]$$
$$+ (s^2_R + s^2_L)\,(\alpha^{\bar{\nu}} - \alpha^{\nu})\,[1 + (1-y)^2]$$

By fitting these expressions to their measured y distributions for neutrino and antineutrino induced charged and neutral current events, the CHARM[80] Collaboration obtains for the coupling of the strange quark

$$s_L^2 + s_R^2 = (1.39 \pm 0.43) \cdot (d_L^2 + d_R^2)$$

in agreement with the expected universality.

The CDHS Collaboration[81] reported recently a value for the corresponding coupling of the charmed quark.

The dimuon mass spectrum of their neutrino induced dimuons shows a peak at the J/ψ mass, which is interpreted as the $c\bar{c}$ bound state produced via Z^0 and gluon fusion. Comparing the observed cross section for this channel of $(4.2 \pm 1.5) \cdot 10^{-41}$ cm^2/nucleon with that of J/ψ production by an incident muon, as measured by the European Muon Collaboration (EMC) and applying the gluon fusion model to both the photon-gluon and the Z^0-gluon vertex, a connection between the $u\bar{u}Z^0$ and the $c\bar{c}Z^0$ coupling can be derived. *In this model dependent way the authors conclude*

$$c_L^2 + c_R^2 = (1.6 \pm 0.5) \cdot (u_L^2 + u_R^2)$$

consistent with universality.

In summary, the neutral current coupling constants to the up, down, strange and charm quarks have been (at least partially) determined. The standard model with $\sin^2\theta_W \approx 0.23$ agrees extraordinarily well with all the available data.

In general, in SU(2) x U(1) models the relative coupling strength $\rho = m_W^2/m_Z^2 \cos^2\theta_W$ (eq. 3.3) is related to the Higgs fields and is equal to one if all Higgs bosons are in doublets.

In a general model the constants u_R, d_R, u_L, d_L etc. have to be replaced by [34]:

$$u_R \rightarrow \rho\, u_R + \rho\, T_{3R}(u)$$

$$d_R \rightarrow \rho\, d_R + \rho\, T_{3R}(d)$$

$$u_L \rightarrow \rho\, u_L$$

$$d_L \rightarrow \rho\, d_L$$

where $T_{3R}(i)$ is the third component of the weak isospin for the right handed component of the fermion i.

Kim et al.[34] have shown that the data are consistent with all right handed fermions being in singlets ($T_{3R}(i) = 0$). They find in a general fit to all available data

$$\rho = 1.018 \pm 0.045 \qquad \sin^2\theta_W = 0.249 \pm 0.031$$
$$T_{3R}(u) = -0.010 \pm 0.040 \qquad T_{3R}(d) = -0.101 \pm 0.058$$
$$T_{3R}(e) = 0.039 \pm 0.047 \ .$$

Assuming, that the third components of the weak isospin are all zero, they find, fitting polarized electron deuteron and deep inelastic scattering data:

$$\rho = 0.992 \pm 0.017 \quad (\pm 0.013)$$
$$\sin^2\theta_W = 0.224 \pm 0.015 \quad (\pm 0.015)$$

where the numbers in parentheses are the theoretical uncertainties. With the same assumptions the CHARM Collaboration[63] obtained from the total cross section for neutral current and charged current (anti) neutrino nucleon reactions for the left and right handed coupling constants:

$$g_L^2 = \rho^2(u_L^2 + d_L^2) = 0.305 \pm 0.013$$
$$g_R^2 = \rho^2(u_R^2 + d_R^2) = 0.036 \pm 0.013 \ .$$

Without constraining ρ, a nonzero value for the right handed coupling was measured (more than 90% C.L.).

The result can also be expressed in terms of the parameters ρ and $\sin^2\theta_W$:

$$\rho = 1.027 \pm 0.023 \qquad \sin^2\theta_W = 0.247 + 0.038.$$

Fig. 3.15 shows this result with the 1, 2 and 3σ contours.

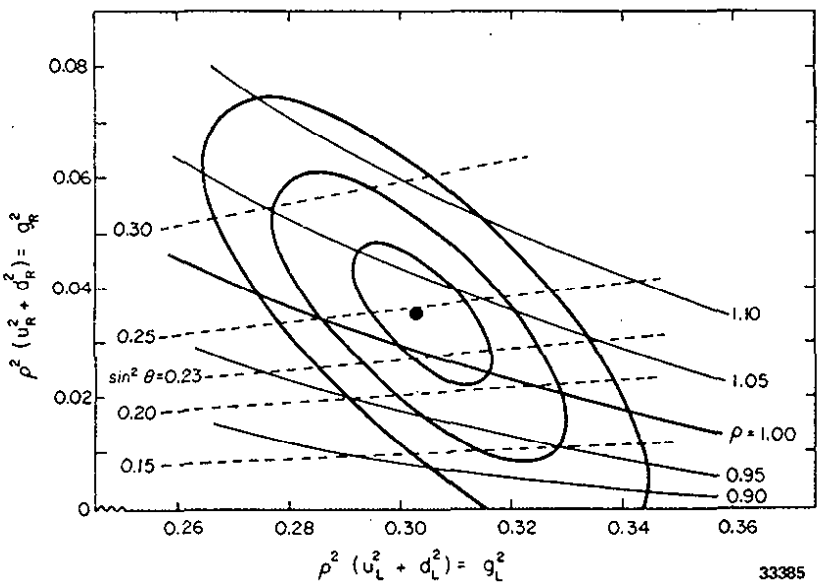

Fig. 3.15
Best fit and confidence limits of 39%, 87%, and 99% on the chiral coupling constants as determined by the CHARM experiment. The drawn curves are lines of constant ρ, and the dashed curves are lines of constant $\sin^2\theta_W$.

The measurements favour the assumption that right handed fermions are grouped in singlets, and Higgs bosons are in doublets, as in the standard model.

3.4.2 Electroweak interference effects in neutral current quark interactions

Electroweak interference effects have been studied over a wide range in q^2 from parity violations in atomic levels via deep-inelastic electron-deuterium scattering to electron-positron annihilation into hadrons. The available data are reviewed briefly below in order of increasing values of q^2.

The neutral weak current interaction between the electrons in the atom and the quarks in the nuclei induces[82] a small opposite parity part in the wave functions of the atomic levels. This parity violation is reflected in the radiative transitions; for example a dominant M1 transition will have a small E1 admixture. This parity violation is expected to be of the order of 10^{-4} (q^2/m_p^2). In atomic transitions $q^2 = (1/R_{atom})^2 = 10^{-5}$ MeV^2 resulting in a signal on the order of 10^{-15}. It was realized[83] that the effect scales as Z^3 resulting in a large gain for transitions in heavy nuclei. However, in order to extract a quantitative value the electron density at the nuclei must be computed and this introduces rather large uncertainties for heavy nuclei.

The parity violation in atomic transitions results from a linear combination of V_qA_e and A_qV_e. V and A are the axial and vector coupling constants of quarks and electrons as denoted by the subscript. The dominant contribution is from V_qA_e since the nucleons contribute coherently. The nucleon spin contributs to A_q but the contribution from individual nucleons tends to cancel. The matrix element of the V_q is in general expressed through the weak charge

$$Q_W = -4V_uA_e(2Z + N) + V_dA_e(Z + eN).$$

The experimental results are quoted using different quantities as the weak charge Q_W, R the ratio of the matrix elements for E1 to M1 or ϕ the amount of rotation due to parity violation. The results are listed in Table 3.8.

Table 3.8 - Results on parity violations in atomic physics

Element	λ	Quantity measured	Result	Prediction	Groups	Ref.
Bi	6476	R	$-20.2 \pm 2.7 \cdot 10^{-8}$	$-(11\text{-}17)\cdot 10^{-8}$	Novosibirsk	84
Bi	6476	R	$2.7 \pm 4.7 \cdot 10^{-8}$	- " -	Oxford	85
			$-10.7 \pm 1.5 \cdot 10^{-8}$			86
Bi	6476	$\Delta\phi_{PNC}$	$-0.22 \pm 1.0 \cdot 10^{-8}$	10^{-7}	Moscow	87
Bi	8757	R	$-0.7 \pm 2.1 \cdot 10^{-8}$	$-(8\text{-}13)\cdot 10^{-8}$	Washington	88
			$-10.4 \pm 1.7 \cdot 10^{-8}$		- " -	89
Bi	2927	W_W	-155 ± 63	- 116.5	Berkeley	90

The range in predicted values for the Bismuth data reflects the spread in the published calculations[91]. Thallium has a simpler electronic configuration and the estimates might therefore be more reliable. The data are now in reasonable agreement with the standard model predictions. Note, however, that there are still discrepancies by a factor of two between different groups. These are very difficult experiments and a complete discussion can be found in reference 92.

The observation of a parity violation in deep inelastic electron (muon) hadron interactions is a unique signature for the interference between the electromagnetic and the neutral weak current (Fig. 2.13). In the SLAC experiment[93] parity violation was observed by measuring the cross section for inelastic electron deuteron scattering using right and left handed electrons.

In the experiment a 40% polarized electron beam with energies between 16 GeV and 22 GeV was passed through a deuterium target and the scattered electrons were observed at 4^0 using a single arm spectrometer. The quantity $A = [d\sigma_+ - d\sigma_-] / [d\sigma_+ + d\sigma_-]$, where $d\sigma_+$ ($d\sigma_-$) stands for the double differential cross section $d^2\sigma/d\Omega dE'$ for right (left) handed electrons, is then a measure of the parity violation. - The experimental data are shown in Fig. 3.16.

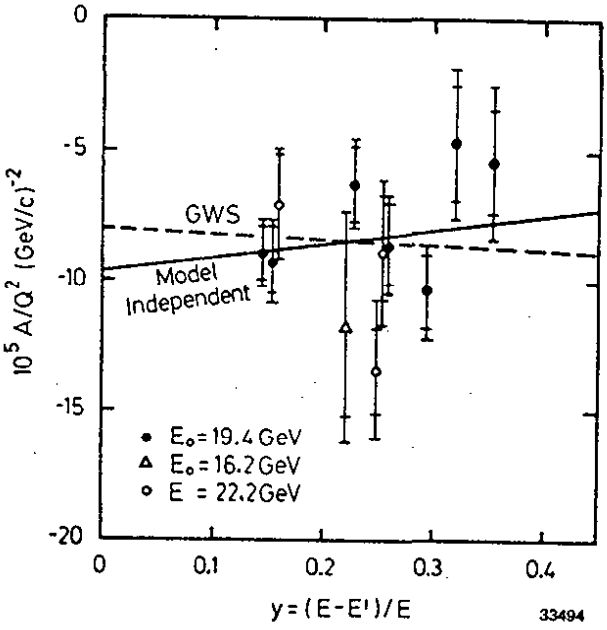

Fig. 3.16
The asymmetry A observed in polarized electron-deuteron scattering versus y. The dashed line shows best fit to the data in the GWS model resulting in $\sin^2\theta_{WS} = 0.224 \pm 0.02$. The solid line is a model independent fit.

The quantity A has been evaluated by Cahn and Gilman[94] in the parton model neglecting the sea contribution.

They find:

$$3.42 \qquad A/q^2 = -\frac{6G_F}{5\sqrt{2}\pi\alpha}\left[(v_u a_e - 1/2\, v_d a_e) + F(y)\,(a_u v_e - 1/2\, a_d v_e)\right]$$

v and a are the vector and axial vector coupling constants for u and d quarks and for electrons as indicated by the subscript. F(y) is defined by

$$3.43 \qquad F(y) = \frac{1 - (1-y)^2}{1 + (1-y)^2} \qquad \text{with } y = \nu/\nu_{max}\,.$$

A fit to the data[93] yields:

$$A/q^2 = ((-9.7 \pm 2.6) + (4.9 \pm 8.1)\, F(y)) \cdot 10^{-5}.$$

Expressed by the coupling constants this results in:

$$v_u a_e - 1/2\ v_d a_e = -0.23 \pm 0.06$$

$$a_u v_e - 1/2\ a_d v_e = 0.11 \pm 0.19\ .$$

In the standard model v and a are expressed by a single parameter $\sin^2\theta_W$ as listed in Table 3.1. A single parameter fit to the data yields

$$\sin^2\theta_W = 0.224 \pm 0.12 \pm 0.008$$

in good agreement with the values found in neutrino induced reactions.

Including the weak neutral current[50] in $e^+e^- \to q\bar{q} \to$ hadrons will lead to a forward-backward asymmetry and to a change in the total cross section. The size of the effects can be estimated within the GWS model using eqs. 3.22 and 3.23 suitably modified with the coupling constants listed in Table 3.1. At PETRA/PEP energies the expected asymmetry in $e^+e^- \to s\bar{s}$ ($d\bar{d}$, $b\bar{b}$) would be on the order of 25%. This is a sizable effect, however, it is at present not possible to identify the quark flavour from the hadrons in a jet. Therefore only the total cross section has been used to test the theory.

As an example, the normalized total cross section for hadron production as measured[95] by MARK J is plotted in Fig. 3.17 versus the c.m. energy. The data are compared to the theoretical expectations for various values of $\sin^2\theta_W$. The prediction also includes the first order QCD correction $(1 + \alpha_s/\pi)$. A similar analysis has also been done by the JADE Collaboration[96]. Including the leptonic data the groups find:

$$\text{MARK J} \qquad \sin^2\theta_W = 0.27\ ^{+\ 0.06}_{-\ 0.04}$$

$$\text{JADE} \qquad \sin^2\theta_W = 0.22 \pm 0.08\ .$$

The error quoted by the JADE group includes a statistical error of 3%, an error of 3% resulting from the assumed uncertainty of 20% in the value of α_s, and a 7% systematic uncertainty including the normalization error.

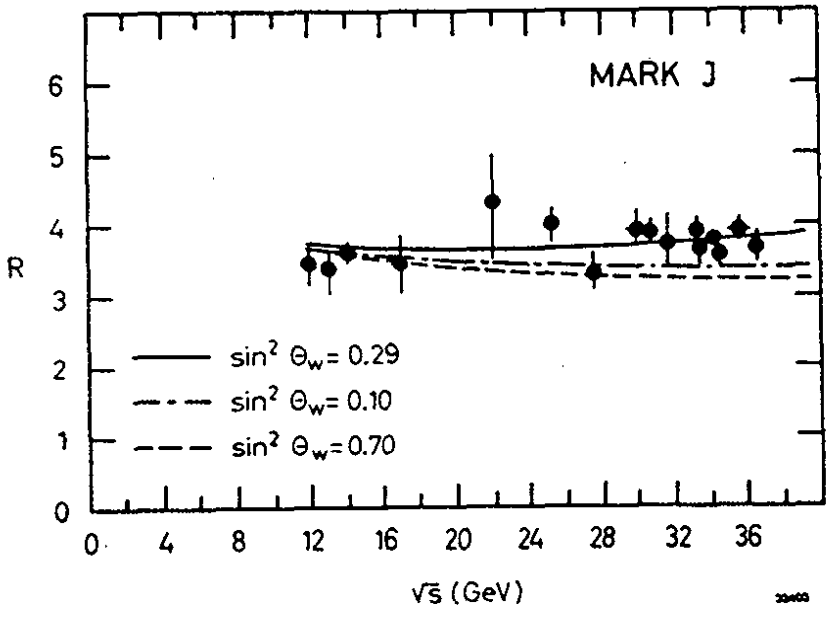

Fig. 3.17
The normalized total cross section for $e^+e^- \to$ hadrons plotted versus the c.m. energy. The data obtained by MARK J are compared to the expected weak effects for various values of $\sin^2\theta_w$.

3.5 Limits on flavour changing neutral currents

The $K^0\bar{K}^0$ mass mixing put stringent limits on the amount of neutral current induced $s \leftrightarrow d$ transitions. In the standard model with the GIM mechanismn the neutral current is diagonal[97] in all flavours forbidding decays of the type shown in Fig. 3.18.

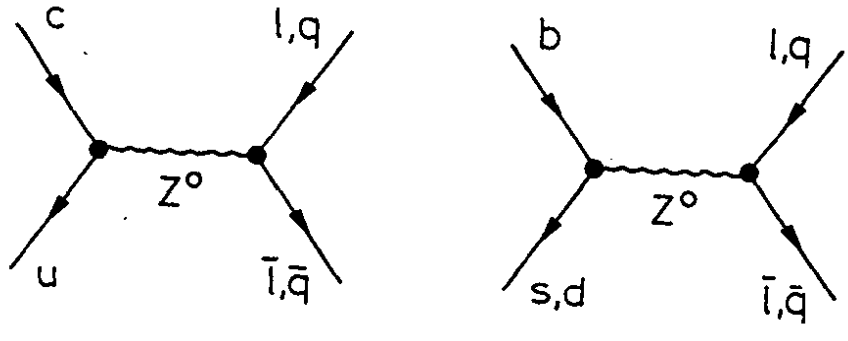

33514

Fig. 3.18 - Possible neutral current induced flavour changes

The MARK II Collaboration at SPEAR obtained limits on the amount of $c \leftrightarrow u$ transitions from a measurement of $E^0 - \bar{D}^0$ mixing. From a sample of initial $D^0\bar{D}^0$ events Goldhaber et al.[98] find

$$\frac{N(K^+K^+) - N(K^-K^-)}{N(K^+K^-)} < 18\% \qquad \text{(90\% upper C.L.)}$$

The same groups[99] also studied the process $e^+e^- \to D^{*+}D^{*-} \to (\pi^+D^0)(\pi^-\bar{D}^0)$. The amount of D^0-$\bar{D}^0$ mixing can now be determined from the number of wrong charge kaons. They did not observe a signal and from the data they set the limit

$$\frac{N(\pi^-K^-\pi^+) + N(\pi^+K^+\pi^-)}{N(\pi^-K^+\pi^-) + N(\pi^+K^-\pi^+)} < 16\% \ .$$

Combining the two experiments yield a theoretical upper limit on the coupling strength of 10^{-7} G_F for the strength of the flavour changing neutral current.

$$F_{FC} / \sqrt{2} \lesssim 10^{-7} G_F / \sqrt{2} \ .$$

Recently the CLEO group[100] at CESR has set a limit on the transition $b \leftrightarrow d$ (s). As a signature they used $e^+e^- \to B\bar{B} \to \ell^+\ell^-$ + hadron. Such final states will of course also arise from pair production of charm or beauty followed by two semileptonic decays $q \to \ell\, \bar{\nu}_e$ + hadrons. The number of observed and expected dilepton events are listed in Table 3.9.

The number of observed events is clearly consistent with the predicted background and they quote as an upper 90% C.L.

$$B(b \to \ell^+\ell^- + X) \leq 7.4 \times 10^{-3} \ .$$

Table 3.9 - Number of mixed dilepton + hadron events

Final state	ee + hadrons	eμ + hadrons	μμ + hadrons
Observed	5	5	0
expected background	3.04	6.04	3.04

3.6 The structure of the charged weak current

The standard V-A picture of charged weak currents[31] has been tested extensively[101] both in purely leptonic reactions and also in reactions involving hadrons. Of the leptonic reactions muon decay $\mu^- \to e^- \bar{\nu}_e \nu_\mu$ has given the most precise information[102]. Both the shape of the spectrum and polarization of the electron are in good agreement with the V-A prediction. A right handed $W^{\pm}$ must have a mass greater than 250 GeV if the corresponding neutrino is massless. The data on leptonic tau decay are also in agreement with a V-A structure.

The charged weak current involving hadrons is defined in the standard picture by eq. 3.11. The matrix[33] U describing the mass mixing is defined by Eq. 3.12. For a four quark system this reduces to the GIM model[78] with one parameter, the Cabibbo angle. A recent analysis[103] of Ke_3 data and baryonic decay data gave $\sin\theta_c = 0.219 \pm 0.011$. A large sample of hyperon semileptonic decays[104] gave $\sin\theta_c = 0.228 \pm 0.012$. Data on the couplings of the charm quark to lighter quarks are consistent with this value as discussed in chapter 5 and 9. Data[100] from Cornell (chapter 5) show that the b quark preferentially mixes with the s quark - i.e. the decay $b \to W^- c$ dominates $b \to W^- u$. Sakurai[101] has recently discussed in detail how the various elements U_{ik} are determined from the available data and finds:

$$U = \begin{pmatrix} 0.974 & 0.219 & 0.059 \\ -0.213 & 0.845 & -0.488 \\ -0.057 & 0.489 & -0.870 \end{pmatrix}$$

Also the data (chapter 4) on hadronic tau decays, although of limited statistics support the standard picture.

Most of the tests have been carried out at low values of Q^2. Recently two high energy neutrino experiments have shown that the V-A structure is also dominant at high values of Q^2. We will now discuss these experiments in more detail.

3.7.1 Muon polarization

The differential cross section [105] $d\sigma/dy$ of the reaction $\bar{\nu}_\mu N \to \mu^+ x$, where $y = E_x/E_\nu$, is proportional to

$$d\sigma/dy \sim 2(g_V - g_A)^2 + 2(g_V + g_A)^2 (1-y)^2 + (|g_S|^2 + |g_P|^2)\, y^2 + 32\, |g_T|^2 (1-1/2y)^2 + 8\, R_e\, [g_T\, (g_S^* + g_P^*)]\, y(1-y/2) \tag{3.43}$$

The g_i (i = V, A, S, P, T) denote the various coupling constants. An increase of $d\sigma/dy$ for $y \to 1$ is clear evidence for a S or/and P term. However, a y distribution decreasing with y, although expected is not a proof [106] for a pure V and A coupling. Such a behaviour may also result from a mixture of S, P and T interactions.

In the recent experiment [107] performed by combining the CDHS [23] and CHARM [24] detectors in the CERN-SPS neutrino beam the helicity of the μ^+ in the final state was measured. The incident antineutrinos are produced in π or K decay and have positive helicity while S, P or T interactions result in a negative helicity of the μ^+. The CDHS detector was used as an active target, while the CHARM detector was used as a polarimeter for the fraction (5%) of produced μ^+, which stopped in the CHARM detector and decayed via $\mu^+ \to e^+ \bar{\nu}_\mu\, \nu_e$. Due to the V-A structure of this decay, the high energy positrons are emitted preferentially in direction of the muon spin. A uniform magnetic field of 5.8×10^{-3} T caused the muon spin to precess.

The positron yield detected in the scintillator plane forward (in μ-flight direction) or backward relative to the stopping plane is thus periodically modulated with the Larmor frequency ω.

3.44 $$N_{B,F}(t) = N_o e^{-t/\tau}\{1 + R_o \cos(\omega t + \phi)$$

The asymmetry

3.45 $$R(t) = \frac{N_B - N_F}{N_B + N_F} = R_o \cos(\omega t + \phi)$$

is a periodic function. The phase ϕ describes the sign of the polarization (ϕ = 0 for negative polarization or S, P or T contribution). R_o is proportional to the magnitude of the polarization. The data (Fig. 3.19)

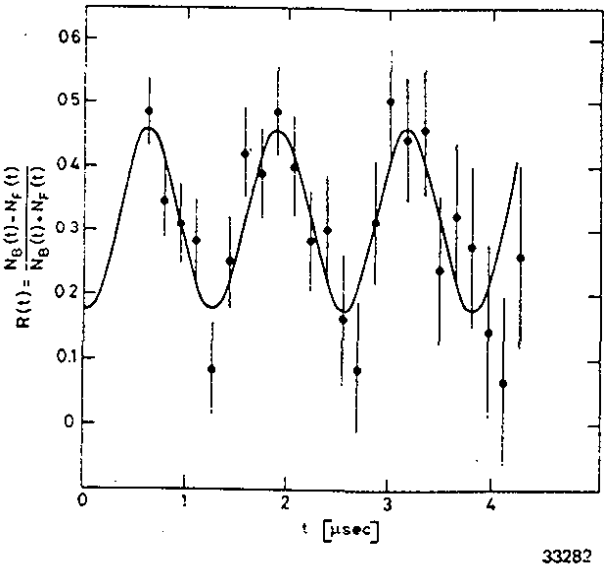

Fig. 29

Fig. 3.19

Oscillation pattern of the forward backward asymmetry of the muon decay.

show a sinosoidal oscillation pattern (ϕ = -3.1 ± 0.2) with no evidence for spin flip contributions. By evaluating the analyzing power with a Monte Carlo calculation, the polarization was determined to be P = +(1.09±0.22). The results put an upper limit of

$$\sigma_{SPT} / \sigma_{tot} < 0.18$$

at 95% confidence level on S, P, or T contributions.

3.7.2 Inverse muon decay

The inverse muon decay

$$\nu_\mu e^- \rightarrow \mu^- \nu_e$$

requires a threshold energy of $E_\nu \gtrsim 11$ GeV. It had therefore not been observed until recently by the Gargamelle[108] and CHARM[109] experiments in the CERN-SPS-neutrino beam. Motivated by the results of the polarization experiment, one can assume the absence of S, P and T contributions in this reaction. Then the differential cross section can be expressed as

3.46 $$d\sigma/dy \sim (1 + P)\ (1 - \lambda)y^2 + (1 - P)\ (1 - \lambda)$$

where $\lambda = -2R_e\ g_V^*/\ g_A\ /\ (|g_V|^2 + |g_A|^2)$ is the relative V-A contribution

3.47 $$P = \frac{N(\nu_R) - N(\nu_L)}{N(\nu_R) + N(\nu_L)}$$

is the polarization of the incident neutrino beam.

In events of the type $\nu_\mu e \rightarrow \mu^- \nu_e$ the muon is produced in a very narrow cone, $\theta_\mu = \sqrt{2m_e(1-y)/E_\mu}$, of less than 10 mrad. No recoil is visible at the vertex. These criteria have been used to discriminate against the four orders of magnitude more abundant events of the type $\nu_\mu N \rightarrow \mu^- x$. Additionally, the remaining background was experimentally determined using the data from an antineutrino exposure where the inverse muon decay cannot occur. Fig.3.20 shows the observed Q^2 distribution of the 171 $\pm$ 29 events remaining after subtraction of the background (CHARM). The dashed curve shows the shape of the Q^2 distributions for the 175 $\pm$ 5 events predicted by the V-A theory. A V+A interaction would result in 65 $\pm$ 2 events.

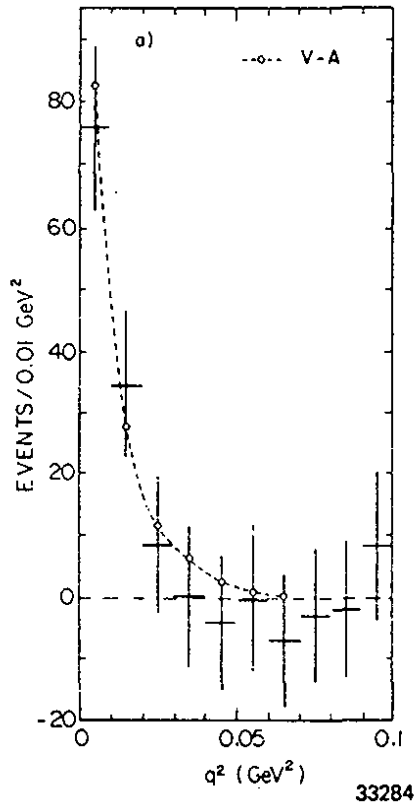

Fig. 3.20

Observed candidates for the inverse μ decay as a function of Q^2 (CHARM).

Fig. 3.21 shows the results of both the CHARM and GGM experiments in terms of upper limits (90% confidence) in the P-λ plane.

Both experiments are therefore consistent with a V-A structure of the charged weak current.

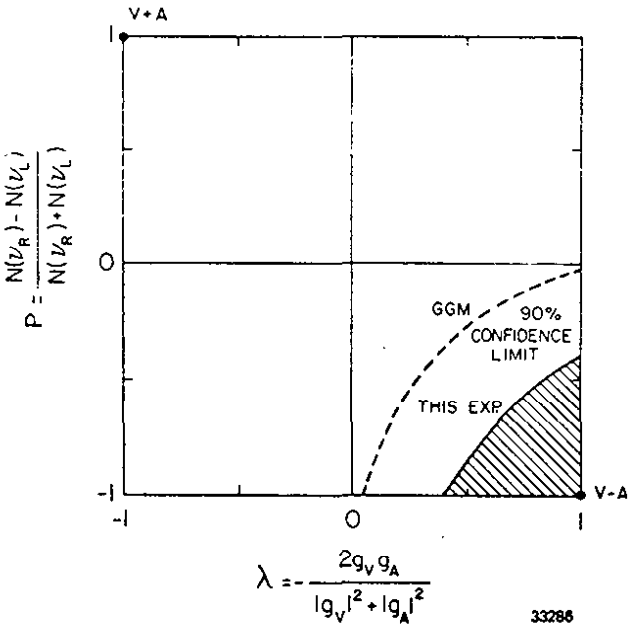

Fig. 3.21

The 90% confidence areas for the relative V-A contribution and the polarization of the incident neutrino beam. Results from GGM and CHARM.

3.7 Summary

The standard picture of the weak interaction outlined in chapter 3.1 has met with great success.

A wide range of neutral current phenomena ranging from atomic physics, purely leptonic reactions and mixed lepton-hadron interactions are described by the standard theory using only one free parameter $\sin^2\theta_W$ with[34] $\sin^2\theta_W = 0.233 \pm 0.009 \pm 0.005$. The best value[34] of the parameter ρ is $1.002 \pm 0.015 \pm 0.011$ in agreement with the value of 1 predicted if the symmetry breaking is caused by scalar Higgs fields with the Higgs particle in an isospin doublet. The standard model has only one Higgs doublet, but the predictions are independent on the number of such doublets. The value of $\sin^2\theta_W$ is determined in models which attempt to unify[110,111] the electro-weak and the strong interaction. The simplest of such models, SU(5)[111] predicts[112] $\sin^2\theta_W = 0.2109$ for purely leptonic reactions at $q^2 = 0$ in consistent with the experimental value.

All the experimental data on charged currents are consistent with a V-A structure of the interaction and mixing angles as given by the GIM mechanism[78] for a 4 quark system or by the Kobayashi-Maskawa[33] matrix for a six quark system.

The great success of the standard picture however, should not lead to the conclusion that weak interactions are solved. Anybody can write his own list of unsolved questions, some of which will hopefully be answered by the next generation of high energy accelerators.

4. The Tau Lepton

The first evidence[113] for the tau lepton, presented by M.Perl and his collaborators, was based on the observation of events of the type $e^+e^- \to e^{\mp} \mu^{\pm}$ + nothing. By now the tau is firmly established and a wealth of information[114] on its properties has become available.

4.1 The mass

The mass of a heavy lepton can be determined with rather high precision from a measurement of the sharply rising production cross section near threshold. Such measurement, first made by the DASP Collaboration[115], has been refined and the DELCO Collaboration[116] finds $m_\tau = (1782 \,^{+\,3}_{-\,4})$ MeV/c^2. The mass of the tau neutrino is rather poorly known. From a measurement of the electron spectrum in $\tau \to \nu_\tau \, \bar{\nu}_e \, e$ the DELCO Collaboration[116] establishes an 95% upper confidence limit of the $m_\tau < 250$ MeV/c^2.

4.2 The space time structure of the current

The DELCO Collaboration has determined [117] the Michel parameter $\rho = 0.72 \pm 0.10$ from a measurement of the electron momentum spectrum in $\tau \to \nu_\tau \, \bar{\nu} \, e$. A V-A interaction yields $\rho = 0.75$ in agreement with the data whereas $\rho = 0$ corresponding to a V+A current is excluded. Pure V or A yielding $\rho = 0.375$ are strongly disfavoured.

4.3 Decay modes

A selected set of decay modes is listed in Table 4.1 together with the theoretical predictions[118].

Table 4.1 - Selected tau decay modes

Decay mode	Theoretical B %	Experimental B %
$\nu_\tau + e^- \nu_e$	17.6	17.5 ± 1.2
$\nu_\tau + \mu^- + \bar{\nu}_\mu$	17.2	17.1 ± 1.2
$\nu_\tau\ \pi$	10.5	$11.7 \pm 0.4 \pm 1.8$
$\nu_\tau\ K$	0.66	$1.2 \pm 0.4 \pm 0.2$
$\nu_\tau\ \rho$	21.5	$21.6 \pm 1.8 \pm 3.2$
$\nu\ K^*(890)$	1.46	1.7 ± 0.7
$\nu\ A_1$	8.7	10.4 ± 0.03

These decay modes can be predicted with little ambiguity if the τ is a sequential lepton which couples to the weak current with the normal strength G_F.

The leptonic decay widths

$$4.1 \qquad \Gamma_e(\tau \to \nu_\tau\ \bar{\nu}_e\ e) = 1.028\ \Gamma_\mu(\tau \to \nu_\tau\ \bar{\nu}_\mu\ \mu) = \frac{G_F^2 \cdot m_\tau^5}{192\pi^3}$$

can be computed unambigously. The decay $\tau \to \nu_\tau\ \pi$ tests the axial vector current and is directly related to $\pi \to \bar{\nu}_\mu\ \mu$. The decay $\tau \to \nu_\tau\ \rho$ tests the vector current and is related to $e^+e^- \to \rho^o$ by CVC. Recent data on $\tau \to \nu_\tau\ \pi^\pm$ [119] and on $\tau \to \nu_\tau\ \rho$ [120] are listed in Table 4.1. They are in good agreement with the predictions.

The expected suppression of strangeness changing decays can be checked by a measurement of the ratio $B(\tau \to \nu_\tau\ K^*(890)) / B(\tau \to \nu_\tau \rho)$. The standard picture of charged weak currents predicts that this ratio is given by $0.93\ tg^2\theta_c$, where 0.93 results from a small phase space correction, and θ_c is the Cabibbo angle.

Experimentally the MARK II group determines[121] this ratio to 0.085±0.038 in agreement with the theoretical value of 0.05.

The decay $\tau \to \nu_\tau K$ is the Cabibbo suppressed partner to the decay $\tau \to \nu_\tau \pi$ and the relative rates are given by:

$$4.2 \qquad \frac{\Gamma(\tau \to \nu_\tau K)}{\Gamma(\tau \to \nu_\tau \pi)} = tg^2\theta_c \left[\frac{1 - (m_K/m_\tau)^2}{1 - (m_\pi/m_\tau)^2} \right]$$

The MARK II group recently published[122] data on $\tau \to \nu_\tau K$. The process is identified by selecting events of the type $e^+e^- \to \tau^+\tau^- \to (\ell\, \bar{\nu}_\ell\, \nu_\tau)(\bar{\nu}_\tau K^+)$. The leptons are positively identified and the kaons separated from the pions by time of flight. From a sample of 47000 $\tau^+\tau^-$ pairs 15 events satisfied the selection criteria with a pion contamination of (3 ± 0.6) events and a background of 2.1 ± 0.9 events from $\tau \to \nu K^*(890)$. They find $B(\tau \to \nu_\tau K) = (1.2 \pm 0.4 \pm 0.2)\%$ in reasonable agreement with the predicted value of 0.0066. The first error is statistical and the second systematic. Tau decays involving strange particles are thus suppressed relative to non strange τ decay by the usual Cabbibo angle.

4.4 The lifetime

In the standard model the tau life time is given by:

$$4.3 \qquad \tau_\tau = B_e \left(\frac{m_\mu}{m_\tau} \right)^5 \qquad \tau_\mu = (2.8 \pm 0.2) \times 10^{-13}\ \text{s}.$$

This lifetime is quite large and 15 GeV tau's travel on the average 0.7 mm before decaying. Hence the lifetime can be determined from a measurement of the vertex distribution of tau decays.

TASSO has placed an upper limit of $\tau_\tau < 5.7 \times 10^{-13}$ s from their measurements of the vertex distribution. The MARK II Collaboration now reports[123] a measurement of the tau lifetime. They measure the vertex distribution by selecting topologies consisting of three charged particles recoiling against a single charged particle or three charged particles. This topology separates tau pairproduction from hadron production and the intercept of the momentum vectors of the charged particles defines the vertex. The observed decay length distribution is plotted in Fig. 4.1 for events with vertex uncertainties of 8 mm and 4 mm. The beam center is indicated by the dashed line. A careful analysis shows that the center of the measured distribution is shifted by (1.07 ± 0.37) mm with respect to the beam center. Various checks show that this shift is real and not due to systematic uncertainties. The resulting value of the lifetime $\tau_\tau = (4.9 \pm 1.8) \times 10^{-13}$ s is in agreement with the theory. Thus the weak coupling strength of the tau is consistent with G_F, the weak coupling strength observed for the electron and the muon.

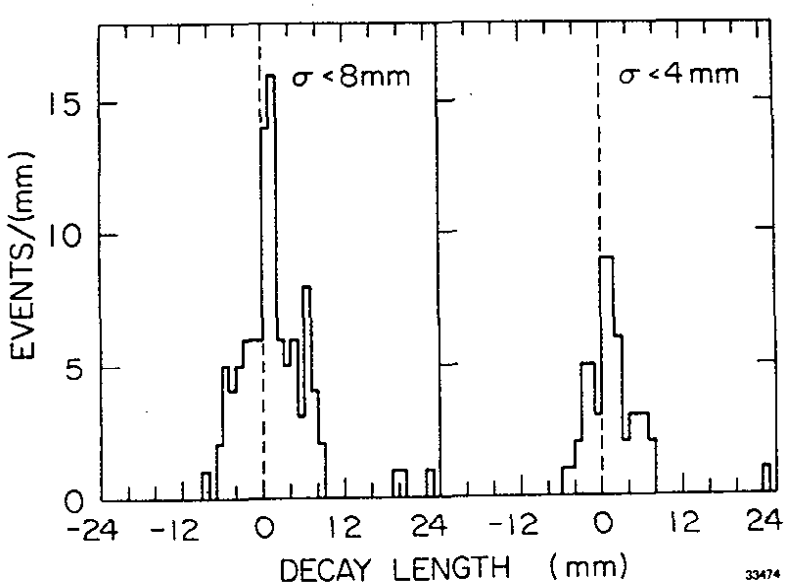

Fig. 4.1
The distribution of τ flight distances at $\sqrt{s}$ = 29 GeV for events with vertex uncertainties less than a) 8 mm b) 4 mm.

So far, the tau was treated as a new sequential lepton arranged in a weak doublet with its own neutrino like the electron and the muon. Indeed all the data[114] are consistent with this assumption. If the τ^- has the same lepton number as the e^+ or the μ^+ then the branching ratios for leptonic decays of the tau into electrons or muons would differ by a factor of two. This is excluded experimentally. It has been found that the $(\tau\ \nu_\mu)$ coupling strength is less than 0.025 of the $(\mu\ \nu_\mu)$ coupling strength excluding that the τ^- has the lepton number of the μ^-. It remains to be shown that the τ^- has not the e^- lepton number. Furthermore the tau neutrino has not been observed directly but inferred from the observed threebody decay $\tau \to \nu_\tau\ \ell\ \nu_e$.

5. Production of New Flavours in e^+e^- Annihilation

A new quark flavour q has very striking signatures in e^+e^- annihilation. Below threshold the production of bound $q\bar{q}$ 1^{--} states show up in the total cross section as narrow peaks. The bound $q\bar{q}$ states become rapidly wider above threshold and the normalized total cross section increases by $\Delta R = 3 \Sigma e_q^2$. In this chapter we will review the data on charm and beauty production in e^+e^- annihilation. The data will be compared to the QCD predictions in chapter 7.

A $q\bar{q}$ system of heavy quarks bound in a steeply rising potential will lead to the level scheme shown in Fig. 5.1. The levels[124] are labeled by J^{PC} with $P = (-1)^{L+1}$ and $C = (-1)^{L+S}$. For each value of angular momentum L there are two bands of radial excitations with opposite charge conjugation depending whether the total spin S is 0 or 1. The spectroscopic notation $n^{2S+1}L$, where n-1 is the number of radial nodes, is used to label the levels. The P levels will split into one $^1P_1$ level with odd and three states $^3P_{2,1,0}$ with even charge conjugation. In a pure coulombic potential the first set of P levels will be degenerated with the 2^3S_1 level. The addition of a confining potential pushes the mass of the 1 P levels below the mass of the 2^3S_1 level.

The D levels will split into one state $^2D_1$ with even and three states $^3D_{3,2,1}$ with odd charge conjugation. The 1^3D_1 state has the quantum number of a photon. The wave function of this state may acquire a finite value at the origin by mixing with the nearby 2^3S_1 state and can be produced directly in e^+e^- collisions.

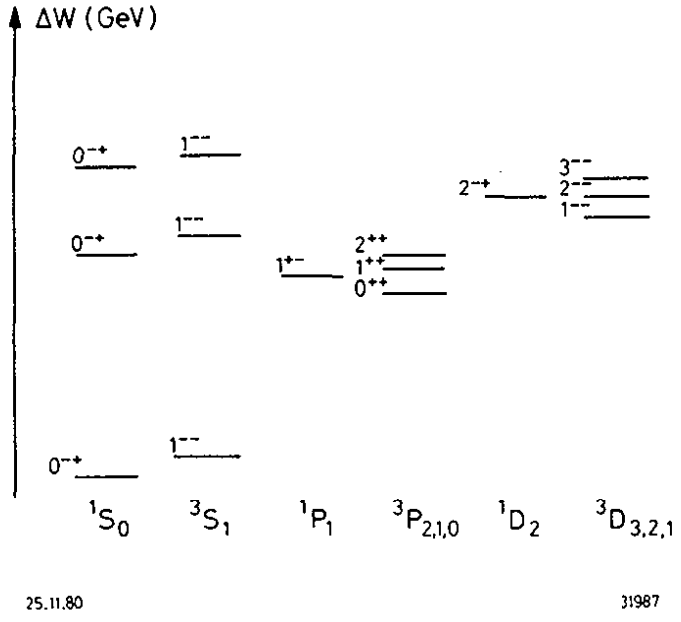

Fig. 5.1

The level scheme of two heavy quarks bound in a steeply rising potential.

The number and quantum numbers of the predicted levels reflect the spin 1/2 nature of the quark. The level spacing and the level widths on the other hand are strongly model dependent and can be used to test the theory.

QCD makes clear first order predictions for various decay modes. The $^3S_1$ state decays to lowest order via a three gluon intermediate state, since one gluon is forbidden by colour and two gluons by charge conjugation The resulting hadronic width[125] is given by:

$$5.1 \qquad \Gamma(^3S_1 \to ggg \to \text{hadrons}) = \frac{160}{81}(\pi^2 - 9)\,\alpha_s^3\,\frac{|^3S_1(0)|^2}{M^2}$$

M is the mass of the quark and $^3S_1(0)$ denotes the wave function at the origin. The strong interaction constant α_s is given by

5.2 $$\alpha_s(Q^2) = \frac{12\pi}{(33 - 2N_f)} \ln (Q^2/\Lambda^2)$$

where N_f is the number of flavours and Λ the characteristic strong interaction mass. The width[126] for the decay into a pair of leptons is given by:

5.3 $$\Gamma(^3S_1 \to e^+e^-) = 16\pi \alpha^2 e_q^2 \frac{|^3S_1 (0)|}{M^2}$$

The pseudoscalar $^1S_0$ states which are expected to lie below the vector states, can decay into ordinary hadrons by a two gluon intermediate state. The width[125] is given by:

5.4 $$\Gamma(^1S_0 \to gg \to \text{hadrons}) = \frac{32\pi}{3} \alpha_s^2 \frac{|^1S_0 (0)|^2}{M^2}$$

The pseudoscalar states are therefore much wider than the corresponding vector states. Indeed if the two states have similar wave functions at the origin as expected then:

5.5 $$\Gamma(^1S_0 \to \text{hadrons}) = \frac{27}{5} \frac{\pi}{(\pi^2-1)\alpha_s} \Gamma(^3S_1 \to \text{hadrons}) \approx 100\, \Gamma(^3S_1 \to \text{hadrons})$$

However, the characteristic distances involved in $c\bar{c}$ and to a lesser degree in $b\bar{b}$ spectroscopy are quite large such that higher order corrections[124] are important and must be included for quantitative conclusions.

A richer level structure than the one predicted by a simple $q\bar{q}$ model might of course exist. Quark pairs may bind to form quark molecules[127] $(c\bar{q})(\bar{c}q)$ with a complex level scheme. The gluon field in a heavy $q\bar{q}$ system may have vibrational excitations[128] which may couple weakly to photons. So far there is no evidence for such states.

5.1 Hadrons with hidden charm

The parameters of $c\bar{c}$ vector states[129] observed in e^+e^- annihilation between 3.0 GeV and 4.5 GeV in c.m. are listed in Table 5.1. The Novosibirsk group reports[129] a very precise value of the J/ψ and the ψ' mass mass obtained by using a spin depolarizing resonance to calibrate the beam energy. The J/ψ, ψ' and ψ" can be identified with the 1^3S_1, 2^3S_1 and 1^3D_1 levels respectively and there is general agreement on the resonance parameters of these states. The situation above the ψ", however, is still not settled. There are indications of a step in the cross section around 3.98 GeV, the DASP group observed two separate states at 4.04 GeV and 4.16 GeV whereas there is general agreement on the existence of a state near 4.41 GeV.

Table 5.1 - Resonance parameters of $c\bar{c}$ vector states

State	Mass (MeV)	Γ_{tot} (MeV)	Γ_{ee} (keV)
J/ψ	3096.93 ± 0.09	0.063 ± 0.009	4.8 ± 0.6
ψ'	3686 ± 0.15	0.215 ± 0.040	0.19 ± 0.2
ψ"	3768 ± 5	26 ± 5	0.27 ± 0.06
ψ(4.030)	4030 ± 5	52 ± 10	0.75 ± 0.10
ψ(4160)	4159 ± 20	78 ± 20	0.78 ± 0.31
ψ(4415)	4415 ± 6	43 ± 20	0.43 ± 0.13

New data on the total cross section between 3.6 GeV and 4.5 GeV in c.m. by the Crystal Ball Collaboration[129] are shown in Fig. 5.2. Plotted is the total annihilation cross section normalized to the point cross section. The data shown are corrected for τ production but not for radiative effects. The radiative correction will enhance the peak

structure. The data confirm the existence of states around 4.03 GeV and 4.16 GeV and indicate structure in the cross section below 4.0 GeV.

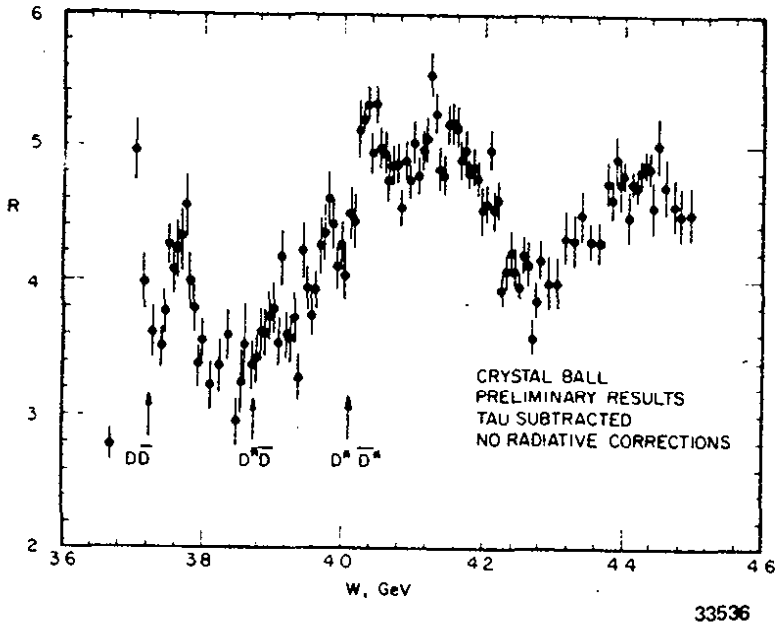

Fig. 5.2

The cross section for $e^+e^- \to$ hadrons as measured by the Crystal Ball Corporation normalized to the point cross section.

Several states with even charge conjugation have been observed in the decays J/ψ or ψ' into final states of γ + anything. The states[130] found at 3.41 GeV, 3.51 GeV and 3.55 GeV can be associated rather naturally with the $^3P_0$, $^3P_1$ and the $^3P_2$ levels whereas the states reported at 2.82 GeV[131], 3.45 GeV[132] and 3.59 GeV[133] were not so easily fit into the $c\bar{c}$ scheme.

The Crystal Ball detector, designed to measure photons with good energy resolution over a large solid angle has produced a wealth of new data on the even charge conjugation states. Their main findings are [134]:

a) They find no evidence for the states at 2.82 GeV and 3.45 GeV with a sensitivity well below that of the earlier experiments.

b) They have observed the decays $\psi' \to \gamma^3p \to \gamma\gamma$ J/ψ with much higher statistics than previous experiments. The inclusive photon spectrum from the ψ' after the final cuts is plotted in Fig. 5.3.

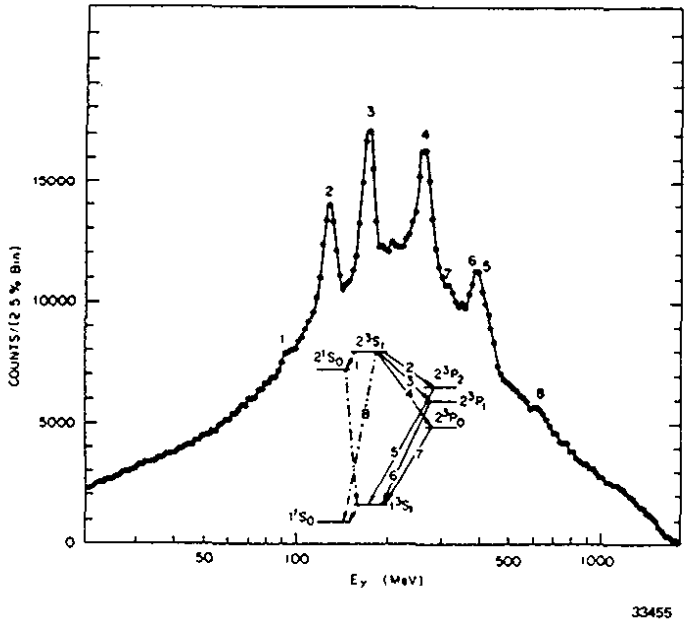

Fig. 5.3

The inclusive photon spectrum observed in ψ' decays by the Crystal Ball group.

The spectrum is very rich and the connection between the observed structure and the level scheme is shown in the insert.

The parameter for the P-states extracted from this spectrum and the cascade decay $\psi' \to \gamma\gamma\ J/\psi$ with $J/\psi \to e^+e^-$ ($\mu^+\mu^-$) are listed in Table 5.2.

Table 5.2 - Parameters for the Charmonium P-states

State (J^{PC})	Mass (MeV)	Width (MeV)	$B(\psi' \to \gamma P)$ (%)	$B(\psi' \to \gamma P)(P \to \gamma J/\psi)$ (%)
2^{++}	$3553.9 \pm 0.5 \pm 4.0$	1.8 ± 0.6	$7.4 \pm 0.4 \pm 1.4$	1.16 ± 0.12
1^{++}	$3508.4 \pm 0.4 \pm 4.0$	< 1.5	$8.4 \pm 0.4 \pm 1.3$	2.34 ± 0.21
0^{++}	3413 ± 5.0	16.3 ± 3.6	$9.3 \pm 0.4 \pm 1.4$	$0.059 \pm 0.015 \pm 0.004$

The values of $B(\psi' \to \gamma P)$ listed are from the Crystal Ball[134] and they are in agreement with earlier data[135]. The first two values for the cascade branching ratio are world averages[136], branching ratios for the cascade decay via the 0^{++} state are from the Crystal Ball[134-136]. The widths are in general agreement with the QCD expectation. Since a spin 1 particle cannot decay with the emission of two massless vector particles one expects the 1^{++} state to be narrower than the 2^{++} and 0^{++} states which can decay by two gluon emission. The values for $B(\psi' \to \gamma P)$ are below the theoretical predictions[137] by roughly a factor of two.

An interesting byproduct is the observation of the isospin forbidden decay $\psi' \to \pi^0 J/\psi$. They find $B(\psi' \to \pi^0 J/\psi) = (0.09 \pm 0.02 \pm 0.01)\%$ consistent with the value $B(\psi' \to \pi^0 J/\psi) = (0.15 \pm 0.06)\%$ obtained[138] in an earlier measurement by the MARK II Collaboration. The electromagnetic interaction predicts a rate which is more than one order of magnitude smaller than the observed rate such that this mechanism appears to be excluded. The decay might arise from an isospin breaking amplitude as in the decay $\eta \to 3\pi$.

c) The Crystal Ball Collaboration has new data[134] on the resonance observed below the J/ψ mass in inclusive transitions[139] from the J/ψ and in exclusive[139,140] final states both from the J/ψ and the ψ'. The state has now also been seen[134] in the inclusive photon spectrum obtained at the ψ'. It is natural to identify this state, with the η_c, the lowest pseudoscalar $^1S_0(c\bar{c})$ state.

The photon spectra from these decays are plotted in Fig. 5.4a, b before and after background subtraction. A simultaneous fit to the most recent

data give the following results:

$$\text{Mass} = 2984 \pm 4 \text{ MeV}$$

$$\text{Width} = 12.4 \pm 4.1 \text{ MeV}$$

$$B(J/\psi \to \gamma \eta_c) = (1.13 \pm 0.33) \cdot 10^{-2}$$

$$B(\psi' \to \gamma \eta_c) = (0.28 \pm 0.08) \cdot 10^{-2}$$

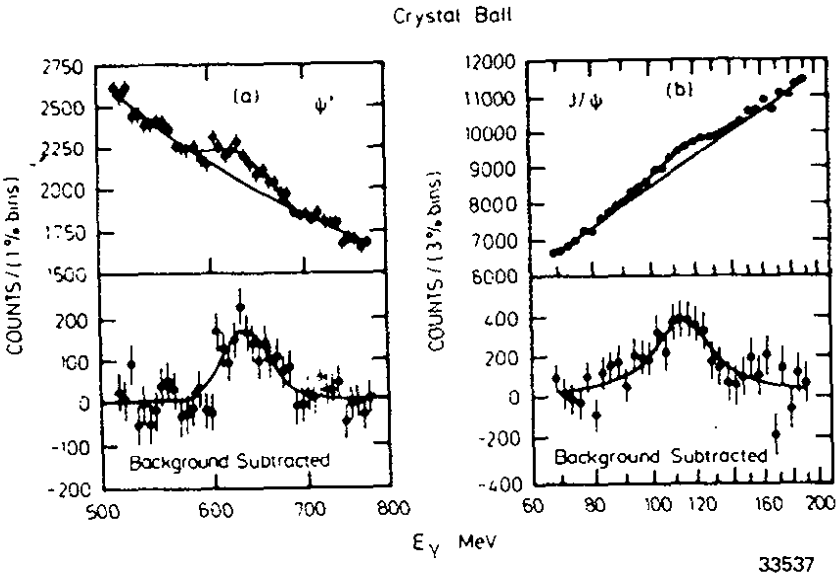

Fig. 5.4 a + b
Inclusive photon spectrum $\psi' \to \gamma X$ and $J/\psi \to \gamma X$ as measured by the Crystal Ball Collaboration shown with and without a smooth background subtraction.

In the $c\bar{c}$ model the transition $B(\psi' \to \gamma \eta_c)$ is a forbidden spin flip transition and this may explain the low branching ration. The width of the η_c is about a factor 200 larger than the width of the J/ψ in qualitative agreement with the QCD prediction.

d) The Crystal Ball group has also observed[134] a new resonance in the inclusive photon spectrum of the ψ'. This state is just below the ψ' and is a candidate for η_c', the long sought 2^1S_0 state.

The photon spectrum from the ψ' for photon energies between 60 MeV and 110 MeV is plotted on a linear scale in Fig. 5.5 with and without a polynominal background subtracted. The statistical significance of the peak is 4.4σ. Representing the resonance by a Gaussian gave a mass of $M = (3592 \pm 5)$ MeV including statistical and systematic errors.

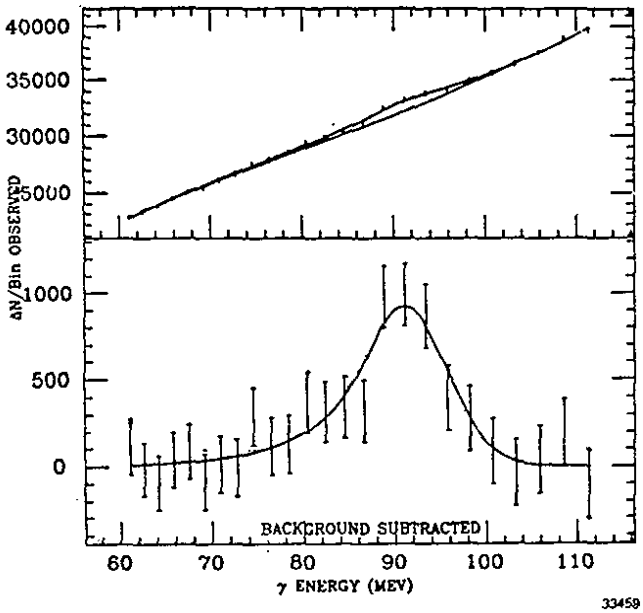

Fig. 5.5

Inclusive photon spectrum $\psi' \to \gamma X$ plotted on a linear scale for photon energies between 60 and 110 MeV. The spectrum with and without background subtraction is shown.

The width is less than 8 MeV and the branching ratio is between (0.2 - 1.3)%. These are 95% confidence limits. The mass value agrees with an earlier measurement[133] by the DESY Heidelberg group, however, the branching ratio observed by Crystal Ball is substantially lower than that found by DESY-Heidelberg.

5.2 Hadrons with hidden beauty

The first evidence[141] for a new quark came from a lepton pair production experiment at FNAL. In this experiment they observed narrow states, the Υ states, in the e^+e^- mass spectrum produced in proton-nucleous collisions. The energy of DORIS was subsequently increased and the two lowest Υ states confirmed[142]. The measured[143,144] Γ_{ee} widths showed[145] that these resonances are 1^{--} $b\bar{b}$ states made of a quark b with charge 1/3e.

The data have been extended to higher energies by the CUSB and CLEO Collaborations at CESR. Some of the total cross section data[100,146] obtained by these groups are plotted in Figs. 5.6 and 5.7. Both experiments find clear evidence for two new 1^{--} states T'' and T''' which can be identified with the 3^3S_1 and the 4^3S_1 state. The T(3S) state, like the T(1S) and T(2S) states, has an observed width consistent with the energy spread of the beams whereas the T(4S) state is considerably wider. It is therefore natural to assume that the threshold for $b\bar{b}$ production is located between the T(3S) and T(4S) state.

The resonance parameters[146,147] for the four observed $T(1^{--})$ states are listed in Table 5.3.

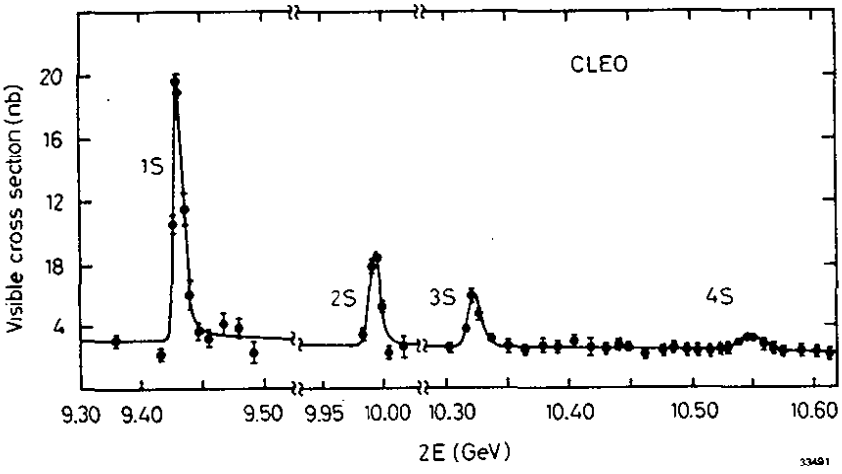

Fig. 5.6

The total hadronic cross section measured by the CLEO Collaboration.

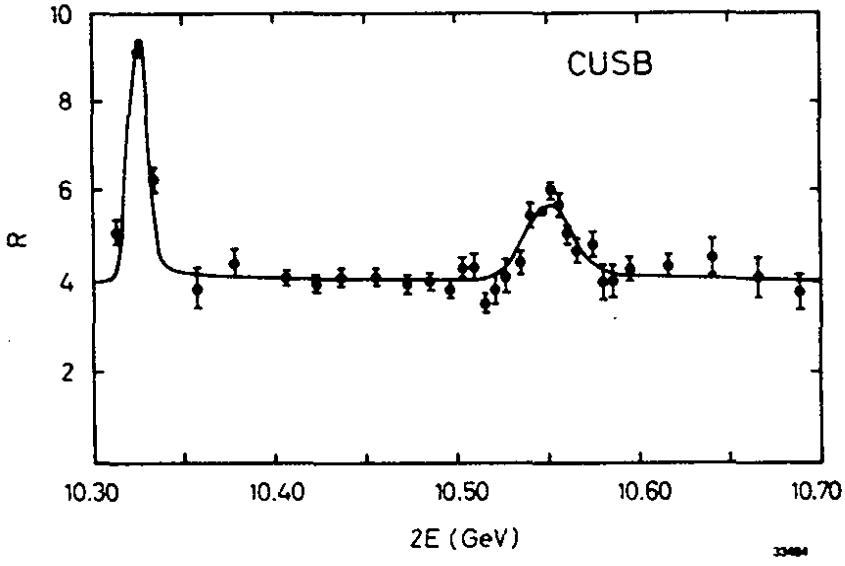

Fig. 5.7

The total hadronic cross section measured by the CUSB Collaboration.

Table 5.3 - Resonance parameters for the $\Upsilon(^3S_1)$ states

State	Mass (MeV)	Excitation energy MeV	Γ_{ee} (keV)	Group
$\Upsilon(1^3S_1)$	9462 ± 10	-	1.29 ± 0.09 ± 0.13	DESY
	9433 ± 28	-	1.19 ± 0.02	CLEO
			1.06 ± 0.04	CUSB
$\Upsilon(2^3S_1)$	-	553 ± 10	0.58 ± 0.08 ± 0.26	DESY
		560 ± 1	0.52 ± 0.02	CLEO
			0.51 ± 0.03	CUSB
$\Upsilon(3^3S_1)$		890 ± 1	0.39 ± 0.02	CLEO
			0.36 ± 0.03	CUSB
$\Upsilon(4^3S_1)$		1114 ± 2	0.31 ± 0.02	CLEO
			0.21 ± 0.02	CUSB

The groups at CESR have measured[100] the total cross section in fine steps for c.m. energies between the $\Upsilon(3S)$ and $\Upsilon(4S)$. The $R_{visible}$ measured by CUSB is plotted in Fig. 5.8 versus the energy in c.m. No structure is seen and the 90% upper confidence limit on Γ_{ee} for a narrow resonance extracted from these data are also shown. 1^{--} states resulting from the quantized excitations of the gluon string joining the quark and the antiquark had been predicted[128] to exist in this mass range with a width $\Gamma_{ee} = 0.2 \pm 0.15$ keV. The sensitivity of the present data are close to the lower limit.

The cascade decays $\Upsilon(2S) \to \pi^+\pi^- \Upsilon(1S)$[100] and $\Upsilon(3S) \to \pi^+\pi^- \Upsilon(1S)$ have been observed[100,146,147] and the data are listed in Table 5.4.

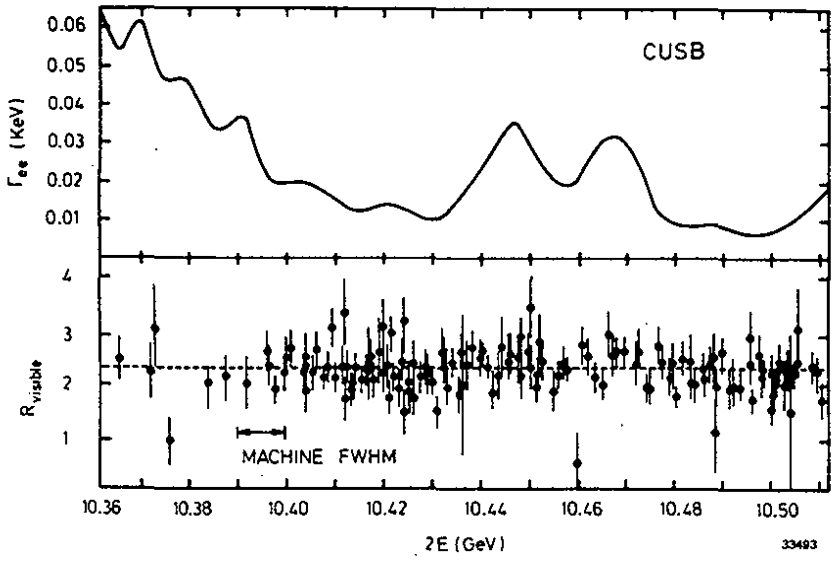

Fig. 5.8

$R_{visible}$ measured by the CUSB Collaboration in fine energy steps between the $\Upsilon(3S)$ and $\Upsilon(4S)$. The 90% upper confidence limit on the leptonic width Γ_{ee} for a narrow resonance is also shown.

Table 5.4 - Data on the cascade decay

Group	$B(\Upsilon(2S) \to \pi^+\pi^- \Upsilon(1S))$ %	$B(\Upsilon(3S) \to \pi^+\pi^- \Upsilon(1S))$ %
LENA	27 ± 9	-
CLEO	19.1 ± 3.1	3.9 ± 1.9
CUSB	-	9.7 ± 4.3

CLEO observed the decay $\Upsilon(2S) \to \pi^+\pi^- \Upsilon(1S)$ by measuring the mass recoiling against all $\pi^+\pi^-$ pairs observed in the $\Upsilon(S)$ decays. The observed mass distribution, plotted in Fig. 5.9, shows a clear peak at the mass of the $\Upsilon(1S)$.

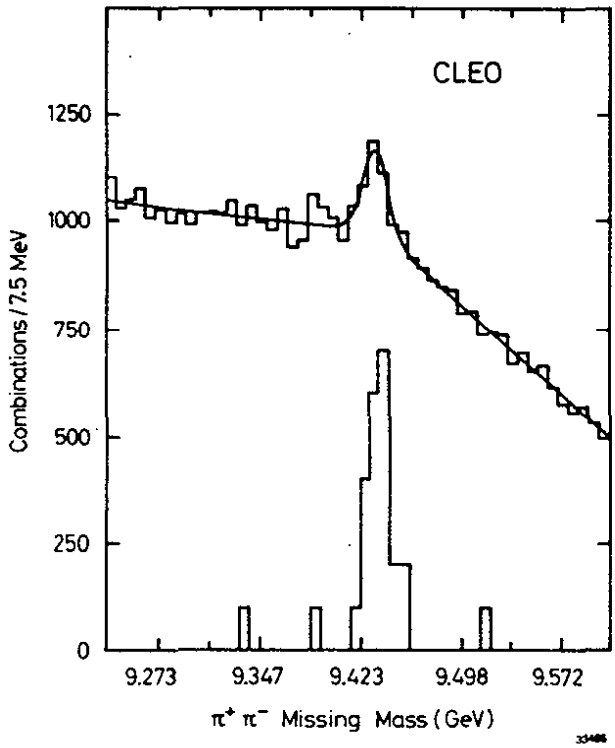

Fig. 5.9

The missing mass recoiling against all opposite charged pion pairs at the $\Upsilon(2S)$. The lower histogram is the $\pi^+\pi^-$ recoil mass for events of the type $\Upsilon(2S) \to \pi^+\pi^-\ e^+e^-\ (\mu^+\mu^-)$

The LENA group at DESY has searched[148] for the radiative decay $\Upsilon(2S) \to \gamma\gamma\ \Upsilon(1S)$ with $\Upsilon(1S) \to \pi^+\pi^-\ (e^+e^-)$. From the data they extracted an upper limit $B(\Upsilon(2S) \to \gamma\gamma\ \Upsilon(1S)) < 7\%$. The theoretical expectations range between 2% and 7%. In QCD (chapter 7) the $P_{2,0}$ states decay in leading order into two gluons. Since the photon in the cascade $\Upsilon \to \gamma\ P_{2,0}$ is soft, these gluons will result in two back to back jets of hadrons. This topology is different from the dominant decay $\Upsilon(^3S_1) \to 3$ gluons. The CUSB Collaboration has observed[146] events with the two jet topology at both the $\Upsilon(2S)$ and $\Upsilon(3S)$. They find from the observed thrust distribution

$$B(\Upsilon(2S) \to 2 \text{ jets}) = 20 \pm 3\%$$

$$B(\Upsilon(3S) \to 2 \text{ jets}) = 8 \pm 2\% .$$

Note that two jet events may also result from $\Upsilon \to \gamma^* \to q\bar{q}$. However, these branching ratios would lead to less two jet events than observed.

5.3 Hadrons with charm

5.3.1 D^0 and $D^{\pm}$ states

Possible transitions between the known D states and the corresponding Q-values are summarized in Fig. 5.10.

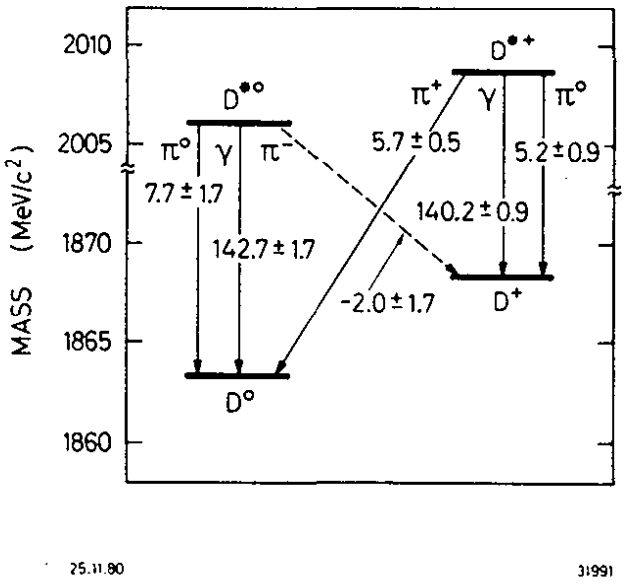

Fig. 5.10

Q-values for $D^* \rightarrow D$ transition.

The ψ'' decays to a good approximation only into $D\bar{D}$ final states. The production cross sections for these mesons at the ψ'' resonance were determined[149] by the MARK II Collaboration to:

$$\sigma(D^0) = (8.0 \pm 1.0 \pm 1.2) \text{ nb}$$
$$\sigma(D^+) = (6.0 \pm 0.7 \pm 0.1) \text{ nb}$$

For comparison, the cross section predicted for $e^+e^- \rightarrow Z^0 \rightarrow c\bar{c}$ is on the order of 4 nb. An additional advantage is that the D's are produced almost at rest and the favourable kinematics allow a precise determination of the mass $M_0 = \sqrt{E^2 - p^2}$ where E is the beam energy and p the D momentum. These nice features have been exploited by the groups working at SPEAR and have lead to a wealth of data[149] on the D states.

Mass-spectra for $K^{\pm}\pi^{\mp}$, $K^0\pi^{\mp}\pi^{\pm}$ and $K^{\pm}\pi^{\mp}\pi^{\pm}$ measured at the ψ'' by the MARK II Collaboration[150] are shown in Fig. 5.11. From such data groups working at SPEAR found $m_{D^0} = (1864.3 \pm 0.9 \text{ MeV})$ and $m_{D^+} = (1868.4 \pm 0.9 \text{ MeV})$.

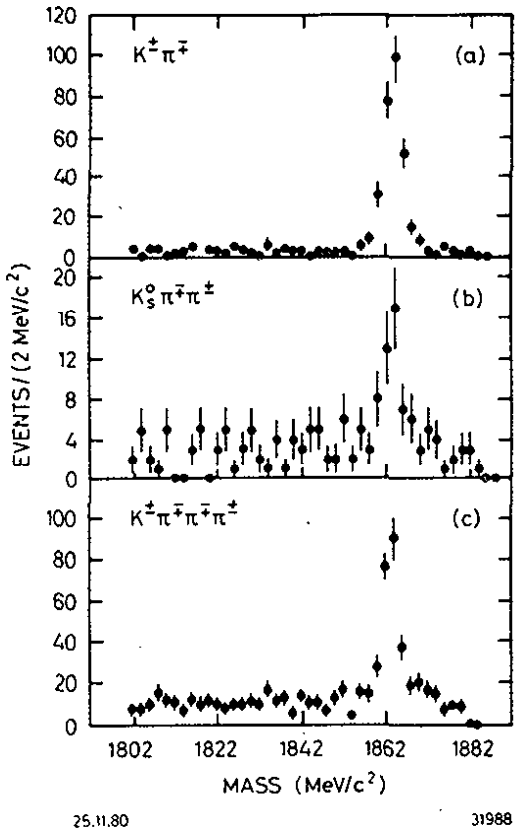

Fig. 5.11

Mass spectra for $\psi'' \to D^0\bar{D}^0$ candidate events with
a) $D \to K^{\pm}\pi^{\mp}$
b) $D \to K^0\pi^{\mp}\pi^{\pm}$
c) $D \to K\pi^{\mp}\pi^{+}\pi^{\pm}$
The data were obtained by the MARK II Collaboration.

A complete list of D branching ratios can be found in Ref. 149. Below we discuss a measurement of the lifetimes and a determination of the GIM mixing angles.

5.3.2 *Lifetime of charmed mesons*

Possible Cabibbo favoured decay modes of charmed mesons into light hadrons are shown in Fig. 5.12. An assumption often made was that the charmed quark would decay according to $c \to -\sin\theta \cdot d + \cos\theta \cdot s$ with the second quark merely acting as a spectator. This mechanism, shown in Fig. 5.12a, c and d predicts that all charmed mesons should have the same lifetime. It has been pointed out by Pais and Treiman[151] that $\Gamma(D^+ \to \ell^+\nu_\ell X) = \Gamma(D^0 \to \ell^+\nu_\ell X)$ since $|\Delta I = 0|$ for the Cabibbo allowed decay $c \to \ell\ \nu_\ell\ s$. The semileptonic branching ratios can therefore be used to determine the ratios of the lifetimes:

$$\frac{B(D^+ \to \ell^+ \nu_\ell X)}{B(D^0 \to \ell^+ \nu_\ell X)} = \frac{\Gamma_{tot}(D^0 \to X)}{\Gamma_{tot}(D^+ \to X)} = \frac{\tau(D^+)}{\tau(D^0)}$$

Both the DELCO[152] and the MARK II[150] Collaborations report results on this ratio. DELCO finds:

$$\tau(D^+) \,/\, \tau(D^0) = 4.3 \quad \text{and} \quad B_e(D^+) = 22 \,^{+\,4.4}_{-\,2.2}\,\% \,.$$

Their results were extracted from a sample of $D\bar{D}$ events in which one or both of the charmed mesons decayed semileptonically.

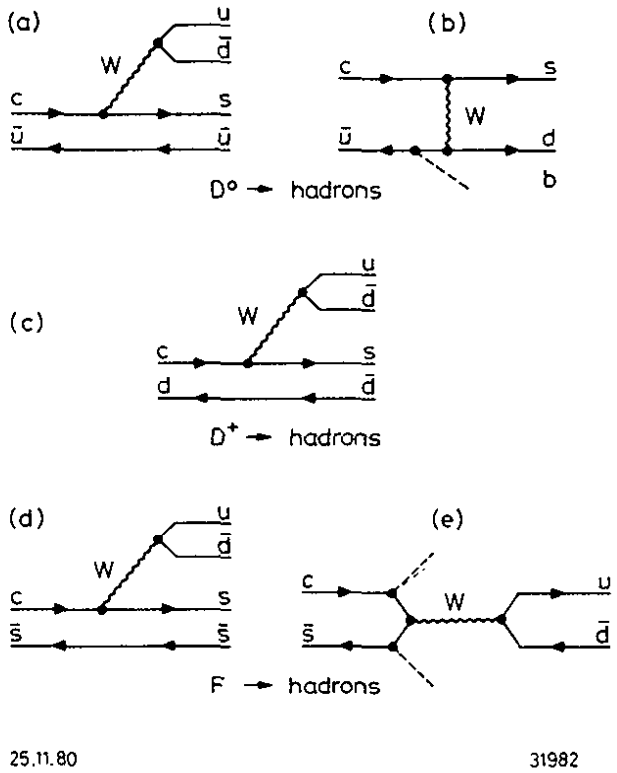

Fig. 5.12

Possible Cabibbo favoured decay modes of charmed mesons into light hadrons.

The MARK II Collaboration determined[150] the branching ratios from an inclusive measurement of charmed meson production. The events were tagged by identifying either a charged or a neutral D meson and measuring

the decay products of its partner. In this way the semileptonic branching ratios are determined directly and they find:

$$\tau(D^+) / \tau(D^0) = 3.1 \begin{matrix} + 4.6 \\ - 1.4 \end{matrix} \text{ and } B_e(D^+) = 18.6 \pm 6.4\%.$$

The lifetime of charmed particles has been determined[153] directly using emulsions or high resolution bubble chambers. The results of the various experiments are summarized in Table 5.5.

Table 5.5 - Lifetimes of charged and neutral D mesons

Particle	Lifetime in (10^{-13}s)	Events	Group
$D^{\pm}$	$8.0 \begin{matrix} + 4.9 \\ - 2.4 \end{matrix}$	7	LEBC CERN
	$6.5 \begin{matrix} + 2.2 \\ - 1.0 \end{matrix}$	4	SLAC Hybrid
	$9.5 \begin{matrix} + 6.5 \\ - 3.3 \end{matrix}$	6	FNAL Emul.
	$9.5 \begin{matrix} + 3.1 \\ - 1.9 \end{matrix}$	(96)	NAI, CERN
D^0	$3.2 \begin{matrix} + 2.2 \\ - 1.0 \end{matrix}$	6	FNAL
	$1.9 \begin{matrix} + 1.7 \\ - 0.6 \end{matrix}$	4	SLAC Hybrid
	$3.0 \begin{matrix} + 1.1 \\ - 0.7 \end{matrix}$	17	FNAL Emulsion
	$1.34 \begin{matrix} + 1.2 \\ - 0.9 \end{matrix}$	5	WA 57 CERN
	$0.5 \begin{matrix} + 0.6 \\ - 0.3 \end{matrix}$	3	WA 17 CERN

The lifetime of charged D mesons has also been measured[154] in a high energy photoproduction experiment at CERN. The experiment used a live target followed by a spectrometer. The target was made of 40 layers of 300μ

thick silicon disks spaced 100 μm apart. The energy loss in the target stack is proportional to the number of charged particles, i.e. it is possible to identify the production vertex and the secondary vertex from the decay of the charm particles by the steps in the observed pulse height and hence to measure the distance which the charmed particle travelled between production and decay. The measured time distribution of identified charmed particles decays is shown in Fig. 5.13. Correcting for the D^0 contamination results in a lifetime $\tau_{D^+} = (9.5 \,^{+\,3.1}_{-\,1.9}) \cdot 10^{-13}$ s.

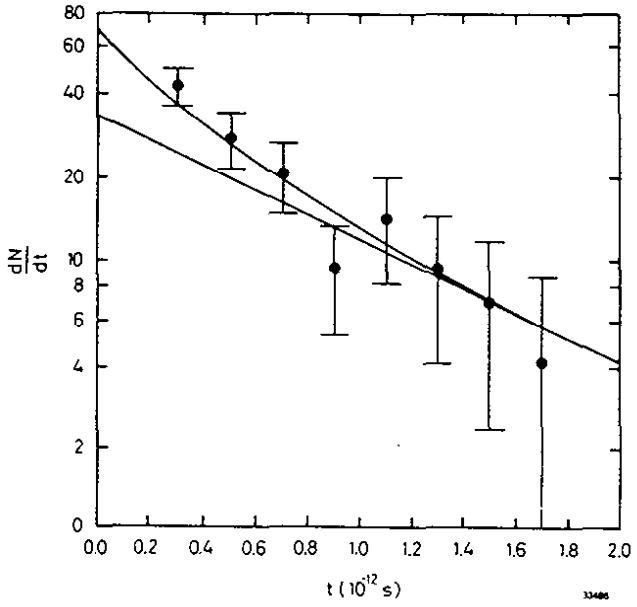

Fig. 5.13
Time distribution of identified charmed particle decays.

The D^+ lifetime combined with the average branching ratio for $D^+ \to e^+ \nu_e X$ results in a semileptonic width

$$\Gamma(D^+ \to e^+ \nu_e X) \approx (1.8 \pm 1) \times 10^{11} \text{ sec}^{-1} .$$

Cabibbo, Maiani and Corbo have evaluated[155] the semileptonic width in the spectator model and they find

$$\Gamma_{SL} = \frac{G_F^2 m_c^5}{192 \pi^3} g(\varepsilon) \left(1 - \frac{2\alpha_s}{B\pi} f(\varepsilon)\right)$$

with $\varepsilon = m_s/m_c$. Here $g(\varepsilon)$ is a phase space correction due to the finite mass of the s quark and the terms in the bracket is a QCD strong interaction correction. With $m_c = 1.75$ GeV/c^2 they find $\Gamma_{SL} = 1 \times 10^{11}$ sec^{-1} consistent with the experimental results. The width of the D^+ is therefore consistent with the prediction based on the spectator model. The experimental results on D^+ and D^0 lifetimes shows that D^0 must have additional decay modes.

Additional decay modes resulting from W^+ annihilation are indeed Cabibbo allowed both for D^0 and F^+ decays whereas they are Cabibbo forbidden for D^+ decays. These decay modes, shown in Fig. 5.12 d and e may account for a factor of 5 in the lifetime ratio $\tau(D^0)/\tau(D^+)$. To conclude, the lifetime of charmed hadrons cannot be reliably computed in the spectator model. Many mechanisms which lead to different lifetimes for different charmed particles have been proposed and the theoretical situation is reviewed in reference 156.

5.3.3 The G I M mechanism

The GIM mechanism[79] predicts that a charmed quark decay predominantly into a strange quark according to

$$c \to \sin\theta_B \cdot d + \cos\theta_B \cdot s$$

The mixing angle θ_B in the GIM model is identified with the familiar Cabibbo angle θ_C with $\sin\theta_C \stackrel{\sim}{=} 0.22$ determined[104,105] from strange particle decays. Both angles θ_A and θ_B can be determined from a measurement of the two-body decay modes

$$D^0 \to K^- \pi^+ , \quad D^0 \to K^- K^+ , \quad D^0 \to \pi^- \pi^+$$

as shown in Fig. 5.14.

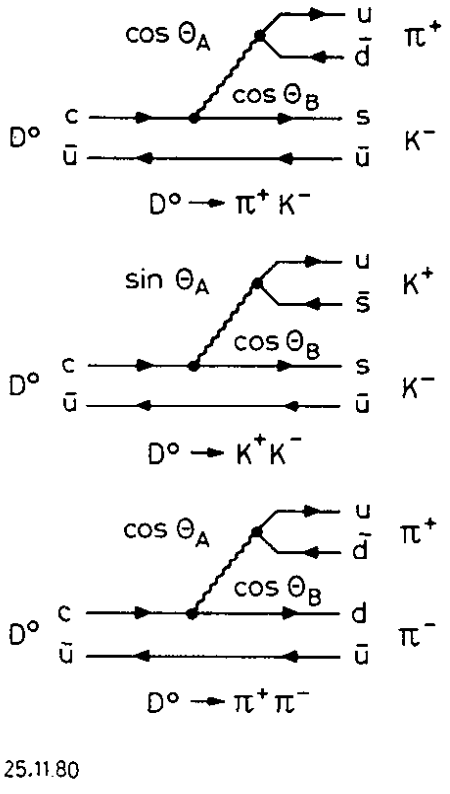

Fig. 5.14

Diagram for two body D^0 decays
a) $D^0 \to \pi^+K^-$
b) $D^0 \to K^+K^-$
c) $D^0 \to \pi^+\pi^-$

These decays yield

$$tg^2\theta_A = 1.08\,\frac{\Gamma(D^0 \to K^-K^+)}{\Gamma(D^0 \to K^-\pi^+)} \quad \text{and} \quad tg^2\theta_B = \frac{0.93 \cdot \Gamma(D^0 \to \pi^+\pi^-)}{\Gamma(D^0 \to K^-\pi^+)}$$

Invoking SU(3) invariance and the GIM mechanism results in:

$$tg^2\theta_A = tg^2\theta_B = tg^2\theta_C = 0.05 \,.$$

The MARK II Collaboration has determined[157] these decay modes making use of the fact that at the ψ'' D^0's are pairproduced with a unique momentum of 288 MeV/c. The invariant mass spectra obtained for the twobody decay modes are shown in Fig. 5.15. The peak occurs at the D^0 mass if the two particles are identified correctly and shifted by about $\pm$ 120 MeV/c^2 if one of the particles is misidentified. Both a $\pi^+\pi^-$ and a K^-K^+ signal is observed yielding:

$$\frac{\Gamma(D^0 \to \pi^-\pi^+)}{\Gamma(D^0 \to K^-\pi^+)} = 0.033 \pm 0.015 \quad \text{and} \quad \frac{\Gamma(D^0 \to K^-K^+)}{\Gamma(D^0 \to K^-\pi^+)} = 0.113 \pm 0.030.$$

The data show that Cabibbo forbidden decays occur at roughly the level predicted. The interpretation however is complicated by strong interaction effects.

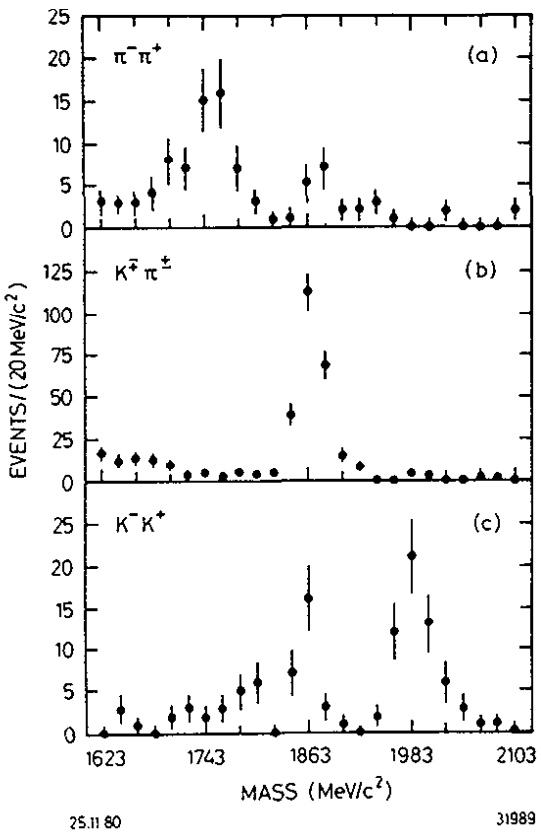

Fig. 5.15

Invariant mass distribution of candidate events for:
a) $D^0 \to \pi^-\pi^+$
b) $D^0 \to K^\mp\pi^\pm$
c) $D^0 \to K^-K^+$.

The $\bar{d}c$ coupling can also be determined, and perhaps more reliably, from a measurement[158] of $\nu + d \to \mu^- + c \to \mu^+\mu^- X$. Using the Kobayashi-Maskawa formalism[32] (chapter 3) this process determines the value of $U_{c\bar{d}} \simeq \sin\theta_1 \cos\theta_2 \approx \sin\theta_c$. The reaction $\nu + s \to \mu^- + c$ will of course also yield opposite sign dileptons. However, the two reactions will have different x dependence since the d is a valence quark whereas the s is a sea quark. An analysis[159] of the observed dilepton rate of about 0.01 yields $0.19 < |U_{c\bar{d}}| < 0.34$ consistent with $\sin\theta_c \simeq 0.22$.

The $\bar{s}c$ coupling can be determined from the branching ratio of $D^+ \to e^+ \nu_e \bar{K}^0$ and the D^+ lifetime. An analysis[159] yields $|U_{sc}| = 0.66 \pm 0.33$.

The GIM mechanism is thus supported by the data.

5.3.4 Evidence for the F meson

The DASP Collaboration observed[160] a signal at 4.42 GeV in c.m. which they attribute to $F^+ \to \eta\,\pi^+$. A scatter plot of the $\eta\,\pi^+$ mass versus the fitted recoil mass assuming $e^+e^- \to FF^*$ is shown in Fig. 5.16 for events at 4.42 GeV and events outside the region. At 4.42 GeV there is a cluster of

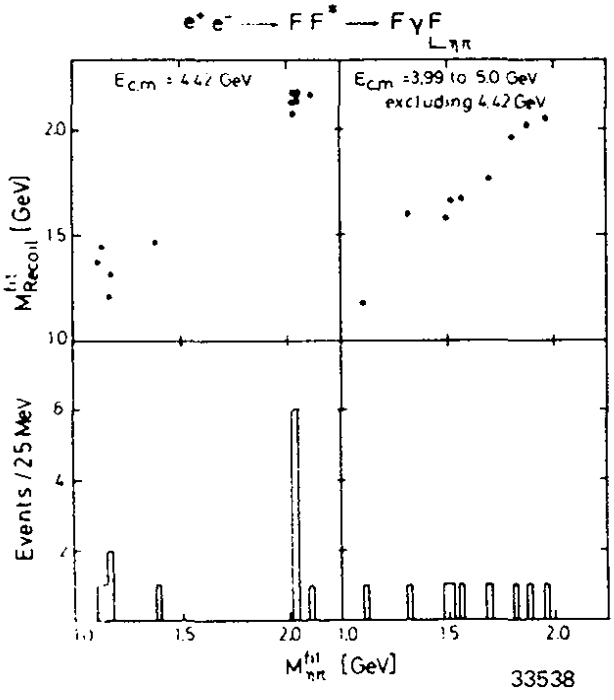

Fig. 5.16

Fitted mass versus fitted recoil mass, assuming $e^+e^- \to FF^*$, where $F^* \to \gamma F$ and $F \to \eta\pi$. a) at 4.42 GeV c) all other energies excluding 4.42 GeV. Histograms (b) and (d) are the projections of (a) and (c) respectively, along the $M(\eta\pi)$ axis. The data were obtained by the DASP Collaboration.

6 events, whereas at other energies the events have a smooth mass distribution. Of the 6 events observed at 4.42 GeV less than 0.2 events can be ascribed to the background. This was estimated from the measured luminosity and the number of events oberved outside of 4.42 GeV in the same mass region with the conservative assumption that all these events are background events. The cluster at 4.42 GeV gives:

$$m_F = 2.03 \pm 0.06 \text{ GeV/c}^2 \text{ and } m_{F^*} = 2.14 \pm 0.06 \text{ GeV/c}^2$$

including systematic uncertainties.

Supporting evidence for the F has come from a photoproduction experiment in the Ω' spectrometer at the SPS and from emulsion exposures. The WA4 Collaboration at the SPS observe[161] a signal in the decay modes

$F \to \eta\pi$, $\eta 3\pi$, $\eta' 3\pi$ and $\phi\rho$. The results are shown in Fig. 5.17 and summarized in Table 5.6.

Table 5.6 - Evidence for F-photoproduction

Decay mode	Mass (MeV)	$B \cdot \sigma$ (nb)
$\eta\ \pi$	2047 ± 23	27 ± 7
$\eta\ 3\ \pi$	2021 ± 13	60 ± 15
$\eta'\ 3\pi$	2008 ± 20	20 ± 8
$\phi\ \rho'$	2049 ± 15	33 ± 10

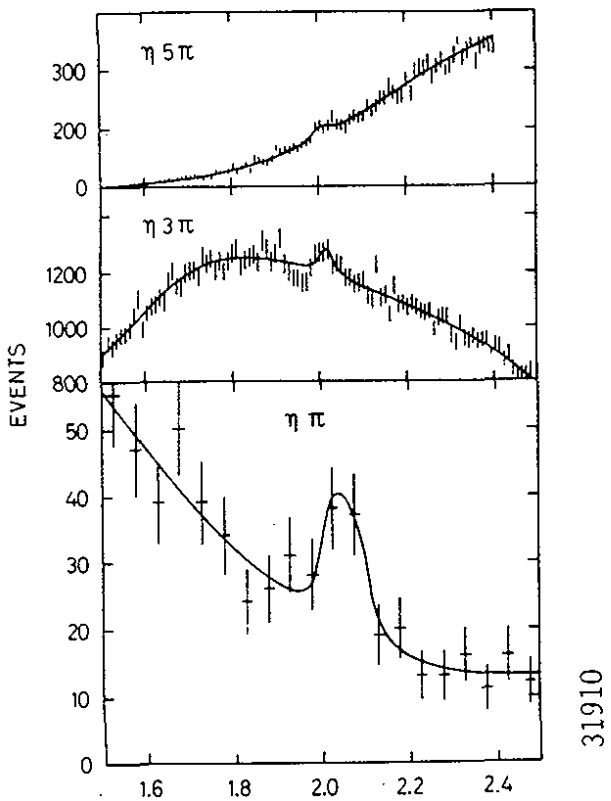

Fig. 5.17

Mass spectra of photoproduced $\eta + n\pi$ final states measured by the WA4 Collaboration at CERN.

Three F candidate events are found in the emulsion data[153]. The observed decay modes and mass values in MeV/c^2 are:

$\pi^-\pi^+\pi^-\pi^0$ (2026 ± 56)

$K^+\pi^-\pi^+K^0$ (2089 ± 121) and

$\pi^+\pi^+\pi^-\pi^0$ (2017 ± 25) .

The mass values observed in the new experiments are consistent with the values reported by the DASP Collaboration.

5.4 Hadrons with beauty

In the standard model the b-quark is the partner of a charge 2/3 quark in a left handed weak doublet. In the Kobayashi-Maskawa[32] scheme the b quark decays weakly as indicated in Fig. 5.18 via a flavour cascade $b \to c \to s$, whereas the direct decay $b \to u$ is strongly suppressed. The model[100] predicts that on the average 1.6 kaons, charged or neutral are produced per b-decay. The semileptonic branching ratio $B(b \to e\bar{\nu}_e \text{ hadrons}) = B(b \to \mu\bar{\nu}_\mu \text{ hadrons})$ is predicted[162] to be in the range 11% to 13%.

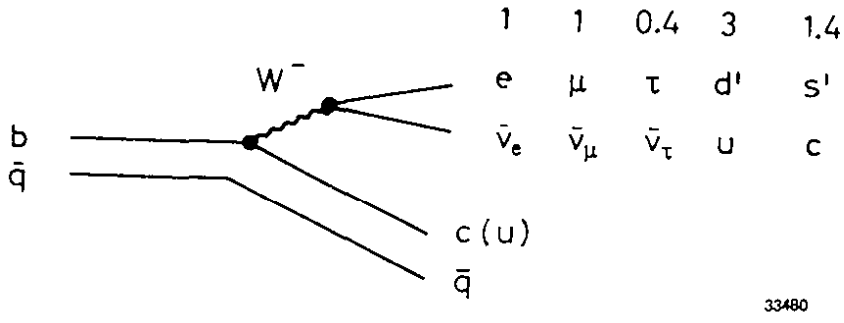

Fig. 5.18

b decays in the spectator model. The relative strength of the various decay modes are indicated.

The large width of the $\Upsilon(4s)$ compared to the width of the adjacent $\Upsilon(3s)$ state shows that the lightest B meson must have a mass between 5.18 GeV/c^2 and 5.28 GeV/c^2 using the DORIS energy scale. The CUSB Collaboration[100,146] has made an unsucessful search for narrow photon lines in the debris of the $\Upsilon(4s)$. Such lines would have been a signature of $B^* \to \gamma B$ and the negative result yields the limit:

$$\frac{\Upsilon(4s) \to B^*B}{\Upsilon(4s) \to \text{all}} \leq 0.20 \ .$$

With the assumption that $\Upsilon(4s)$ is below B^*B threshold and with the observed $\Upsilon(4s)$ width as an input, a theoretical estimate[146] gives $m_B = 5.26 \pm 0.01$ GeV/c^2 as the mass of the lightest B meson.

The CUSB and the CLEO Collaborations[100] have measured the yield of mixed electron-hadron events in the vicinity of the $\Upsilon(4s)$. Both experiments only accept electrons with momenta above 1 GeV/c. This cut strongly reduces the number of events resulting from charm production whereas 2/3 of the B decays survive. Both experiments show a strong increase in the inclusive electron yield at the $\Upsilon(4s)$ resonance demonstrating that the $\Upsilon(4s)$ is indeed disintegrating into weakly decaying particles. The normalized cross sections for inclusive electron hadron events and for hadron production measured by the CUSB Collaboration is plotted in Fig. 5.19. From these data they find $B(B \to e\, \bar{\nu}_e\, x) = 13.1 \pm 2.5 \pm 3.0\%$ in agreement with the value of $B(B \to e\, \bar{\nu}_e\, x) = 13.6 \pm 2.1 \pm 1.7\%$ measured by the CLEO group. The first error is the statistical uncertainty, the second the systematic. The CLEO Collaboration has also measured[100] the branching ratio for $B \to \mu\bar{\nu}x$ and they find $B(B \to \mu\bar{\nu}_\mu) = 10.0 \pm 1.3 \pm 2.1\%$.

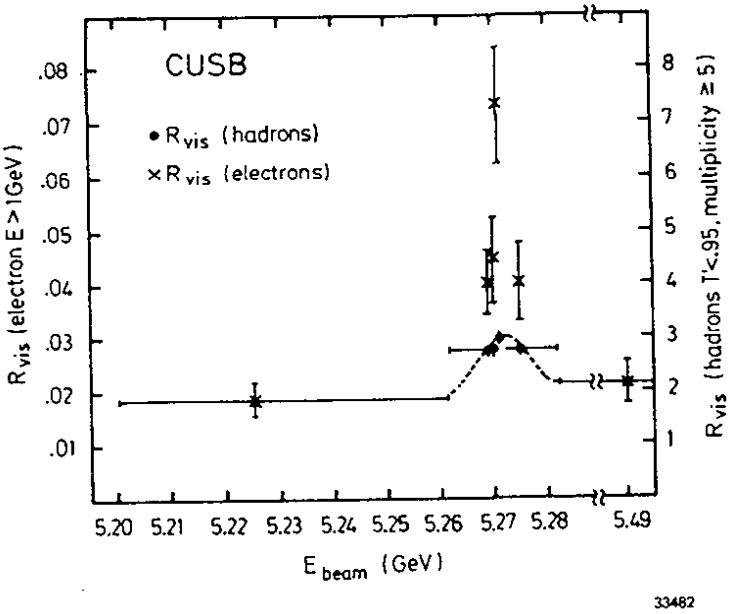

Fig. 5.19

The visible normalized cross sections for inclusive electron (p_e > 1.0 GeV/c) production and the normalized total hadron cross section. The data are from CUSB.

The electron momentum spectrum observed in mixed electron hadron events at the $\Upsilon(4s)$ and corrected for the continuum contribution is plotted in Figs. 5.20 a and b for the CUSB and the CLEO data respectively. The momentum spectra from both experiments favours a hadronic recoil mass of the order of 2 GeV/c^2. A hadronic recoil mass around 1 GeV/c^2 would result in a lepton spectrum much harder than the spectrum observed.

From the observed multiplicity distributions in $B\bar{B}$ decays the CLEO Collaboration finds an average charged multiplicity of $\langle N_{ch} \rangle = 3.50 \pm 0.35$ in semileptonic B decays and $\langle N_{ch} \rangle = 6.31 \pm 0.35$ in nonleptonic B decays. Subtracting the electron they find that on the average 2.5 ± 0.3 hadrons are produced per semileptonic B decay. Groups at SPEAR finds[163] that an average number of 2.5 ± 0.1 charged hadrons are produced in the decays of an equal mixture of D and D^* mesons.

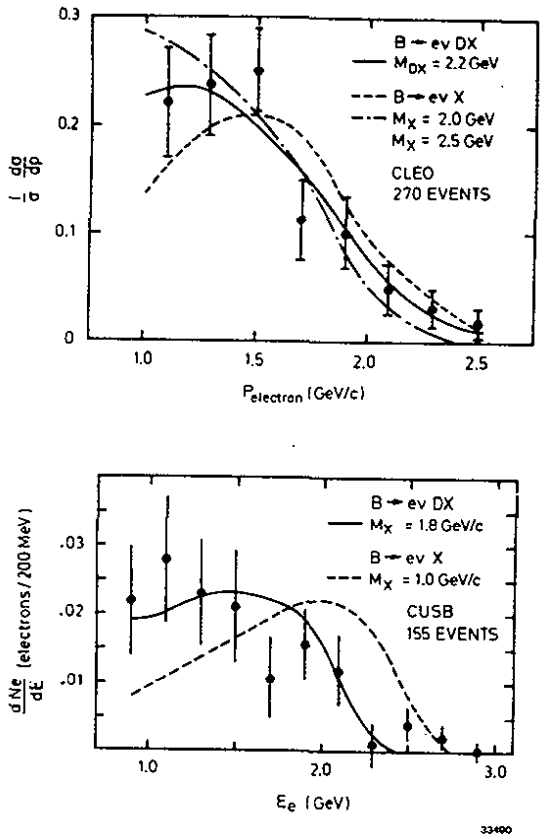

Fig. 5.20

The electron momentum spectrum from $B \to e \bar{\nu} X$.
a) data obtained by CLEO
b) data obtained by CUSB.

The semileptonic branching ratios, the lepton momentum spectrum, and the average charged multiplicities observed in semileptonic B-decays are therefore in agreement with predictions based on the standard model.

Since c quarks predominantly decay into s quarks, the observed kaon yield can be used to determine the relative strengths of $b \to W \bar{c}$ and $b \to W \bar{u}$. Neutral kaons are identified in CLEO for momenta above 0.3 GeV/c by demanding a secondary vertex at least 7 mm from the beam line. The mass is reconstructed assuming the particles to be pions. CUSB identifies neutral kaons using topology only. CLEO identifies charged kaons for momenta between 0.5 GeV/c and 1.0 GeV/c by time of flight. To be less sensitive to normalization uncertainties the groups compare the ratios of kaons per event at the $\Upsilon(4s)$ to the number of kaons per event in the continuum.

The yield of neutral kaons observed by the CUSB Collaboration normalized to the hadronic cross section is plotted in Fig. 5.21 versus c.m. energy. It is clear that relatively more K^o events are produced in $\Upsilon(4s)$ decays than in the continuum. The same behaviour is also observed for charged kaons and the results are summarized in Table 5.6 from reference [100].

Table 5.6 - Comparison of the observed kaon yield with Monte Carlo predictions

Data	Number of kaons observed per event		
	K^o CLEO	K^o CUSB	K^+ CLEO
Continuum	0.73 ± 0.05	0.82 ± 0.08	1.12 ± 0.16
$B\bar{B}$ decay	1.43 ± 0.25	1.52 ± 0.20	2.02 ± 0.25
$R=\frac{B\bar{B}\ \text{decays}}{\text{continuum}}$	1.96 ± 0.34	1.85 ± 0.30	1.80 ± 0.32
	Monte Carlo predictions for $1/2\ (K^{\pm} + K^o)$		
Continuum	0.90		
$B\bar{B}$: $b \to W\bar{c}$	1.60 R = 1.78		
$B\bar{B}$: $b \to W\bar{u}$	0.90 R = 1.00		

The Monte Carlo calculations predict R = 1.8 for $B \to W\bar{c}$ in agreement with the observed ratio of about R = 1.9. The data therefore are consistent with this decay mode only. To set a limit on the fraction (1-f) of the decay $b \to W\bar{u}$ they evaluate

$$R_{measured} = f\ R\ (b \to W\bar{c}) + (1-f)\ R\ (b \to W\bar{u})\ .$$

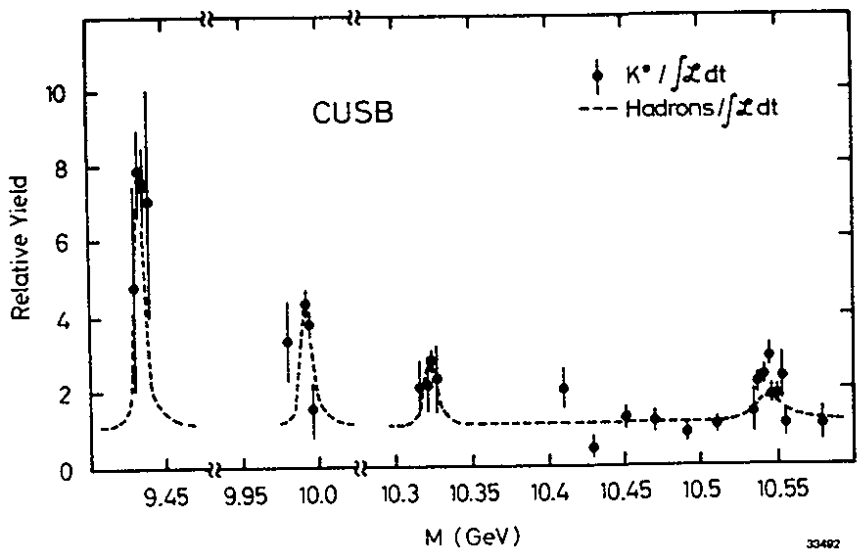

Fig. 5.21

The yield of neutral kaons measured by CLEO as a function of center of mass energy

This expression gives f = 1.12 ± 0.25 and a 90% upper confidence limit of

$$\frac{|b \to W\bar{u}|^2}{|b \to W\bar{c}|^2} < 0.4$$

The CLEO Collaboration has measured the cross section for $e^+e^- \to e(\mu)KX$ and the data are plotted in Fig. 5.22. A strong peak is seen at $\Upsilon(4s)$. From these data and the average number of kaons per B decay it is possible to extract the average number of kaons per B decay for both semileptonic and non leptonic decays and 0.8 ± 0.7 kaon per semileptonic B decay.

About 1.0 kaons are expected per semileptonic decay for $b \to W\bar{c}$ and approximately no kaons for $b \to W\bar{u}$. The number of kaons in semileptonic decays is therefore a sensitive measure of the relative strength of these transitions, however, more data are clearly needed.

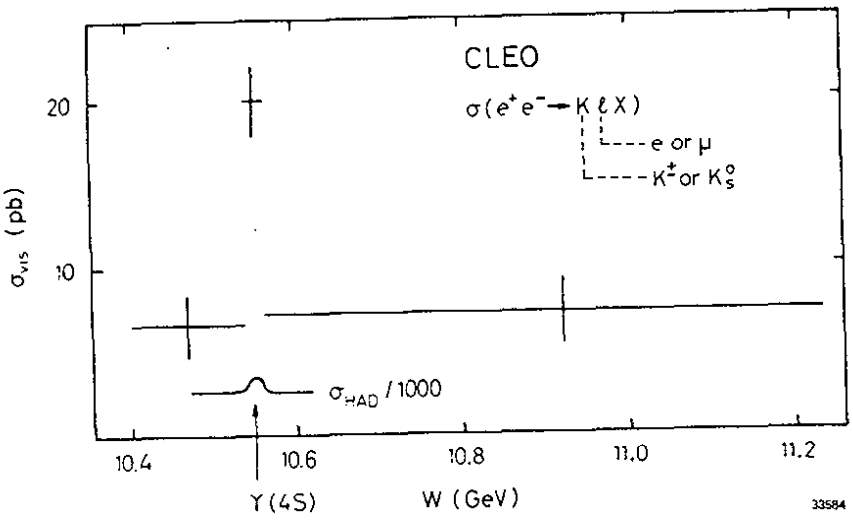

Fig. 5.22

The yield of $e^+e^- \rightarrow e(\mu)$ KX measured by CLEO

The data on B decays are in agreement with the standard model and rule out many of the non standard models. It is indeed very likely that the t quark exists.

6. Hadron Production in e^+e^- Annihilation

At the parton level, e^+e^- annihilation proceeds [7-10] to lowest order by the first graph shown in Fig. 6.1. The neutral timelike current, electromagnetic or weak, couples directly to a pair of quarks. At small distances the quarks behave as if they were free resulting in a total cross section which is proportional to the muon cross section. Neglecting the weak contribution:

$$R = \sigma(e^+e^- \to q\bar{q} \to \text{hadrons}) \; / \; \sigma(e^+e^- \to \mu^+\mu^-) = 3 \; \Sigma \; e_i^2.$$

The factor of three accounts for the number of colours.

The cross section for pointlike scalar quarks would be a factor of four smaller. The spin 1/2 nature of the quarks is also reflected in the angular distribution of $(1 + \cos^2\theta)$ with respect to the beam axis compared to a $\sin^2\theta$ distribution for scalar quarks.

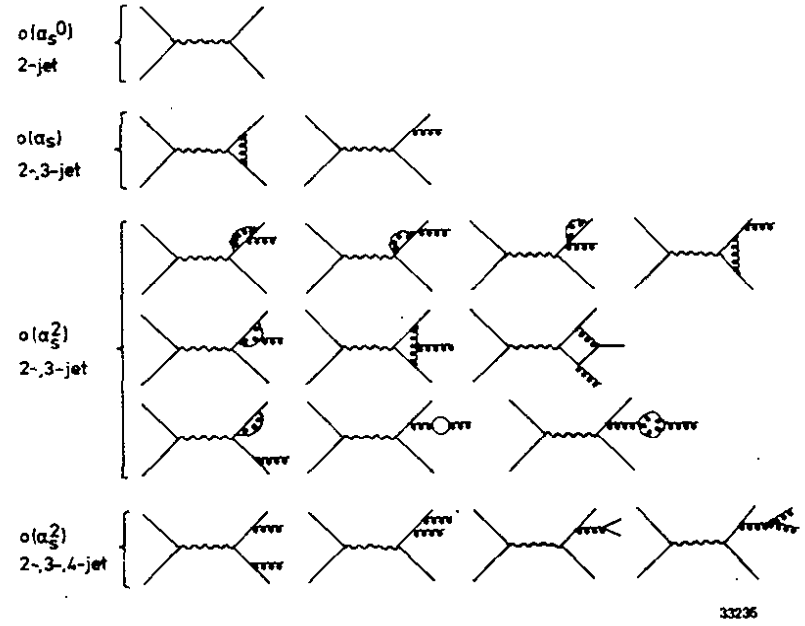

Fig. 6.1 - Leading and next to leading order QCD diagrams for hadron production.

However, quarks are confined and as they move apart new quark pairs are created. At distances greater than 10^{-13} cm the quarks have condensed into hadrons such that quark pairproduction materializes as two back to back hadron jets travelling along the direction of the primary quarks. The hadrons in the jet have typical transverse momenta of 300 MeV with respect to the jet axis independent of energy, and large and increasing momenta along the jet axis.

To first order this picture will be modified in any field theory [12] of strong interactions by the graphs shown in Fig. 6.1. The produced quarks radiate [11] a field quantum which materializes as a hadron jet in the final state leading to planar three jet events. With increasing energy multiple gluon emission with four or more partons in the final state will become visible. This final state is in general not planar. Higher order gluon emission is particularly interesting since these processes can be used to identify the nature of the theory. For example, the last Feynman graph in Fig. 6.1 depicts the gluon self coupling. This coupling is an essential property of Quantum Chromo-Dynamics [14] (QCD); the leading candidate for a strong interaction theory and is absent in abelian field theories like QED.

We might arbitrarily divide the physics which can be extracted from a study of hadron production in e^+e^- annihilation into two classes. Firstly one might try to identify the process on the parton level from the observed final state hadrons. Secondly one can study the mechanism by which a struck quark or a radiated gluon converts into a jet of hadrons. This is presumably a non-perturbative process and so far there is little theoretical guidance.

In this chapter we first discuss some data which directly support the simple picture outlined above and then the more general properties of the hadronic final state.

The evidence for gluons and their properties as determined in e^+e^- annihilation will be discussed in chapter 7.

6.1 The total cross section

The normalized (electron-positron) annihilation cross section R is a well defined quantity in QCD and can be evaluated [164] to all orders in the coupling constant α_s/π defined in Eq. 5.2.

$$6.1 \quad R = 3 \sum_i e_i^2 \left(1 + \alpha_s/\pi + C_2 (\alpha_s/\pi)^2 + \ldots\ldots\ldots\right)$$

R is the sum of the squares of the quark charges, as in the naive quark model, with a small correction due to emission and absorption of gluons. The first term (α_s/π) contributes on the order of 5%, the size of the second order term depends on the renormalization scheme but its value is always less than the first order term. For example in the $\overline{MS}$ scheme $C_2 = 1.99 - 0.12\ N_f$ where N_f is the number of quark flavours - i.e. $C_2\ (\alpha_s/\pi) = 0.02$.

The R values determined [165] by the PETRA groups are plotted in Fig. 6.2 together with some lower energy data [166,167]. Only statistical errors are included and the systematic uncertainties vary between 5% and 10% for the different experiments. The small angle luminosity monitors, the radiative corrections and the acceptance corrections make the largest contribution to the systematic error.

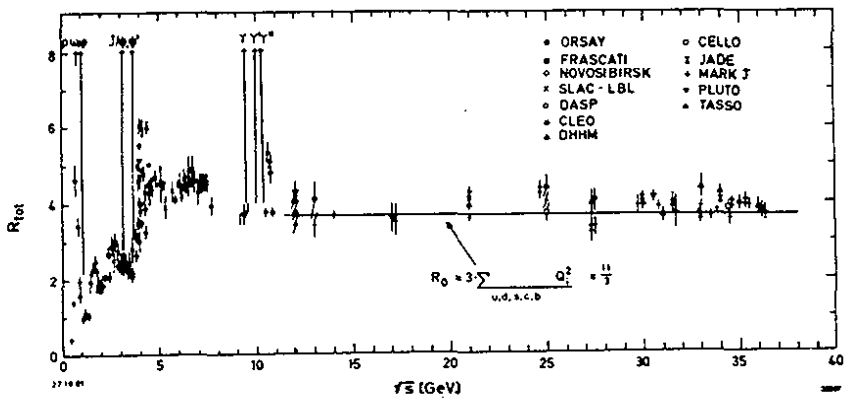

Fig. 6.2 - R, the cross section for $e^+e^- \to$ hadrons normalized to the point cross section $e^+e^- \to \mu^+\mu^-$ plotted versus c.m. energy. Only statistical errors are shown. The solid line indicates the quark model prediction for u, d, s, c and b quarks.

The general features of the observed cross section are in striking agreement with the quark model predictions, both the narrow vector states and the steps in R associated with the liberation of new quark flavours are clearly seen. R does not change between thresholds and its value is roughly given by Eq. 6.1.

The MARK I Collaboration has measured [167] R for c.m. energies between 5.5 GeV and 7.5 GeV with good statistics and an estimated systematic uncertainty of 10%. A careful comparison [168] of these data with QCD shows that the experimental values are on the average 16% above the theoretical prediction.

A precise measurement of R is an many ways easier to do at high than at low energies. As shown below the events are jetlike with a high multiplicity and an angular distribution of the jet axis with respect to the beam axis of $1 + \cos^2\theta$ resulting in a large, well defined acceptance on

the order of 70 - 80%. The contamination from tau pair production is reduced by a cut on multiplicity and the two photon contributions by a cut on visible energy to a very low level.

The PETRA groups find R to be constant within errors above $b\bar{b}$ threshold and the data exclude the production of a new charge 2/3 flavour in this energy region. Above $b\bar{b}$ threshold the quark-parton model predicts R = 11/3 for u, d, s, c and b quarks and this prediction is shown as the solid line in Fig. 6.2. The data seem to be slightly above this value.

Since the data from the various groups agree within the statistical errors they can be averaged and the resulting R value is plotted [165] on an expanded scale in Fig. 6.3. The naive quark-parton model is shown as the dotted line. The QCD predictions [169] with and without weak effects (chapter 3) included are also plotted. Weak effects are negligible in the present PETRA energy for $\sin^2\theta_W = 0.23$. However, note that the total cross section data do constrain the value of $\sin^2\theta_W$ as discussed in chapter 3.6.

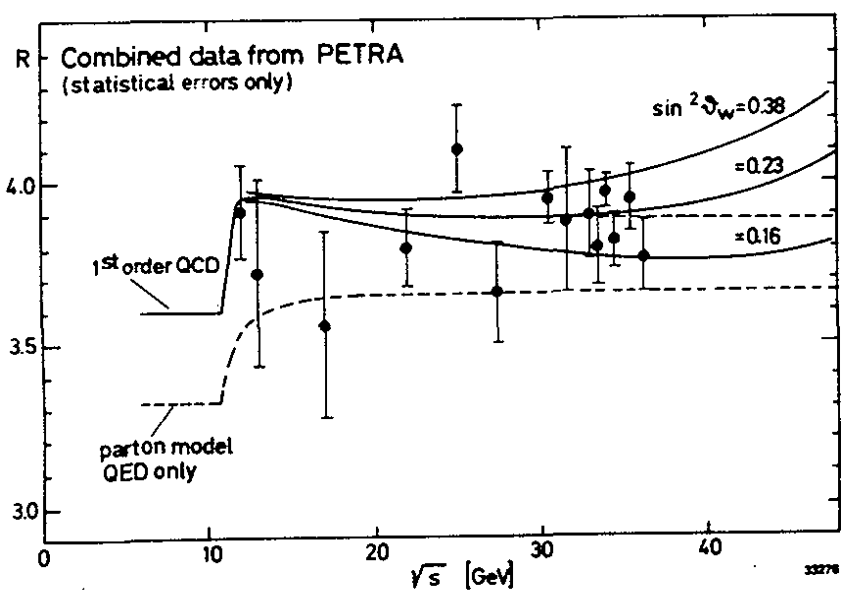

Fig. 6.3 - The R values obtained by combining the data from the various PETRA groups are plotted versus $\sqrt{s}$. The lower dashed line is the quark model prediction. The upper curves show the first order QCD prediction with Λ = 300 MeV for various values of $\sin^2\theta_W$.

The data clearly favour the presence of a QCD correction term, but only on the one standard deviation level. To turn a measurement of the total cross section into a determination of α_s requires that the combined statistical and systematic errors are kept on the 2% level.

The proliferation of leptons and quarks has lead to suggestions [170] that these particles are not elementary but composite made of new entities. In this case the quark will have a size and this will modify the value of R.

Two different fits have been made to limit the quark size from present data.

Söding and Wolf [171] introduce an electric $G_E(s)$ and a magnetic $G_M(s)$ form factor of the quarks and this yields:

$$6.2 \qquad R = 3 \Sigma e_i^2 \{ \frac{2m_q^2}{s} | G_E(s)|^2 + |G_M(s)|^2 \}$$

However, since $m_q^2 << s$, the data can be expressed in terms of $G_M(s)$ only. Assuming $G_M = (1 - s/M^2)^{-1}$ leads to a limit $M > 124$ GeV whereas a dipole form factor $G_M(s) = (1 - s/M_D^2)^{-2}$ leads to $M_D > 176$ GeV. Both limits are 90% confidence lower limits.

The MARK J group fit their data [36] to the form

$$6.3 \qquad R = R_o (1 \mp \frac{s}{s-\Lambda^2}).$$

The value for R_o includes both the gluon correction and effects due to the neutral weak current. They find $\Lambda_+ > 180$ GeV and $\Lambda_- > 285$ GeV. We may thus conclude that quarks are pointlike down to distances of 10^{-16} cm.

6.2 Hadron jets

The jet structure is generally analyzed in terms of sphericity [172] or thrust [173].

The sphericity S is defined as:

$$S = \frac{3}{2} \min \frac{\sum_i (p_T^i)^2}{\sum_i (p^i)^2} \qquad 6.4$$

Here p^i is the momentum and p_T^i the transverse momentum of a track with respect to a given axis. The jet axis is defined as the axis which minimizes transverse momentum squared. Sphericity measures the square of δ, the jet cone opening angle $S = 3/2 \langle\delta^2\rangle$ is 0 for a perfect jet and 1 for a spherical event.

Thrust T is defined as:

$$T = \max \frac{\sum_i |p_\parallel^i|}{\sum_i |p^i|} \qquad 6.5$$

Here p^i is the momentum of a track and $p_\parallel^i$ its projection along a given axis. The jet axis is defined as the axis which maximizes the directed momentum. Expressed in terms of δ, $T \gtrsim (1 - \langle\delta^2\rangle^{1/2}$ and it approaches 1 for a perfect jet event and 1/2 for an isotropic event.

The two jet structure of hadronic events was first seen [174] by the MARK I group at SPEAR in a sphericity analysis of their data. At PETRA/PEP energies the jet structure is already visible in the raw data. Fig. 6.4 shows a typical 2 jet event observed by the TASSO detector.

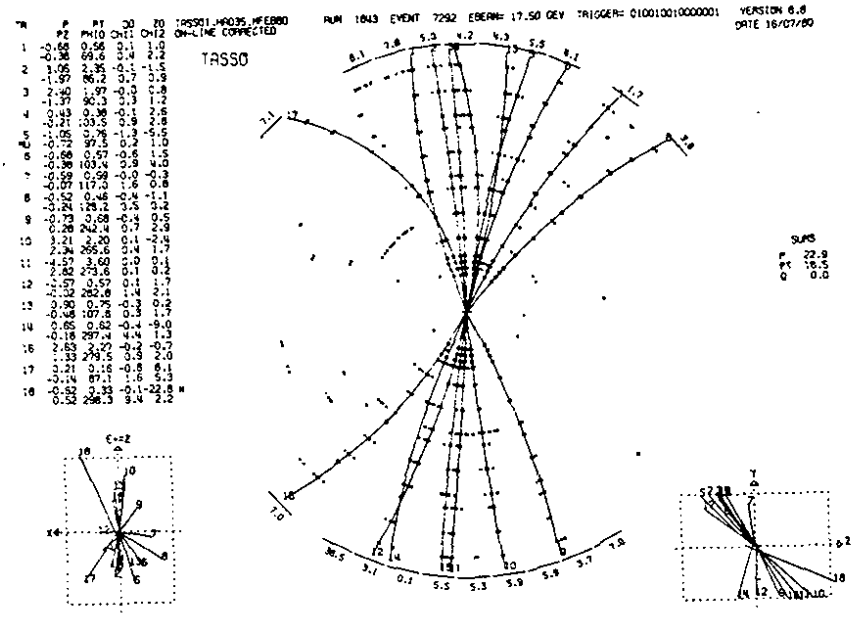

Fig. 6.4 - Two jet events observed by the TASSO group. The jet is viewed along the beam direction.

The average sphericity [175] measured at DORIS and at PETRA is plotted versus the c.m. energy W in Fig. 6.5. The sphericity decreases proportional to $W^{-1/2}$ demonstrating that the jets indeed become more collimated at high energies. The jet cone half opening angle shrinks from 31^{o} at 4 GeV to 17^{o} at 36 GeV - i.e. the hadrons in a 18 GeV jet occupy only 2% of 4π.

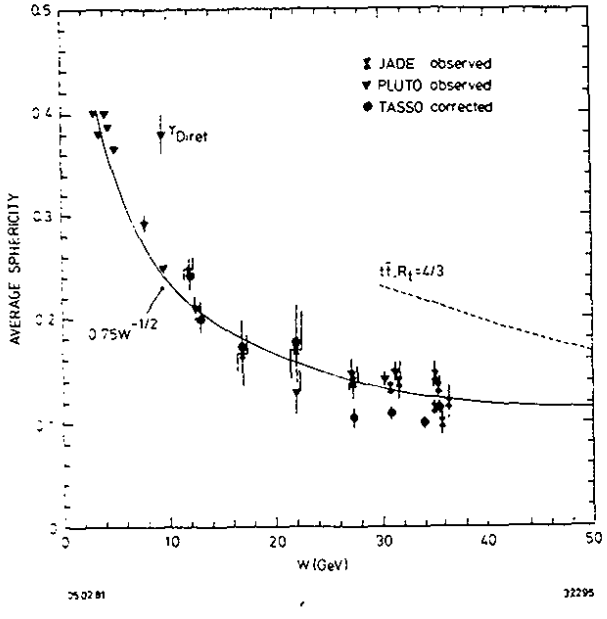

Fig. 6.5
The average sphericity plotted versus the c.m. energy.

The spin of the quark is reflected in the angular distribution of the jet axis with respect to the beam axis. A spin 1/2 quark has $d\sigma/d\Omega \sim 1 + \cos^2\theta$. The angular distribution was first measured [174] by the MARK I Collaboration at SPEAR and they confirmed that the quarks are fermions. The angular distribution of two jet events measured at high energies by the TASSO groups is plotted in Fig. 6.6. The data are in good agreement with the predicted $1 + \cos^2\theta$ distribution shown as the solid line.

6.3 Charge Correlation

The back to back produced quarks have opposite charge. According to the standard picture they will fragment into hadrons by a neutral quark-gluon cascade conserving the initial charge. Therefore, apart from fluctuation, the resulting jet should remember the charge of the primary quark such that the charge found in one jet should be correlated [176] with the charge of the other jet. Furthermore one expects this long range correlation to be found among the fast particles and that the slow particles should exhibit short range correlations only. The TASSO group has found evidence [177] for these correlations using two different methods.

The first method is based on a suggestion [178] by Field and Feynman to use the momentum weighted particle charge as a definition of the jet charge:

$$6.6 \qquad q_{jet}(\gamma) = \sum_{i=1}^{n} e_i \, x_i^{\gamma}$$

Here e_i is the particle charge and $x_i = p_i/p_{beam}$ its relative momentum. The sum is over all particles in the jet. γ must be positive since the

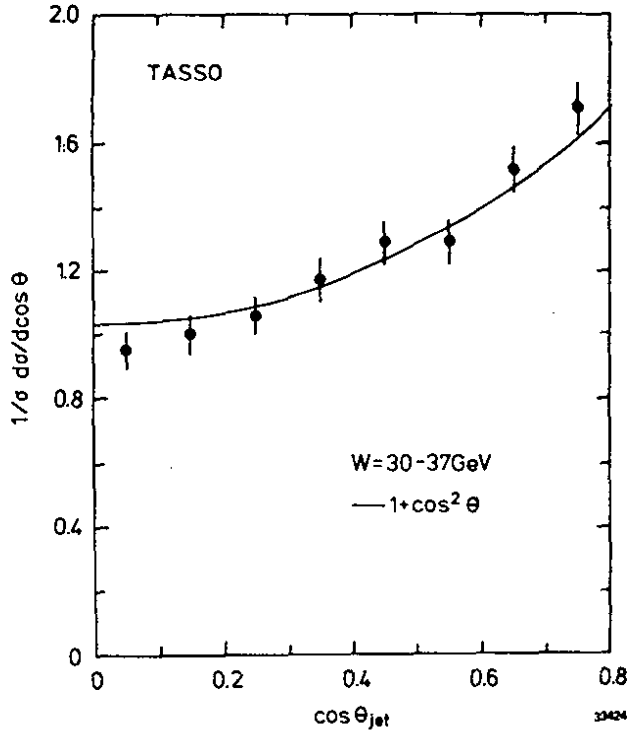

Fig. 6.6
The angular distribution of the jet axis in multihadron events with respect of the beam axis. The jet axis was determined by the TASSO group using the sphericity method. The solid line shows the $1 + \cos^2\theta$ distribution expected from pairproduction of fermions.

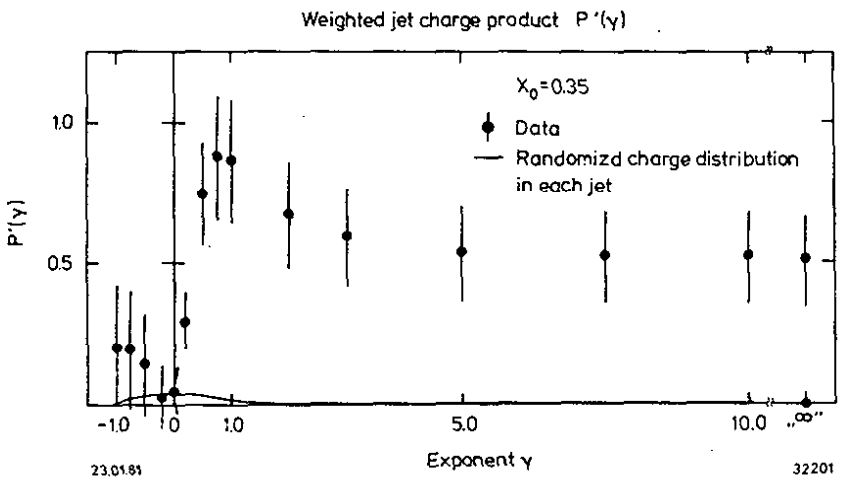

Fig. 6.7 - The value of the momentum weighted charge correlation product $P'(\gamma)$ as a function of γ for events with at least one particle with $x_1 > 0.35$ in each jet. The solid line shows the charge correlation for a randomized charge distribution. The data were obtained by TASSO.

primary quark is expected to be a constituent of a particle with large x_i. A slightly modified definition of the charge is used in order to cancel the strong γ dependence:

$$6.7 \qquad q'_{jet}(\gamma) = \frac{\Sigma\, x_i^{\gamma}}{\Sigma\, x_i^{2\gamma}}\, q_{jet}(\gamma)$$

With this definition of a jet charge they define a correlation:

$$6.8 \qquad P'(\gamma) = - \langle q'_1(\gamma) \cdot q'_2(\gamma) \rangle \quad .$$

$P'(\gamma)$ is evaluated for all events which have at least one particle with $x_i \geq 0.35$ in each jet. The result, plotted in Fig. 6.7 versus γ, shows a strong positive correlation as expected if long range charge correlations are present.

A long range charge correlation is also trivially imposed by the fact that the event as a whole must be neutral - i.e. if one jet is negativly charged then the other must be positivly charged by charge conservation. This effect has been evaluated by randomly redistributing all the chargee in the jet and then evaluating $P'(\gamma)$. The result is shown as the solid line. The observed charge correlation cannot be explained by charge conservation above.

The charge correlation has been further investigated by evaluating the function:

$$6.9 \qquad \bar{\phi}(y,y') = - \frac{1}{\Delta y \Delta y'} < 1/n \sum_{k=i}^{n} \sum_{i \neq k} e_i(y)\, e_k(y') >$$

In this expression $e_i(y)$ is the charge of a particle i at rapidity y in the interval Δy and $e_k(y')$ is the charge of a particle k at a rapidity y' in the interval $\Delta y'$. The rapidity is defined as

$$y = \frac{1}{2} \ln \left(\frac{(E + p_{\parallel})}{(E - p_{\parallel})} \right)$$

where $p_{\parallel}$ is the particle momentum along the jet axis. The function $\bar{\phi}(y,y')$ is related to the probability that the particles i and k have opposite sign charges minus the probability that the charges have the same sign. Since the event as a whole is neutral the function $\bar{\phi}(y,y')$ simply shows how the charge of particle i at a rapidity y is being compensated. The normalization is choosen such that $\int \bar{\phi}(y,y')\, dy' = 1$. In Fig. 6.8 a,b,c,d the ratio $\tilde{\phi}(y,y') = \bar{\phi}(y,y') \,/ \int \phi(y,y')\, dy$ is plotted versus y with the test particle in various rapidity intervals y'.

The distribution for $-0.75 \leq y' \leq 0$ i.e. a slow particle is shown in Fig. 6.8a. This distribution peaks at small negative values of y and shows that the charge of a slow particle is indeed compensated locally as expected if only short range correlations are present. The data are in good agreement with the standard Monte Carlo calculations (see below) based on $q\bar{q}$ and $q\bar{q}g$ production shown as the solid line.

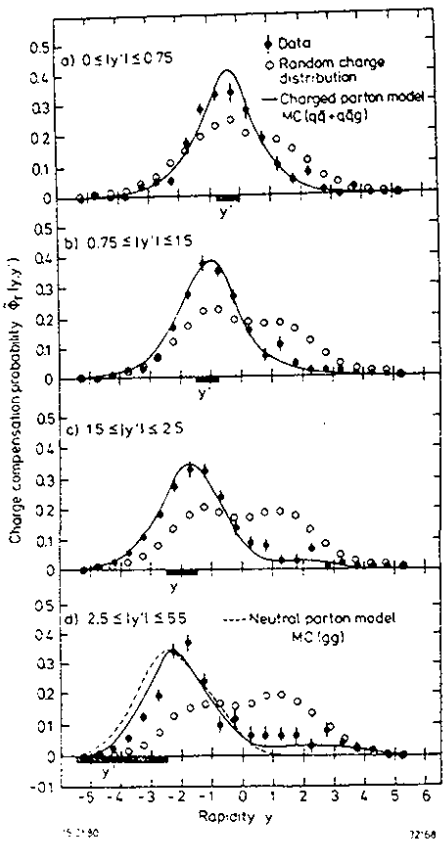

Fig. 6.8
The charge compensation probability plotted versus rapidity y for various rapidity intervals $\Delta y'$ of the test particle. The prediction for a charged and neutral parton model is shown by the solid and the dashed line. The charge compensation probability for a randomized charge distribution is shown by the open circles. The data were obtained by TASSO.

As the test particle becomes faster the distribution becomes increasingly skewed with a tail extending to positive y values. In Fig. 6.8d the correlation function is plotted for $-5.5 \leq y' \leq -2.5$. Although the bulk of the charge is still compensated locally there is now a significant signal at the opposite end of the rapidity plot. The probability that the charge of particle with $y' < -2.5$ is compensated by a particle in the opposite jet with $y > 1$ is $(15.4 \pm 2.6)\%$.

This long range correlation is also reproduced by the standard Monte Carlo programm (see chapter 7). However, this correlation is not present if the initial partons are neutral. This was demonstrated by using the same M.C. programme but assuming the initial quark to be neutral. The results shown as the dashed line in Fig. 6.8 d, fail to reproduce the long range correlation observed.

The charges were also distributed at random among the particles in an event and the resulting correlation function evaluated. The ensuing correlation functions, shown as the open circles in Fig. 6.8 are much wider than the data. Thus the TASSO group has demonstrated that a long range charge correlation between particles in opposite jets exists and that the initial partons are charged.

6.4 The gross properties of the final state

The data above confirm the basic mechanism $e^+e^- \to q\bar{q}(g) \to$ hadron - i.e. the hadrons result from the fragmentation of quarks and gluons. We next discuss some of the gross properties of the final state.

6.4.1 The neutral energy fraction

The JADE and the CELLO Collaborations have determined ρ_γ, the fraction of total energy converted into photons, by a direct measurement of the photon energy deposited in lead glass counters surrounding the detector. JADE has also determined the total neutral energy fraction ρ_N by a measurement of the energy carried away by charged particles and subtracting this from the known c.m. energy. The results [165] are plotted in Fig. 6.9 versus energy and shows that both the neutral energy fraction and the gamma energy fraction are constant within errors for energies between 12 GeV and 35 GeV. The data are also in agreement with a measurement [179] of the neutral energy fraction by the Crystal Ball Collaboration.

The JADE group has also evaluated the neutrino energy fraction ρ_ν

$$\rho_\nu = \rho_N - \rho_\gamma - \rho_{K_L^0,\, n}.$$

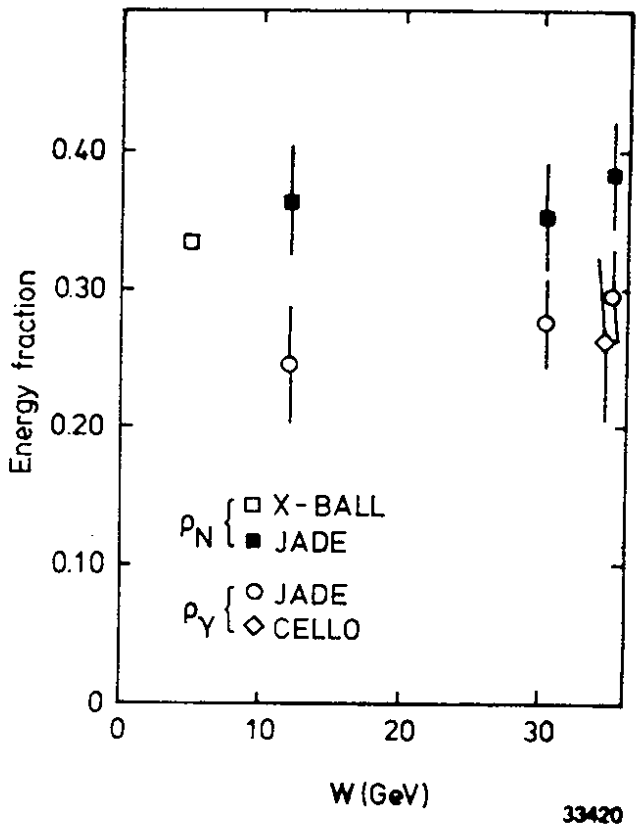

Fig. 6.9
The fraction of total energy into photons ρ_γ and neutral energy ρ_N plotted versus c.m. energy.

The energy fraction $\rho_{K_L^0,n}$ carried off by K_L^0 and neutrons was estimated. They find ρ_γ < 10% with 95% c.l. The Pati-Salam model [180] with integral charged quarks predict that between 18% and 28% of c.m. energy is carried off by neutrinos in disagreement with the experimental results.

6.4.2 Charged multiplicity

The averaged charged multiplicity observed at high energies [165,181] is plotted together with lower energy data [182] in Fig. 6.10. The high energy data points from various groups are in reasonable agreement and well above the multiplicity predicted by extrapolating lower energy data according to the a + b lns dependence predicted in the naive quark-parton model.

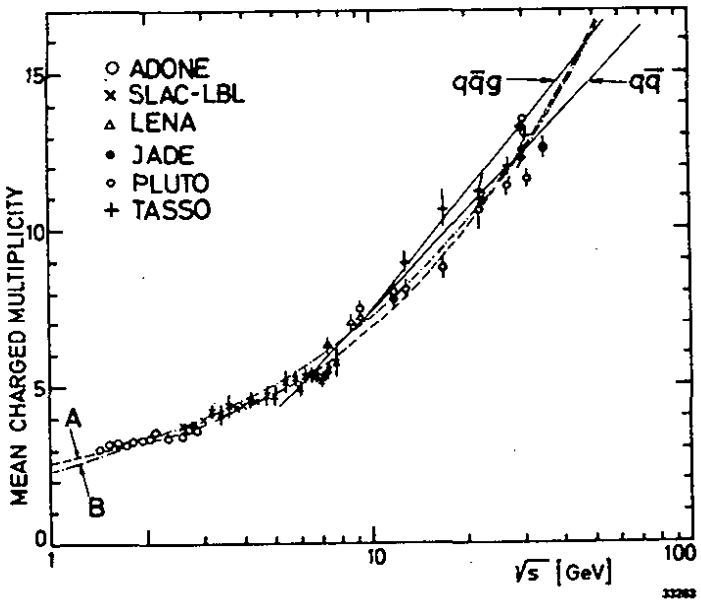

Fig. 6.10
The charged particle multiplicity plotted versus c.m. energy. The dashed line (A) indicates a fit using the QCD form $\langle n_{ch} \rangle = n_o + a \exp(b\sqrt{\ln(s/\Lambda^2)})$. The dashed-dotted line indicates a fit of the form $\langle n_{ch} \rangle \sim s^{1/4}$. The solid lines marked $q\bar{q}g$ and $q\bar{q}$ are M.C. results using a standard fragmentation model with and without gluons.

In the leading log QCD, the averaged charged multiplicity n_{ch} is expected [183] to increase as

6.11 $$\langle n_{ch} \rangle = n_o + a \cdot \exp\left(b\sqrt{\ln(s/\Lambda^2)}\right) \text{ with } b = 1.77.$$

Indeed the data are well represented[165] in the entire energy region by this form with $n_\rho = 2.0 \pm 0.2$, $a = 0.027 \pm 0.01$ and $b = 1.9 \pm 0.2$. The fit is shown as the dashed curve marked A in Fig. 6.8. However, most of the sharp increase in multiplicity seem to be unrelated to multiple gluon emission. This is demonstrated by a computation of the charged multiplicity expected for quark pairproduction with subsequent fragmentation. The result of this computation which does not include gluon emission is shown as the solid line marked $q\bar{q}$ in Fig. 6.8. A similar computation including gluon emission predicts a charged multiplicity higher by only one unit of charge at the highest PETRA energy. The bulk of the strong increase in

multiplicity is therefore apparently a phase space effect; the full cascade process can only develop at c.m. energies above 10 GeV.

A simple statistical model [184] predicts the multiplicity to rise proportional to $s^{1/4}$. This dependence - shown as the curve marked (B) in Fig. 6.8 represents the data rather well. The model, however, fails to fit [165] the charged particle dispersion

$$D_{ch} = \sqrt{\langle N_{ch}^2 \rangle - \langle N_{ch} \rangle^2}$$

6.5 Particle ratios and momentum spectra

Hadrons have now been identified over a large range in momentum and the available data with references are summarized in Table 6.1.

The pion fraction, measured by the TASSO Collaboration, is plotted versus momentum for various c.m. energies in Fig. 6.11. The pion fraction is nearly independent of c.m. energy and decreases slowly with increasing pion momentum from nearly 100% at low momenta to around 50-60% at the highest momenta measured.

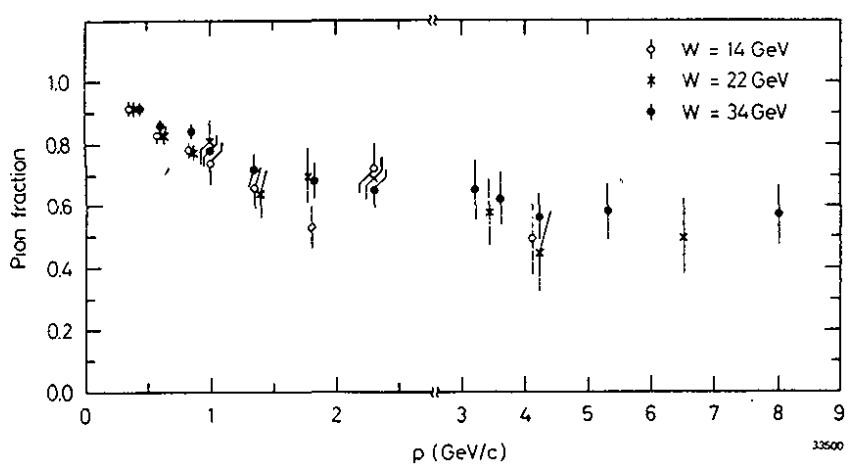

Fig. 6.11 - The pion fraction in e^+e^- → hadrons as a function of momentum for various c.m. energies. The data are from the TASSO Collaboration.

The cross section $d\sigma/dp$ to produce $\pi^{\pm}$, π^{0}, $K^{\pm}$, $K^{0}\overline{K^{0}}$, $p\bar{p}$ and $\Lambda\bar{\Lambda}$ at a c.m. energy of 30 GeV is plotted in Fig. 6.12 versus momentum. The data show that the cross section for $\pi^{+} + \pi^{-}$ production is equal to twice the cross section for π^{0} production. Also the cross sections for charged and neutral kaon production are in rough agreement in the momentum region where they overlap. Although pions dominate at low energies, other particle species become increasingly important with momentum. For example at 10 GeV a ratio of $\pi^{\pm}$: $K^{0}\overline{K^{0}}$: $\Lambda\bar{\Lambda}$ of 90 : 50 : 20 is observed. Thus a substantial number of heavy particles is produced and a typical event at 30 GeV in c.m. contains 11 $\pi^{\pm}$, 5.5 π^{0}, 1.4 $K^{0}\overline{K^{0}}$ (1.4 $K^{+}K^{-}$) $\geq$ 0.4 $p\bar{p}$ and 0.3 $\Lambda\bar{\Lambda}$ in the final state. The number of neutral kaons is about a factor of three larger than the yield observed in pp interactions.

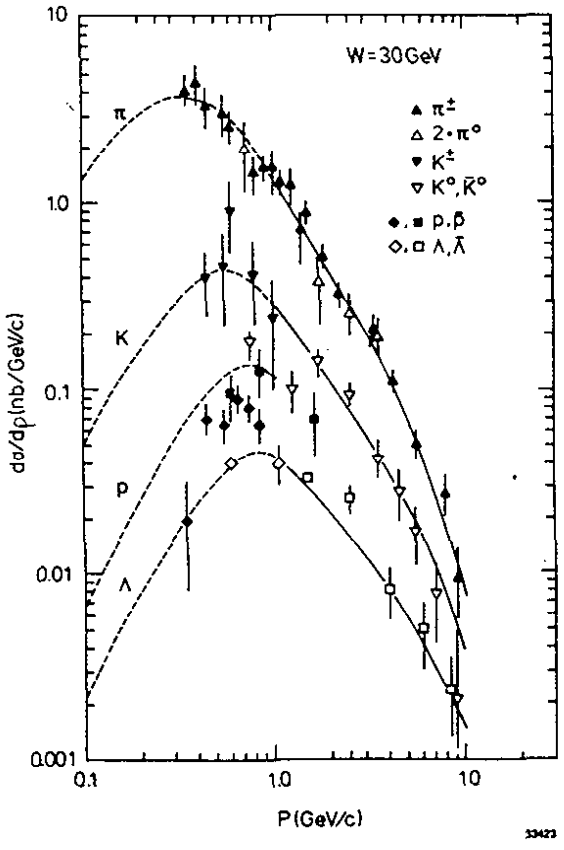

Fig. 6.12
Differential cross sections $d\sigma/dp$ for inclusive particle production $e^{+}e^{-} \to h\ x$ for $\pi^{+} + \pi^{-}$ (TASSO, preliminary), $2\ \pi^{0}$ (TASSO), $K^{+} + K^{-}$ (TASSO), $K^{0} + \bar{K}^{0}$ (TASSO), $p + p$ (JADE, TASSO), $\Lambda + \bar{\Lambda}$ (JADE, TASSO). The dashed curves are of the form $E^{2}/p^{2}\ d\sigma/dp \sim \exp(-bE)$ with $b = 3.6$ GeV. The solid curves are drawn just to guide the eye.

Table 6.1 - Data on identified hadrons at high energies

Particles	Group	Technique	Momentum range (GeV/c)	Reference
π^0	TASSO	Liquid Argon	0.5 - 4.0	185
$\pi^\pm$	JADE	dE/dx	< 0.7, 2-7	Preliminary (165)
	TASSO	TOF Cerenkov	0.4 - 10.0	186
$K^\pm$	JADE	dE/dx	< 0.7	Preliminary (165)
	TASSO	TOF	< 1.1	186
K^0, $\bar{K}^0$	JADE	$K^0_S \to \pi^+\pi^-$	all momenta	Preliminary (165)
	PLUTO	- " -	all momenta	187
	TASSO	- " -	all momenta	188, 189
	MARK II	- " -	all momenta	Preliminary (37)
Λ, $\bar{\Lambda}$	JADE	$\bar{\Lambda} \to \bar{p}\,\pi^+$ ($\bar{p}$ and π^+ by dE/dx)	0.4 - 1.1	190
	TASSO	vertex fits to oppositly charged pairs	1 - 10	189
	MARK II	- " -	1 - 10	Preliminary (37)
$p\bar{p}$	JADE	dE/dx	0.3 - 0.9	Preliminary (165)
	TASSO	TOF	0.5 - 2.2	186
	MARK II	TOF	0.5 - 2.0	Preliminary (37)

The invariant cross section for neutral kaon production is plotted [191] in Fig. 6.13 for data obtained at different c.m. energies. The strange constituent quark in the K^0 result from primary $s\bar{s}$ production, weak decays of $c\bar{c}$ and $b\bar{b}$ quarks, plus the contribution from $s\bar{s}$ pairs created from the vacuum. The contribution from these sources and their sum have been eva-

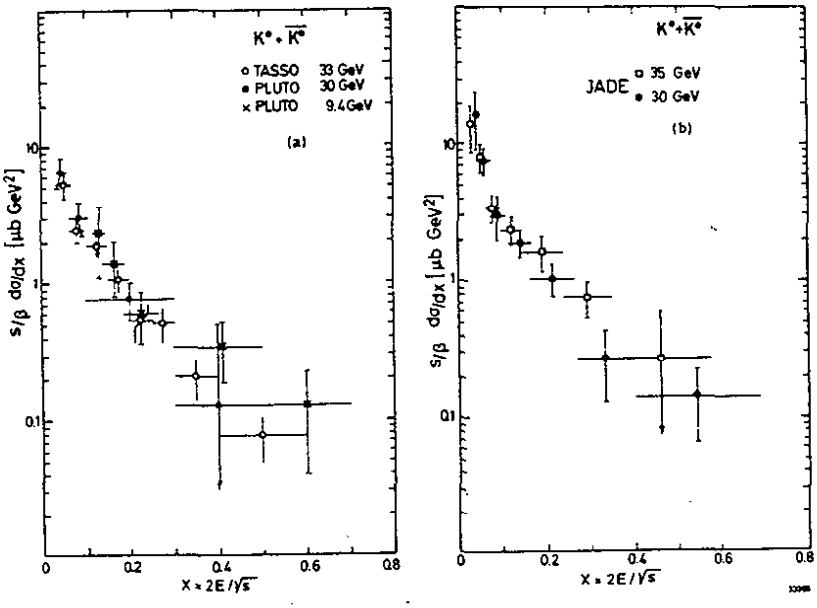

Fig. 6.13 - The invariant cross section $s/\beta\ d\sigma/dx$ for inclusive $K^0 + \bar{K}^0$ production versus x for various c.m. energies.

luated using the standard M.C. model and are plotted in Fig. 6.14. The M.C. computations are in fair agreement with the data and indicate that the sea contribution is the dominant contribution even up to large values of x.

To form a baryon requires three quarks in a colour singlet. One might therefore naivly expect baryon production to be strongly suppressed relativ to meson production. Maybe the most surprising results obtained in the inclusive measurements has been the large cross section for baryon production. This may reflect the fact that the qaurks have baryon charge 1/3. The measured cross sections $d\sigma/dp$ for inclusive p, $\bar{p}$ production around 30 GeV in c.m. are plotted [37] in Fig. 6.15. The to-

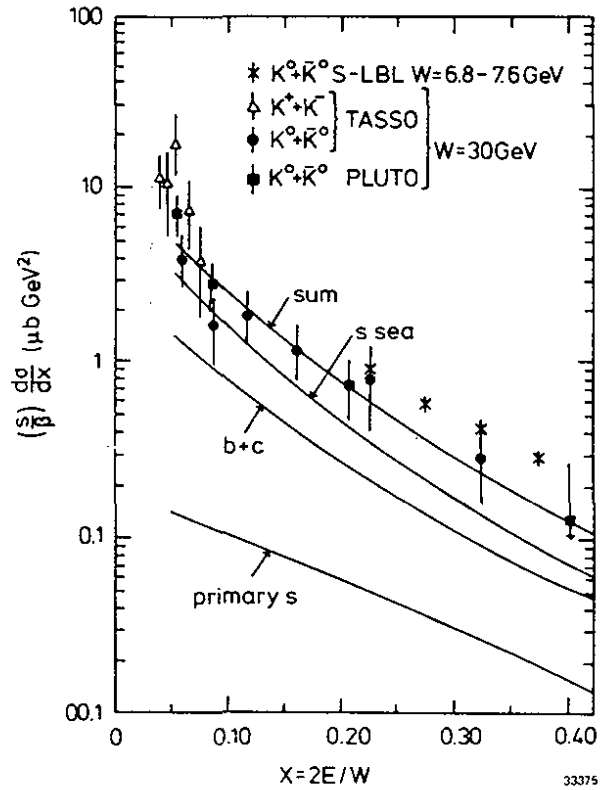

Fig. 6.14

The invariant cross section $s/\beta\ d\sigma/dx$ for inclusive $K^0 + \bar{K}^0$ production is plotted versus x. The estimated contributions from primary $s\bar{s}$, $c\bar{c}$ and $b\bar{b}$ production and from $s\bar{s}$ paircreation from the vacuum together with the sum is also shown.

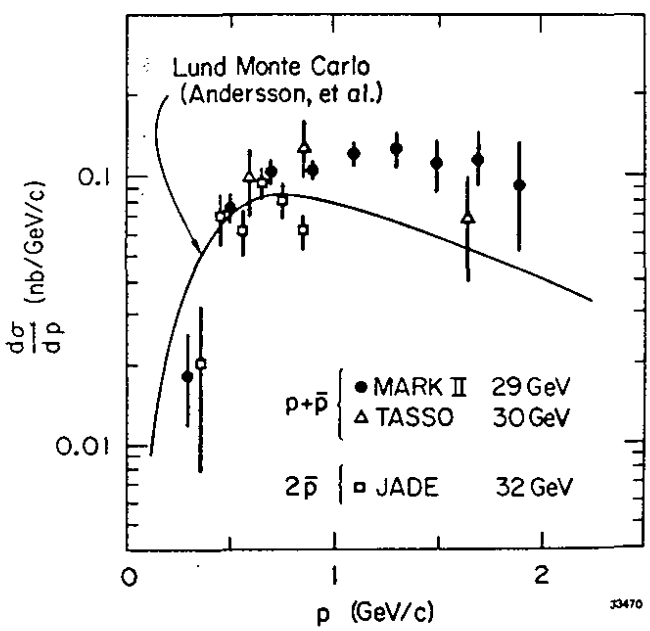

Fig. 6.15

The cross section $d\sigma/dp$ for inclusive $p + \bar{p}$ production versus momentum.

tal cross section for $p\bar{p}$ production is plotted in Fig. 6.16 versus energy together with data at lower energies. The error at the proton data is quite large since the cross sections have only been measured over a limited momentum range. The data indicate that about 0.7 nucleon pairs are produced per event.

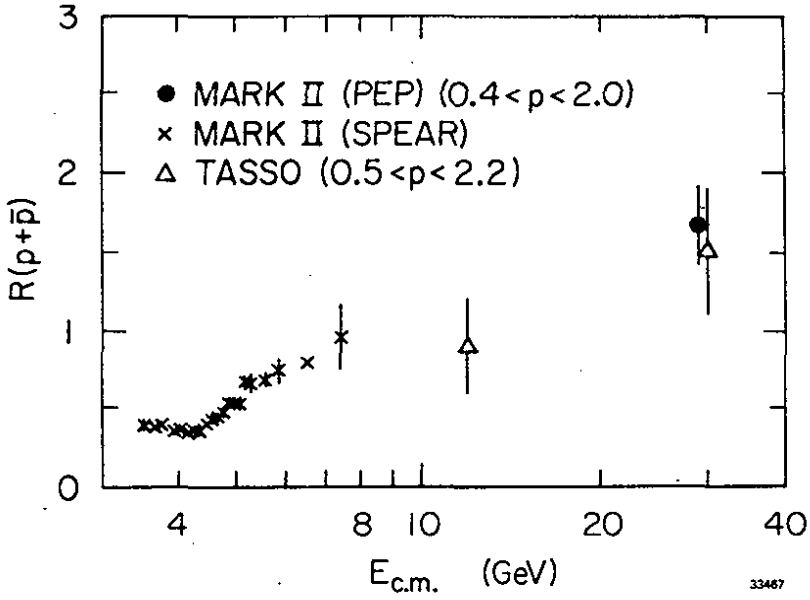

Fig. 6.16 - The total cross section for inclusive p + $\bar{p}$ production normalized to the muon pair production cross section versus c.m. energy.

Inclusive $\Lambda\bar{\Lambda}$ production however, can be measured over a wide momentum range since the Λ's can be identified via the decay mode $\Lambda \rightarrow p\pi$. The invariant cross section for $\Lambda\bar{\Lambda}$ production measured by the TASSO Collaboration is plotted in Fig. 6.17 and compared to the invariant cross sections for inclusive charged pion and neutral kaon production measured by the same group. The invariant cross section for $\Lambda\bar{\Lambda}$ production normalized to the invariant cross sections for kaon or pion production is apparently independent of momentum - i.e. the relative probability of creating a colourless diquark system and a colourless threequark system is independent of momentum.

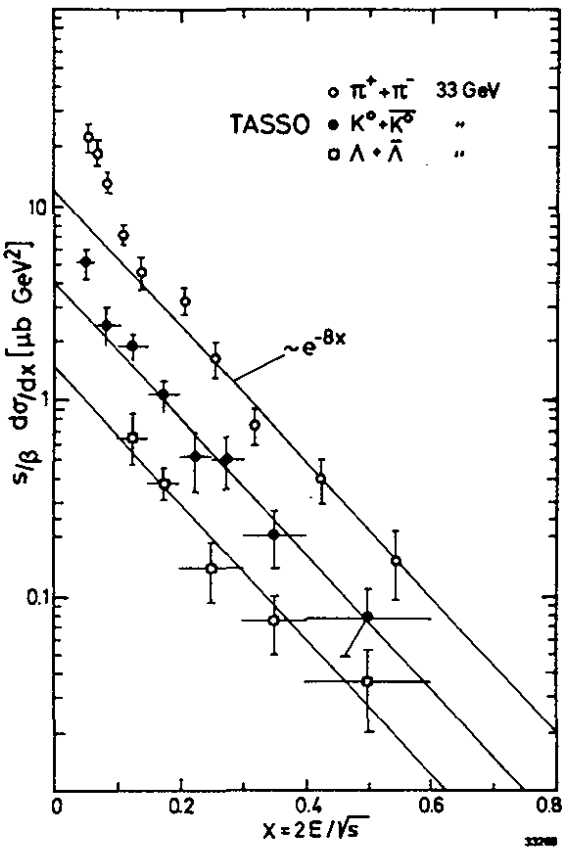

Fig. 6.17
The invariant cross section $s/\beta\ d\sigma/dx$ for inclusive $\pi^+ + \pi^-$, $K^0 + \bar{K}^0$ and $\Lambda + \bar{\Lambda}$ production versus x.

This has lead many authors [192,193] to consider diquark production - i.e. not only quark pairs ($q\bar{q}$) but also ($qq \cdot \bar{q}\bar{q}$) states are produced in the quark cascade.

In fact the available data can be well fit assuming the relative probability for creating a diquark is 0.075%. The prediction[194] of such a simple model is shown in Fig. 6.17. More detailed models of baryon production based on the string model and incorporating diquarks have also been given. The dashed-dotted curve in Fig. 6.17 and the solid line in Fig. 6.18 show the prediction [192] from the Lund group based on such a model. The model fits the proton data at low momenta but decreases faster with momentum than the observed cross section. The model fails to predict the Λ data by a factor of 2 to 3.

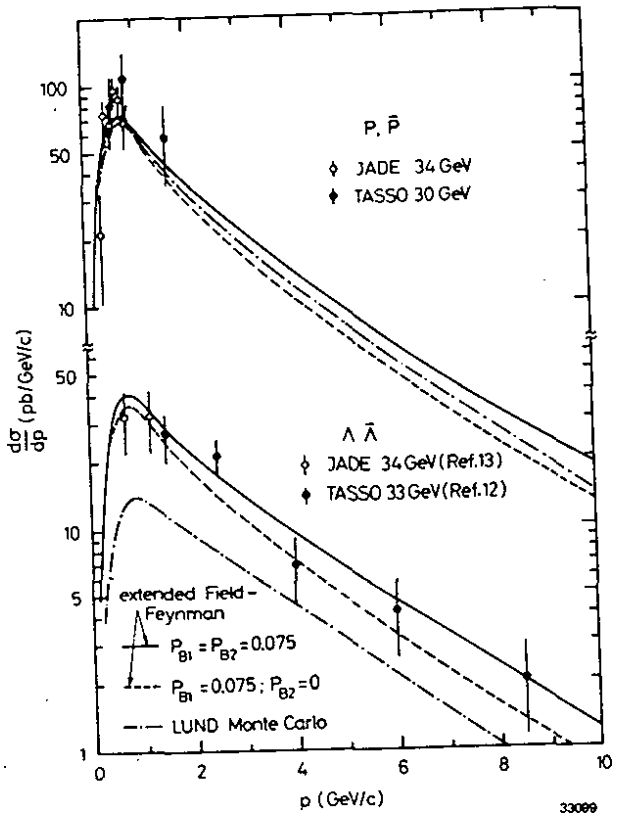

Fig. 6.18
The cross section dσ/dp for inclusive production of $p + \bar{p}$ and $\Lambda + \bar{\Lambda}$ at c.m. energies between 30 and 34 GeV. The solid and dashed curves show the prediction based on the model of Meyer. The dashed-dotted curves show the prediction of the Lund model.

6.7 Scaling violations

The differential cross section for producing a hadron with energy E, momentum p and mass m at an angle θ with respect to the beam axis can be written [195] in terms of two structure functions W_1 and W_2 as:

$$6.12 \qquad \frac{d\sigma}{dx d\Omega} = \frac{\alpha^2}{s} \beta \times (mW_1 + 1/4\ \beta^2 \times \nu W_2 \sin^2\theta)$$

with $\beta = P_h/E_h$, $x = 2E_h/\sqrt{s}$ and $\nu = (E_h/m\sqrt{s})$.

ν is the energy of the virtual photon viewed in the rest system of h.

Integrating this expression over angles and retaining only the leading terms yield:

6.13 $$\frac{d\sigma}{dx} \simeq \frac{4\pi\alpha^2}{s} \beta \times mW_1 .$$

The quark model predict W_1 to scale - i.e. to be a function of x only. This leads to:

6.14 $$\frac{d\sigma}{dx} (e^+e^- \to h\ x) = \sum_q \sigma(q\bar{q}) [D_q^h(x) + D_{\bar{q}}^h(x)]$$

$D_q^h(x)$, the fragmentation function gives the probability that a primary quark q yield a hadron h with relative momentum x.

In QCD $s/\beta\ d\sigma/dx$ no longer scales; soft collinear gluon emission (Fig. 6.1) will deplete the particle yield at large values of x and enhance the yield at small values of x since the energy is now shared between the quark and the gluon. In general - since q^2 is very large compared to Λ^2 - the effects are rather small of the order of 10 - 20% in the PETRA/PEP energy range. To see a clear effect data in the SPEAR and DORIS energy range must be compared with data obtained at higher energies at PETRA and PEP.

The scaled cross sections $s\ d\sigma/dx$ for inclusive charged particle production as measured by DASP at DORIS, by MARK I at SPEAR and by TASSO, JADE and CELLO at PETRA are plotted[165] in Fig. 6.19 versus y. The solid line - $s\ d\sigma/dx = 23 \exp(-8x_p)$ μb GeV^2 - is drawn to guide the eye. The cross section at $x < 0.2$ increases dramatically with energy and shows that the observed increase in the multiplicity is due to slow particles. The low energy cross section is above the high energy cross section at larger values of x as expected in QCD. In order to reduce the systematic uncertainties it is advantagous to compare data collected with the same detector

over a large range in energies. In Fig. 6.20 the inclusive cross section s $d\sigma/dx$ measured at 5.2 GeV and at 29 GeV using the MARK II detector is shown. The low energy data are clearly above the high energy data at $x \geq 0.3$.

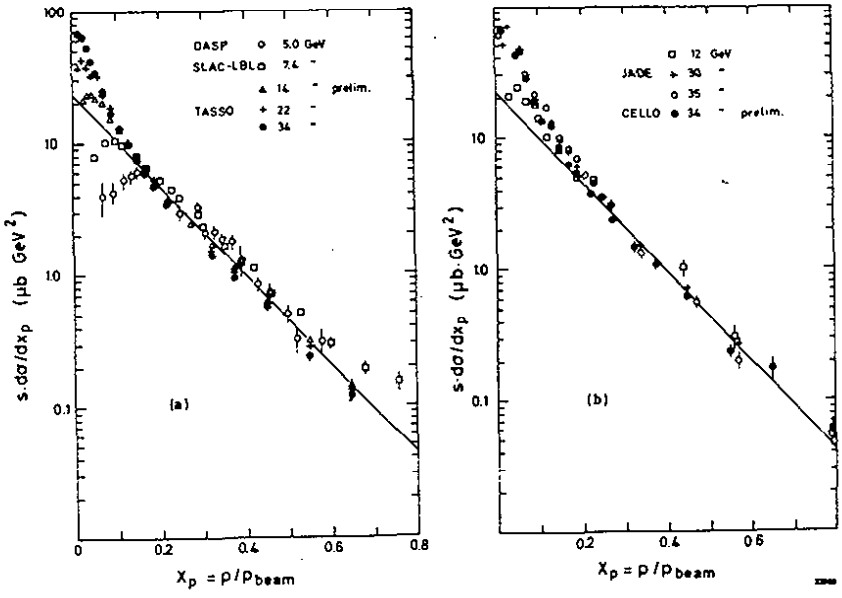

Fig. 6.19 - The invariant cross section s $d\sigma/dx_0$ plotted versus x for c.m. energies between 5.0 and 34 GeV. The solid line, s $d\sigma/dx = 23 \exp(-8\, x_p)$ GeV^2 μb, is drawn to guide the eye.

In Fig. 6.21 the invariant cross section is plotted versus the c.m. energy for fixed values of x. The energy dependence is consistent with that expected in QCD. A direct comparison with QCD might be premature since effects caused by crossing the $c\bar{c}$ and the $b\bar{b}$ threshold and the fact that the hadrons are not identified still remains to be studied.

The invariant cross section $s/\beta\, d\sigma/dx$ for identified charged pions is plotted in Fig. 6.22 versus x for c.m. energies between 4.5 GeV and 34 GeV. Also these data, which came from the DASP and the TASSO Collaborations, indicate a sizable scaling violation.

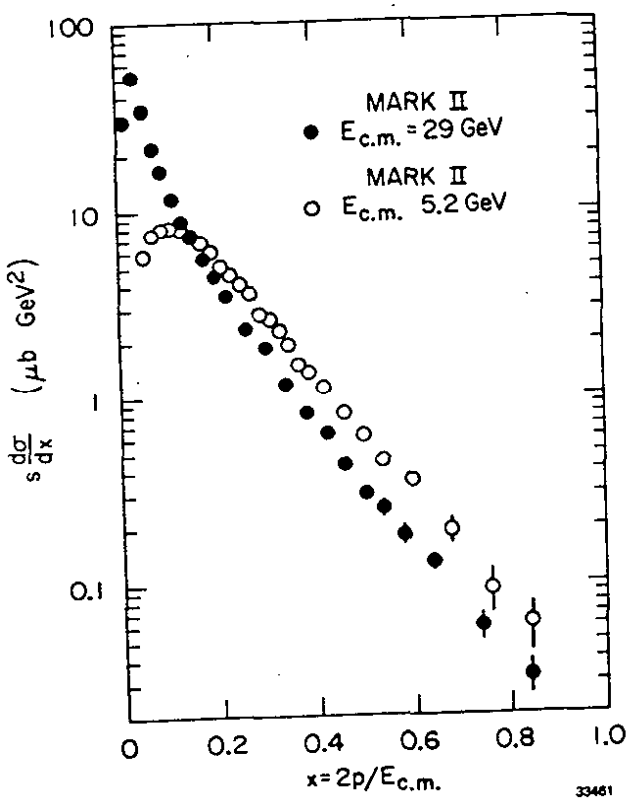

Fig. 6.20
Comparison of the inclusive cross sections $s\, d\sigma/dx$ for $e^+e^- \to h^\pm x$ measured by the MARK II Collaboration at 5.2 and 29 GeV.

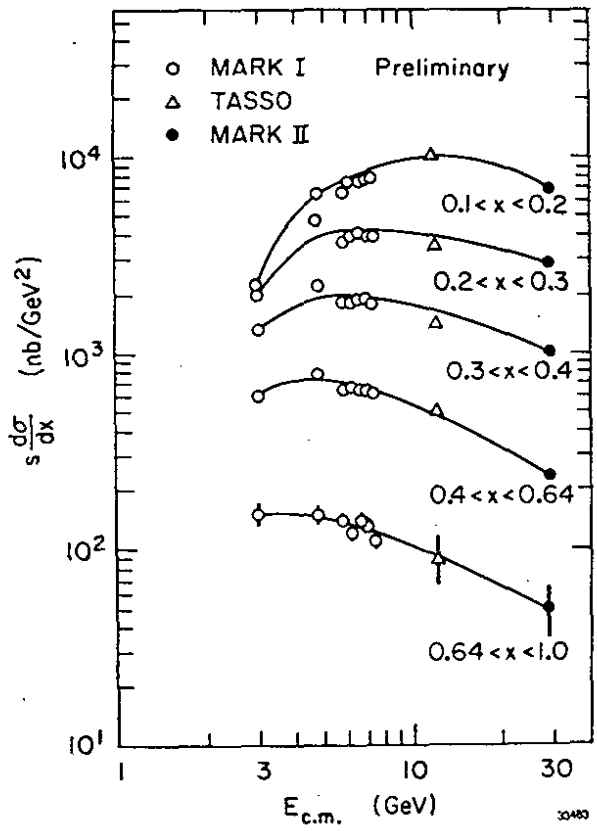

Fig. 6.21
The invariant cross section s dσ/dx plotted versus c.m. energy for fixed values of $x = 2P/\sqrt{s}$. The solid lines are drawn just to guide the eye.

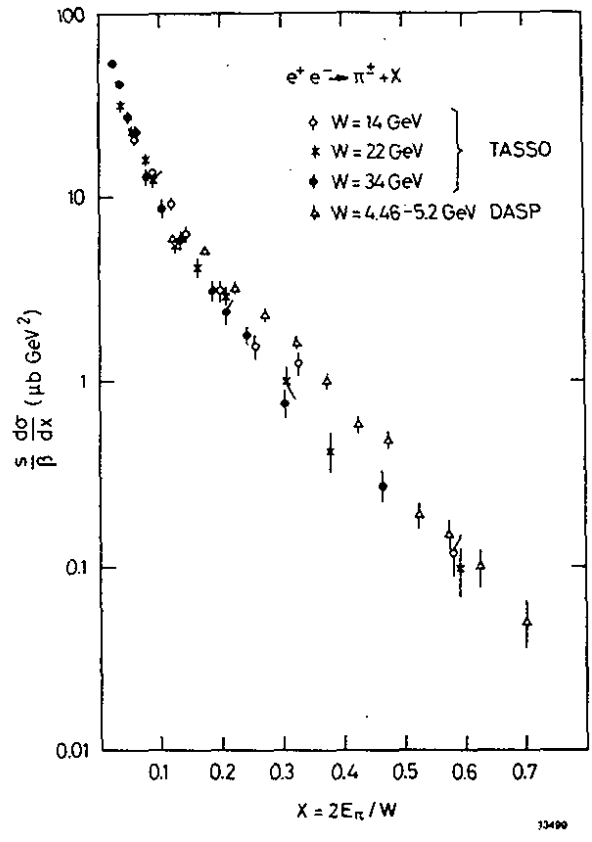

Fig. 6.22
The invariant cross section $s/\beta\ d\sigma/dx$ for inclusive $\pi^+ + \pi^-$ production plotted versus $x = 2E_\pi/\sqrt{s}$.

7. The Gluon

The leading candidate for a field theory of strong interactions is at present Quantum-Chromo-Dynamics [14] (QCD). In QCD the strong force is mediated by eight massless coloured vector particles, the gluons, which couple directly to colour. The strong charge, or coupling strength α_s (Eq. 5.2) is independent of quark flavour but depends on the momentum transfer Q in the process, resulting in a coupling which is strong at small values of Q^2 (large separations) and weak at large values of Q^2 (small separations). The Q^2 dependence of the coupling constant reflects the fact that gluons are coloured objects with self interactions (Fig. 6.1).

To demonstrate that QCD is indeed the correct theory of strong interactions one must show that gluons with the properties listed above exist. The first evidence for gluons came from deep inelastic lepton-nucleon experiments and will be discussed in chapter 9. Electron-positron interaction has given direct evidence for gluons from a study of heavy quarkonium states and from quark gluon bremsstrahlung.

7.1 Quarkonium

7.1.1 The three gluon decay of T(1S)

In QCD a 1^{--} state is expected to decay predominantly via a three gluon intermediate state.

The energy distribution of the gluons in $1^{--} \to ggg$ can be written[196] as:

$$7.1 \quad \frac{1}{\Gamma} \frac{d\Gamma}{dx_1 dx_2} = \frac{6}{\pi^2 - 9} \frac{x_1^2(1-x_1)^2 + x_2^2(1-x_2)^2 + x_3^2(1-x_3)^2}{x_1^2 x_2^2 x_3^2}$$

where $x_i = E_i/E_b$ is the scaled energy.

This should lead to planar events defined by the three gluons fragmenting into three jets of hadrons. However, Υ decays yield in general two energetic gluon jets plus one low energy gluon jet. The symmetric case $x_1 = x_2 = x_3 = 2/3$ is rather unlikely and even in this case each jet will on the average have an energy of only 3 GeV. The data on $e^+e^- \to$ hadrons do not show a clear jet structure at 6 GeV in c.m.

PLUTO has analyzed the hadron data[197] from Υ decays using triplicity[198], a generalization of thrust to three axes. In this method the final state hadrons with momenta $\vec{p}_1$, $\vec{p}_2$ .... $\vec{p}_N$ are grouped into three classes C_1, C_2 and C_3 with momenta $\vec{p}(C_N) = \Sigma|\vec{p}_i|$ where the sum is over all particles assigned to class C_N. Triplicity T_3, is then defined as:

$$7.2 \quad T_3 = \frac{1}{\sum_i p_i} \cdot \max \{|\vec{p}(C_1)| + |\vec{p}(C_2)| + |\vec{p}(C_3)|\}$$

T_3 is 1 for a perfect 3-jet event and $3(\sqrt{3}/8)$ for a spherical event.

The momenta of the three jets are given by $\vec{p}_1 = \vec{p}(C_1)$, $\vec{p}_2 = \vec{p}(C_2)$ and $\vec{p}_3 = \vec{p}(C_3)$ and the angles between these vectors θ_1, θ_2, and θ_3 are the angles between the three jets. The triplicity and the thrust distribution for events on the Υ are plotted in Fig. 7.1. The data include both neutral and charged tracks and they have been corrected for the continuum contribution $e^+e^- \to q\bar{q}$ and for the vacuum polarisation. The triplicity and thrust distributions for the following decay modes have been evaluated:

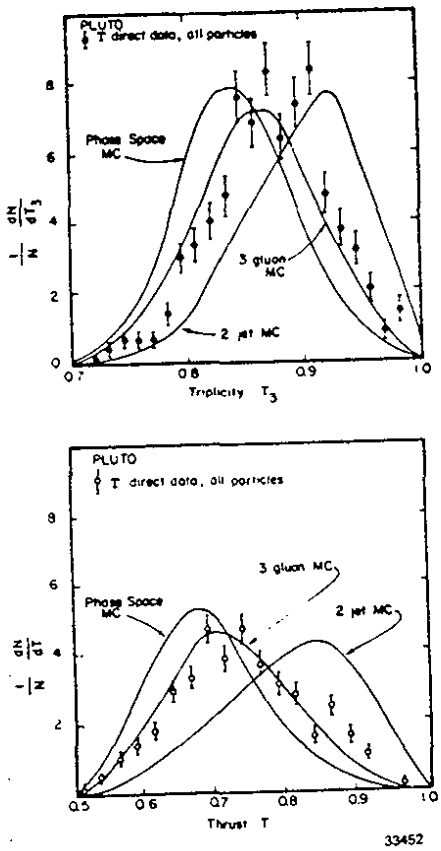

Fig. 7.1
Triplicity and thrust distributions observed by the PLUTO group for events at the Υ(1S) resonance. Predictions based on a phase space model, twobody $q\bar{q}$ and threebody ggg final states are also shown.

i) $e^+e^- \to \Upsilon \to$ hadrons, where the hadrons are distributed according to phase space.

ii) $e^+e^- \to \Upsilon \to q\bar{q}$. Such a distribution might be expected if the Υ decays via a one gluon intermediate state. Also $e^+e^- \to \Upsilon \to gg$ would lead to a similar topology.

iii) $e^+e^- \to \Upsilon \to ggg$. This is the lowest order diagram in QCD.

The results are also plotted in Fig. 7.1 and it is clear that the 3 gluon distribution agrees well with the data whereas neither phase space nor twobody $q\bar{q}$ (gg) decays fit the observed distributions. The thrust distribution for events collected in the continuum adjacent to the Υ is plotted in Fig. 7.2. This distribution is peaked at large values of thrust

and is well fit by $e^+e^- \to q\bar{q}$ but not by $e^+e^- \to ggg$.

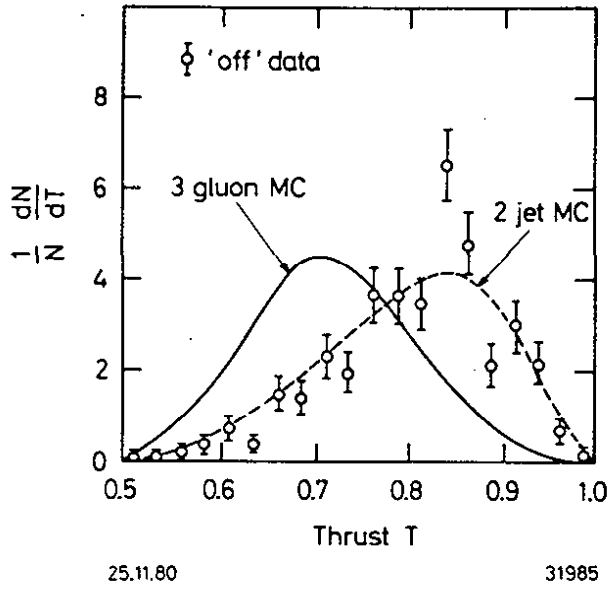

Fig. 7.2
The thrust distribution in the continuum observed by the PLUTO group at energies adjacent to the T(1S) resonance.

With a colourless gluon T would decay[199] to lowest order via a one gluon intermediate state producing a final state with two collinear hadron jets resulting in similar thrust distributions on and off resonance. The marked difference in event topology observed on and off the resonance is strong indirect evidence that the gluon has colour.

The angular distribution of the thrust axis observed in the continuum[148,200] and at the T(1S) is plotted in Fig. 7.3. The continuum events clearly favour the $1 + \cos^2\theta$ distribution predicted for $e^+e^- \to q\bar{q}$, whereas the data at the T(1S) favour a somewhat flatter distribution.

A fit to the data of the form $1 + \alpha_T\cos^2\theta$ gives[148] $\alpha_T = 0.33 \pm 0.16$ consistent with $\alpha_T = 0.39$ predicted[196,201] for the decay T(1S) → 3 gluons with vector gluons and disagree strongly with the value $\alpha_T = -1.0$ predicted for scalar gluons. The CLEO Collaboration has carried out similar measurements at CESR and finds[100] $\alpha_T = 0.35 \pm 0.11$ consistent with

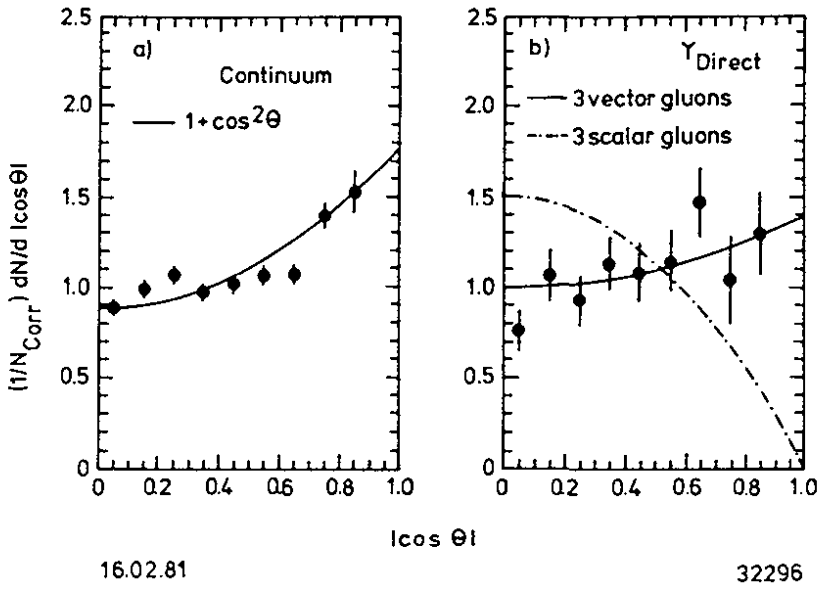

Fig. 7.3 - Data on the distribution of the thrust axis with respect to the beam axis observed for continuum and $\Upsilon(1S)$ events by the LENA group. The data are compared to theoretical predictions.

the PLUTO value. QCD also predicts that the normal to the plane defined by the three gluons should be distributed as $1 + \alpha_N \cdot \cos^2\phi$ with $\alpha_N = -0.33$ for vector gluons and $\alpha_N = +1$ or -1 for 0^+ or 0^- gluons. From a fit to their data CLEO obtains[100] $\alpha_N = -0.26 \pm 0.03$ in good agreement with the vector hypothesis.

Independent information on the gluon spin comes from a measurement[100,200] of the ratio

$$A = \frac{\Gamma(\Upsilon' \to \pi^+\pi^- \Upsilon)}{\Gamma(\psi' \to \pi^+\pi^- J/\psi)}$$

For vector gluons this ratio depends on the size of the system whereas for scalar gluons the value is independent of size. The value of A has been evaluated[202] by Gottfried and he finds A = 0.1 or 1 for respectively vector and scalar gluons. Experimentally the early LENA result[200] of $A = 0.09 \pm 0.05$ has been confirmed by the CLEO group[100] which finds $A = 0.085 \pm 0.058$.

7.1.2 QQ spectra and decay widths

The observed[146,203] $c\bar{c}$ and $b\bar{b}$ states identified by the spectroscopic notation $n^{2S+1}L_J$ are plotted in Fig. 7.4 as a function of excitation energy. The level ordering is in agreement with the spectrum shown in

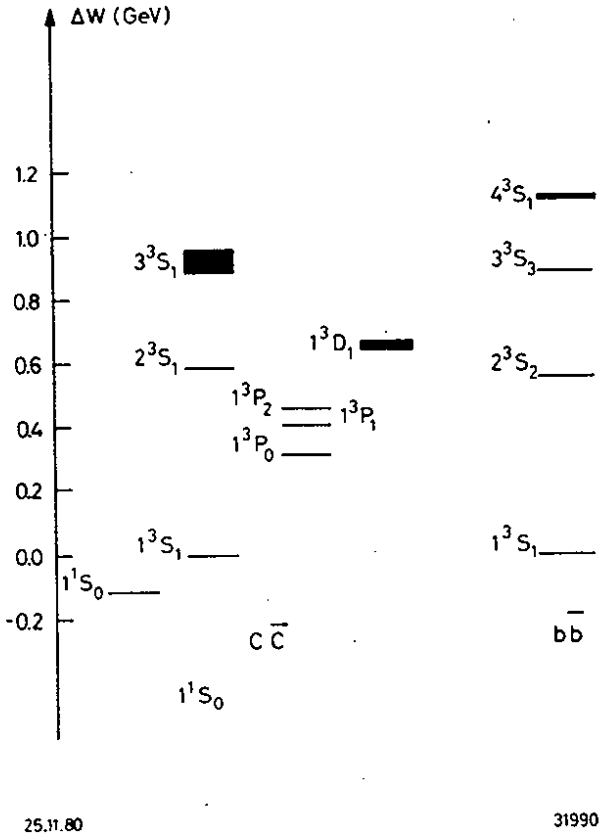

Fig. 7.4
Observed $c\bar{c}$ and $b\bar{b}$ states plotted versus excitation energy. The states are identified using the spectroscopic notation $n^{2S+1}L_J$.

Fig. 5.1 for two non-relativistic fermions bound in a steeply rising potential. The excitation energy E^* measured with respect to the 1^3S_1 state and the ratio $R_{ee} = \Gamma_{ee}(n^3S_1) / \Gamma_{ee}(1^3S_1)$ of the leptonic widths are listed in Table 7.1. It is hoped that some of the uncertainties[204] caused by higher order QCD radiative effects will cancel and that R_{ee} can be compared directly to first order calculations.

Table 7.1 - Properties of the $c\bar{c}$ and $b\bar{b}$ system

State	Measurement		Emp.Potential [208]		QCD Potential [209]	
	E^*(MeV)	R_{ee}	E^*(MeV)	R_{ee}	E^*(MeV)	R_{ee}
ψ'	589.1 ± 0.1	0.44 ± 0.06	589	0.35	589	0.45
ψ''	671 ± 2		705		715	
$^3P_{2,1,0}$	426 ± 4		425		425	
$\Upsilon(2S)$	560.0 ± 0.3	0.46 ± 0.03	560	0.43	550	0.45
$\Upsilon(3S)$	890.3 ± 0.4	0.33 ± 0.03	890	0.28	890	0.32
$\Upsilon(4S)$	1113.0 ± 1.0	0.23 ± 0.02	1120	0.20	1160	0.26

Several attempts [205-209] have been made to extract information on the strong force from the data on the $c\bar{c}$ and the $b\bar{b}$ system.

One approach is to derive[205] the potential directly from the observed levels using the inverse scattering formalism. It has also been shown[208] that a rather simple potential of the form $V(r) = A + B\, r^{\nu}$ with the parameters determined by the lowest levels can fit both the $c\bar{c}$ and $b\bar{b}$ states using identical parameter values.

In a complementary approach one tries to derive a potential from first principles. Richardson[207] has obtained a QCD potential of the form

$$7.3 \qquad V(Q^2) = -\frac{4}{3}\,\frac{12\pi}{33 - 2N_f}\,\frac{1}{Q^2}\,\frac{1}{\ln(1 + Q^2/\Lambda^2)}$$

written in momentum space. The potential has only one parameter Λ which may be identified with the characteristic strong interaction mass. The Fourier transform results in a potential which is proportional to $1/r$ at small distances as expected for the exchange of a massless vector particle and proportional to r at large distances as expected for the confining term. The potential, with second order QCD corrections[209] included, is plotted in Fig. 7.5 versus r.

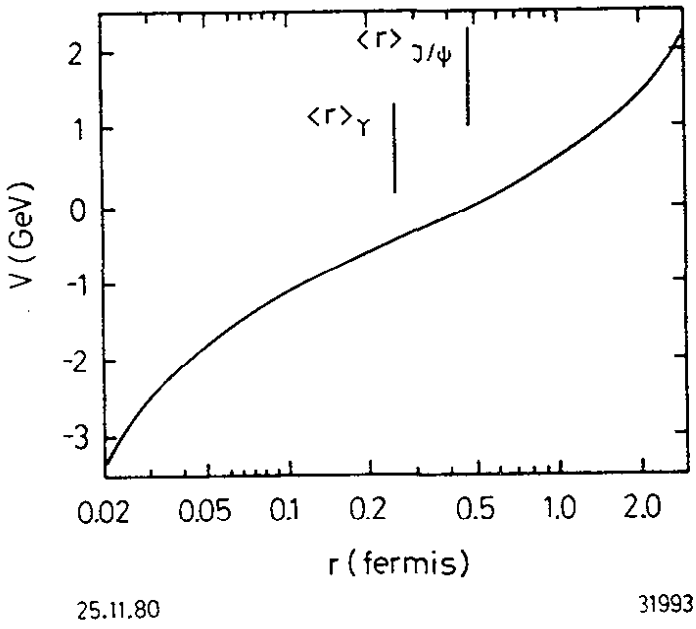

Fig. 7.5
The modified Richardson potential versus r.

The average r values for the J/ψ and the Υ are indicated. It is clear that both the $c\bar{c}$ and the $b\bar{b}$ family are mainly sensitive to the intermediate part of the potential between the Coulombic and the linear part. A fit to the observed spectrum gives $\Lambda_{\overline{MS}} = 0.508$ GeV which is consistent but larger than the value of α_s determined in other processes. The results are also listed in Table 7.1.

Both QCD and simple potential models reproduce the available data on $c\bar{c}$ and $b\bar{b}$ rather well using the same values of the parameters for both flavours. This shows that the strong force does not depend on the quark flavour.

7.1.3 Determination of the coupling constant α_s

The data on the Υ states are in good agreement with predictions based on QCD and can therefore be used to determine α_s. The ratio of the gluonic and the leptonic widths of the $\Upsilon(1S)$ is given in leading order by equations 5.1 and 5.3:

$$7.4 \qquad \Gamma_{3g} / \Gamma_{ee} = \frac{10(\pi^2 - 9) \cdot \alpha_s^3(M)}{81\, e_b^2\, \alpha^2}$$

Lepage and Makenzie have calculated[210] the first order QCD correction to this ratio. They find, using the $\overline{MS}$ scheme:

$$7.5 \quad \Gamma_{3g} / \Gamma_{ee} = \frac{10(\pi^2 - 9)}{81\pi\, e_b^2} \frac{\alpha_s^3(M)}{\alpha^2} [1 + (9.1 \pm 0.5) \frac{\alpha_s(M_\Upsilon)}{\pi} + ...]$$

The coefficient in front of $\alpha_s(M_\Upsilon)/\pi$ depends on renormalization scheme and scale.

The renormalization scale can be choosen such that eqn. 7.4 is correct and the authors find this to be the case for $M = 0.48\, M_\Upsilon$.

Experimentally the three gluon width is related to the total width by:

$$7.6 \qquad \Gamma_{3g} = \Gamma_{tot} - \Gamma_{ee} - \Gamma_{\mu\mu} - \Gamma_{\tau\tau} - R\Gamma_{\mu\mu} - \Gamma_{\gamma 2g}$$
$$= \Gamma_{tot} - (3 + R + \Gamma_{\gamma 2g}/\Gamma_{ee}) \cdot \Gamma_{ee} \quad .$$

The term $R\Gamma_{ee}$ is the contribution from the vacuum polarization and $\Gamma_{\gamma 2g}/\Gamma_{ee}$ is a small correction for the decay $\Upsilon \to \gamma gg$.

$$7.7 \qquad \Gamma_{3g} / \Gamma_{ee} = \frac{1 - (3 + R + \Gamma_{\gamma 2g}/\Gamma_{ee}) \cdot B_{ee}}{B_{ee}}$$

The values for Γ_{ee} are listed in table 5.3.

New data on the leptonic branching ratio of the T(1S) resonance have been reported[100,146] by the CLEO and CUSB Collaborations from a measurement of the cascade decay:

$$T(2S) \rightarrow \pi^+\pi^- T(1S) \rightarrow \pi^+\pi^- e^+e^- (\mu^+\mu^-)$$

The CLEO and the CUSB Collaborations find $B_{ee} = (3.6 \pm 0.4)\%$ respectively $B_{ee} = (3.2 \pm 0.8)\%$ using the known[100,148] branching ratio $B(T(2S) \rightarrow \pi^+\pi^- T(1S) = (19.1 \pm 3.1)\%$. Combining results with earlier value of $B_{ee} = (3.0 \pm 0.8)\%$ measured by the DORIS groups give a world average of $B_{ee} = (3.3 \pm 0.5)\%$.

With these values Lepage and McKenzie obtain:

$$\alpha_s(0.48\ M_p) = 0.152\ ^{+\ 0.012}_{-\ 0.010} \quad \text{and} \quad \Lambda_{\overline{MS}} = 100\ ^{+\ 34}_{-\ 25}\ \text{MeV}.$$

The value for α_s is in good agreement with the value determined from quark-gluon bremsstrahlung.

7.2 Search for gluonium states in J/ψ radiative decays

Two or more gluons are expected[211] to form gluonium states, bound colorless particles with a mass spectrum starting perhaps around 1 - 1.5 GeV. Replacing one of the gluons in the decay $J/\psi \rightarrow ggg$ by a photon results in a final state which consists of one photon and two gluons. This decay mode, observed[212] by the MARK II Collaboration with a branching ratio consistent with the QCD prediction, seems to be well suited to search for gluonium since the two gluons recoiling against the colorless photon must be in a color singlet state. At present two possible candidates for gluonium, ι(1440) and θ(1640), have been observed in radiative J/ψ decays.

7.2.1 $J/\psi \to \gamma\, \iota(1440)$

The decay $J/\psi \to \gamma\, \iota(1440)$ was first observed[212] by the MARK II Collaboration in the channel $K_S K^{\pm}\pi^{\mp}$. The $K_S K^{\pm}\pi^{\mp}$ mass distribution for candidate events, plotted in Fig. 7.6, shows a clear peak centered at 1440 MeV. Selecting events with $m_{K\bar{K}} < 1.05$ GeV enhances the signal as shown by the shaded distribution. The resonance parameters determined from the 5 C mass distribution are listed in Table 7.2.

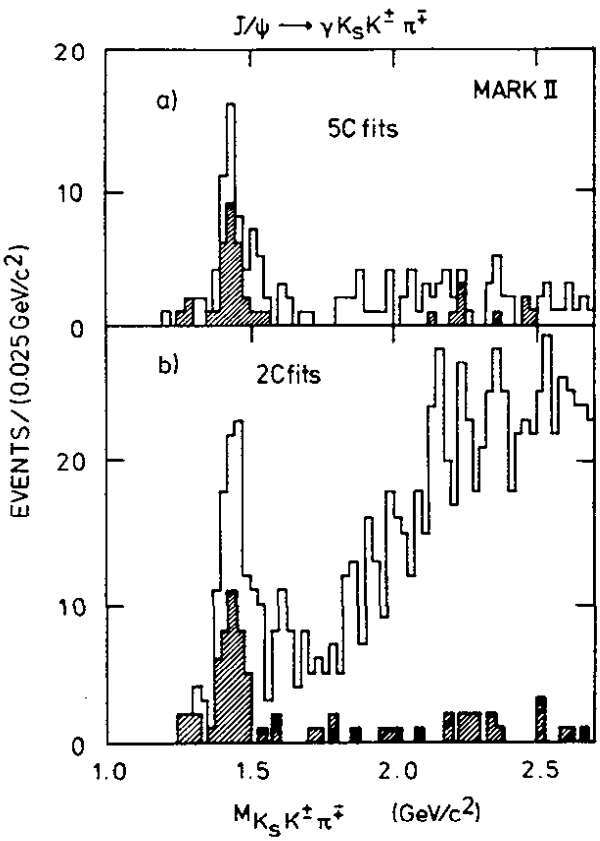

Fig. 7.6
The $K_S K^{\pm}\pi^{\mp}$ mass spectrum for $J/\psi \to K_S K^{\pm}\pi^{\mp}$ candidate event which satisfy
a) a 5C fit to this hypothesis.
b) A 2C fit (observation of the photon not required). Events in the shaded region have $m_{K\bar{K}} < 1.05$ GeV. The data were obtained by the MARK II Collaboration.

Table 7.2 - The $\iota(1440)$

	MARK II	Crystal Ball	E-Meson
Mass (MeV)	$1440 \,^{+\,10}_{-\,15}$	$1440 \,^{+\,20}_{-\,15}$	1418 ± 10
Width (MeV)	$50 \,^{+\,30}_{-\,20}$	$60 \,^{+\,20}_{-\,30}$	50 ± 10
$B(J/\psi\to\gamma\eta)\cdot B(\eta\to K\bar{K}\pi)$	$4.3 \pm 1.7 \cdot 10^{-3}$	$4.0 \pm 1.2 \cdot 10^{-3}$	

The $\iota(1440)$ has also been observed[134] by the Crystal Ball Collaboration in $J/\psi \to \gamma K^+K^-\pi^0$ and the $K^+K^-\pi^0$ mass distribution for candidate events is plotted in Fig. 7.7. The shaded distribution corresponds to events with $M_{K\bar{K}} < 1125$ MeV. The mass, width and the cascade branching ratio determined from these data are also listed in Table 7.2. The two data sets are in excellent agreement; in particular both groups find a large cascade branching ratio and this makes it tempting[213] to associate the $\iota(1440)$ with a gluonium state.

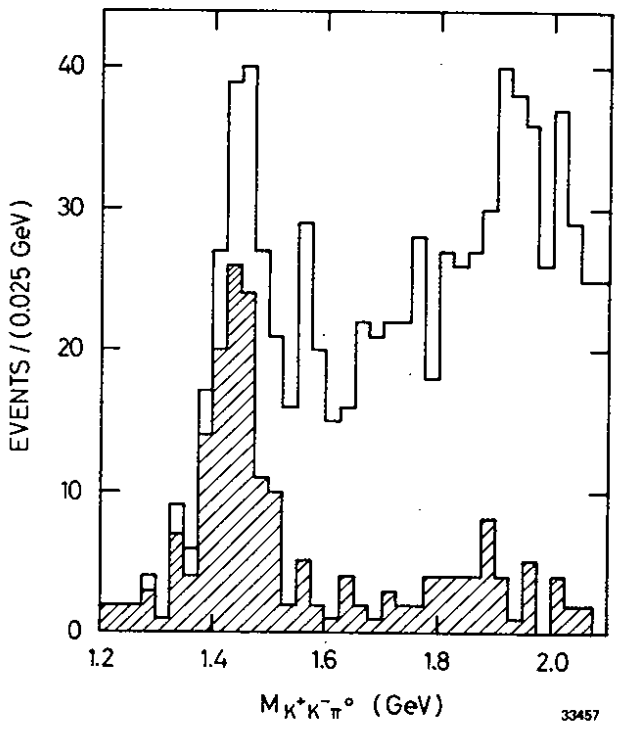

Fig. 7.7

The $K^+K^-K^0$ mass spectrum for $J/\psi \to \gamma K^+K^-\pi^0$ candidate events. Events in the shaded region have $m_{K\bar{K}} < 1125$ MeV. The data were obtained by the Crystal Ball Collaboration.

The values for the mass and the width of the $\iota(1440)$ are consistent with the values reported[214] for the well established E meson. However, the spin parity of the E meson has been found to be 1^- and this makes it a natural candidate for the axial nonet together with the D, A, and Q_A mesons. The question whether ι is the E particle or not have now been decided by a measurement of the quantum numbers of the ι.

The Crystal Ball Collaboration has determined[134] the quantum numbers of the $\iota(1440)$ to be 0^- from a spin parity analysis. The analysis was carried out in 100 MeV steps for an invariant $K\bar{K}\pi$ mass between 1300 and 1800 MeV. The analysis included $K\bar{K}\pi$ (phase space), $\delta^0\pi^0$ (0^-), $\delta^0\pi^0$ (1^+), $K^*\bar{K}$ + C.C. (0^-) and $K^*\bar{K}$ + C.C. (1^+).

The $K\bar{K}\pi$ phase space contribution was assumed to be incoherent whereas the other partial waves were allowed to interfere with arbitrary phase. The ι and K^* helicities were allowed to vary. Significant contributions to the $K\bar{K}\pi$ yield came only from $KK\pi$ (phase space), $\delta^0\pi^0$ (0^-) and $K^*\bar{K}$ + C.C. (1^+). These contributions, corrected for the detection efficiency are plotted versus $K^+K^-\pi^0$ mass in Fig. 7.8. The $K^*\bar{K}$ + C.C. (1^+) partial wave contribution is small and independent of mass. The $\delta\pi(0^-)$ contribution, however, shows a clear resonance structure around the ι mass. The spin parity of the ι is therefore 0^-. Many cross checks have been made[134] and they all support the results of the partial wave analysis.

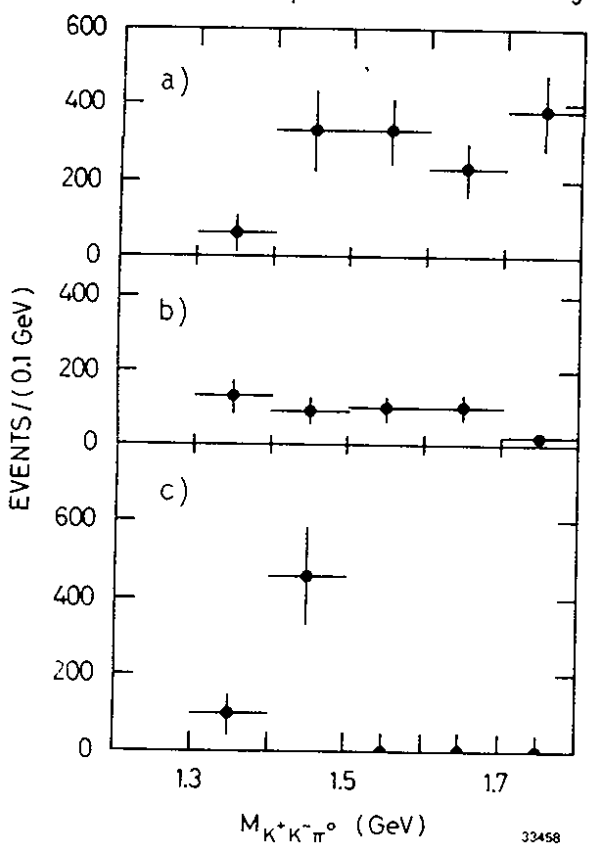

Fig. 7.8
The contributions for various partial wave as a function of $K\bar{K}$ mass.
a) Phase space ($K\bar{K}\pi$ flat)
b) K^*K^- + C.C. in $J^P = 1^+$
c) $\delta\pi$ in $J^P = 0^-$
The analysis was made by the Crystal Ball Collaboration.

The analysis also finds:

$$\frac{B(\iota \to K^{*}\bar{K} + C.C.)}{B(\iota \to K^{*}\bar{K} + C.C. + \delta\pi)} < 0.25 \quad (90\% \text{ C.L.}) .$$

Note that Dionisi et al.[215] determines

$$\frac{B(E \to K^{*}\bar{K} + C.C.)}{B(E \to K^{*}\bar{K} + C.C. + \delta\pi)} = 0.86 \pm 0.12.$$

The ι spin can be determined from the angular distributions with the assumption that the ι decays predominantly into $\delta\pi$. A fit to the full three dimensional decay distribution favours strongly spin 0. If the relative probability for spin 0 is taken to be 1 the spin 1 and spin 2 have relative probabilities of 10^{-4} respectively 0.008.

The experimentalists therefore conclude that the $\iota(1440)$ is a new pseudoscalar meson which cannot be assigned to the ground state nonet. It has been suggested that the $\iota(1440)$ is a radially excited $q\bar{q}$ state and such states have been predicted[216] to exist in this mass range.

It is of course still tempting to identify the $\iota(1440)$ with a gluonium resonance.

7.2.2 $J/\psi \to \gamma\, \theta(1640)$

The Crystal Ball Collaboration has observed[134] a new resonance $\theta(1640)$ in the decay $J/\psi \to \gamma\, \eta\, \eta$. The $\eta\, \eta$ invariant mass distribution for events which satisfay the 5C fit to this decay mode is plotted in Fig. 7.9.

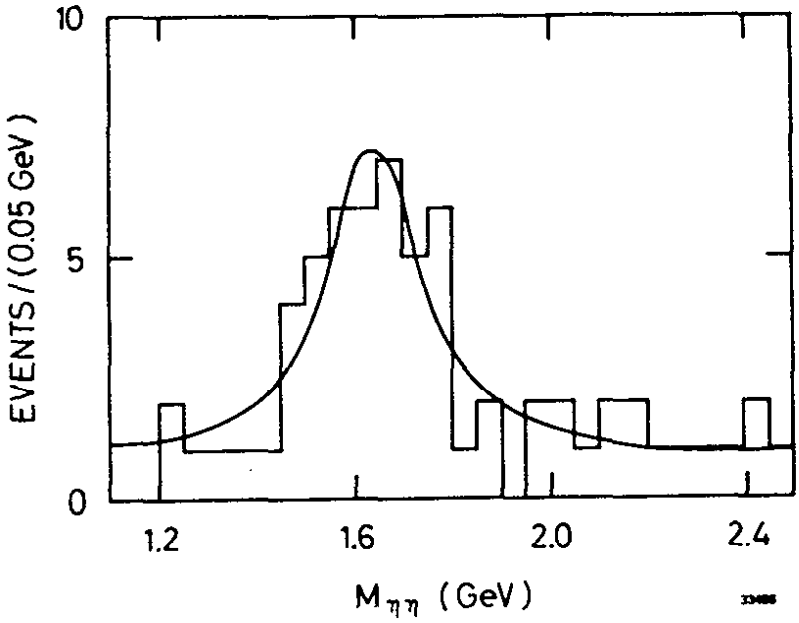

Fig. 7.9 - The $\eta\eta$ mass distribution for $J/\psi \to \gamma\ \eta\ \eta$ candidate events. The data are from Crystal Ball Collaboration and the solid line is the result of a Breit-Wigner plus a flat background fit.

A clear resonance signal is seen in the data and a fit to a Breit-Wigner resonance plus a flat background result in a mass M = 1640 $\pm$ 50 MeV and a width $\Gamma = 220 \begin{smallmatrix} + 100 \\ - 70 \end{smallmatrix}$ MeV. The cascade branching ratio $B(J/\psi \to \gamma\theta) \cdot B(\theta \to \eta\eta) = (4.9 \pm 1.4 \pm 1.0) \cdot 10^{-4}$ is nearly an order of magnitude smaller than the corresponding cascade branching ratio for the $\iota(1440)$. A search for the decay mode $\theta \to \pi^\circ\pi^\circ$ was negative and the resulting 90% upper C.L. is:

$$B(J/\psi \to \gamma\theta) \cdot B(\theta \to \pi^\circ\pi^\circ) < 6 \times 10^{-4}.$$

The $\theta(1640)$ must have $J^{PC} = 0^{++}, 2^{++}$, since it is produced in J/ψ radiative decays and decays into $\eta\eta$. A spin-parity analysis favours 2^{++}.

The θ(1640) does not fit into the ground state 2^{++} nonet and the mass is probably to low for the θ(1640) to be a radial excitation. Another possibility is that the θ is a four quark ($q\bar{q}\ q\bar{q}$) state. However, such a state is expected to have a rather large width.

The θ(1640) has the quantum number of the bound two gluon ground state. Although its mass is somewhat larger than expected[217] for the gluon ground state, this assignment is still a possibility.

7.3 Quark-Gluon Bremsstrahlung

A quark which is being accelerated will radiate gluons analogous to normal bremsstrahlung. Quark-gluon bremsstrahlung[12, 218], shown to first-order in the coupling constant in Fig. 7.10a is expected to occur in any field theory of strong interaction. The first order cross section in QCD is given by:

$$7.8 \qquad \frac{1}{\sigma_o}\,\frac{d\sigma(q\bar{q}g)}{dx_1 dx_2} = \frac{2\alpha_s}{3\pi}\,\frac{x_1^2 + x_2^2}{(1-x_1)(1-x_2)}$$

x_1 and x_2 are the fractional quark energies, $x_i = 2E_i / \sqrt{s}$ and σ_o is the cross section. The energy and the angular distribution of the radiated gluon is equal to that of bremsstrahlungsphotons:

$$7.9 \qquad \frac{d\sigma}{dk\,d\Omega} \sim \frac{\alpha_s}{k \cdot \sin\theta}$$

k is the energy of the gluon and θ its angle with respect to the jet axis as defined in Fig. 7.10b. The gluons are colored and will materialize as a jet of hadrons with a mean p_T on the order of 300 MeV/c similar to the value observed in quark fragmentation, and a normal multiplicity distribution.

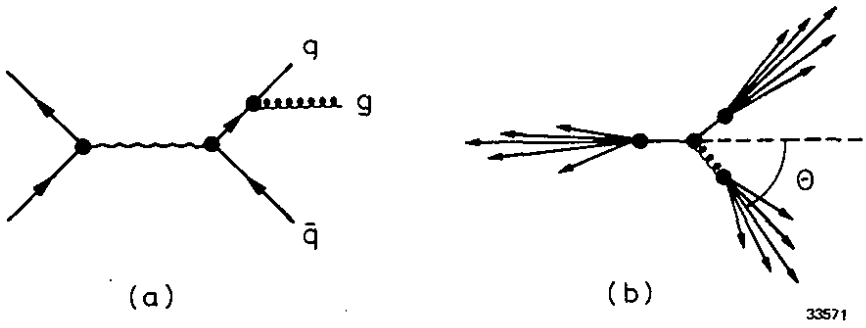

Fig. 7.10 - a) Quark-gluon bremsstrahlung to first order in α_s.
b) Final state in quark-gluon bremsstrahlung.

Quark gluon bremsstrahlung has well defined experimental signatures. The transverse momentum with respect to the jet axis will grow with energy

$$\langle p_T^2 \rangle \sim Q^2 / \ln (Q^2 / \Lambda^2) \quad . \tag{7.10}$$

In some rare cases the gluon will be emitted with a transverse momentum which is large compared to 300 MeV/c. In this case the event will consist of three well defined jets defining a plane.

Events with these properties were found[219] almost immediately at the turn on of PETRA and at the Batavia Conference all groups[220-223] working at PETRA reported data.

Examples of three jet events are shown in Fig. 7.11. Before reviewing the evidence for gluon bremsstrahlung I will briefly describe the Monte Carlo models used[224] to compare theory and data.

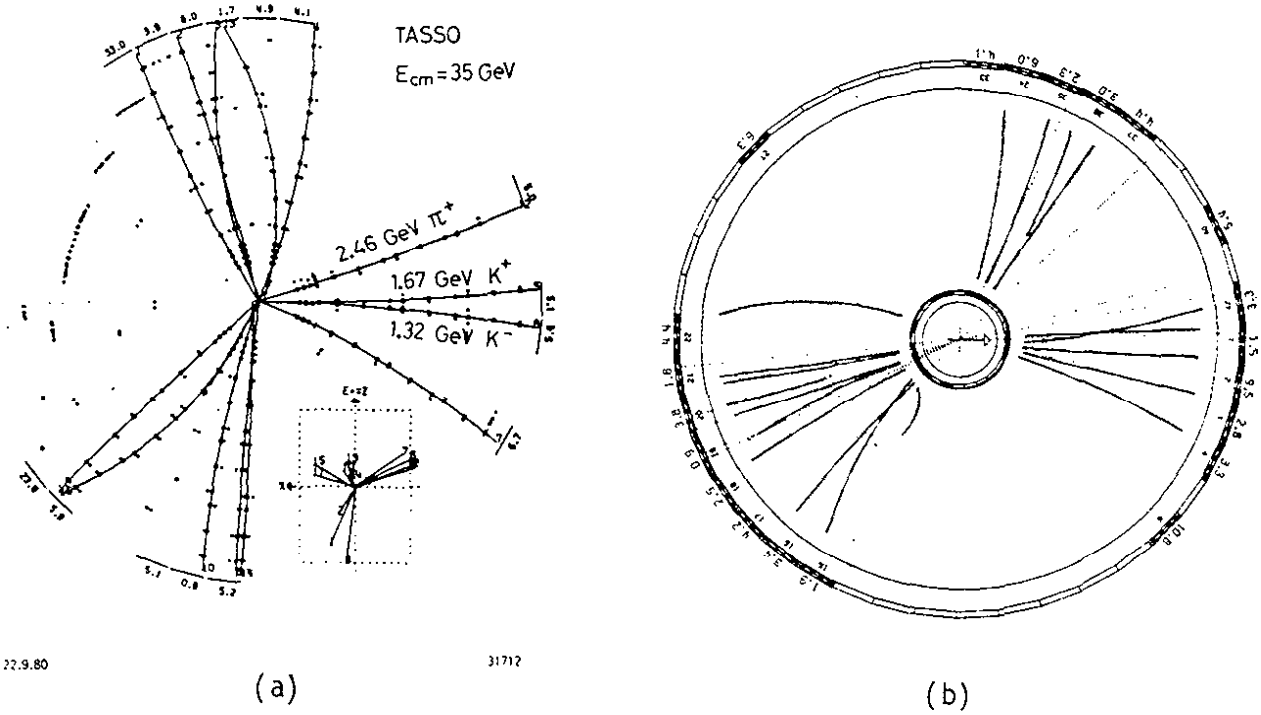

Fig. 7.11 - Examples of three jet events observed by a) TASSO and b) JADE.

7.3.1 Monte Carlo Simulation

All groups have made extensive Monte Carlo computations to confront the various production mechanisms with the data. The inputs to these calculation are summarized below:

a) Quark pairs are pair-produced with a cross section proportional to e_i^2.

b) The basic gluon bremsstrahlung process (Fig. 6.1) is treated to first order in the strong coupling constant α_s by Hoyer et al.[225], whereas the computation by Ali et al.[227] includes all second order diagrams except those with internal gluon lines (Fig. 4.4 h, k).

c) The formalism of Field and Feynman[178] or the one set up by the Lund group[228] is then used to compute the fragmentation of the constituents.

In the Field-Feynman model quark fragmentation is a cascade process where light quark pairs $u\bar{u}$, $d\bar{d}$ and $s\bar{s}$ are created by the colour field from the vacuum in the ratio 2 : 2 : 1. The $q\bar{q}$ pairs recombine with their neighbours to form mesons: i.e. $q \rightarrow q + q_1\bar{q}_1 \rightarrow (q\bar{q}_1) + q_1 \rightarrow M_1 + q_1$ $M_1 + q_1 \rightarrow M_1 + q_1 + \bar{q}_2 q_2 \rightarrow M_1 + (q_1\bar{q}_2) + q_2 \rightarrow M_1 + M_2 + q_2$ ..... . The process stops when the "free" quark reaches a threshold energy E_o; the quark then combines with the left-over quark from the other jet to form a wee hadron.

The cascade process is described by three parameters a_F, σ_q and P/(P+V).

i) a_F : $f_q^h(z)$ is the probability that a quark q with energy E_q fragments into a hadron h with relative energy $z = (E + p)_h/(E + p)_q$. This probability function is given by: $f_q^h(z) = 1 - a_F + 3a_F(1 - z)^2$.
a_F is assumed to be the same for u, d and s quarks and its value is determined experimentally. For heavy quarks $f_q^h(z)$ is assumed to be constant.

ii) σ_q : The quarks in the $q\bar{q}$ pair are created with equal and opposite transverse momenta according to a Gaussian with a rms width σ_q. The quarks from two different $q\bar{q}$ pairs are combined yielding a meson with a net transverse momentum with respect to the jet axis.

iii) (P/P+V) : Only pseudoscalar P(π, K ...) and vector mesons V (ρ, K ...) are produced in the premordial chain. The program has lately been extended to include[193] baryon production. This is done by assigning a small probability to the production of diquarks ($q_1\bar{q}_1$ $q_1\bar{q}_1$) in the fragmentation chain.

iiii) The fragmentation of gluons is treated as a two-step process in which the gluon first fragments into a $q\bar{q}$ pair and then the quark subsequently fragments into hadrons as outlined above. In the Hoyer et al.

program the gluon impacts all its energy to one of the quarks - i.e. in this model quark and gluon fragmentation are identical. Ali et al. describe $g \to q\bar{q}$ by the splitting function[229] $f(z) = z^2 + (1 - z)^2$ with $z = E_g/E_q$.

Field and Feynman found[178] that deep inelastic lepton-hadron interactions and also hadron-hadron interactions are simultaneously described by the following values of the parameters

$$a_F = 0.77, \quad \sigma_q = 0.30 \text{ GeV/c and } \quad P/(P+V) = 0.5 .$$

The TASSO group has made a fit to their data in a region dominated by two jet events. Simultaneous fits varying a_F, σ_q and $P/(P+V)$ were made to the x distribution ($x = p_h/E_b$), the mean $\langle p_T^2 \rangle_{out}$ distribution normal to the event plane (see below) and the charged multiplicity distribution. The best fits were obtained[230] for $a_F = 0.57 \pm 0.20$, $\sigma_q = 0.32 \pm 0.04$ GeV/c and $P/(P+V) = 0.56 \pm 0.15$ in agreement with the values found in lepton-hadron and hadron-hadron interactions. The quality of the fits is shown in Fig. 7.12.

The Lund model[227] is based on the massless string model[228]. In this model the two quarks are no longer independent objects and the string fragments as a whole. The Lund model predicts that quark and gluon fragments differently and that the jets do not longer coincide directly with the parton momenta. The model has been used extensively by the JADE group and agrees with the data.

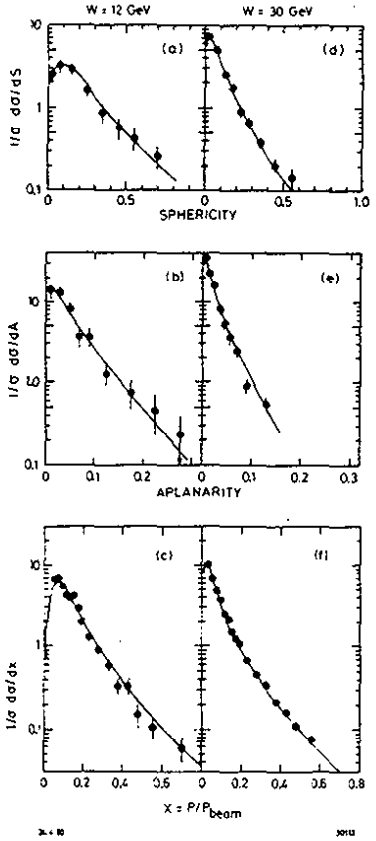

Fig. 7.12

Comparison of the data with the QCD model (curves) at 12 GeV and 30 GeV in c.m.

7.3.2 Event topology

The production mechanism can be delineated from the event shape. For example light $q\bar{q}$ production results in two well defined jets defined by an axis with small momenta transverse to this axis, $q\bar{q}g$ results in planar events, four parton events like qqgg define two planes, heavy $q\bar{q}$ production gives spherical events. There are by now several methods used to determine the shape and the topology of an event. Some of these methods are briefly discussed below.

The shape of an event is conveniently evaluated by constructing the second rank tensor[172,231]

$$7.11 \qquad M_{\alpha\beta} = \sum_{j=1} p_{j\alpha} \cdot p_{j\beta} \quad (\alpha, \beta = x, y, z)$$

where $p_{j\alpha}$ and $p_{j\beta}$ are momentum components along the α and the β axes for the jth particle in the event. The sum is over all charged particles in the

event. Let $\vec{n}_1$, $\vec{n}_2$ and $\vec{n}_3$ be the unit eigenvectors of this tensor associated with the normalized eigenvalues Q_i, where $Q_i = \Sigma(\vec{p}_j \cdot \vec{n}_j)^2/\Sigma\vec{p}_j^2$.

These eigenvalues are ordered such that $Q_1 \leq Q_2 \leq Q_3$ and are normalized with $Q_1 + Q_2 + Q_3 = 1$. The principal jet axis is then the $\vec{n}_3$ direction. The event plane is spanned by $\vec{n}_2$ and $\vec{n}_3$; and $\vec{n}_1$ defines the direction in which the sum of the square of the momentum component is minimized. Every event can be represented in a two dimensional plot of aplanarity $A = (3/2)\ Q_1$ (i.e. normalized momentum squared out of the event plane) versus sphericity $S = (3/2)(Q_1 + Q_2)$. In such a plot two jet events will cluster at small values of A and S, planar events have small values of A whereas both A and S will be large for spherical events. This method has been used by TASSO[220] and JADE[223].

MARK J[221,232] uses a linear method based on energy flow where the coordinate system is defined as follows: the $\vec{e}_1$ axis coincides with the thrust axis which is defined as the direction of maximum energy flow. They next investigate the energy flow in a plane perpendicular to the thrust axis. The direction of maximum energy flow in that plane defines a direction $\vec{e}_2$ with a normalized energy flow

$$7.12 \qquad \text{major} = \sum_i |\vec{p}^i \cdot \vec{e}_2| \ / \ E_{vis},$$

where $E_{vis} = \Sigma|\vec{p}^i|$. The third $\vec{e}_3$ is orthogonal to both the thrust and the major axis $\vec{e}_2$, and it is very close to the minimum of the momentum projection along any axis i.e.

$$7.13 \qquad \text{minor} = \sum_i |\vec{p}^i \cdot \vec{e}_3| \ / \ E_{vis}.$$

The PLUTO group[233] has developed a two step cluster method to determine the event topology. The first stage associates all particles into preclusters irrespective of their momenta. Particles belong to the same precluster if the angles between any two tracks are less than a limiting angle α. The momentum of a precluster is the sum of the momenta of all the particles assigned to that precluster. The preclusters are then combined to clusters if the angle between the momentum vectors is less than a given value β. The number of clusters n is defined as the minimum number of clusters which fulfil the inequalities:

$$7.14 \qquad \sum_{i=1}^{n} E_{ci} > E_{vis} (1 - \varepsilon)$$

where E_{ci} is the cluster energy and ε a small number. If the energy of a cluster, defined as the sum of the energies of all particles assigned to the cluster, exceeds a threshold energy E_{th} then the cluster is called a jet. Typical values for the various parameters are $\alpha = 30^{o}$, $\beta = 45^{o}$, $\varepsilon = 0.1$ and $E_{th} = 2.0$ GeV. A similar cluster method[234] has also been used by MARK II.

7.3.3 The evidence for gluons

In this part we review the evidence[37,171,235,236] for the process $e^{+}e^{-} \rightarrow q\bar{q}g$ (Fig. 6.1).

A) The average transverse momentum of the hadrons with respect to the jet axis will grow with energy. Normalized transverse momentum distributions, measured by TASSO and evaluated with respect to the sphericity axis are plotted in Fig. 7.13 versus p_T^2 for different c.m. energies. The observed

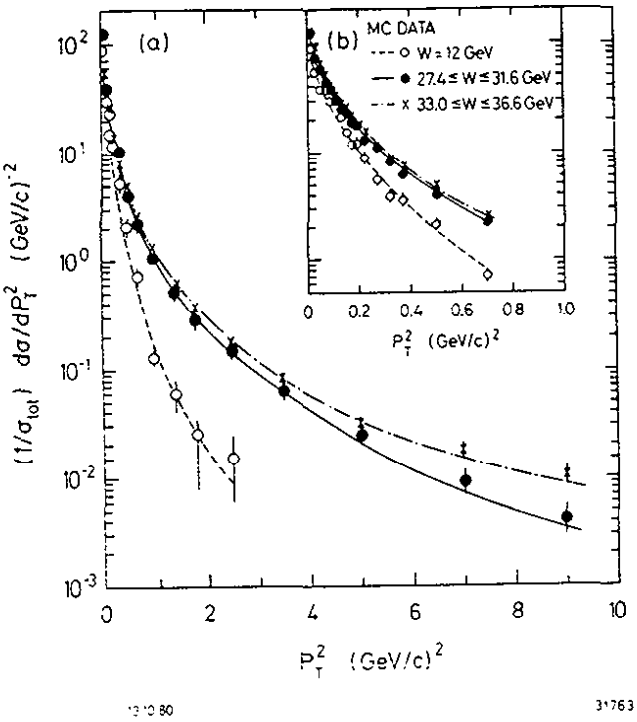

Fig. 7.13

$1/\sigma\ d\sigma/dp_T^2$ at 12 GeV, 27.4 - 31.6 GeV as a function of p_T^2. The curves are QCD fits to the data with σ_q = 320 MeV/c.

p_T^2 distribution clearly broadens with energy. In QCD the growth is explained as hard non-collinear gluon emission. Fits based on this mechanism are shown in Fig. 7.13. However, it is also possible to fit the data up to moderate values of p_T^2 by increasing σ_q as a function of c.m. energy.

B) Planarity. Regardless of the value of σ_q (or the mean p_T), hadrons resulting from the fragmentation of a quark must on the average be uniformly distributed in azimuthal angle around the quark axis. Therefore, apart from statistical fluctuations, the two jet process $e^+e^- \to q\bar{q}$ will not lead to planar events whereas the radiation of a hard gluon, $e^+e^- \to q\bar{q}g$ will result in an approximately planar configuration of hadrons with large transverse momentum in the plane and small transverse momentum with respect to the plane. Thus the observation of such planar events, at a rate significantly above the rate expected from statistical fluctuations of the $q\bar{q}$ jets, shows in a model independent way that there must be a third confined particle in the final state. The third particle is not a quark since it has baryon number zero and cannot have 1/2 integer spin.

We first compare the distribution of $\langle p_T^2 \rangle_{out}$, the momentum component normal to the event plane squared, with that of $\langle p_T^2 \rangle_{in}$, the momentum component in the event plane perpendicular to the jet axis.

The data obtained by the TASSO group are plotted in Fig. 7.14 and Fig. 7.15 for c.m. energies between 12 GeV and 36.6 GeV. The distribution of $\langle p_T^2 \rangle_{out}$ changes little with energy in contrast to the distribution of $\langle p_T^2 \rangle_{in}$ which grows rapidly with energy, in particular there is a long tail of events not observed at lower energies. Fits to the data assuming $e^+e^- \to q\bar{q}$ and σ_q = 300 MeV/c (solid curves) or σ_q = 450 MeV/c (dotted curves) are shown in Fig. 7.14. The $\langle p_T^2 \rangle_{out}$ distribution at high energies is not fit by σ_q = 300 MeV/c, however a good fit can be obtained by increasing σ_q to 450 MeV/c. The $q\bar{q}$ model however, completely fails to reproduce the long tail observed in $\langle p_T^2 \rangle_{in}$ at high energies. This discrepancy cannot be removed by increasing the mean transverse momentum of the jet. Fig.7.14b shows a fit assuming σ_q = 450 MeV/c (which gives a good fit to $1/\sigma\ d\sigma/dp_T^2$ and to $\langle p_T^2 \rangle_{out}$). The agreement is poor. We therefore conclude that the data include a number of planar events not reproduced by the $q\bar{q}$ model independent of the average p_T assumed.

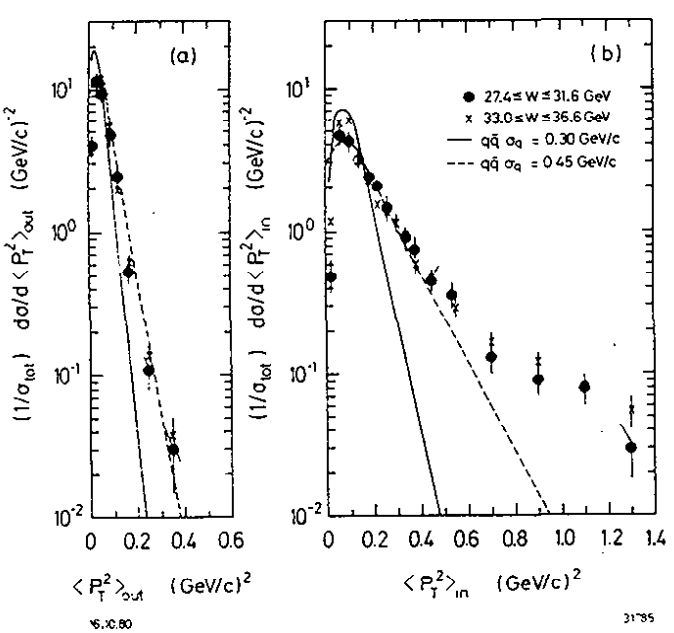

Fig. 7.14
Distributions of mean transverse momentum squared per event for charged particles, normal to ($\langle p_T^2 \rangle_{out}$) and in ($\langle p_T^2 \rangle_{in}$) the event plane measured by the TASSO Collaboration at low and high energies. The curves are the predictions for a $q\bar{q}$ final state with σ_q = 300 MeV/c (solid lines) and σ_q = 450 MeV/c (dashed lines).

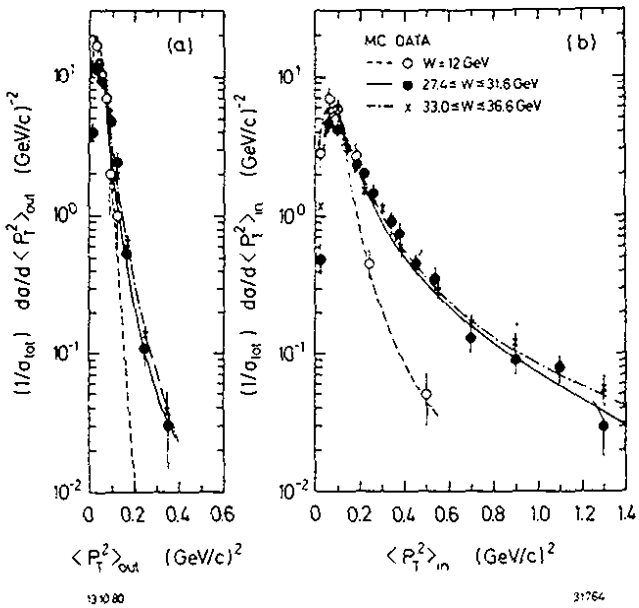

Fig. 7.15

Same plot as above. The curves are the second order QCD predictions with $\alpha_s = 0.17$ and $\sigma_q = 320$ MeV/c.

Gluon bremsstrahlung offers a natural mechanism to explain the observed planarity of the events. Fig. 7.15 shows a second order QCD fit to the data using the Monte Carlo method outlined above. The fit assumed a constant value of $\sigma_q = 320$ MeV and $\alpha_s = 0.17$ (see below). The long tail in $<p_T^2>_{in}$ is reproduced in this model. Note, that the growth in $<p_T^2>_{out}$ is explained by the occurence at small fraction of 4 (or more) jet events which, in general, are not planar.

The data from PLUTO[222] and JADE[223] analyzed in a similar manner are in full agreement with the findings of the TASSO group.

The planarity of the events is also observed[226,232] by the MARK J group using a different technique. They divided each event into two hemispheres using the plane defined by the major and the minor axis (see above) and analyzed the energy distribution in each hemisphere as if it resulted from a single jet. The jet with the smallest transverse momentum with

respect to the thrust axis is defined as the narrow jet. The other as the broad jet. The oblateness defined as O = major - minor is a measure of the planarity of the event and is zero for phase space and two jet events and finite for three jet final states. The normalized event distribution measured for c.m. energies between 27 and 37 GeV is plotted versus oblateness in Fig. 7.16 for the narrow and the wide jet separately and compared to the predictions for $e^+e^- \to q\bar{q}$ (dashed curve) and $e^+e^- \to q\bar{q}g$ (solid line). A good fit is obtained with the $q\bar{q}g$ final state whereas the $q\bar{q}$ final state does not fit the oblateness distribution for the braod jet.

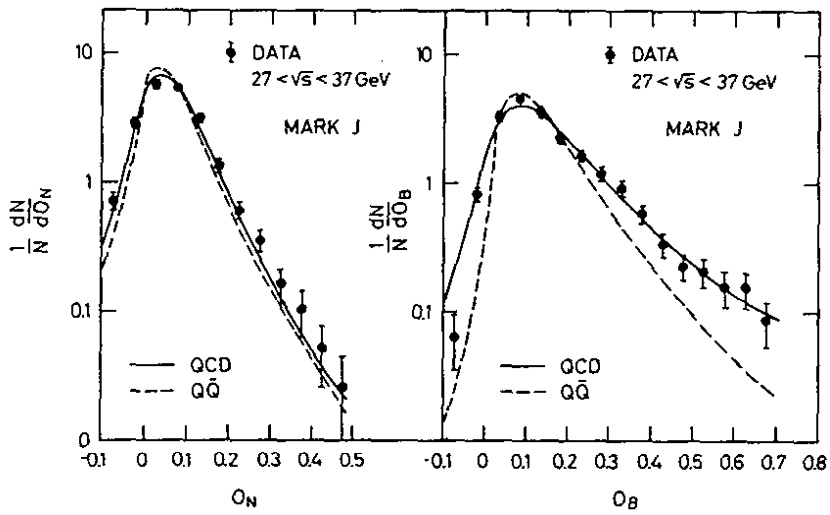

Fig. 7.16 - The distribution 1/N dN/dO determined by the MARK J Collaboration as a function of oblateness O for the narrow and the wide jet separately. The solid curves are predictions based on $e^+e^- \to q\bar{q}g$, the dashed curve shows the prediction for $e^+e^- \to q\bar{q}$.

The data discussed above demonstrate that the observed planar events cannot result from fluctuations in the quark pair production with a Gaussian distribution in transverse momentum around the jet axis defined by the hadrons. Each PETRA group has now observed more than 1000 planar events

with an estimated background from fluctuations of two jet events of about 20%. Wide angle gluon bremsstrahlung $e^+e^- \to q\bar{q}g$ naturally result in planar events. The observed rate for such events is consistent with the QCD predictions. Besides this source there are two ad hoc possibilities; a flat phase space of unknown origin, or that the transverse momentum distribution of the quark fragmentation has a long non-Gaussian tail. The first possibility can be excluded by observing events with 3 axes, the second by excluding the possibility that the 3 axes are defined by 2 multiparticle jets and a single high momentum particle at a large angle with respect to the jet axes.

C) Properties of planar events. The TASSO Collaboration uses a generalization[237] of sphericity to define three-jet events. In this method the tracks are projected on to the event plane defined by $\vec{n}_2$ and $\vec{n}_3$ (see above). The projections are divided into three groups and the sphericity for each group S_1, S_2 and S_3 determined. The three axes and the particle assignment to the three groups are defined by minimizing the sum of S_1, S_2 and S_3. This defines the direction of the three jets and assigns the particles to these jet directions.

In Fig. 7.17 the TASSO events are plotted versus tri-jettiness J_3 defined as

$$J_3 = \langle p_T^2 \rangle_{in} \; / \; (\tfrac{1}{2} \, (300 \text{ MeV}/c^2)^2).$$

Here $\langle p_T^2 \rangle_{in}$ is evaluated for all charged tracks in an event with respect to their assigned axes. Thus for three jet events with a mean transverse momentum of 300 MeV with respect to the jet axis we expect to find the events clustered around $J_3 = 1$, compared with a wide distribution in J_3 in case of a flat phase space distribution. The data agree with the expectations for $e^+e^- \to q\bar{q}g$, shown as the solid line and

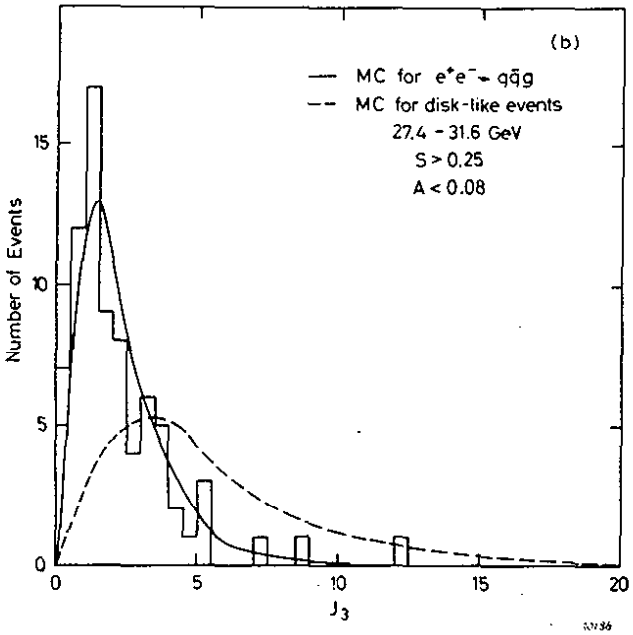

Fig. 7.17
Planar events ($S \geq 0.25$, $A \leq 0.08$) measured by the TASSO Collaboration and plotted versus the tri-jettiness J_3. The Monte Carlo predictions for $e^+e^- \to q\bar{q}g$ (solid) and for $e^+e^- \to$ hadrons (phase-space dashed).

disagree with the phase space distribution plotted as the dashed curve.

The MARK J group observes[232,238] a three jet structure in the energy flow analysis discussed above. To enhance effects resulting from gluon emission they select planar events with oblateness $O > 0.3$. The result of superimposing events with the thrust axis pointing to the left and the event plane in the plane of the paper is shown in Fig. 7.18. An antennea pattern is clearly visible. The energy flow is projected on to the event plane and its polar angle distribution is compared with various models. Due to the event selection criteria both phase space models and $q\bar{q}$ models show three lobes. These models however, do not fit the observed distribution independentwhether the fragmentation is assumed to have a Gaussian or an exponential p_T distribution. The data are well fit by the QCD model shown as the solid line.

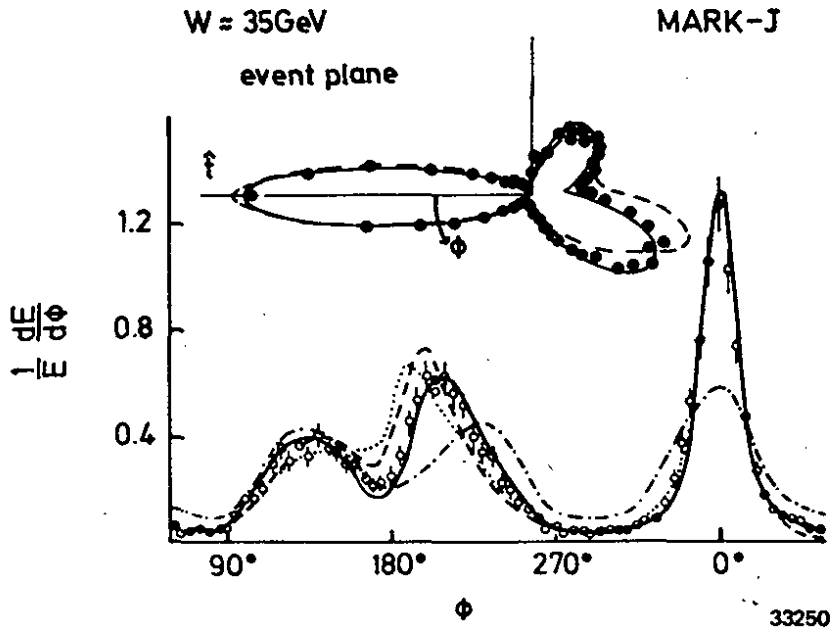

Fig. 7.18 - A plot of the energy distribution in the plane defined by the thrust and the major axis for events with oblateness greater than 0.3. The curve shows fits according to
1) a QCD calculation (full curve) with $\alpha_s = 0.18$
2) a two jet $q\bar{q}$ model with a Gaussian (dashed) or exponential (dotted) p_T distribution
3) a pure phase space distribution.
The results were obtained by the MARK J Collaboration.

The three jet structure is also seen[223,239] in the JADE data. They selected 3 jet events by demanding $Q_2 - Q_1 > 0.07$. The event plane is defined by the two least energetic jets and the 0^o direction by the most energetic jet. The tracks were then projected on to the event plane and the resulting momentum flow $1/\Sigma_p \, d\sigma/dp$ plotted. Superimposing the events leads to the momentum distribution shown in Fig. 7.19. There is a clear dip at 180^o opposite the fast jet and two adjacent peaks demonstrating the three lobe structure. A good fit can be obtained using QCD whereas $q\bar{q}$ production fails to reproduce the data.

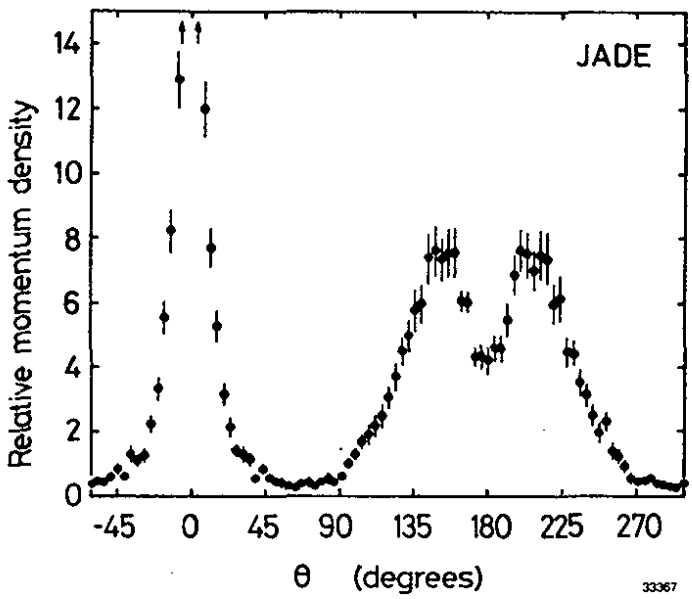

Fig. 7.19

Relative momentum flow in the event plane. The data are from the JADE group.

The same conclusion is also reached using the cluster analysis with no assumption on the number of jets. This analysis has been done[233] by the PLUTO group using the cluster method described above. The distribution of the observed number of jets per event are listed in Table 7.3 and compared to the predictions based on $q\bar{q}$, $q\bar{q}$ + $q\bar{q}g$ (α_s = 0.15) and phase space. The models are all normalized to the number of observed events. The data clearly favour a clustering of the particles around 3 axes.

Table 7.3 - Number of clusters

n_j	1	2	3	4	5	6	7
Data	2	551	249	53	3	1	
phase space	1	30	154	306	268	86	14
$q\bar{q}$	3	680	152	23	1		
$q\bar{q}$ + $q\bar{q}g$	3	567	247	46	2		

The remaining question is then to decide whether the third jet is defined by a single particle or by a group of particles. This can be done by examining the events. Fig. 7.11 shows typical candidates for three jet events as observed by JADE and TASSO. Note, that several tracks cluster around each axis.

The multiplicity distributions as measured by the TASSO Collaboration for each of the three jets are plotted in Fig. 7.20. The jets are ordered according to energy $E_1 > E_2 > E_3$. The energies of the jets were computed from the observed opening angles between the jets neglecting parton masses.

It is obvious that in general each jet contains several charged particles and that the observed multiplicity distribution is reproduced by the QCD calculation shown as the solid line in Fig. 7.20.

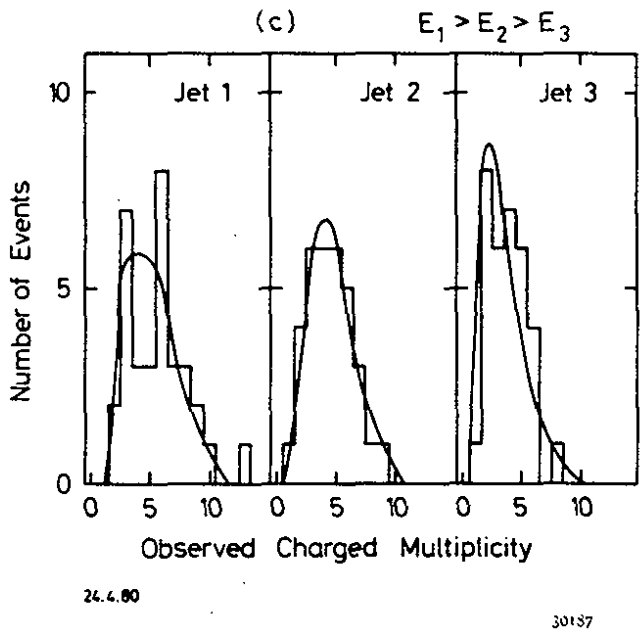

Fig. 7.20 - The charged particle multiplicity distribution for each of the three jets in a planar event with the jets ordered according to energy. The QCD prediction is shown as the solid line. The data are from the TASSO Collaboration.

The TASSO group has also evaluated the transverse momentum of charged particles in planar events with respect to the jet axis to which they were assigned. The jet direction and the assignment of particles to one of the three jets were determined using the generalized sphericity method. The distribution $1/N\ dN/dp_T^2$ is plotted as the solid points in Fig. 7.21 versus p_T^2. The distribution is in agreement with the QCD prediction shown as the solid line. Also plotted (open points) in Fig. 7.21 is the p_T^2 distribution measured with respect to the jet axis in two jet events at 12 GeV. The distributions are in excellent agreement and the data support the conjecture that the mean p_T occuring in the fragmentation of a parton is independent of energy.

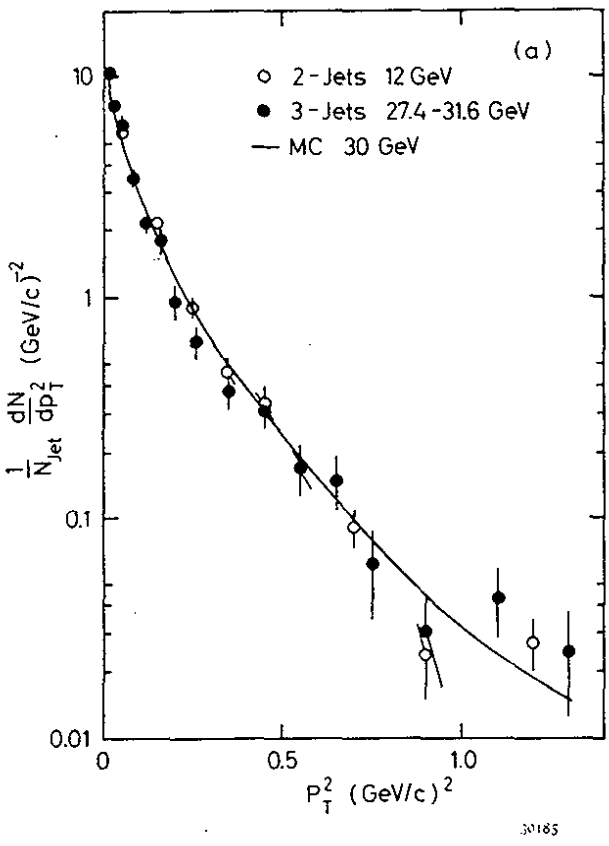

Fig. 7.21

The transverse momentum distribution $1/N\ dN/dp_T^2$ of the hadrons in planar events with respect to the three jet axes is shown as the solid points. The open points represent the transverse momentum distribution with respect to the jet axis in two jet events at lower energies. The solid curve represents the Monte Carlo QCD prediction. The data were obtained by the TASSO group.

The JADE group[240] uses an independent method suggested by Ellis and Karliner[241] to demonstrate the existence of three jet events. From the data taken at c.m. energies around 30 GeV they select planar events which satisfy the condition $Q_2 - Q_1 > 0.1$ and determine the thrust axis. The event is then divided into two jets by a plane normal to the thrust axis and p_T computed separately for each jet; the jet with the smallest p_T is called the slim jet, the other the broad jet. The broad jet is then transformed into its own rest system. If the broad jet consists of two jets they will now appear as two back to back jets along the new thrust axis T^*. The distribution of T^* in this system is plotted in Fig. 7.22 together with the thrust distribution of two jet events measured at 12 GeV. The two distributions are in excellent agreement. Also other quantities like the invariant mass, mean p_T and charged multiplicity evaluated for the broad jet in its own rest system are in agreement with the same quantities evaluated for a two jet event at 12 GeV.

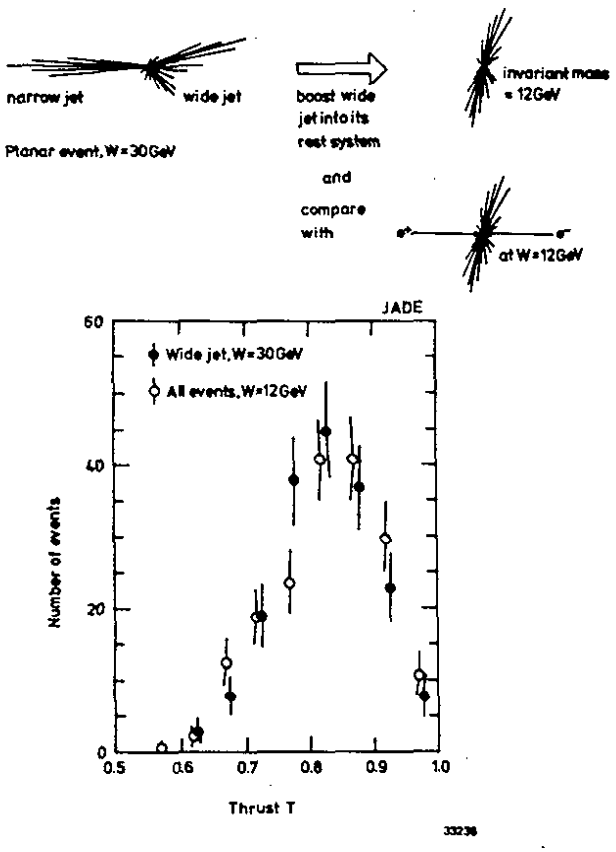

Fig. 7.22
The broad jet in planar events at 30 GeV is boosted into its own rest system. The full circles show the thrust distribution of the broad jet in this system. The open circles show the thrust distribution of two jet events at 12 GeV. The data are from the JADE Collaboration.

In conclusion: The data on $e^+e^- \rightarrow$ hadrons at high energies show clear evidence for a three jet structure resulting from the fragmentation of a new light parton with baryon number zero. This observation is naturally explained in any field theory of strong interactions as quark-gluon bremsstrahlung. Actual fits based on QCD are in excellent agreement with the data.

7.3.4 The spin of the gluon

The spin of the gluon can be determined from the angular correlation observed between the three partons in $e^+e^- \rightarrow q\bar{q}g$ events. It is convenient to describe this process using the variables $x_i = E_i/E_b$ where the energy carried off by the quark or the gluon E_i is measured in units of the beam energy E_b. The three jet event is defined in Fig. 7.23a with the variables ordered such that $x_1 > x_2 > x_3$. The thrust of the $q\bar{q}g$ event is given by x_1 with $x_1 + x_2 + x_3 = 2$. The variable x_i is related to the angles between the partons θ_i (Fig. 7.23) as

$$x_i = \frac{2\sin\theta_i}{\sin\theta_1 + \sin\theta_2 + \sin\theta_3} \qquad 7.15$$

The distribution of the events as function of x_i, averaged over production angles relative to the incident e^+e^- directions, can be written[241] as:

$$\frac{1}{\sigma_o}\left(\frac{d\sigma}{dx_1 dx_2}\right)_V = \frac{2\alpha_s}{3\pi}\left(\frac{x_1^2 + x_2^2}{(1-x_1)(1-x_2)} + \text{cyclic permutations of } 1,2,3\right) \qquad 7.16$$

for the vector case and as:

$$\frac{1}{\sigma_o}\left(\frac{d\sigma}{dx_1 dx_2}\right)_S = \frac{\tilde{\alpha}_s}{3\pi}\left(\frac{x_3^2}{(1-x_1)(1-x_2)} + \text{cyclic permutations of } 1,2,3\right) \qquad 7.17$$

for the scalar case.

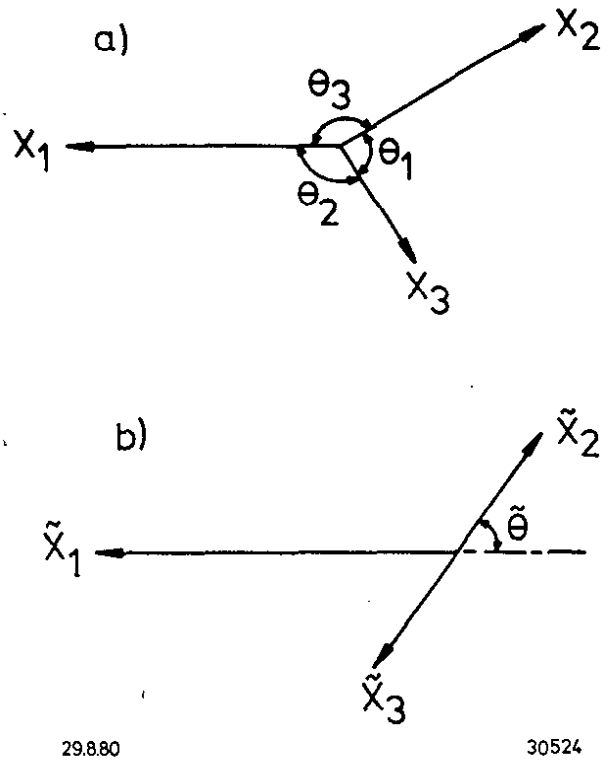

Fig. 7.23

a) Kinematic variables to describe $e^+e^- \to q\bar{q}g$.

b) Definition of the angle $\tilde{\theta}$.

TASSO multihadron events collected at c.m. energies between 25 GeV and 36.6 GeV have been analyzed[235,242] using these variables with the angles θ_i determined from the jet directions defined by charged tracks. Monte Carlo computations show that the x_i values determined in this manner agree well with those of the parent partons. The resolution in x_1 was found to be on the order of 6% with systematic uncertainties of the order of 1%. The observed distribution is shown in Fig. 7.24. Collinear two jet events cluster along the base line with $x_1 = 1$ and dominates the event sample. Well defined three jet events occur for $x_1 < 0.9$ with symmetrie three star events at the top of the diagram.

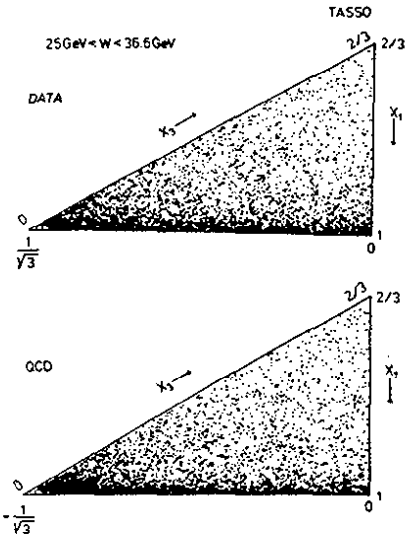

Fig. 7.24

Dalitz plot of e^+e^- → hadron events at 33 GeV using the normalized variables $x_i = E_i/E_b$ where E_i is the jet and E_b the beam energy. For comparison the QCD prediction with $\alpha_s = 0.17$ is also shown. Both distributions contain the same number of events.

The TASSO group has determined the spin using the variables $\cos\tilde{\theta} = (x_2 - x_3) / x_1$ suggested by Ellis and Karliner[241]. $\tilde{\theta}$ is the angle between parton 1 and the axis of the parton 2 and 3 system boosted to its own rest frame, as defined in Fig. 7.23b.

To ensure that the spin analysis is not affected by higher order terms one should avoid x_1 close to 1. Furthermore for x_1 close to 1 the distributions vary rapidly so that smearing effects caused by the hadronization of gluons and quarks are important. For these reasons only events with $x_1 < 0.9$ are used in the analysis. In this case the lowest energy jet has a mean energy around 6 GeV and the smallest opening angle between any two partons is 70^o.

The distribution[236,242] of the events as a function of $\cos\tilde{\theta}$ is plotted in Fig. 7.25 and compared with the distributions predicted for vector (solid) and scalar dashed-dotted gluons. The prediction was made using

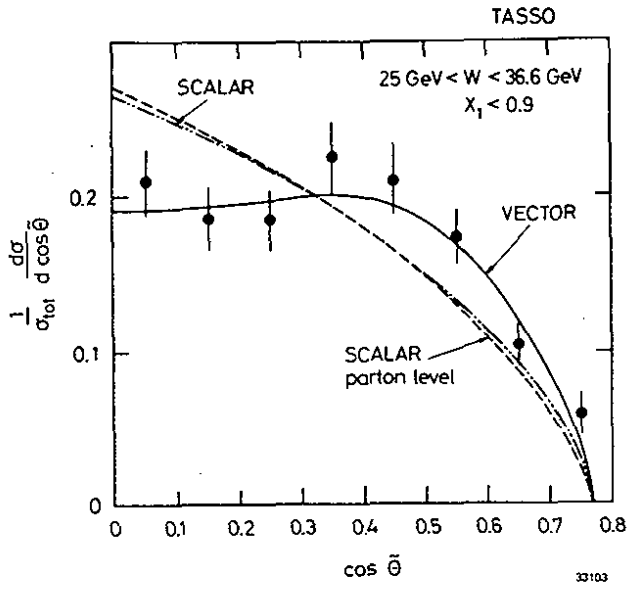

Fig. 7.25
The $\cos\theta$ distribution of events with $x_1 < 0.9$. The solid line and the dashed-dotted line show the distribution predicted for vector gluons and scalar gluons respectively. The predictions include hadronization. For comparison the prediction for a scalar gluon on the parton level is shown in Fig. 7.24. The distributions are normalized to the number of observed events.

the model of Hoyer et al.[225] and including hadronization according to Field-Feynman [178]. The distribution predicted for scalar gluons on the parton level without hadronization is also plotted (dashed curve). A comparison shows that the distribution is rather insensitive to hadronization effects. Note, that the distributions are normalized to the number of events in the plot i.e. the scalar and vector cases are discriminated using the shape only. The data clearly favour the vector case. To avoid binning effect the mean value of $\cos\tilde{\theta}$ was evaluated and compared to the theoretical prediction. The experimental value of $\langle\cos\theta\rangle = 0.3391 \pm 0.0079$ can be compared to the values $\langle\cos\tilde{\theta}\rangle_V = 0.341 \pm 0.003$ for vector gluons and $\langle\cos\tilde{\theta}\rangle_S = 0.298 \pm 0.003$ for scalar gluons.

The comparison yields:

$$\langle\cos\tilde{\theta}\rangle_{Exp} - \langle\cos\tilde{\theta}\rangle_{QCD} = (2 \pm 8) \times 10^{-3}$$

$$\langle\cos\tilde{\theta}\rangle_{Exp} - \langle\cos\tilde{\theta}\rangle_{S} = (41 \pm 8) \times 10^{-3} .$$

The data are thus in excellent agreement with the QCD prediction but differ from the scalar prediction by roughly 5 standard deviations corresponding to a confidence level of 10^{-6}. The result is remarkably insensitive both to the exact value of α_s and the details of the fragmentation. Varying the value of α_s by $\pm$ 20% changes the computed value of $\langle\cos\hat{\theta}\rangle$ by about 1%. Evaluating $\langle\cos\hat{\theta}\rangle$ in the parton model without fragmentation leaves the scalar prediction unchanged and increases the predicted value for a vector gluon by about 2%.

The gluon spin can also be determined from the x_1 distribution - i.e. the distribution of the most energetic jet in three jet events. The results obtained [243] by the CELLO group are shown in Fig. 7.26. The data clearly favour vector gluons (χ^2 = 5.1) over scalar gluons χ^2 = 30.8). The data obtained by PLUTO and by MARK II also support a vector gluon.

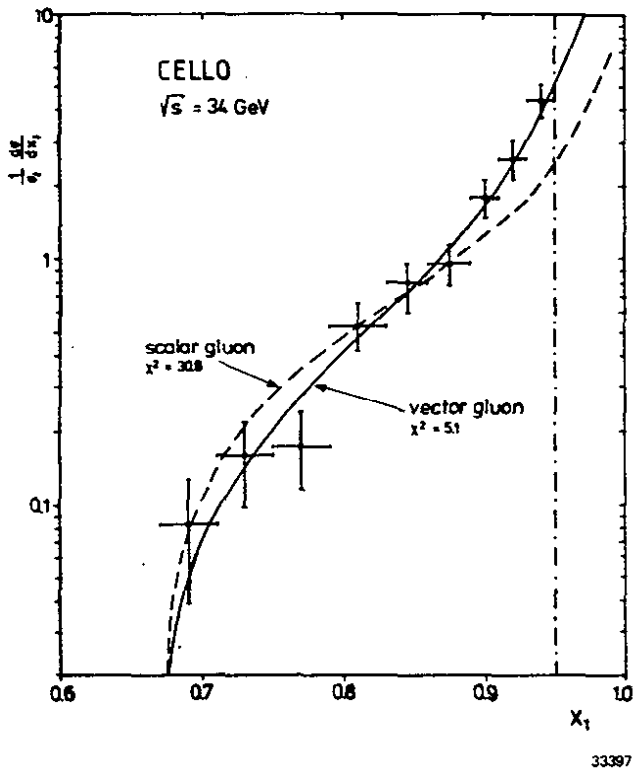

Fig. 7.26
The thrust distribution observed by the CELLO Collaboration in three jet events. The predictions for vector and scalar gluons are shown by the solid and the dashed line respectively.

Independent information on the gluon spin can be obtained from the angular distribution of the thrust axis with respect to the beam axis. According to QCD the angular distribution is given by $1 + a(T) \cos^2\theta_T$ where the coefficient a(T) decreases with the thrust. The TASSO group finds[236] $a(T) = 1.00 \pm 0.11$ for events with thrust between 0.9 and 1.0 and $a(T) = 0.75 \pm 0.18$ for events with thrust below 0.9. The QCD predictions of $a(T) = 0.97$ respectively 0.75 are in good agreement with the data but better statistics is clearly needed.

7.3.5 Alternative sources of three jet events

Several alternative mechanisms have been proposed to explain the occurence of three jet events. These models have been examined in detail by Söding[235] using the TASSO data. He finds that although all models can explain some of the observed features none of the models can explain all. In particular the models proposed do not produce the fractional energy distributions i.e. the angular correlations between jets.

The constituent interchange model[244] explains three jet events as a $e^+e^- \rightarrow q\bar{q}M$ process where the gluon is replaced by a meson M emitted at large angles with respect to the quark direction. The observed multiplicity distribution shows that single pion production must be strongly suppressed and M must stand for a serie of high mass mesons. This higher twist contribution results in a constant value of $\langle p_T^2 \rangle$ independent of c.m. energy W whereas both the data and QCD show that $\langle p_T^2 \rangle$ increases as $W^2/\ln(W^2/\Lambda^2)$. To account for this observation the effective quark coupling constant must increase by a factor of 4 between 12 GeV and 33 GeV. However, the model,

even with the coupling constant adjusted, fails to fit the observed x_1 distribution as shown in Fig. 7.27. This has also been noted in an earlier analysis[245] by the PLUTO group. Söding estimates that not more than 5% of the cross section in the three jet region can be attributed to higher twists.

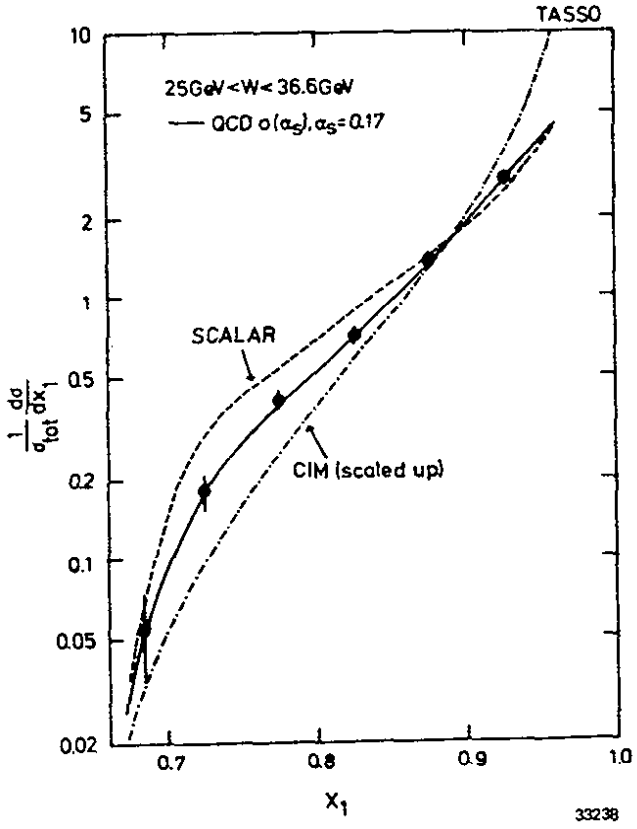

Fig. 7.27

The thrust distribution observed by TASSO and compared to the prediction of scalar gluons (dashed), vector gluons (solid) and the constituent interchange model (CIM) scaled up to agree with the p_T^2 distribution.

It has been suggested that three jet events may be described as a $e^+e^- \to q\bar{q}$ process in which the hadronization is given a long exponential tail. Such models can be made to fit the p_T^2 distribution and the $\langle p_T^2 \rangle$ distribution in and normal to the event plane. However, they completely fail to reproduce the x_1 distribution.

It has also been suggested[246] that the long p_T^2 tail observed at high energies is due to the fragmentation of heavy quarks which may have a much

larger intrinsic value of σ_q. Assuming a Gaussian distribution in p_T^2 with σ_q = 310 MeV/c for u, d and s quarks and σ_q = 800 MeV/c for the c and the b quark leads to distributions in p_T^2, $\langle p_T^2 \rangle_{in}$ and $\langle p_T^2 \rangle_{out}$ in accordance with the data. However, also this model fails to reproduce the x_1 distribution and the predicted transverse distribution of momentum with respect to the three axis is to broad.

7.3.6 Determination of the quark-gluon coupling constant α_s

Attempts to extract the quark-gluon coupling constant α_s from $e^+e^- \rightarrow$ hadrons are met with problems of both experimental and theoretical nature:

1) The omission of neutrals in some experiments. It has been shown that neutral and charged particles behave similarily. Using only charged particles will therefore not change the mean value of a quantity like thrust but will increase its error.

2) Apparent multijet contributions from b-decays.

3) QED corrections[247], in particular hard photon emission in the initial state.

4) Fluctuations in the hadronization process may cause events to be improperly classified - i.e. an event with two or four primary partons might be classified as a three jet event due to fluctuations or to overlap between the final state jets. These effects may not be crucial as long as the minimum angle between any two partons is large compared to the opening angle of the jet and a jet is defined using a Sterman-Weinberg criteria[248].

5) Contribution from higher order QCD diagrams (Fig. 6.1). These corrections have been evaluated by various groups with apparantly contradictory results. Fabricius, Schmitt, Schierholz and Kramer[249] computed the thrust distribution to order α_s^2 and found this correction to be small and in general negative. Ellis, Ross and Terrano[250] and independently Vermaseren, Gaemers and Oldham[251] found a positive α_s^2 correction of the order of 30 - 40%. It was later realized[218,252] that both results may be correct, since the groups compute different quantities. Consider the diagram for two gluon emission depicted in Fig. 7.28. The effective mass squared of the two partons ij is given by $s_{ij} = (p_i + p_j)^2 = y_c \, s$. p_i, p_j are the four momenta of the partons, y_c is a numerical parameter and s is the total c.m. energy squared. Ellis et al. and Vermaseren et al. calculate the three and four jet cross sections of the parton level - i.e. a four parton state remains a four parton state down to extremely small values of $y_c \sim 10^{-5}$, i.e. for a typical PETRA value of $s = 1000$ GeV^2, $s_{ij} \sim s \cdot 10^{-5} \gtrsim 10^{-2}$ GeV^2. The result of such a computation is very sensitive[253] to the cut off mass. However, since a typical jet has a mass around 6 GeV the two partons would appear experimentally as one jet - i.e. as one primary parton, due to the non-perturbative hadronization process.

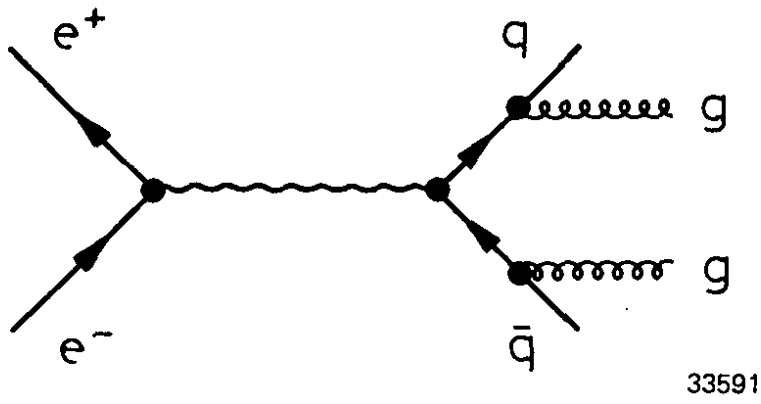

Fig. 7.28 - Double gluon bremsstrahlung leading to four jet events.

This problem is avoided in the computation by Fabricius et al. They start with the three and four parton bare cross sections but they use a Sterman-Weinberg definition of an observable jet. Two partons cannot be separated if the opening between the partons is less than δ or if either parton carries less than $\varepsilon \cdot E_b$ of the energy. Fabricius et al. defines an event as a three jet event if all but a fraction $\varepsilon/2$ of its total energy is contained within three separate cones of full opening angle δ. For the calculation they use $\varepsilon = 0.2$ and $\delta = 45^{o}$. Although this calculation is better suited to compare theory and experiment there may still be problems due to ambiguities arising from emission of soft final state partons.

The value of α_s has been determined by several groups using a varity of methods and the results are listed in Table 7.4. Some of the results

were obtained in leading order (α_s), others were evaluated using the Ali et al. program which includes some of the next to leading order diagrams (α_s^2).

Table 7.4 - Determination of α_s

Group	Ref.	α_s	Method
CELLO	(254)	$0.16 \pm 0.02 \pm 0.03$	Three jet events. Momentum tensor (α_s)
JADE	(239)	$0.18 \pm 0.03 \pm 0.03$	Three jet events. Momentum tensor (α_s)
MARK J	(238)	0.19 ± 0.02	Three jet events. Energy ow (α_s^2)
MARK II	(37)	$0.18 \pm 0.015 \pm 0.03$	Energy-Energy correlation (α_s)
PLUTO	(233)	$0.15 \pm 0.03 \pm 0.02$	Three jet events. Cluster analysis (α_s)
PLUTO	(255)	0.18 ± 0.02	Event shapes (α_s)
TASSO	(230)	$0.17 \pm 0.02 \pm 0.03$	Three jet events. Momentum tensor $(\alpha_s)^2$

* statistical error $\pm$ systematic uncertainty.

The methods used by various groups to extract a value of α_s is discussed in some detail below.

The strong coupling constant α_s is directly related to the number of three jet events. After choosing a minimum opening angle between any pairs of partons (q, $\bar{q}$ or g) the QCD cross section can be integrated and normalized to the total e^+e^- annihilation cross section. This ratio depends only on α_s and can be compared directly to the experimental ratio of three jet events to the total number of hadronic events. In practice corrections

must be made for the effects discussed above. An example of the quality of such fits is shown in Fig. 7.12. The data are from TASSO[230]. Note, that the fragmentation parameter were determined at low energies. Similar fits have been made by JADE[223,239] and CELLO[254]. PLUTO determined[233] the number of three jet events from a cluster analysis.

MARK J has determined[238] α_s from the number of three jet events defined by $O_b > 0.3$ or $O_b \geq O_n \geq 0.3$ with $O_n > 0$. O_b and O_n is the oblateness (Fig. 7.16) for the broad and the narrow jet respectively. They have also determined α_s from the average oblateness $\langle O_b \rangle$.

The value of α_s has also been determined from a measurement of the energy-energy correlations[256,257]. This correlation is defined as

$$7.18 \qquad \frac{1}{\sigma}\frac{d\Sigma_E}{d\theta} = \frac{2}{\sigma}\sum_{j,k}\int \frac{d^3\sigma}{dz_j dz_k d\theta} z_j z_k \, dz_j \, dz_k$$

$z_j = E_j/E_{beam}$ is the fractional energy of particle j and θ is the opening angle between the momentum vectors of particles j and k. The sum is over all pairs j and k which satisfy this condition and the result is averaged over all events. This expression has been calculated to first order in QCD neglecting hadronization.

The energy-energy correlation has been evaluated by various groups. The data obtained by the MARK II Collaboration[37] at PEP are plotted in Fig. 7.29 ($\chi \equiv \theta$). The dashed curve shows the perturbative QCD prediction, the solid line gives the prediction including hadronization. It is obvious that non-perturbative effects are still very important at

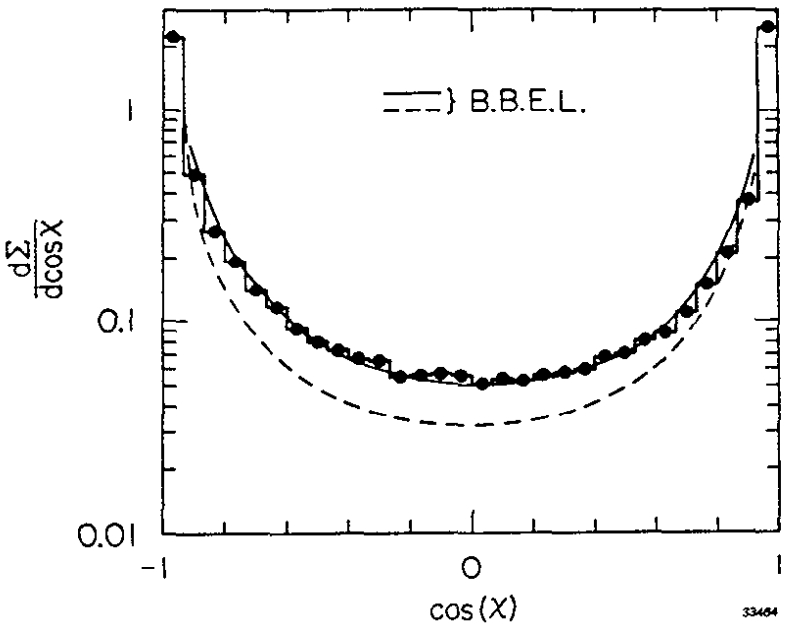

Fig. 7.29 - The angular dependence of the energy-energy correlation function. The dashed curve shows the parton level QCD prediction, the solid line includes hadronization effects. The data are from the MARK II Collaboration.

30 GeV. To extract a value of α_s which is less dependent on non perturbative effects the groups consider the difference

$$A(\theta) = \frac{1}{\sigma}\left(\frac{d\Sigma_E}{d\theta}(\pi-\theta) - \frac{d\Sigma_E}{d\theta}(\theta)\right) \qquad 7.19$$

To first order non perturbative effects cancel and the observed effect should mainly result from gluon bremsstrahlung. Data from PLUTO[258], MARK II[37] and CELLO[224] are plotted in Fig. 7.30 and compared with the QCD prediction for $\alpha_s = 0.18$. The data are in agreement with the predictions. The PLUTO group has investigated the uncertainties resulting from detector imperfection, radiative corrections and hadronization effects. They find that these effects introduce uncertainties on the order of 10 - 20% for θ between 45^o and 90^o. The corrections are larger at smaller angles.

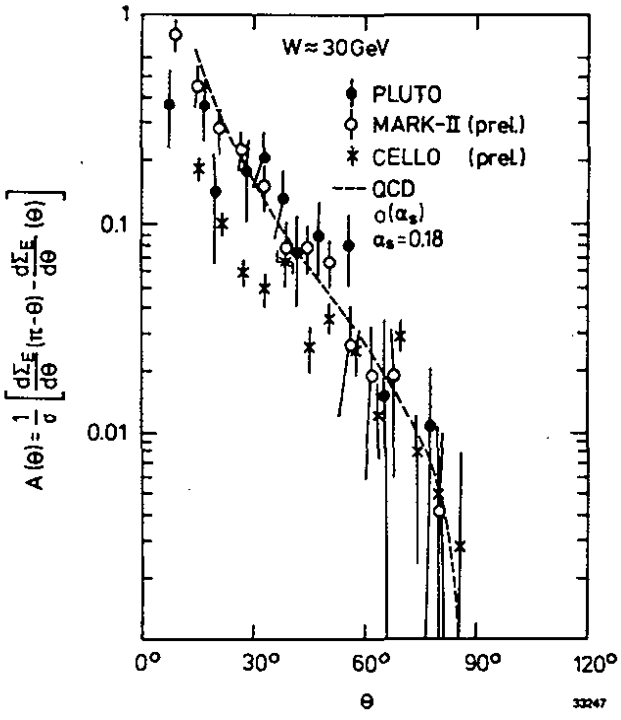

Fig. 7.30
Forward-backware asymmetry of the energy-energy correlation function. The QCD prediction for $\alpha_s \simeq 0.18$ is shown as the dashed curve. The data were obtained by PLUTO, CELLO and MARK II.

PLUTO has also determined[255] the value of α_s using the following shape dependent observables:

a) <1-T>, where T is the thrust.

b) The energy weighted jet broadness $\langle \sin^2\eta \rangle = \langle \frac{E_i}{W} \sin^2\delta_i \rangle$. E_i and δ_i is the energy and the angle of a track with respect to the jet axis, - i.e. η is an energy weighted jet opening angle.

c) The squared invariant mass[259] of the wider of the two jets normalized to s, the total energy aquared.

d) The integral over the energy-energy correlation function in the large angle region $60^o < \theta < 120^o$.

Effects due to perturbative QCD has an energy dependence proportional to $1/\ln(W^2/\Lambda^2)$, whereas non-perturbative effects will decrease with energy

as 1/W. The PLUTO data span a large energy range and can be used to separate perturbative and non perturbative effects by the different dependence on energy. The data and the results of the fits are plotted in Fig. 7.31. The perturbative contribution is shown by the dashed line, the solid curve includes both effects. The fits are rather good and all constant with the value $\alpha_s = 0.18 \pm 0.02$.

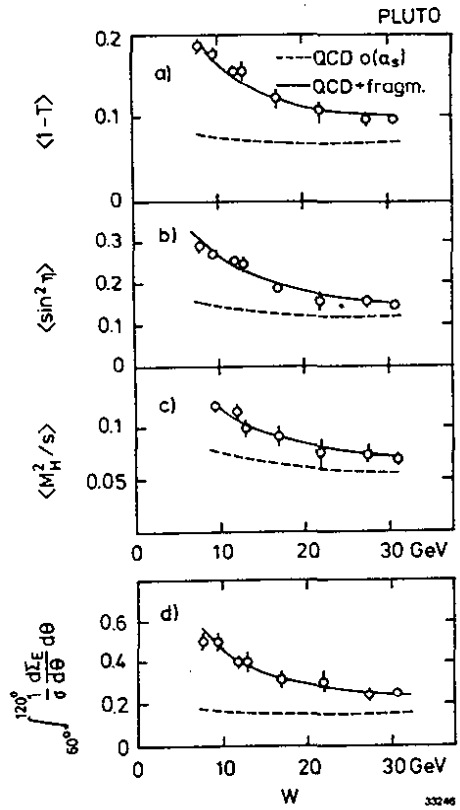

Fig. 7.31
The energy dependence of the average thrust, energy weighted jet opening angle, invariant mass of the broad jet and the integral over the energy-energy correlations for θ between 60° and 120°. The dashed line shows the perturbative QCD contribution $a/\ln(W^2/\Lambda^2)$, the solid line includes hadronization effects (b/W). The data are from the PLUTO Collaboration.

The value of α_s has thus been extracted by several methods with different sensitives to the theoretical problems like higher order QCD corrections or to experimental effects like b decays. It is quite remarkable that all determinations listed in Table 7.4 are consistent with $\alpha_s = 0.17$.

The same value $\alpha_s = 0.17$ is also found by Fabricius et al. using the full second order calculation. With the second order formalism developed by Ellis et al., Ali[260] finds $\alpha_s = 0.12 - 0.13$.

One of the crucial predictions of QCD is that the strength of the coupling α_s decreases logarithmically with increasing value of the momentum transfer squared (Eq. 5.2). The MARK II Collaboration at PEP has done an interesting attempt to determine this Q^2 dependence from an analysis of the $p_\perp$ distribution within a jet. The method is based on work by Konishi, Ukawa and Veneziano[261]. They compute the energy weighted cross section for particles within a jet using a quark-gluon cascade model. The relevant momentum transfer entering the formula for α_s depends on the jet cone opening angle 2δ as $Q^2\delta^2$ - i.e. the energy weighted cross section for single jet production can be used to determine α_s at various values of the momentum transfer. The method is discussed in detail by Hollebeek[37], The results shown in Fig. 7.32 are quite intriguing but more work both experimentally and theoretically is needed to ensure the α_s is indeed running.

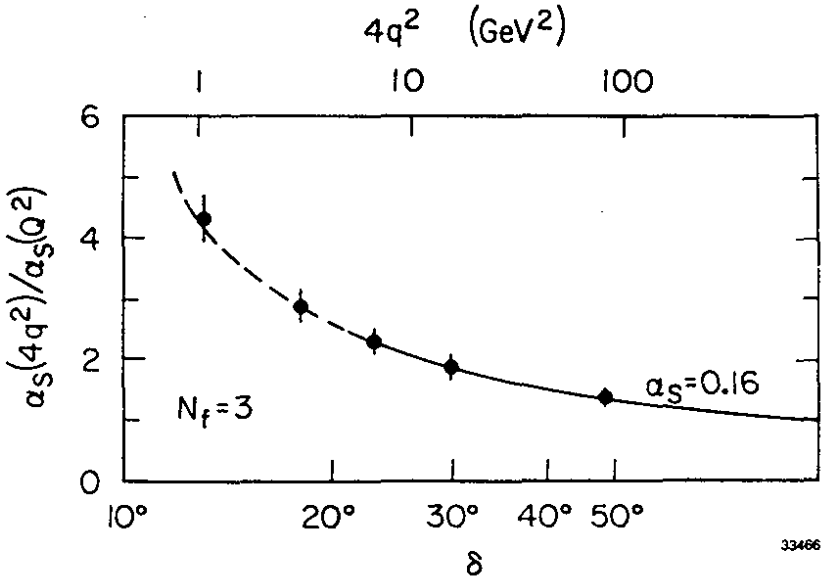

Fig. 7.32 - The dependence of α_s as a function of the jet opening angle δ or $4q^2$. The data are from the MARK II Collaboration.

7.3.7 Do quarks and gluons fragment differently ?

One might expect on general grounds that gluons and quarks hadronize into different final states. A gluon may fluctuate into pairs of quarks and gluons. Futhermore the ggg coupling is 9/4 times stronger than the $q\bar{q}g$ coupling such that gluon emission will be more frequent for gluons than for quarks. This leads us to expect that a gluon and a quark will fragment into hadrons differently - the hadron spectrum from a gluon fragmentation will be softer with a correspondingly higher multiplicity. Computations[261,262] show that at asymptotic energies a gluon will fragment into a jet of hadrons with multiplicity and opening angle which are larger by a factor 9/4 than the corresponding quantities for a quark jet of the same energy.

Using the string model Anderson, Gustafson and Collaborators have predicted[227] that the yield of low-energy particles emitted at large angles with respect to the jet axis depends whether the jet is a result from the fragmentation of a quark or a gluon. The JADE group[239] has carried out this analysis using charged and neutral particles. Planar events with $Q_2 - Q_1 > 0.10$ were divided into a slim jet and a broad jet by the plane normal to the thrust axis. The broad jet is then boosted into its own rest system and the particles assigned to the two subjets. The softest jet is called the gluon jet. Monte Carlo calculations show that with the cuts used this is true more than 50% of the time and it simply reflects the softness of a bremsstrahlung spectrum. All the particles are projected on to the plane defined by T, thrust axis of the event and T^* the thrust axis of the boosted two jet system. They then plot the particle densities between the gluon jet and the slim jet and the quark jet and the

slim jet in terms of normalized angles θ_i/θ_{max}, where θ_{max} is the opening angle between the gluon jet and the slim jet or the quark jet and the slim jet respectively. The data plotted in Fig. 7.33 show that the density of tracks is larger by a factor of 2 between the slim jet and the quark jet.

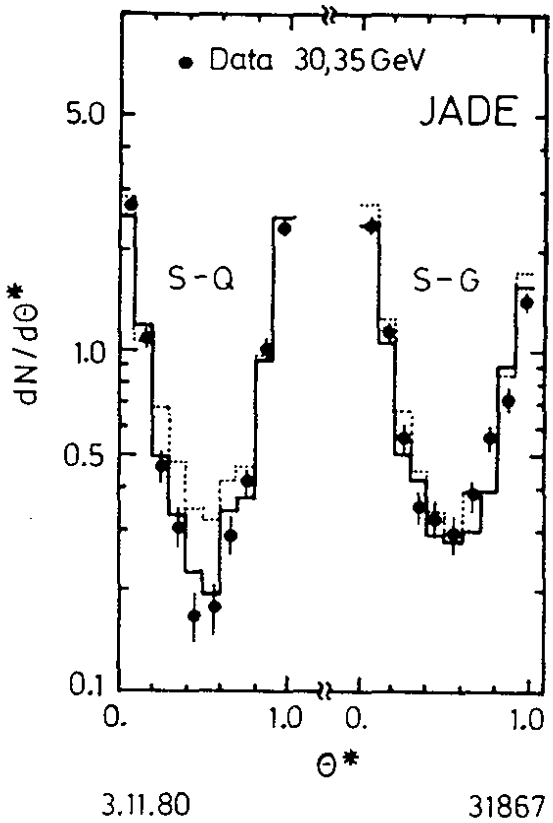

Fig. 7.33
Angular distribution of charged particles between the slim jet and the gluon jet and between the slim jet and the quark jet as a function of the normalized angles θ/θ_{max}.

The result of a Monte Carlo computation[225] based on similar fragmentation functions for quarks and gluons fails to reproduce the dip observed in the particle density distribution between the quark and the slim jet, as shown by the dotted histogram in Fig. 7.34. The data, however, are reproduced in the Lund Monte Carlo program [227], where the quark has a harder fragmentation function than the gluon jet. The fit using the Lund Monte Carlo is shown by the solid histogram.

These findings have been confirmed[224] by a recent analysis.

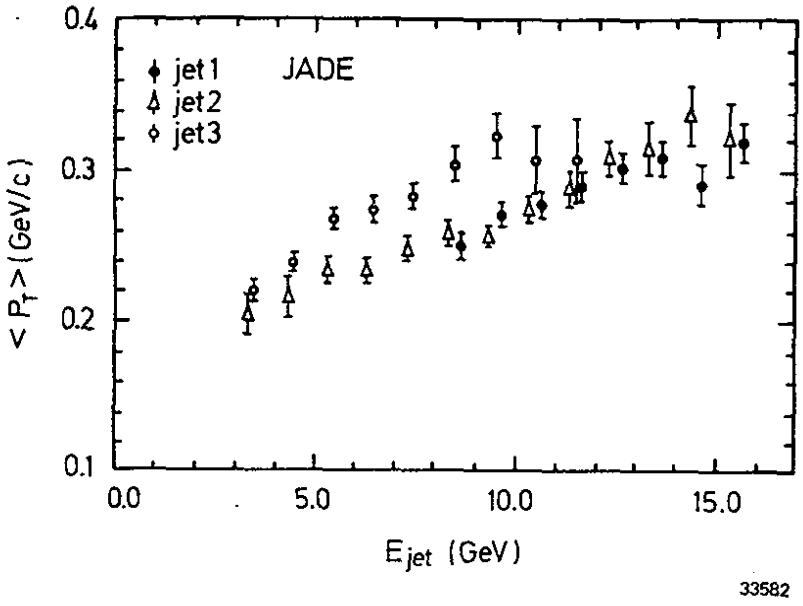

Fig. 7.34 - The mean transverse momentum of particles with respect to their assigned jet axis in planar three jet events as a function of jet energy. The jets are ordered according to energy as $E_1 > E_2 > E_3$.

The JADE group has determined[236] the $p_\perp$ growth displayed by the individual jets in planar three jet events. In this analysis planar events were selected by demanding $Q_2 - Q_1 > 0.07$ and $Q_1 < 0.06$ where Q_j are the normalized eigenvectors of the sphericity tensor with $Q_1 > Q_2 > Q_3$. The three jet directions and the particle assignments to the jets were determined by maximizing triplicity i.e. the directed momentum along three axes. The jet energies E_j is computed from the direction of the jets ordered such that $E_1 > E_2 > E_3$. Monte Carlo studies show that in this case the gluon jet can be assigned to the jet 1, 2, or 3 with the probability 12%, 22% and 51%. In 16% of the cases no gluon was emitted, a two jet event was mislabled as a three jet event due to fluctuations in the hadronization process. The mean transverse momentum of the three jets is plotted in Fig. 7.34 as a function of jet energy. The data show that the softest jet

has the largest $p_\perp$ with respect to its jet axis for a given energy, whereas there is little difference between the two quark jets 1 and 2.

The JADE group also finds that the jet broadening is more important to the event plane than normal to the plane. Both findings are reproduced in the LUND model but not by the Hoyer et al. simulation in which quarks and gluons have identical hadronization.

The effects are very interesting, however, the findings of the JADE group are not confirmed by similar analysis carried out by the MARK J[236] and the MARK II Collaboration[37].

7.4 Summary

To demonstrate that QCD is the correct theory of strong interaction one has to show that gluons, massless, coloured vector particles with flavour neutral couplings exist. Furthermore the gluons should have self coupling leading to a running coupling constant.

i) Gluons exist. They offer the only consistent explanation of all the features observed in e^+e^- annihilation into hadrons at high energies, in particular the occurance of three jet events. There is also no alternative explanation of the properties of the final state hadrons in the decay $\Upsilon \to$ hadrons.

ii) Gluons have spin one. Maybe the cleanest observation is from the angular correlation observed between the jets in three jet events. Both $\Upsilon \to$ hadrons and $\Upsilon' \to \pi^+\pi^- \Upsilon$ is in agreement with vector spin predictions and disagree with predictions based on scalar gluons.

iii) The gluon is flavour neutral. The $c\bar{c}$ and $b\bar{b}$ mass spectrum and the leptonic widths can be explained using the same potential for both c and

b quarks.

iv) Gluons may be coloured. This would explain why $\Upsilon \rightarrow g \rightarrow$ hadrons is forbidden.

v) Gluon self interaction. This crucial feature of QCD has not yet been convincingly observed. Some early evidence of an analysis of the angular width of gluon jets may indicate that α_s is running. Furthermore there are candidates for gluonium.

8. Two Photon Interactions

Electron-positron collisions are a prolific source of photon-photon collisions[263,264] as shown in Fig. 8.1, where Q^2 and ν of the spacelike photon is determined from a measurement of energy and angle of the scattered lepton. These processes offer a unique opportunity to vary the mass of the target and the projectile over a wide range from collisions of two nearly real photons via deep inelastic electron scattering on a photon target to collisions of two heavy photons. The interest in these studies are enhanced by the dual rôle of the photon as a hadron and as a point-like particle which can initiate hard scattering processes even on its mass shell.

Experimentally, two photon events are separated from annihilation events by a cut on the observed energy. The c.m. energy of the $\gamma\gamma$ system is in general much lower than the available energy reflecting the product of two bremsstrahlungs spectra. In some case one (or rarely) both of the scattered electrons are detected in shower counters mounted at small angles with respect to the beam axis. The background from beam gas events is low

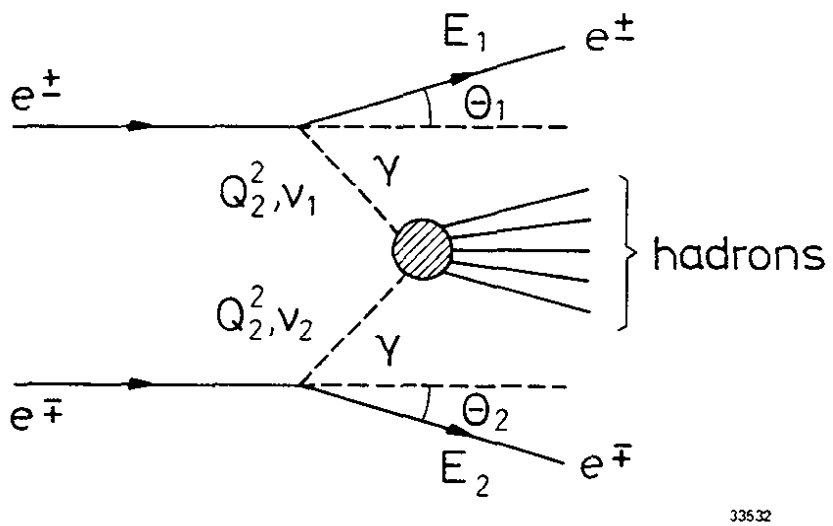

Fig. 8.1
Hadron production in $e^+e^- \to e^+e^-X$.

and can be measured from the number of events which satisfy the selection criteria but originates outside of the interaction volume. Another potential source of background results from inelastic Compton scattering. However, estimates of this process find it to be negligible.

The mass of the produced hadron system can be computed from the energy and angles of the scattered electrons. However, tagging both electrons leads to a large reduction in rate such that in practice only one or none of the electrons is detected. This has no drawbacks in the case of real photons and a simple final state like $e^+e^- \to \gamma\gamma\, e^+e^- \to \pi^+\pi^-\, e^+e^-$ where the energy can be determined from the final state pions. In general, however, the final state particles are both charged and neutral and are travelling at small angles with respect to the beam direction. It is therefore difficult to detect and measure the momenta of all particles in the final state. Thus the measured visible mass of the hadron system W_{vis} can only be related to the true mass W of the produced hadron system by a Monte Carlo calculation. Furthermore tagging is required in order to study the Q^2 dependence of a process.

During the past few years several groups have reported experimental results on photon-photon interactions. An up to date discussion of the data and the theoretical aspects of $\gamma\gamma$ collisions including a complete set of references can be found in the talks given by Wedemeyer[265] and Bardeen[266] at the Bonn meeting.

8.1 Resonance production

All hadrons with even charge conjugation and spin different from one can be produced [267] in $\gamma\gamma$ collisions. The corresponding cross section can be written as

$$8.1 \qquad \sigma(e^+e^- \to e^+e^-X) = (2\alpha \ln s/m_e^2)^2 \, f(x) \, \frac{(2J+1)\Gamma(X\to 2\gamma)}{M_X^3}$$

with $x = m_X^2/s$ and $f(x) = 1/2\,(2+x)^2 \ln(1/x) - (1-x)(3+x)$.

Thus such a measurement determines the partial width $\Gamma(X \to \gamma\gamma)$ and if the branching ratio $B(X \to 2\gamma)$ is known, Γ_{tot}, the total width of the resonance.

The data available on $\eta'(958)$, $f^o(1270)$ and $A_2(1310)$ are listed in Table 8.1. These data were all collected in the no tag mode. Beam gas background, annihilation events and cosmic ray events were removed by kinematical cuts. The results obtained by the various groups are in agreement within the quoted errors.

Table 8.1 - Data on $\Gamma_{\gamma\gamma}(x)$

Particles (J^{PC})	Group	Decay mode	$\Gamma_{\gamma\gamma}$(keV)*	Reference
$\eta'(958)$	MARK II	$\rho^o\gamma$	$5.9 \pm 1.6 \pm 1.2$	268
(0^{-+})	JADE	$\rho^o\gamma$	7.5 ± 0.7	265
$f^o(1270)$	PLUTO	$\pi^+\pi^-$	$2.3 \pm 0.5 \pm 0.35$	269
(2^{++})	TASSO	$\pi^+\pi^-$	$3.2 \pm 0.2 \pm 0.6$	270
	MARK II	$\pi^+\pi^-$	$3.6 \pm 0.3 \pm 0.5$	271
	CELLO	$\pi^+\pi^-$	$3.6 \pm 0.2 \pm 0.7$	272
	Crystal Ball	$\pi^o\pi^o$	$2.9 \,{}^{+\,0.55}_{-\,0.39} \pm 0.6$	273
A_2	JADE	$\rho^\pm\pi^\mp$	1.2 ± 0.4	265
(2^{++})	Crystal Ball	$\eta\,\pi^o$	$0.77 \pm 0.18 \pm 0.27$	273

* width ± systematic uncertainty ± statistical error.

As an example of such an analysis let us consider the reaction $e^+e^- \to f^0\, e^+e^- \to \pi^+\pi^-\, e^+e^-$ as measured [270] by the TASSO Collaboration. They selected two positively charged tracks originating from the interaction region. To reduce the background from beam gas events the tracks should be coplanar to within 10^o with respect to the beam axis and each track should have a transverse momentum with respect to the beam axis of 0.3 GeV/c or more. Two prong cosmic rays and annihilation events are rejected by requiring the two tracks to be non-collinear by more than 7.5^o and the sum of the magnitude of the momenta to be less than 20% of the beam energy. The transverse momentum imbalance of the event with respect to the beam axis should be less than 0.3 GeV/c.

The mass distribution of the remaining events, assigning pion masses to the particles, is shown in Fig. 8.2. The data represent a total integrated luminosity of 9240 nb^{-1} at c.m. energies between 22.4 GeV and 36.7 GeV. The contribution [274] from $e^+e^- \to e^+e^-\, e^+e^-$ and $e^+e^- \to e^+e^+\, \mu^+\mu^-$ is shown as the solid line. The data are in good agreement with the prediction except for an excess of events near 1.3 GeV.

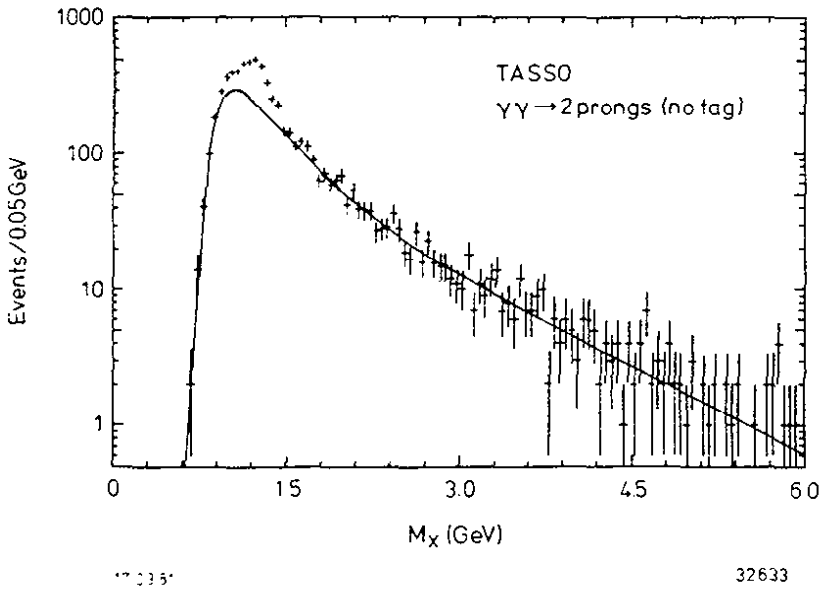

Fig. 8.2
Untagged two prong events from TASSO plotted versus the pair mass. The QED contribution is represented by the solid line.

The invariant mass distribution after subtracting the QED contribution is shown in Fig. 8.3. It is natural to identify the observed mass peak near 1.27 GeV with the $f^0(1270)$. A spin two resonance like the f^0 can be produced with helicity amplitudes 0, 1 or 2. To determine the dominant amplitude the data are plotted as a function of $\cos\theta^*$ where θ^* is the angle between the beam axis and one of the charged particles in the events. Fig. 8.4 shows data [273] from Crystal Ball which have the largest acceptance in $\cos\theta^*$. The angular distribution expected for the three helicity amplitudes are shown. The data, in agreement with theoretical expectations and the findings of other groups, clearly favour the helicity two amplitude. In fact all the groups use only this amplitude to determine $\Gamma_{\gamma\gamma}$. The observed mass distribution in Fig. 8.3 can be fit to the f^0 using the standard values of f^0 mass and the width plus an additional term resulting either from $\pi^+\pi^-$ continuum production or from a lower mass resonance.

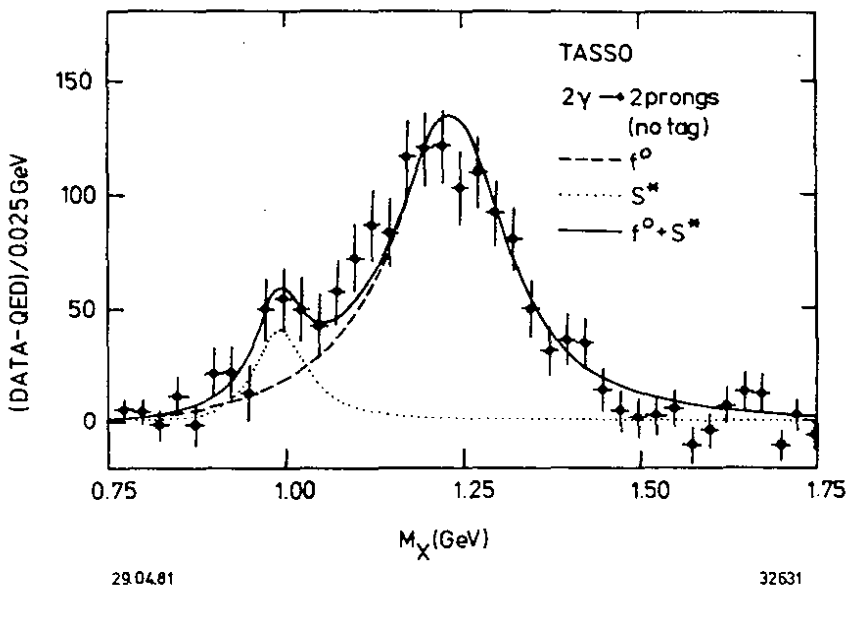

Fig. 8.3 - Invariant mass distribution of $\gamma\gamma \rightarrow$ 2 prongs assuming the tracks to be pions.

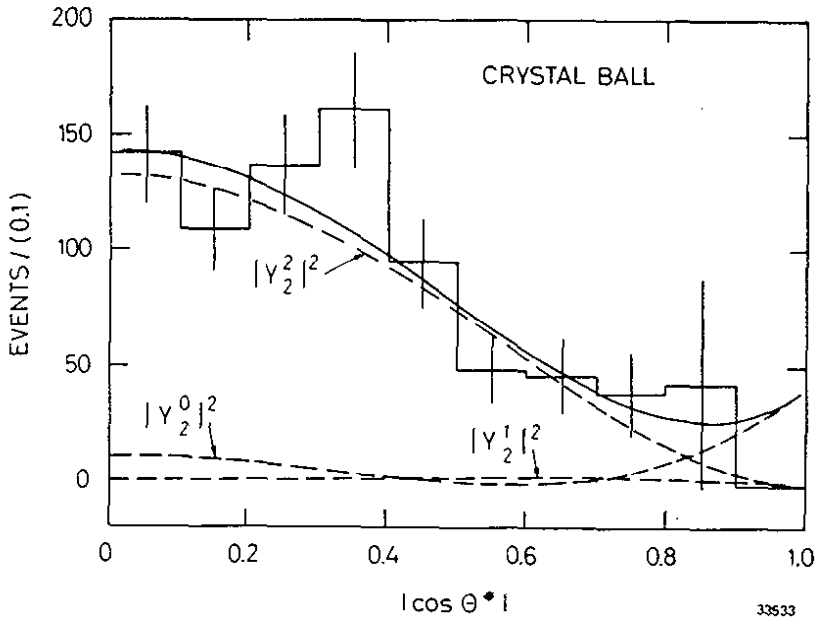

Fig. 8.4 - The decay angular distribution of $f^0 \to \pi^0\pi^0$. The data - corrected for the acceptance - are from the Crystal Ball Collaboration.

8.2 Exclusive Channels

Exclusive particle production in $\gamma\gamma$ collisions[264,275] has recently received some attention.

At the Wisconsin Conference the TASSO Collaboration reported[276] the first data on $e^+e^- \to \pi^+\pi^-\pi^+\pi^-e^+e^-$. They found the four pion channel to be dominated by $\rho^0\rho^0$ production with a cross section which rises sharply at threshold and reaches a level well above the cross section estimated from the vector dominance model.

New data are reported by several groups. The four pion invariant mass spectra observed bv the TASSO group[265] and by the JADE group[265] are shown in Fig. 8.5 a, b These data may contain some structure and a more refind analysis including $\rho^0\rho^0$, $\rho^0\pi^+\pi^-$ and $\pi^+\pi^-\pi^+\pi^-$ phase space production are now underway. MARK II [277] and CELLO[272] have determined the $\rho^0\rho^0$ cross section using a less complex analysis and the data are shown in Fig. 8.6. The data agree both in shape and magnitude with the old TASSO data.

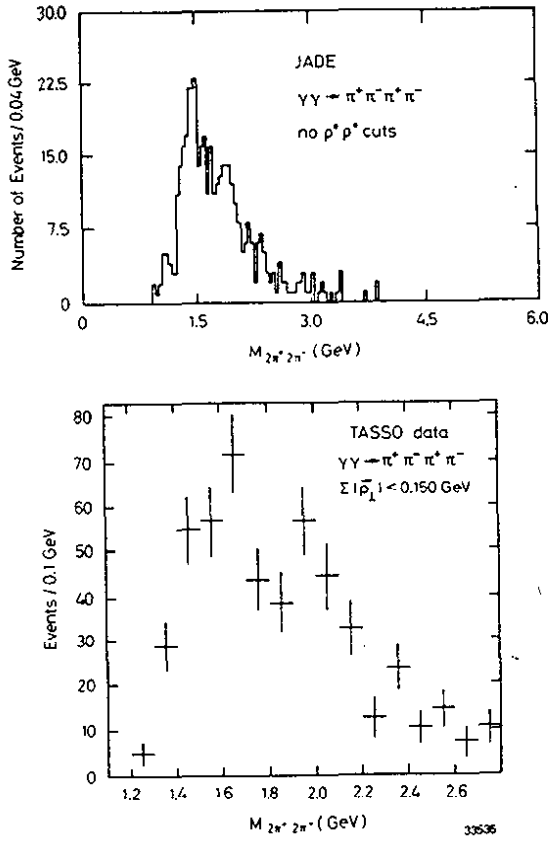

Fig. 8.5 - Invariant four pion mass spectra observed by (a) TASSO and (b) JADE.

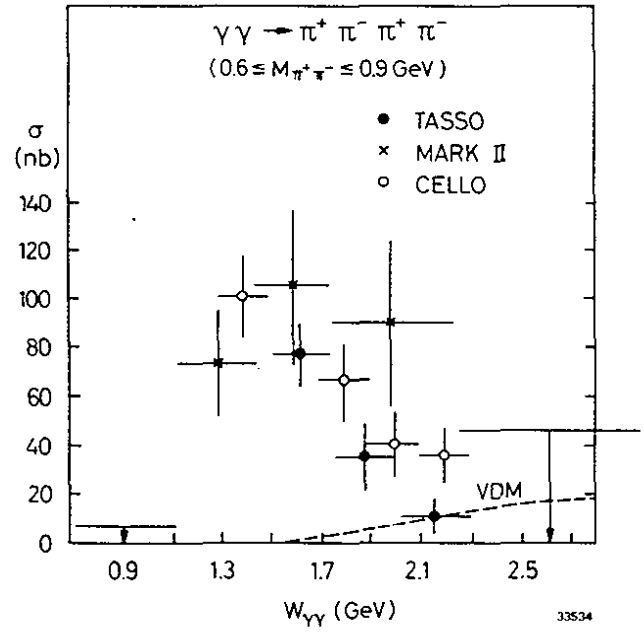

Fig. 8.6 - The cross section for $e^+e^- \to \rho^0\rho^0$ as measured by TASSO, MARK II and CELLO plotted versus the c.m. energy. The vector dominance prediction is shown by the solid line.

Recently the TASSO Collaboration reported [278] data on $e^+e^- \to p\bar{p}\, e^+e^-$ at a c.m. energy of 2.0 - 2.6 GeV. They find a cross section of $4.5 \pm 1.6 \pm 0.8$ nb where the first error is statistical and the second systematic. An estimate of the cross section using the reaction $p\bar{p} \to \rho\,\rho$, $p\bar{p} \to \rho\,\omega$ and the vector dominance model gives values between 0.2 nb and 1.0 nb.

8.3 The total cross section for $\gamma\gamma \to$ hadrons

The amplitude for $\gamma\gamma \to$ hadrons will presumably contain both the hadron-like piece[279] and the pointlike piece[280] shown in Fig. 8.7. In the hadronic piece the photons convert into vector mesons which subsequently interact producing a final state similar to that observed in hadron-hadron collisions, where the secondary hadrons tend to be produced with low transverse momenta with respect to the beam axis. In addition, however, the photon has a point-like piece where the photon couples directly to a quark pair initiating a hard scattering process. In this case the secondary hadrons will appear as two jets of hadrons distributed roughly as $1/p_T^4$ with respect to the beam axis. Although the hadronlike piece will dominate at small p_T the pointlike contribution with its slower p_T dependence will be dominant at large values of p_T.

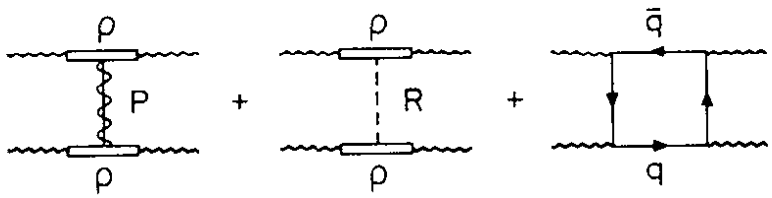

Fig. 8.7 - The hadron-like and the point-like contribution to the total cross section for $\gamma\,\gamma \to$ hadrons.

The total cross section for $\gamma\gamma \to$ hadrons can be estimated from the imaginary part of the elastic scattering amplitude to be:

$$8.2 \quad \sigma(\gamma\gamma \to \text{hadrons}) = 240 \text{ nb} + \frac{270 \text{ (nb GeV)}}{W} + \sigma^{p}_{\gamma\gamma} \quad .$$

The first term result from Pomeron exchange and is estimated using the factorization relation $\sigma_{\gamma\gamma} \cdot \sigma_{pp} = (\sigma_{\gamma p})^2$. The second term involves both f and A_2 exchange and leads to a cross section which decreases as 1/W where W is the $\gamma\gamma$ c.m. energy. The pointlike contribution can be crudely estimated using the box diagram in Fig. 8.7. This process is analogous to the QED process $e^+e^- \to \mu^+\mu^-e^+e^-$ and yields

$$8.3 \quad \sigma^{p}_{\gamma\gamma} = \frac{4\pi\alpha^2}{W^2} \cdot 3\sum_i e_i^4 \ln (W^2/m_i^2).$$

where e_i denotes the charge and m_i the mass of the i-th quark. This cross section decreases roughly as $1/W^2$. Including only u, d and s quarks with a mass of 100 MeV results in a cross section value of 650 nb at a $\gamma\gamma$ c.m. energy of 1 GeV.

The PLUTO group has measured [281] the cross section for $e^+e^- \to \gamma^*\gamma^*e^+e^- \to$ hadrons + e^+e^-. The data were obtained by requiring that one of the electrons is scattered between 23mrad and 55 mrad and deposit at least 4 GeV in the shower counter. The second electron is not detected such that its photon is nearly real. The process can be considered as inelastic electron scattering on a real transversely polarized photon i.e. $e\,\gamma \to e'X$. The kinematic is defined above in Fig. 8.1 and the cross section $d\sigma(e\,\gamma \to e\,X)$ can be written in terms of the transverse and longitudinal cross section σ_t and σ_ℓ as:

8.4 $$d\sigma(e\gamma \to eX) = \Gamma_t \, [\sigma_t(Q^2, W) + \varepsilon \, \sigma_\ell (Q^2, W)] \, d\Omega dE'_1$$

In this expression is Γ_t the flux and ε the polarization of the virtual photon. These quantities are given by

8.5 $$\Gamma_t = \frac{\alpha E'(1 + (1-y)^2)}{2\pi^2 Q^2 y}$$

$$\varepsilon = 2(1-y) \; / \; (1 + (1-y)^2)$$

where $y = (1-(E'_1/E) \cdot \cos^2\theta/2)$ is the relative energy of the virtual photon.

The resulting cross section is plotted in Fig. 8.8 as a function of W_{vis} at an average $\langle Q^2 \rangle$ of 0.25 GeV/c^2. The VDM prediction is shown as the solid line.

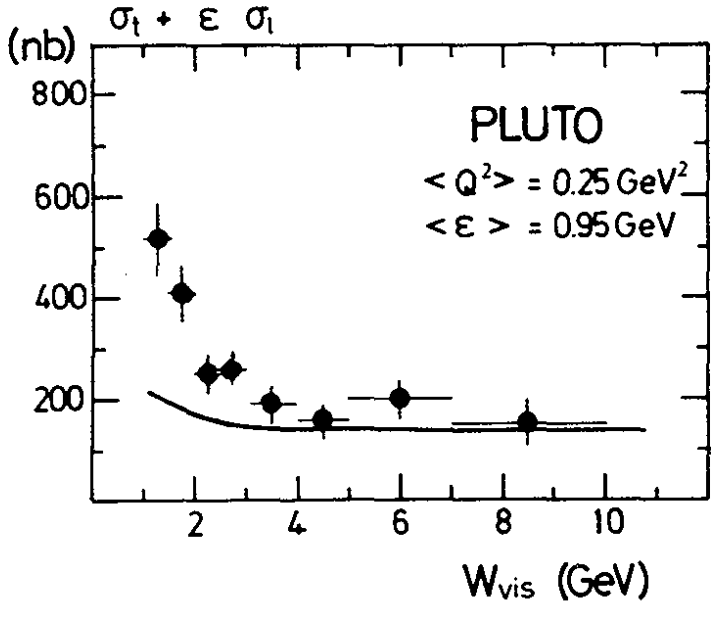

Fig. 8.8

The cross section $\gamma^* e \to e'X$ plotted versus the visible energy W_{vis}. The VDM prediction is shown as the solid line. The data were obtained by the PLUTO group.

The observed energy W_{vis} was converted into the c.m. energy W using a multipion phase space model with limited transverse momentum. The corrections are on the order of 15 - 20%. The longitudinal cross section was neglected in the rest of the analysis in agreement with the data on electroproduction on a hadron target. The Q^2-dependence of the transverse cross section was taken from the vector dominance model using the ρ pole only

$$8.6 \qquad \sigma_f(Q^2\ W) = \sigma_{\gamma\gamma} \cdot \left(\frac{m_\rho^2}{Q^2 + m_\rho^2} \right)^2$$

The data at small Q^2 are indeed consistant with this model as shown below in Fig. 8.8.

The total cross section $\sigma_{\gamma\gamma}$ for two real photons was obtained by extrapolating to $Q^2 = 0$ and correcting for the difference between W and W_{vis}. The cross sections are well represented by the expression

$$8.7 \qquad \sigma_{\gamma\gamma} = A \left(240\ nb + \frac{270\ nb\ GeV}{W}\right) + B/W^2) \left(\frac{m_\rho^2}{m_\rho^2 + Q^2} \right)$$

with $A = 0.97 \pm 0.16$ and $B = 2250 \pm 500$ nb GeV^2.

This fit, with one standard deviation error bars, is plotted in Fig. 8.9. The cross section agrees with the VDM prediction for $W \gtrsim 6$ GeV. The rapid rise at small W might be indicative of a pointlike contribution.

Preliminary data [282] from the TASSO group are also shown. Note, that these data have a systamatic error of 25% in addition to the statistical error shown.

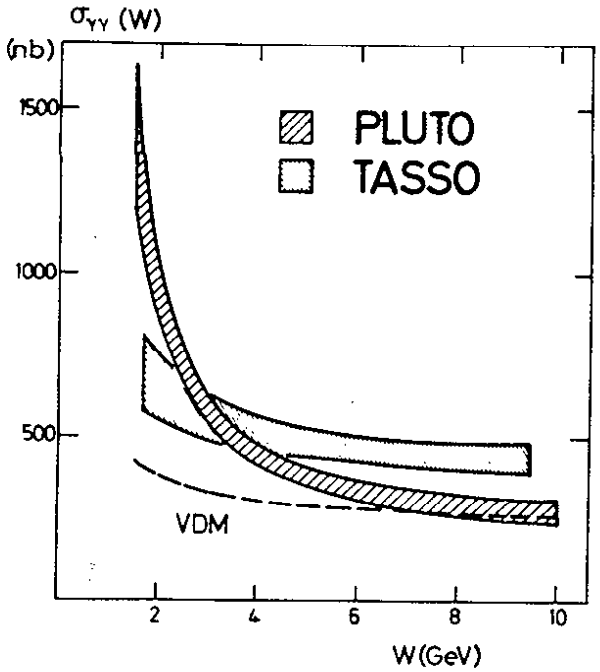

Fig. 8.9
The total cross section for $\gamma\gamma \to$ hadrons as measured by PLUTO plotted versus the $\gamma\gamma$ c.m. energy. Preliminary TASSO data are also shown.

8.4 Evidence for a pointlike coupling in $\gamma\gamma \to$ hadrons

The pointlike contribution (Fig. 8.7) might show up more clearly in the transverse momentum distribution of the hadrons at large values of p_T where the hadronlike contribution is very small.

The TASSO group [283] selected events with a tagged electron between 24 and 60 mrad depositing at least 4 GeV in the shower counter. There should be at least three charged particles observed in the inner detector, one with $p_T > 0.3$ GeV/c, two and more with $p_T > 0.2$ GeV/c. A total of 1125 events with an average c.m. energy of 6.1 GeV satisfied the criteria.

The cross section $d\sigma/dp_T^2$ is plotted in Fig. 8.10. The data show a steep exponential drop at small $p_\perp$ which flattens out for $p_\perp \gtrsim 1.5$ GeV/c.

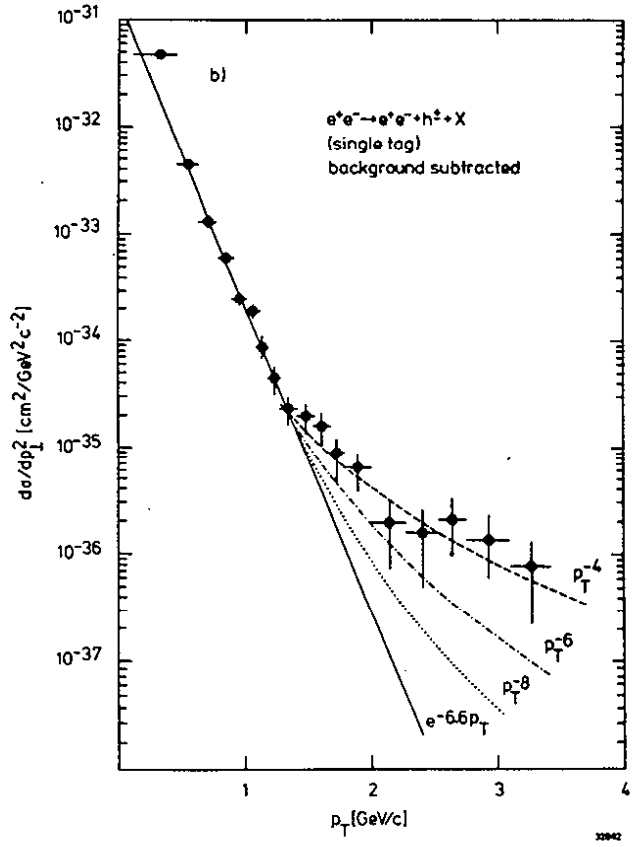

Fig. 8.10

The differential cross section $d\sigma/d^2_{p_\perp}$ plotted versus $p_\perp$. The data are from TASSO.

A fit to the data of the form $C_1 \exp(a\ p_T) + C_2(p_\perp^b)$ gave $a = -7.4 \pm 0.3$ GeV and $b = -3.87 \pm 0.6$ GeV. This should be compared to pp interactions where the produced pion spectrum falls exponentially as $\exp(-a\ p_T)$ with $6\ \text{GeV}^{-1} \leq a \leq 7\ \text{GeV}^{-1}$. This cross section always falls faster than p_T^{-8} and approaches this value only at large c.m. energies. Secondary hadrons from $\gamma\gamma$ collisions and pp interactions have a similar steep exponential $p_\perp$ dependence at low values of $p_\perp$. However, the two distributions are markedly different at large values of $p_\perp$, the $p_\perp$ distributions of hadrons from $\gamma\gamma$ collisions have a break around $p_\perp \simeq 2$ GeV/c with a long tail extending to large values of $p_\perp$. The hadrons at large $p_\perp$ are thus not produced by the hadronlike piece of the photon. Note that the pointlike diagram in Fig. 8.7 predicts the p_T^{-4} dependence observed.

The pointlike diagram leads to jets which are back to back in the $\gamma\gamma$ c.m. system. Due to the Lorentz boost of the $\gamma\gamma$ system the hadrons will in general be focused forward and backward along the jet direction yielding two non collinear hadron jets. An example of a $\gamma\gamma \to q\bar{q}$ candidate event is shown in Fig. 8.11.

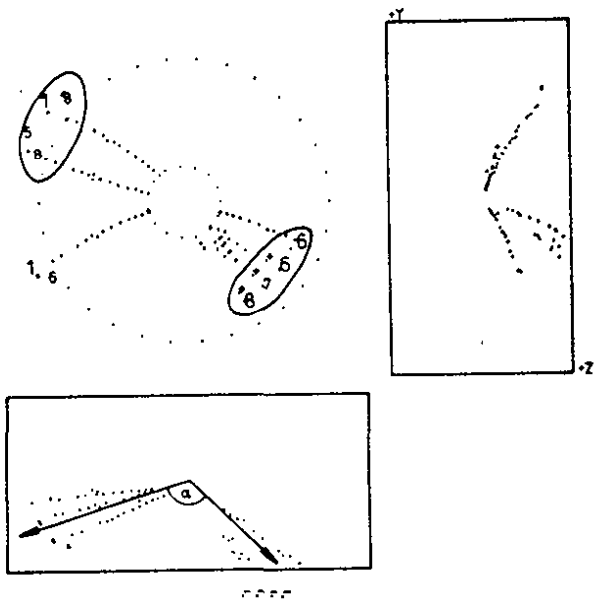

Fig. 8.11 - A candidate event for $\gamma\gamma \to q\bar{q} \to$ hadrons observed by PLUTO.

Two procedures have been used to search for acollinear jet events in $\gamma\gamma$ collisions. In the first method all particles were divided into two groups C_1 and C_2 and a quantity twoplicity T_2 defined:

$$8.8 \qquad T_2 = \text{Max} \frac{\left|\sum_{i\varepsilon C_1} \vec{P}_i\right| + \left|\sum_{i\varepsilon C_2} \vec{P}_2\right|}{\sum_{\text{all } i} |\vec{P}_i|}$$

i.e. the thrust of event is maximized using two independent axes. This method[284] has been used by PLUTO and by TASSO. In the second method jets are defined as particle clusters. In this method particles spaced within 30^o were combined into preclusters and preclusters spaced within 45^o were combined into clusters. Clusters which consist of at least two particles and a total energy of 2 GeV or more are called jets. The events are classified as 1 jet, 2 jets or more than 2 jet events. This method has been used by JADE[285].

The PLUTO and TASSO groups have evaluated the mean p_T of the hadrons with respect to the jet axis as defined above. Both groups found a value of 300 MeV/c consistant with the value measured in $e^+e^- \to q\bar{q} \to$ hadrons.

The transverse momentum distribution of jets with respect to the beam axis (PLUTO and TASSO) or the direction of the c.m. system (JADE) is plotted in Fig. 8.12 a,b,c.

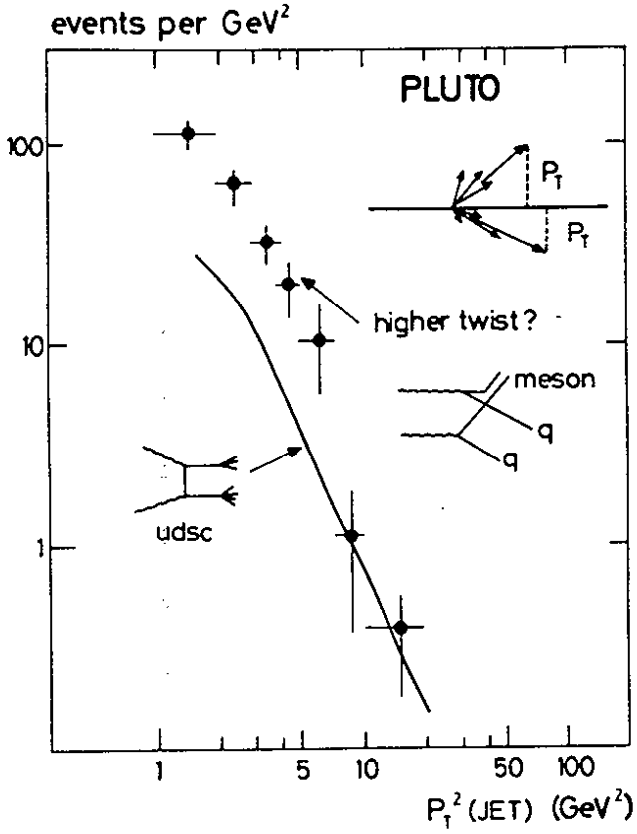

a)

Fig. 8.12
The transverse momentum distribution of the jets as observed by PLUTO, TASSO and JADE. The prediction based on
$\sigma(\gamma\gamma \to q\bar{q}) = R_{\gamma\gamma} \cdot \sigma(\gamma\gamma \to \mu^+\mu^-)$
with $R_{\gamma\gamma} = 3 \cdot \Sigma_{u,d,s,c} e^4 = 34/27$
is also shown.

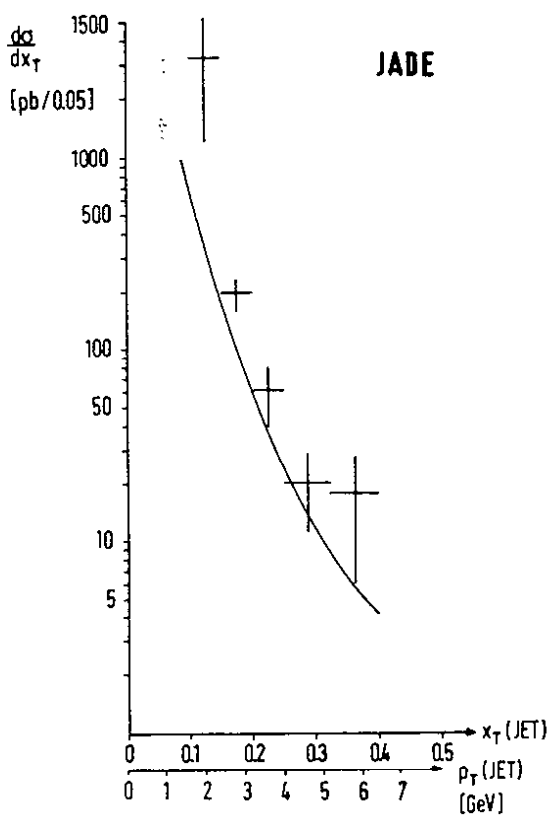

c)

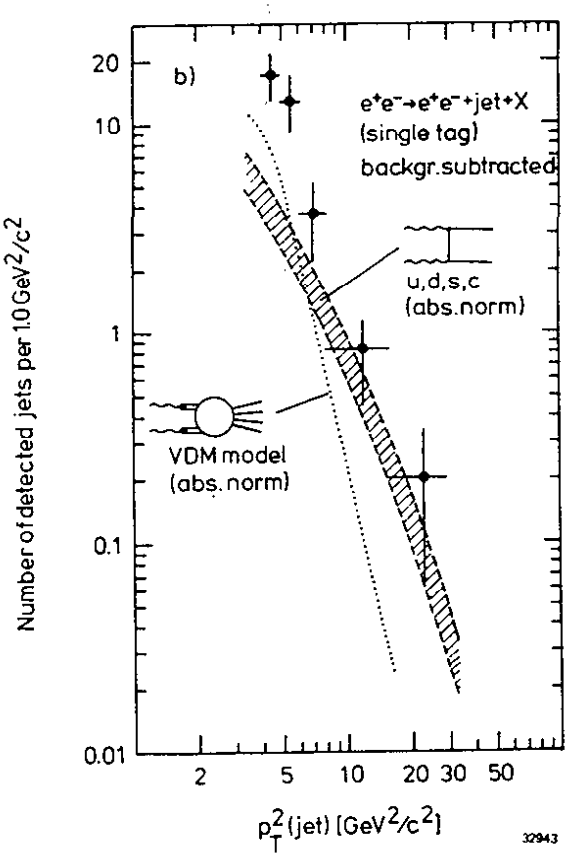

b)

The masses of the light quarks are not important at large $p_\perp$ and we expect

$$8.9 \qquad R_{\gamma\gamma} = \frac{\sigma(\gamma\gamma \to q\bar{q})}{\sigma(\gamma\gamma \to \mu^+\mu^-)} = 3 \sum_i e_i^4 = 34/27 \text{ at large } p_\perp .$$

The cross section based on this prediction including u, d, s and c quarks is also shown in Fig. 8.12. The data seem to approach the predicted cross section from above and are consistent with the prediction at large values of $p_\perp$.

The data at large $p_\perp$ are indeed consistent with resulting from a point-like component of the photon. However, at such low energies hadron jets are not well defined on an event to event basis. Also the processes[280] shown in Fig. 8.13 can contribute to large $p_\perp$ jets. However, the first process is expected to be smaller and the second process will lead to a $1/p_\perp^6$ behaviour which seems excluded as the sole source of large $p_\perp$ $\gamma\gamma$-events.

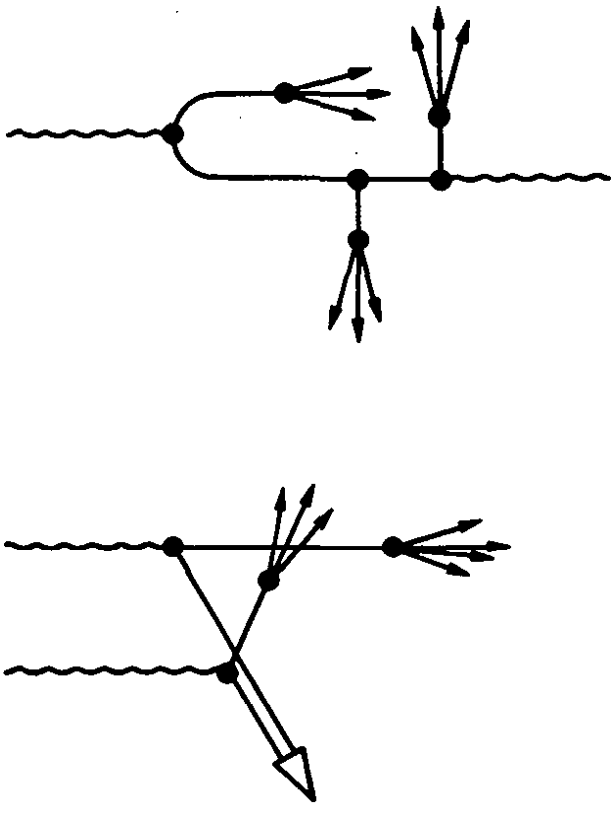

Fig. 8.13
Two possible processes resulting in large $p_\perp$ jets.

8.5 Electron Scattering on a photon target

The PLUTO group has now completed [286] the analysis of their large Q^2 data on inelastic electron photon scattering $e^+e^- \rightarrow$ hadrons. The process is shown in Fig. 8.14. In this recation they measure the direction and the

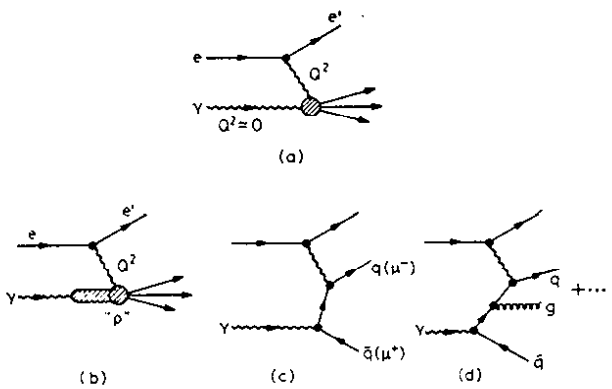

Fig. 8.14

Diagrams contributing to $e\gamma \rightarrow e'$ hadrons.

energy of one of the outgoing leptons thus defining Q^2 and ν of the virtual photon. The second electron is untagged resulting in a nearly real transversely polarized target photon. The data were selected using the following cuts: the tagged electron (positron) should scatter between 100 mrad and 250 mrad and deposit at least 8 GeV in the tagging counter. The corresponding Q^2 value should be greater than 1 $(GeV/c)^2$. Less than 4 GeV should be deposited in the tagging counters on the opposite side of the interaction point. At least three hadrons with a visible invariant mass $W_{vis} > 0.75$ GeV should be observed in the central detector. These cuts resulted in 117 events

for an integrated luminosity of 2500 nb^{-1} at an average beam energy of 15.5 GeV. Beam gas scattering, annihilation events and inelastic Compton scattering e(e $\gamma \rightarrow$ e X) contributes an estimated background of 6 events resulting in a final data sample of 111 events. The data have not been radiatively correcteed. However, this correction is expected to be small.

The value of $\sigma_t + \varepsilon\sigma_\ell$ extracted from these data are plotted versus Q^2 in Fig. 8.15 together with data at lower values of Q^2 discussed above. The solid line is the vector dominance prediction using a simple ρ pole:

8.10 $$\sigma_t(Q^2, W_{vis}) = \frac{\sigma\,(W_{vis})}{(1 + Q^2/m_\rho^2)^2}$$

The data are in agreement with the VDM model for Q^2 values below 1 $(GeV/c)^2$, but the observed cross section is well above the prediction at higher values of Q^2 indicating the presence of a hard component.

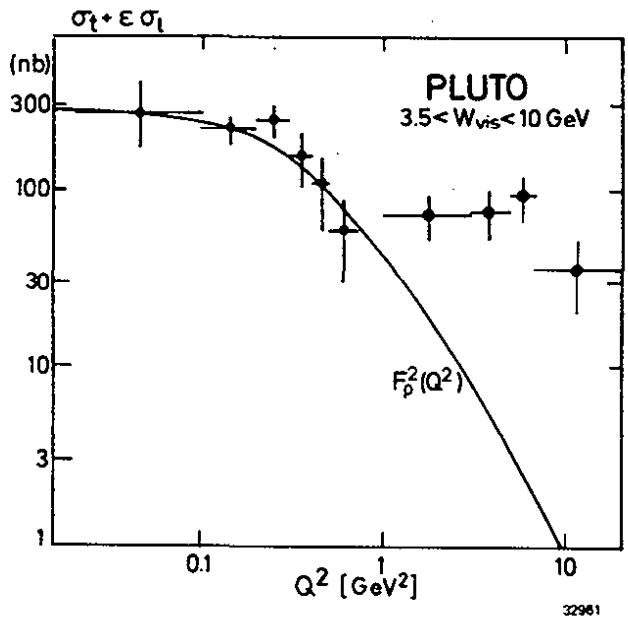

Fig. 8.15
The cross section for $\gamma\gamma$ as a function of Q^2 for a fixed cut on visible energy. The data are from the PLUTO Collaboration. The solid line represents the ρ formfactor

$$\left(\frac{m_\rho^2}{m_\rho^2+Q^2}\right).$$

The data for $Q^2 > 1$ (GeV/c)^2 were analyzed in terms of deep inelastic electron-photon scattering[287]. Deep inelastic electron-photon scattering can be parametrized in terms of three structure functions. $F_L(x, Q^2)$, $F_T(x, Q^2)$ and $F_3(x, Q^2 \cdot F_L(x, Q^2)$ and $F_T(x, Q^2)$ correspond to the longitudinal and transverse polarization vector of the virtual photon, $F_3(x, Q^2)$ is the transverse polarization vector of the target photon in the scattering plane and $x = Q^2/(Q^2 + W^2)$. $F_3(x, Q^2)$ will average to zero since the scattering plane was not determined. The cross section for $e\gamma \to e X$ with x and $y = 1 - (E_1'/E) \cos^2\theta_{1/2}$ as variables is given by:

$$8.11 \quad \frac{d\sigma(e\gamma \to eX)}{dx\, dy} = \frac{16\pi\alpha^2\, EE_\gamma}{Q^4} \left((1-y)\, F_2(x,Q^2) + xy^2\, F_1(x,Q^2) \right)$$

with $F_2(x,Q^2) = 2x\, F_T(x,Q^2) + F_L(x,Q^2)$. The data can be analyzed in terms of $F_2(x,Q^2)$ only, since x^2y averaged over the acceptance is rather small.

$$8.12 \quad \frac{d\sigma(e\gamma \to eX)}{dx\, dy} = \frac{16\pi\, \alpha^2\, EE}{Q^2} \quad (1-y)\, F_2(x,Q^2) \; .$$

It is necessary to convert the measured quantities x_{vis} and W_{vis} into x and W in order to extract the experimental value of $F_2(x,Q^2)$ from the data. This can only be done assuming a model for hadron production in $e\gamma \to \gamma X$. Various models give consistent results and the measured value of $F_2(x,Q^2)$ normalized to α is plotted in Fig. 8.16a versus Q^2. $F_2(x,Q^2)/\alpha$ has changed somewhat from the earlier evaluation and is more consistent with a constant value of 0.35. The average Q^2 value is 5 (GeV/c)^2 and its x dependence is shown in Fig. 8.16.

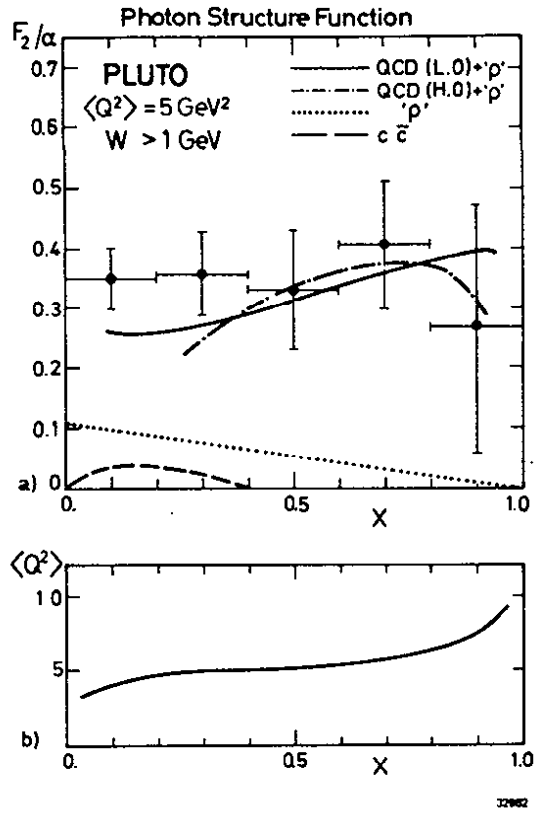

Fig. 8.16
a) The photon structure function $F_2(x)/\alpha$. The data are averaged over Q^2 values between 1 and 15 GeV^2. The dotted line represents the contribution from the hadronic part of the photon including u,d, and s quarks. The additional contribution from c quarks is shown as the dashed line. The solid line shows the pointlike contribution to $F_2(\alpha)/\alpha$ in leading order QCD will Λ = 200 MeV (u,d,s quarks). The dashed-dotted curve is the QCD computation including higher order.
b) Shows the correlation between the average value of Q^2 and x.

Both the hadronlike part and the pointlike part of the photon contribute to $F_2(x,Q^2)$.

In the hadronlike part the photon transforms into a vector meson and the virtual photon interacts with the quarks in the vector meson analogous to lepton hadron scattering. This contribution cannot be estimated from first principles, however, it will have a x dependence similar to that observed in the structure function of the pion and its evolution with Q^2 can be predicted. The PLUTO group uses

8.13 $$F_{2\,\rho} \simeq \frac{\alpha}{f_\rho^2/4\pi} \cdot 1/4\,(1-x)\,.$$

This contribution, shown as the dotted curve in Fig. 8.16 can be increased by a factor 1.5 by including the contribution from the ϕ. The hadron part of the photons contributes mainly at low x and it is clear that the bulk of the observed formfactor must be of a different origin.

The pointlike contribution can be computed in all orders of perturbative theory. The simple quanta box diagram leads to

8.14 $$F_2,box = \alpha/\pi \; e^4(x(x^2 + (1-x)^2) \ln W^2/m_q^2 + 4x^2 (1-x))$$

Gluon corrections modify this to

8.15 $$F_{2,LO} = h(x) \cdot \ln Q^2 / \Lambda^2$$

h(x) has been evaluated by many authors. The result for u, d and s quarks with Λ = 0.2 GeV/c and including the ρ contribution is shown as the dotted line. The agreement is good and can be improved by including the contribution from the charmed quarks. Its contribution evaluated, using the quark box diagram and m_c = 1.0 GeV, is shown as the dashed line.

QCD correction beyond the leading order have been calculated [288] and the results are also plotted as the dashed-dotted curve in Fig. 8.16. These corrections mainly reduce the predicted value at large and small values of x and charges the formfactor and little at for medium x value.

Since the QCD higher order contribution is well behaved at medium x values a measurement of the F_2 formfactor in the region as a function of Q^2 may afford a precise determination of Λ without some of the difficulties which beset its determination in lepton-hadron interactions.

9. Deep Inelastic Lepton-Hadron Interaction

The properties of spacelike currents, both electromagnetic and weak, have been determined from measurements of deep inelastic lepton-nucleon or neutrino-electron interactions. The findings, discussed in chapter 3, are in full agreement with the standard picture, indeed the neutral weak current was discovered in such experiments.

The well understood electroweak current is ideally suited to probe the nucleon at small distances and such studies have resulted in several important discoveries. The existence of pointlike hadronic constituents was first revealed[25,289] in electron-nucleon collisions. Deep inelastic neutrino-hadron experiments[22,290-293] showed that these constituents can be identified with the quarks used to explain the quantum numbers of the hadrons. Measurements of the quark momentum distribution demonstrated that only about one half of the nucleon momentum is carried by quarks - the other half by particles which have neither electromagnetic nor weak interactions. This was the first, albeit indirect evidence, for gluons. The variation of the structure functions with Q^2 for fixed x, i.e. the scaling violation, is in agreement with the QCD predictions.

In the first part of this chapter we will interpret the nucleon structure - as observed in deep inelastic lepton-hadron interactions - in terms of the quark model.

Any field theory of strong interactions predict that the momentum distributions of the quarks should vary with Q^2 at fixed x.

In the second part we will discuss the observed scaling violation pattern and compare the data to QCD predictions.

These topics have been the subject of numerous review talks. A more complete discussion including a complete list of references can be found in reference 294.

9.1. Cross sections and kinematics

The general form of the lepton-nucleon interactions is shown in Fig. 9.1.

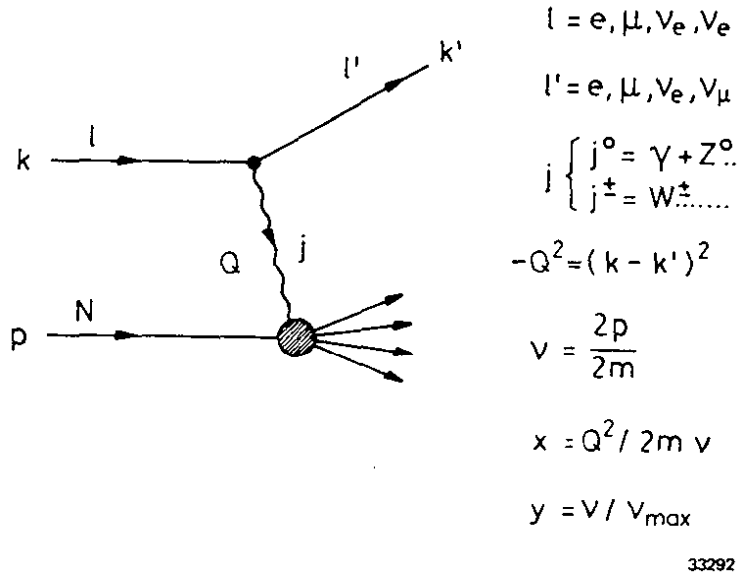

Fig. 9.1 - Diagram for lepton-hadron scattering.

The incoming lepton ℓ with energy E interacts with the hadron via a neutral ($\gamma + Z^0$) or charged ($W^{\pm}$) spacelike current. This current has the four momentum squared

$$9.1 \qquad Q^2 = -(k - k')^2 \simeq 4E_\ell E_\ell \sin^2\theta/2 \; ;$$

The energy transfer ν measured in the rest system of the hadrons is given by:

9.2 $$\nu = \frac{2p\,Q}{2m} = E_\ell - E_{\ell'} = E_h - m.$$

E_ℓ and $E_{\ell'}$ are the energies of the incident and scattered lepton, θ is the scattering angle in the laboratory system, and p is the four-momentum of the target nucleon and m its mass. The mass W of the final hadron system is given by:

9.3 $$W^2 = Q^2 \left(\frac{2\,m\,\nu}{Q^2} - 1 \right) + m^2 .$$

The properties of the current are thus determined by the upper vertex- i.e. by the momentum of the incident lepton and the momentum and angle of the scattered lepton. Such inclusive experiments, summing over all final state hadrons, determines the total absorption cross section for a virtual current of mass Q^2 and energy ν on a nucleon target. This process can be parametrized for an electromagnetic current in terms of two formfactors F_1 and F_2 corresponding to the longitudinal and transverse polarization of the virtual photon. The absorption cross section in the case of a weak charged or neutral current can be parametrized in terms of the form factors F_1, F_2 and F_3 for the three helicity states of the current. F_3 is the parity violating formfactor forbidden in purely electromagnetic interactions.

The formfactors F_1, F_2 and F_3 are in general functions of two variables i.e. Q^2 and ν. Besides Q^2 and ν also the normalized variables x, y or a combination of Q^2, ν, x or y can be used. The scaled variables x and y are defined as follows:

9.4 $$x = Q^2 / 2pQ = Q^2 / 2 m \nu$$
$$y = 2pQ / s = \nu / E .$$

If the current interacts with a single pointlike constituent - the parton - then the formfactors scale[295] i.e. they are functions of only a single variable x. In any field theory this scaling behaviour will be broken resulting in formfactors which for fixed x vary only slowly with Q^2. It has therefore become customary to use x and Q^2 as variables.

The differential cross section for deep inelastic electron (muon) scattering on a nucleon target (one photon exchange) is given by:

9.5 $$\frac{d\sigma^{\ell^\pm}}{dxdy} = \frac{4\pi \alpha^2 s}{Q^4} \{ F_2^\ell (x,Q^2) (1-y + \frac{mxy}{2E}) + 2 x F_1 (x,Q^2) y^2/2 \}$$

In this formula we have neglected the neutral weak current contribution. The weak effects are on the order of $10^{-4} Q^2$ and are in general negligible at present energies. The only exception is the parity violating effect observed in e d scattering and discussed above.

Neutrinos can interact with matter only through the weak interaction. The different couplings of the two vector bosons, the $W^\pm$ and the Z^o, have already been discussed in chapter 3. In terms of structure functions the differential cross section for the reaction

$$\nu (\bar{\nu}) + N \rightarrow \mu^\pm + X$$

can be written as:

$$9.6 \quad \left.\frac{d^2\sigma^{\nu\bar{\nu}}}{dxdy}\right|_{cc} = \frac{G_F^2 M_N s}{2\left(1+\frac{Q^2}{M_W^2}\right)^2}\{[F_2^{\nu\bar{\nu}}(x,Q^2)\,(1-y-mxy/2E_\ell) + 2x F_1^{\nu\bar{\nu}}(x,Q^2)\, y^2/2 \pm \frac{(1-(1-y)^2)}{2} x F_3^{\nu\bar{\nu}}(x,Q^2)]\}$$

F_i^{ν} and $F_i^{\bar{\nu}}$ are the formfactors for neutrino, respectively antineutrino induced charged current reactions on a nucleon target. Note, that the relative sign of the term proportional to $x F_3$ changes from neutrinos to antineutrinos. G_F is the Fermi constant.

The cross section $\left(\frac{d^2\sigma^{\nu\bar{\nu}}}{dxdy}\right)_{NC}$ for the neutral current interaction $(\bar{\nu}) + N \to \nu\ (\bar{\nu}) + X$ can be written completely analogously to Eq. 9.6.

The processes discussed above are in principle described by 28 different structure functions: Four for the charged leptons (on proton or neutron), six for the neutrinos (charged current), six for the antineutrinos (charged currents) and accordingly twelve for the (anti)neutrino neutral current interactions. However, simple relations between these functions are predicted by the quark parton model[296] (and the Glashow-Weinberg-Salam model for the neutral currents). These relations reduce the number of independent functions to two.

Let us first assume that the quark with mass m_q carries a fractional momentum μ. In this case:

$$(\mu + (k-k'))^2 = m_q^2 ,$$

and neglecting all masses: $\mu = Q^2 / 2 m \nu = x$.

The variable x can be identified with the fractional momentum carried by the quarks in the nucleon.

The physical interpretation of the formfactors $2xF_1(x,Q^2)$ and $F_2(x,Q^2)$ can be clarified [294] by evaluating the general cross section (eq. 9.5) for some simple cases.

The Rutherford cross section is obtained from eq. 9.5 in the limit $\theta \to 0$ and $y \to 0$:

$$9.7 \qquad \frac{d\sigma}{dQ^2} = \frac{4\pi\alpha^2}{Q^4} \int_0^1 \frac{F_2(x)}{x}\, dx$$

A comparison with the Rutherford formula shows that $\int_0^1 \frac{F_2(x)}{x}\, dx$ measures $\sum_i e_i^2$, where e_i is the charge of the constituents participating.

Rewriting eq. 9.5 in terms of the lepton scattering angle θ yields:

$$9.8 \qquad \frac{d^2\sigma}{dq^2 dx} = \frac{4\pi\,\alpha^2}{q^4} \frac{F_2(x)}{x} \left(\cos^2\theta/2 + \frac{2x\,F_1(x)}{F_2(x)} \cdot \frac{q^2}{2M^2x^2} \sin^2\theta/2 \right)$$

This form can be directly compared to the cross section for $e + \mu \to e + \mu$:

$$9.9 \qquad \frac{d\sigma}{dq^2} = \frac{4\pi\alpha^2}{q^4} \cdot \frac{E'}{E} \left(\cos^2\theta/2 + \frac{q^2}{2m^2} \sin^2\theta/2 \right)$$

The comparison yields the Callan-Gross relation for spin 1/2 partons:

9.10 $$2 \times F_1(x) = F_2(x)$$

$F_1(x) = 0$ for scalar partons.

Thus the spin of the constituents can be determined from a measurement of $2 \times F_1(x) / F_2(x)$.

To see the significance of $x F_3(x)$ eq. 9.6 is written as:

9.11 $$\frac{d\sigma^{\nu,\bar{\nu}}}{dydx} = \frac{G^2 s}{2\pi} \left[\frac{F_2(x) \pm x F_3(x)}{2} + \frac{F_2(x) \mp F_3(x)}{2} (1-y)^2 \right]$$

This equation was obtained from eq. 9.8 using the Callan-Gross relation and neglecting the term $mxy/2E_\ell$.

Eq. 9.11 can then be compared with the cross section for $\nu_e e \to \nu_e e$ and $\bar{\nu}_e e \to \bar{\nu}_e e$ discussed in chapter 3.

9.12 $$\frac{d\sigma}{dy}(\nu_e e^- \to \nu_e e^-) = \frac{d\sigma}{dy}(\bar{\nu}_e e^+ \to \bar{\nu}_e e^+) = \frac{G_F^2 \cdot s}{2\pi}$$

$$\frac{d\sigma}{dy}(\bar{\nu}_e e^- \to \bar{\nu}_e e^-) = \frac{d\sigma}{dy}(\nu_e e^+ \to \nu_e e^+) = \frac{G_F^2 \cdot s}{2\pi} (1-y)^2$$

Comparing eqs. 9.11 and 9.12 result in the following relationships:

9.13 $$F_2(x) = 2x (q(x) + \bar{q}(x))$$
$$xF_3(x) = 2x (q(x) - \bar{q}(x))$$

$q(x)$ and $(\bar{q}(x))$ denotes the parton (antiparton) densities as function of momentum. $xF_3(x)$ thus counts the difference between partons and antipartons in the nucleon.

It is clear from the discussion above that the properties of the constituents and their density distributions can be determined from deep inelastic experiments. We will now consider the data.

9.2 Comparison of the data with the quark-parton model

9.2.1 The total neutrino-hadron cross section

As we have seen above the formfactors scale if the current interacts directly with pointlike constituents. In this case the total cross section for neutrin-hadron interactions, obtained by integrating eq. 9.6 over x and y, increases linearly with the incident neutrino energy. The measured cross section, divided by the neutrino energy is plotted in Fig. 9.2 versus neutrino energy for both incident neutrinos and antineutrinos. The slope

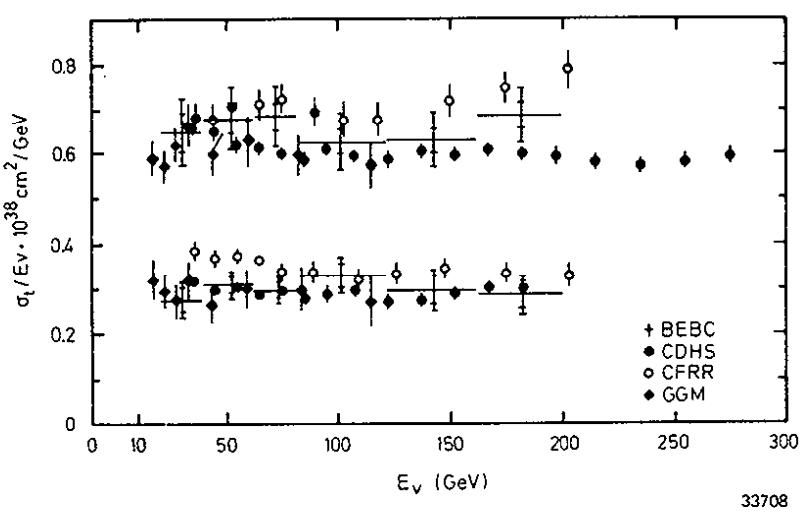

Fig. 9.2 - The slopes of the total neutrino and antineutrino cross sections plotted versus incident energy (Ref. 297).

is clearly constant over a large energy range providing striking evidence for the pointlike nature of the interactions. The cross section ratio $\sigma(\nu N) / \sigma(\bar{\nu}N)$ is of the order of 1/2. It follows from eqs. 9.11 and 9.13 that a nucleon made of only quarks yields $\sigma(\bar{\nu}N) / \sigma(\nu N) = 1/3$.

Table 9.1 - Total cross sections on isoscalar targets
$\sigma_{tot} / E_\nu \times 10^{-38}$ cm^2/GeV

Experiment	Beam (GeV)	$\bar{\nu}$	ν	$\bar{\nu}/\nu$	Ref.:
CITFR	NB 45-225	0.29 ± 0.015	0.61 ± 0.03	-	298
CDHS	NB 30-200	0.30 ± 0.02	0.62 ± 0.05	0.48 ± 0.02	293
BEBC	NB 20-200	0.305 ± 0.016	0.663± 0.032	0.463± 0.025	299
CHARM	NB 20-200	0.301 ± 0.018	0.604± 0.032	0.498± 0.019	63
CFRR	NB 40-220	0.371 ± 0.020	0.719± 0.037	0.517± 0.020	64
GGM	WB 10-150	0.29 ± 0.04	0.62 ± 0.08	0.47 ± 0.09	300

The systematic error varies between 4% and 10%.

The cross sections measured by CFRR is significantly above the values reported by other groups. This discrepancy is reflected in all structure functions, integrals and ratios. The absolute values of the neutrino structure functions have to be taken with some care as long as the source of the discripancy remains unknown. Fortunately all groups agree on the value for the ratio of antineutrino to neutrino cross sections. Thus quantities which involve the neutrino and antineutrino data with relative normalizations are not affected.

9.2.2 The spin of the constituents

The spin of the constituents can be determined from a measurement of the formfactors $2xF_1(x)$ and $F_2(x)$. Spin 1/2 constituents satisfy the Callan-Gross relation $2x\,F_1(x) = F_2(x)$ whereas scalar constituents yield $2x\,F_1(x) = 0$.

Usually the ratio $R = \sigma_L/\sigma_T$ is determined in charged lepton nucleon interactions. σ_L and σ_T are the cross sections for longitudinal and transversly polarized photons. In the Bjorken limit ($Q^2 \to \infty$ $\nu \to \infty$, $x = Q^2/2m\nu$ = constant, i.e. $Q^2/\nu^2 \to 0$) σ_L vanishes for spin 1/2 constituents and σ_T vanishes for scalar constituents. R can also be written in terms of the formfactors $2x\,F_1(x)$ and $F_2(x)$ as:

$$9.14 \qquad R = \sigma_L/\sigma_T = \frac{F_2(x)}{2x\,F_1(x)} \cdot (1 + Q^2/\nu^2) - 1$$

An equivalent definition is often used:

$$9.15 \qquad R' = \frac{F_2(x) - 2x\,F_1(x)}{F_2(x)} = R\,(1 + Q^2/\nu^2) - Q^2/\nu^2 \,.$$

The definitions are identical in the scaling limit and lead to $R = R' = 0$ for spin 1/2 constituents and $R = R' = \infty$ for scalar constituents.

It is rather difficult to determine $R(x,Q^2)$. A measurement of the cross section at a particular value of x,Q^2 gives information only on a combination of the formfactors. To disentangle the formfactors requires cross section measurements at different lepton energies.

Because of its importance several groups have determined R (or R'). The results are summarized in Table 9.2 and some recent data[307] from the CDHS Collaboration are plotted in Fig. 9.3. The value of R (averaged over Q^2) is measured as a function of ν. The Q^2 values are of the order of 20 GeV^2/c^2. R is small and for higher ν clearly compatible with zero. The curve, labelled "QCD" is a QCD calculation and will be discussed below.

Table 9.2 Average value of R (R')

Experiment	Reaction	R	R'	Ref.
SLAC	ep	$0.21 \pm 0.1o$		301
SLAC-MIT	ed	0.17 ± 0.07		302
CHIO	μp	0.38 ± 0.38		28
EMC (prelim.)	μp	0.03 ± 0.10		303
	μN	-0.13 ± 0.19		304
GGM	νN		0.32 ± 0.15	305
HPWFOR	νN		0.11 ± 0.07 *	306
CDHS	νN	0.10 ± 0.07 *		307
BEBC	νN		0.04 ± 0.16	299
FIIM	νN		0.03 ± 0.12	308
CHARM	νN (NC)		0.01 ± 0.11 *	309

* radiatively corrected neutrino data.

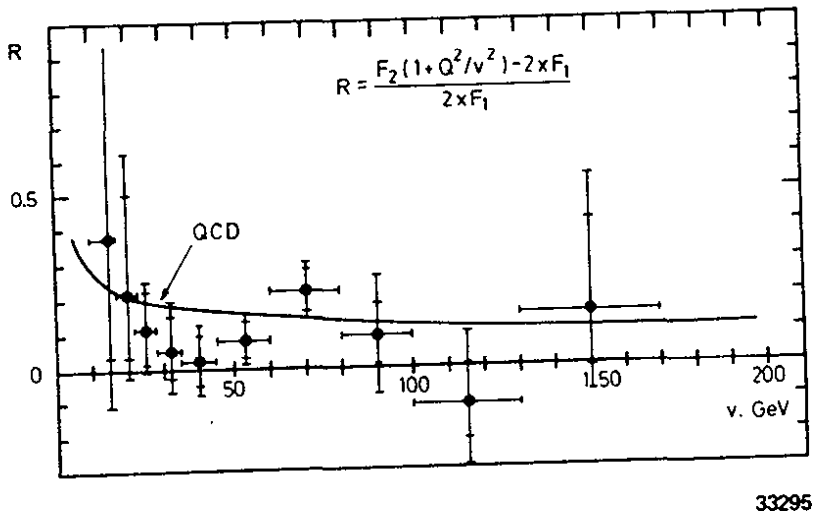

Fig. 9.3 - $R = \sigma_L/\sigma_T$ as measured by the CDHS Collaboration in neutrino-hadron interactions plotted versus ν. The QCD prediction is shown by the solid curve.

With the exception of the low Q^2 Gargamelle and SLAC data, all experiments are roughly compatible with R = 0, but a careful study of the systematic errors is needed in such an analysis. Note, that from the neutrino experiments only the results marked with a "*" have been radiatively corrected. The correction is typically of the order of $\Delta R \simeq -0.05$. The measurements have been done at somewhat different Q^2, typically around $Q^2 = 25\ GeV^2/c^2$ with the exception of the quoted two low Q^2 experiments.

The data in Table 9.2 show that R is in general small, and hence the spin of the parton is 1/2.

9.2.3 Structure functions in the quark-parton model

It is of course natural to identify partons with quarks and in this chapter we will write the formfactors in terms of the quark (antiquark) distribution functions. $u(x)\,dx$ is the probability of finding an "up" quark with fractional momentum between x and $x + dx$ in a proton and a similar notation is used for the other flavours. Note, that by isospin invariance $u(x)\,dx$ is also the probability of finding a "down" quark in a neutron. Present energies are too small for significant contributions from the "beauty" or "truth" quark and we will hence limit the discussion to u, d, s and c quarks.

The structure functions measured in charged lepton nucleon interactions can be written in terms of the quark distribution functions according to eq. 9.13 as:

$$9.16 \quad \begin{aligned} F_2^{\ell p}(x) = 2x\,F_1^{\ell p}(x) &= \frac{4}{9}\,x\,\{\,u + \bar{u} + c + \bar{c}\,\} + \frac{1}{9}\,x\,\{\,d + \bar{d} + s + \bar{s}\,\} \\ F_2^{\ell n}(x) = 2x\,F_1^{\ell n}(x) &= \frac{4}{9}\,x\,\{\,d + \bar{d} + c + \bar{c}\,\} + \frac{1}{9}\,x\,\{\,u + \bar{u} + s + \bar{s}\,\} \end{aligned}$$

The weak interaction is slightly more complicated since not the quarks but rather some linear combination are the eigenstates of the weak interactions. The mixing angles as discussed in chapter 3 are generally believed to be of the order of the Cabibbo angle and hence small. To simplify the notation we ignore this effect.

For the charged weak current ($W^{\pm}$ exchange) the structure functions can then be written as:

$$F_2^{\nu p} = 2 \times F_1^{\nu p} = 2 \times \{ d + \bar{u} + s + \bar{c} \}$$

$$F_2^{\nu n} = 2 \times F_1^{\nu n} = 2 \times \{ u + \bar{d} + s + \bar{c} \}$$

$$F_2^{\bar{\nu} p} = 2 \times F_1^{\nu p} = 2 \times \{ u + \bar{d} + \bar{s} + c \}$$

$$F_2^{\bar{\nu} n} = 2 \times F_1^{\nu n} = 2 \times \{ d + \bar{u} + \bar{s} + c \}$$

9.17

$$F_3^{\nu p} = 2 \{ d - \bar{u} + s - \bar{c} \}$$

$$F_3^{\nu n} = 2 \{ u - \bar{d} + s - \bar{c} \}$$

$$F_3^{\bar{\nu} p} = 2 \{ u - \bar{d} - \bar{s} + c \}$$

$$F_3^{\bar{\nu} n} = 2 \{ d - \bar{u} - \bar{s} + c \}$$

The factor 2 enters, because both V and A currents contribute.

The coupling constants of the neutral current have been introduced in chapter 3. Following the notations of equation 3.28 and using the abreviations NC and CC for neutral and charged currents respectively the structure functions can be written

9.18

$$F_2(NC) = F_2(CC) \cdot (u_L^2 + d_L^2 + u_R^2 + d_R^2) + (s + \bar{s} - c - \bar{c})((d_L^2 + d_R^2) - (u_L^2 + u_R^2))$$

$$F_3(NC) = F_3(CC) \cdot ((u_L^2 + d_L^2) - (u_R^2 + d_R^2))$$

The second term in the expression for $F_2(NC)$ is expected to be small. At large values of Q^2 the probability to find a strange or charmed quark is about equal. No results on the neutral current structure functions have been published so far. The experiment is by far more difficult than the extraction of the charged current structure functions or the electromagnetic structure functions. Only the momentum of the incident neutrino and the hadronic energy and its direction of flow can be measured. Both are correlated with the momentum of the struck quark, but in a rather indirect way. The direction

of energy flow is not easy to measure, and this results in large uncertainties in Q^2. Rough comparisons [310] of the hadronic energy spectra measured in neutral and charged current reactions respectively do not reveal striking differences between the structure functions except for a scale factor. It is therefore likely, that the neutral current structure functions are indeed very similar to those seen by charged currents.

The experiments have mostly be performed on isoscalar targets. Before we turn to the data it is useful to calculate the structure functions for an equal mixture of protons and neutrons in the target by averaging over the proton and neutron structure functions

$$F_2^{\ell N} = \frac{1}{2}\,(F_2^{\ell p} + F_2^{\ell n}) = \frac{5}{18}\,x\,\{\,u + \bar{u} + d + \bar{d} + s + \bar{s} + c + \bar{c}\,\} - \frac{1}{6}\,(\,s + \bar{s} - c - \bar{c})$$

9.19
$$F_2^{\nu N} = x\,\{\,u + \bar{u} + d + \bar{d} + 2s + 2\bar{c}\,\}$$

$$F_2^{\bar{\nu} N} = x\,\{\,u + \bar{u} + d + \bar{d} + 2\bar{s} + 2c\,\}$$

$$F_3^{\nu N} = x\,\{\,u - \bar{u} + d - \bar{d} + 2s - 2\bar{c}\,\}$$

$$F_3^{\bar{\nu} N} = x\,\{\,u - \bar{u} + d - \bar{d} - 2\bar{s} + 2c\,\}$$

With the assumption of SU(4) symmetry of quark flavours, expected to hold at high values of Q^2, the sea quark distributions are all equal ($\bar{u} = \bar{d} = s = \bar{s} = c = \bar{c}$). Under these circumstances or for regions in x where the contribution of the sea is small one gets:

9.20
$$F_2^{\ell N} \approx \frac{5}{18}\,F_2^{\nu N} \approx \frac{5}{18}\,F_2^{\bar{\nu} N}$$

$$F_3^{\nu N} \approx F_3^{\bar{\nu} N}$$

The 24 different structure functions have been reduced to two universal functions. Unfortunately, a good fraction of the data is still below the charm threshold. In this case the reduced couplings due to the Kobayashi-Maskawa matrix has to be taken into account and final differences between the neutrino and antineutrino structure functions remain

$$9.21 \qquad \begin{aligned} F_2^{\nu N} - F_2^{\bar{\nu} N} &= \sin^2\theta_c \; x \; (\bar{u} + \bar{d} - u - d) \\ F_3^{\nu N} - F_3^{\bar{\nu} N} &= \sin^2\theta_c \; (4s - u - d - \bar{u} - \bar{d}) \end{aligned}$$

9.2.4 Quark distributions

The aim is to measure the x distribution of the formfactors over a wide range in y. The data must be collected at fixed values of Q^2 to exclude effects due to scaling violation. Since $xy = Q^2/s$ this implies that data must be collected over a wide range in lepton energies. The energy is of course well defined in the case of charged leptons whereas the neutrino energy, even in the best case, is rather poorly known.

The kinematical region available in x and Q^2 (y) for various experiments is illustrated in Fig. 9.4. The upper limits on Q^2 for fixed x is determined by the available lepton energy. The quickly worsening energy resolution at low hadron energies defines the lower limit in Q^2. The x resolution at high x values is mainly given by the momentum measurement of the final state lepton. Bubble chambers tend to be superior in this energy region.

To extract F_2 most experiments assume R to have a small constant value. In some cases R was assumed to be a function of x with the functional form

taken either from theory or from experiments. Fig. 9.5 shows $F_2^{\mu p}$ and F_2^{ep} measured at SLAC[301,302], FNAL[28] and CERN[303]. The mean Q^2 is of the order of 10 GeV^2/c^2 in all four experiments. At high x, where the SLAC data can be compared with the other data the agreement is remarkable. At low x the CERN EMC data, with superior statistics, tend to stay below the FNAL data.

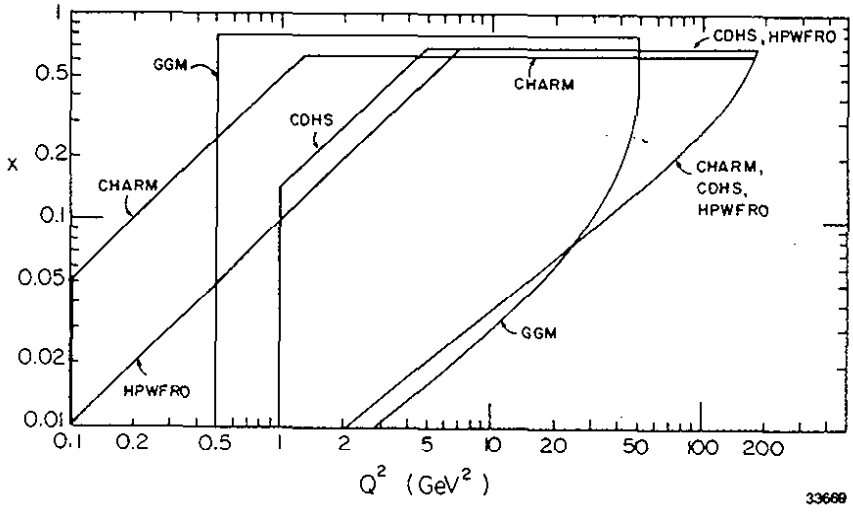

Fig. 9.4 - The kinematical region in x and Q^2 available to different experiments.

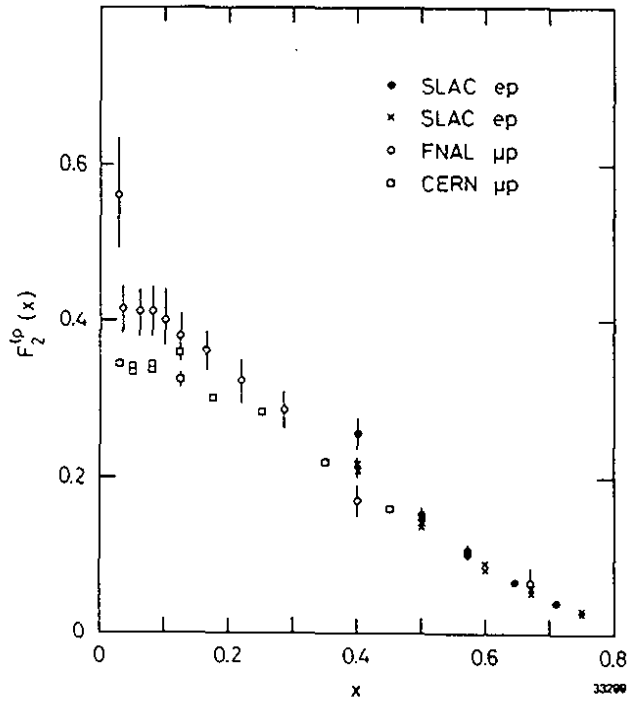

Fig. 9.5
Structure function F_2 for charged lepton cattering on protons. The average Q^2 is around 10 GeV^2/c^2.
(Data from Ref.

The form factors F_2^{ν} is determined from the sum of neutrino and anti-neutrino data which effectively cancel the x F_3 term in equation 9.6. Small model dependent corrections for the differences between the F_2^{ν}, F_3^{ν} and $F_2^{\bar{\nu}}$ and $F_3^{\bar{\nu}}$ for the various targets have been made and the data are radiatively corrected. In Fig. 9.6 neutrino data[311] on a Fe target are compared with data from three charged lepton experiments[28,302,304]. The charged lepton data have been multiplied by 18/5 following the prescription of eq. 9.20. The structure functions of the various experiments are extracted with slightly different assumption on R, but, nevertheless, the electromagnetic current and the weak charged current data agree remarkably well. To be able to relate two such different processes is a great triumph for the quark-parton model.

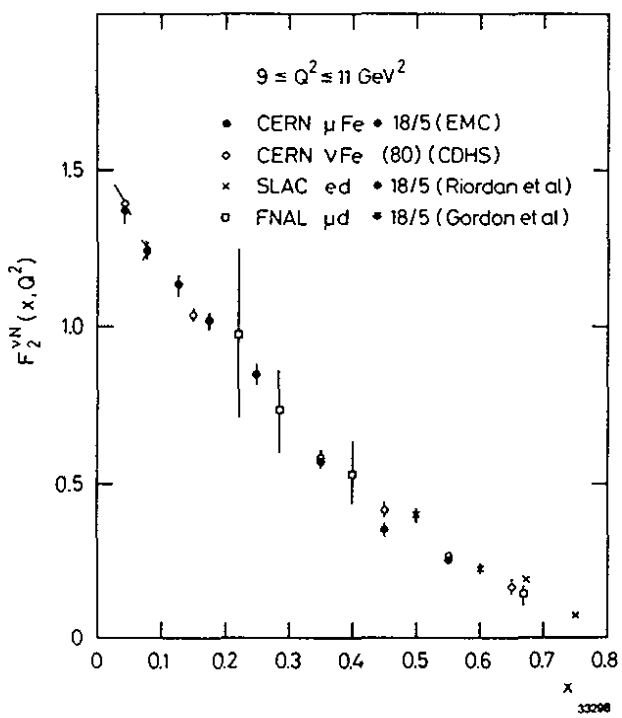

Fig. 9.6

Structure function F_2 for neutrino scattering on nucleons. The data from the charged lepton experiments are scaled by 18/5. (Data from Ref.

The structure function x F_3 appears only in neutrino scattering. This structure function is determined from the difference between the neutrino and antineutrino cross sections (eqs. 9.11, 9.13). Terms containing F_2 and 2 x F_1 cancel (up to small model dependent corrections).

The cross section difference is mainly proportional to the average

9.22 $$x\,\bar{F}_3 = 1/2\,(x\,F_3^{\nu} + x\,F_3^{\bar{\nu}})\ .$$

This average is in the QPM just the sum of the valence quark structure functions

9.23 $$\bar{F}_3^p = \bar{F}_3^n = \bar{F}_3^N = 2\,[\,u - \bar{u} + d - \bar{d}\,] + \text{small corrections}$$

Fig. 9.7 shows a recent measurement [311] of $F_2^{\nu N}(x)$ and $x\,F_3^{\nu N}(x)$ on iron together with scaled data on F_2^{ed} from SLAC [302]. The resolution in x is just sufficient to demonstrate, that $x\,F_3$ approaches zero for $x \to 0$, as one would naively guess.

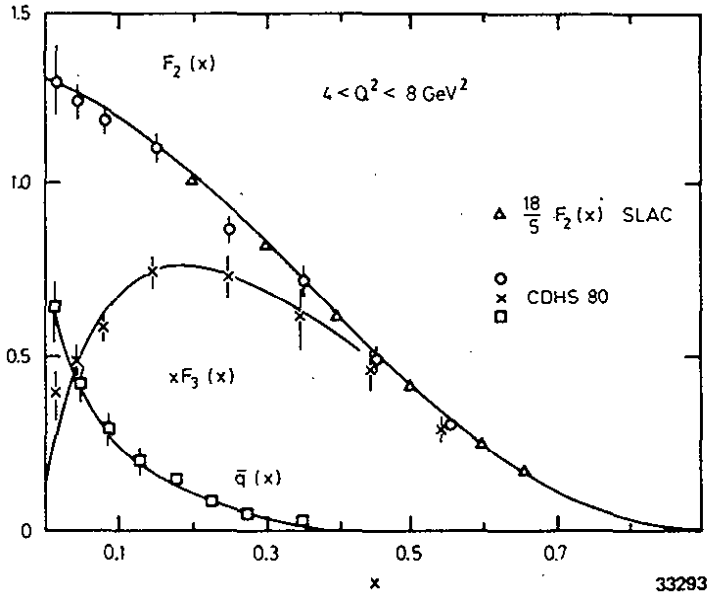

Fig. 9.7

The structure functions F_2, F_3 and the antiquarks in neutrino nucleon scattering. The sea contribution is zero beyond $x \approx 0.4$. (Data from Ref.

Looking back at the equations 9.19, one sees that the average of $F_2^{\nu N}$ and $F_2^{\bar{\nu}N}$

9.24 $$\bar{F}_2^{\nu N} = 1/2\,(F_2^{\nu N} + F_2^{\bar{\nu}N})$$

is the momentum distribution function of quarks and antiquarks inside the nucleon. The difference $F_2^{\bar{\nu}N} - x\,F_3^{\bar{\nu}N}$ is therefore the momentum distribution function of the sea quarks. This result is plotted as squares in Fig. 9.7.

One notes that the seq quarks ($\bar{q}$) are concentrated at low x values. Above x = 0.4 the sea contribution is negligible. The curves drawn are fits of the empirical form

$$x F_3 = A \cdot x^a (1-x)^b$$

$$2\bar{q} = B \cdot (1-x)^2 .$$

The results of several experiments (with slightly different experimental conditions) are summarized in Table 9.3.

Table 9.3 - Results on the shape of the structure functions

Parameter	Experiments			
	CHARM[309]	CDHS[293]	HPWF[312]	BEBC[22,291]
A	2.63 ± 0.81			
a	0.41 ± 0.11	0.5 fixed		
b	2.96 ± 0.31	3.5 ± 0.5	3.7 ± 0.1 ± 0.3	
B	0.80 ± 0.09			
c	4.93 ± 0.91	6.5 ± 0.5	4.6 ± 0.5 ± 0.6	$4.9 \,^{+\,2.7}_{-\,1.7}$

It will become clear later that the results depend on the Q^2 range. The data listed in Table 9.3 all result from experiments done in a similar kinematic region.

Information on the ratio of d to u quark distributions can be obtained by measuring the ratio $F_2^{\ell n}/F_2^{\ell p}$. This ratio can be written (Eq. 9.17) in the quark parton model as:

$$F_2^{\ell n} / F_2^{\ell p} = \frac{1 + 4\, d/u}{4 + d/u}$$

permitting a determination of the ratio d/u. Several predictions for this ratio exist[313-316]. The first measurements were reported by the SLAC MIT group[302]. The figure 9.8 shows these data together with recent measurement by the EMC Collaboration[317] in an completely different Q^2 range. The scale on the right hand side gives the ratio d/u. In the region above $x \simeq 0.4$, where the sea quark distribution is practically zero, the u quarks clearly dominate over the d quarks. Similar results are obtained [318] by comparing νp data with ep and μp data. In apparent contradiction to the naive QPM the ratio falls below 0.5 for $x > 0.4$. While the QPM is obviously failing, there are other models:

- Field and Feynman[313] predict a (1-x) behaviour with $d/u = 0$ at $x = 1$.
- Farrar and Jackson[314] predict $d/u = 0.2$ at $x = 1$ (a QCD type model)
- Close, Roberts[316], Donnachie and Landshoff[315] expect in diquark models $d/u = 1/2 \times 3/7$ at $x = 1$.

None of these models can be excluded but the Field and Feynman fit describes the data best.

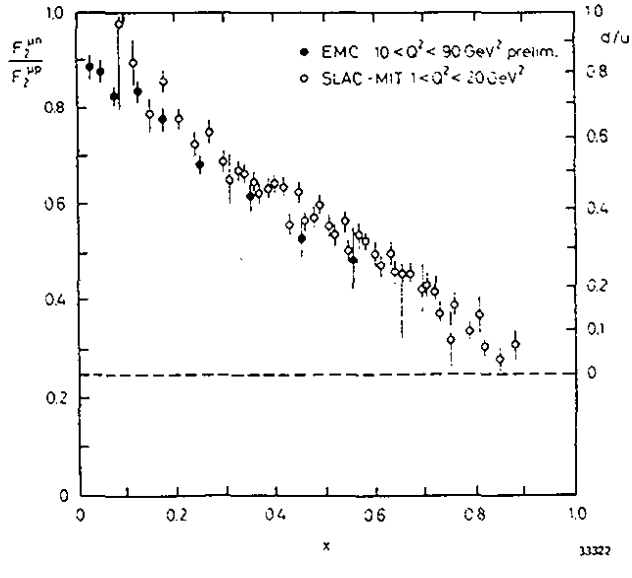

Fig. 9.8
The ratio $F_2^{\mu N}/F_2^{\mu p}$ as a function of x. This corresponds to ratio of "down" to "up" quarks indicated on the righ hand scale. The naive QPM prediction is $d/u = 1/4$ at $x = 0$.
(Data from Ref.

$\bar{F}_3(x)$ is the probability to find a valence quark with relative momentum x. In the naive quark-parton model $\int_0^1 \bar{F}_3(x)\,dx = 3$, the number of valence quarks. In practice $x\,\bar{F}_3$ is measured and the ratio $x\,\bar{F}_3/x$ is experimentally poorly defined at small x. The procedure adopted by most experiments is to integrate down to a small but variable x_{min} and extrapolate to zero. CHARM Collaboration uses a slightly different procedure:

$$\int_0^1 x\,\bar{F}_3\,dx = \begin{array}{lll} 3.2 \pm 0.5 & \text{CDHS} & (293) \\ 2.5 \pm 0.5 & \text{BEBC} & (22, 291) \\ 2.66 \pm 0.41 & \text{CHARM} & (309) \end{array}$$

It should be emphazied, that scaling violating effects have a strong influence on the result. But nevertheless, the agreement with the naive quark-parton model prediction is striking.

$\bar{F}_2^{\nu}(x)$ describes the momentum distribution of quarks and antiquarks inside the nucleon. The integral $\int_0^1 x\,\bar{F}_2^{\nu}\,dx$ therefore determines the momentum fraction carried by all objects which couple to the charged current. This sum rule can be rather well determined and the results are:

$$\int_0^1 x\bar{F}_2\,dx = \begin{array}{lll} 0.51 \pm 0.05 & \text{BEBC} & (319) \\ 0.45 \pm 0.02 & \text{CITF} & (320) \\ 0.45 \pm 0.03 & \text{CDHS} & (293) \\ 0.44 \pm 0.02 & \text{CHARM} & (63) \end{array}$$

Therefore one half of the proton momentum is carried by objects which are invisible to the electromagnetic and the weak current.

The fractional momentum of the valence quarks

$$\int_0^1 x \bar{F}_3 \, dx = 0.32 \pm 0.01 \qquad \text{CDHS}$$

is about one third of the total momentum. Therefore some (13 ± 1)% of the momentum is carried by the sea quarks.

The quark-parton model describes data taken at the same value of Q^2 very well. However, the data vary with Q^2 and this feature cannot be understood in the naive quark parton model. Furthermore 50% of the proton momentum is carried by objects different from partons. In the next part we will discuss the Q^2 variation of the data and a possible explanation.

9.3 Scaling violations and QCD

9.3.1 Altarelli-Parisi equations

The resolving power of a spacelike current increases with Q^2 as $1/\sqrt{Q^2}$, i.e. with increasing Q^2 a spacelike current explores clusters of progressivly smaller size. It is common to all field theories[12] that a parton can split into smaller clusters of two or more partons sharing the parent momentum. The relevant Feynman graphs , to first order in the strong coupling constant, are shown in Fig. 9.9. A comparison of deep inelastic scattering at two

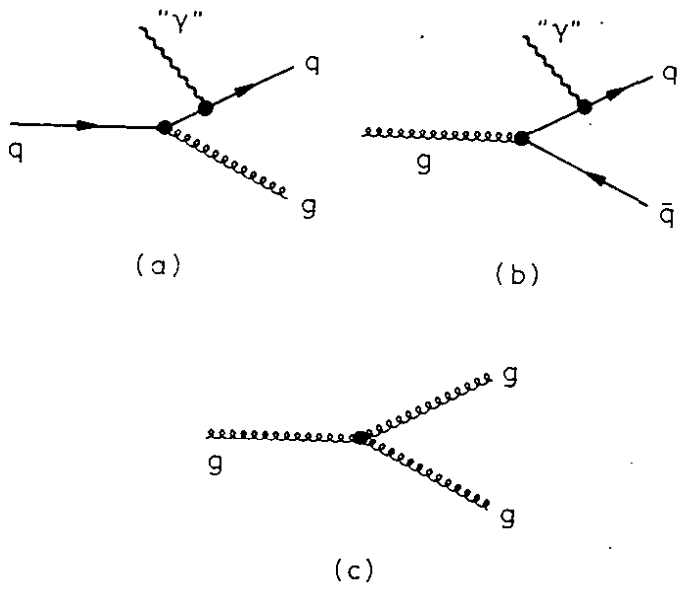

Fig. 9.9

Feynman graphs for:
a) quark gluon bremsstrahlung
b) splitting of a gluon into a $q\bar{q}$ pair
c) splitting of a gluon into two gluons.

different values of Q^2 is shown in Fig. 9.10. Fig. 9.10 a,b shows that the effect of gluon bremsstrahlung is to decrease the x value of the quark. Fig. 9.10. c,d illustrates the fact that a gluon which is invisible to the electroweak current at low Q^2 may be resolved into its $Q\bar{Q}$ content by a high Q^2 current leading to a strong increase of the sea quarks. Therefore the pattern of scaling violations indicated in Fig. 9.11, where with increasing values of Q^2 the parton density is enhanced at low x and depleted at large x, is common to all field theories and the Q^2 evolution of the structure function must be studied in detail in order to confront QCD with the data. Note that QCD makes absolute predictions of this evolution.

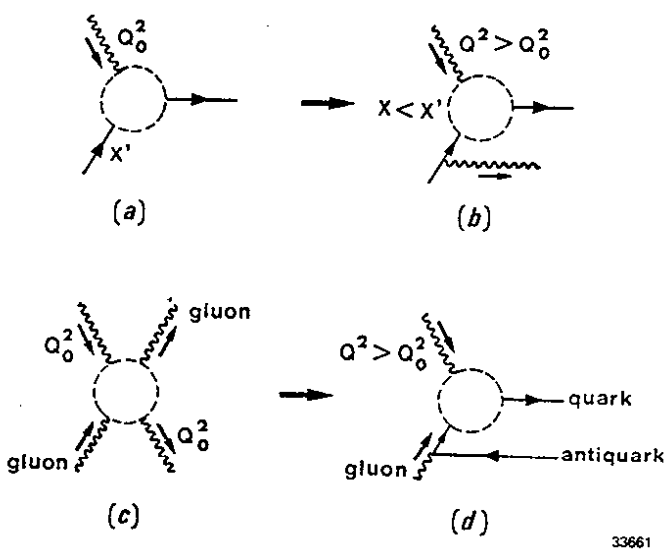

Fig. 9.10 - a) A virtual photon with Q_0^2 striking a quark
b) a virtual photon of higher Q^2 resolving the quark into a quark and a gluon
c) a virtual photon with Q_0^2 traversing a gluon without interaction
d) a virtual photon of higher Q^2 resolving the gluon into a quark-antiquark pair.

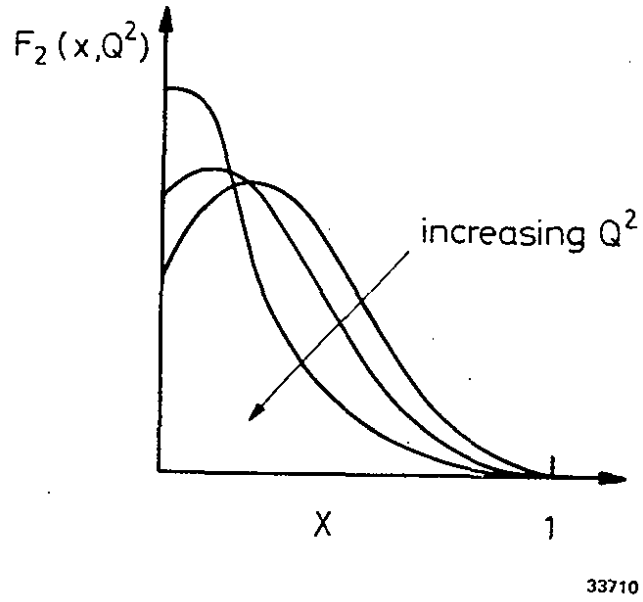

Fig. 9.11 - The qualitative change of deep inelastic formfactors with Q^2 expected in field theories of the strong interaction.

The cleanest tests[294] on the theory are obtained from measurements of the flavour non-singlet structure functions like for example $x F_3(x,Q^2)$, the valence quark distribution. The reason is that only gluon bremsstrahlung (Fig. 9.9a) contributes to the Q^2 evaluation of the non singlet structure factors, whereas both gluon bremsstrahlung and gluon quark pair production (Fig. 9.9a,b) contribute to the singlet functions like $F_2^{ep}(x,Q^2)$.

The Q^2-evolution[229,321] of the valence quark distribution $q_V(x,Q^2)$ can be written as:

$$9.25 \quad Q^2 \cdot \frac{\partial q_V(x,Q^2)}{\partial Q^2} = \frac{\alpha_s(Q^2)}{2\pi} \int_0^1 \frac{dy}{y} P_{qq}(x/y)\, q_V(y,Q^2)$$

$\alpha_s(Q^2)$ is the strong coupling constant defined in Eq.5. $P_{qq}(z)$ is the probability to find a quark inside the quark with a relative momentum $z = x/y$. The splitting function $p_{qq}(z)$ can be calculated in QCD from the analogy to electron bremsstrahlung. The energy spectrum of the radiated gluon should

be proportional to the bremsspectrum of a real photon i.e.

$$9.26 \qquad P_{qg}(z) = \frac{4}{3} \frac{1 + (1-z)^2}{z}$$

z is the energy of the gluon in units of the parent energy and 4/3 is a colour factor. The probability to find a gluon with relative energy z is equal to the probability of finding a quark with relative momentum 1-z. This leads[229] to:

$$P_{qq}(z) = \frac{4}{3} \frac{1 + z^2}{(1-z)}$$

At $z \to 1$ the quark only contains itself and the complete splitting function can be written as:

$$9.27 \qquad P_{qq}(z) = \frac{4}{3} \frac{1 + z^2}{(1-z)} + \frac{3}{2} \delta(z-1) .$$

Similar evolution equations can be written for the singlet quark (antiquark) distribution function $q(x,q^2)$ and the gluon distribution function $G(x,Q^2)$:

$$Q^2 \frac{\partial q}{\partial Q^2}(x,Q^2) = \frac{\alpha_s}{2\pi} \int_x^1 \frac{dy}{y} [q(y,Q^2)\, P_{qq}(x/y) + G(g,Q^2)\, P_{gq}(x/y) \ldots]$$

9.28

$$Q^2 \frac{\partial G(x,Q^2)}{\partial Q^2} = \frac{\alpha_s}{2\pi} \int_x^1 \frac{dy}{y} [q(y,Q^2)\, P_{qq}(x/y) + G(g,Q^2)\, P_{gq}(x/y) \ldots]$$

The gluon-quark pairproduction function $P_{gq}(z)$ and the three gluon vertex function (Fig. 9.9c) $P_{gg}(z)$ are given by:

$$9.29 \qquad P_{gq}(z) = \frac{1}{2}(z^2 + (1-z)^2)$$

$$P_{gg}(z) = 6 \left[\frac{z}{(1-z)_+} + \frac{1-z}{z} + z(1-z) + \left(\frac{11}{12} - \frac{N_f}{18} \right) \delta(z-1) \right]$$

N_f is the number of flavours participating. It is clear that the singlet functions are more difficult to analyze since they involve the unknown gluon distribution function. In addition there are several theoretical uncertainties[322,23] which must be evaluated before firm conclusion can be drawn from the data. These involve higher twist corrections, target mass effects and higher orders in QCD.

Two methods are in general use to compare predictions with theory.

The first method involves taking the moments[323] of the distributions given by eqs. 9.25 and 9.28 i.e. both sides of the equations are mutliplied by x^{N-1} and integrated over x. The results are a set of simple,well defined equations. The non singlet moments can be written[324] as:

$$M_N^{(3)}(Q^2) = [\ln Q^2/\Lambda^2]^{-d_N}$$

9.30

$$d_N = \frac{4}{33-2N_f}\left[1 - \frac{2}{N(N+1)} + 4\sum_{i=1}^{N} 1/i\right]$$

The second method is to try to solve the Altarelli-Parisi equations directly. This method[325-327] has the advantage that it only uses measured data whereas in the moment method data at all x values are needed to perform the integration. Both analysis however, suffers from uncertainties due to higher order twist or higher order QCD effects.

9.3.2 The value of R

In the naive quark-parton model σ_L approaches 0 in the Bjorken limit. In QCD however, the radiated gluon carries away transverse momentum leading to a transverse momentum distribution of the quarks and hence to a longitudinal form factor $F_L(x,Q^2)$

9.31 $$F_L(x,Q^2) = F_2(x,Q^2) - 2x\,F_1(x,Q^2).$$

This formfactor can be written to first order in α_s [294] as:

9.32 $$F_L(x,Q^2) = \frac{\alpha_s(Q^2)}{2\pi} \int_x^1 \frac{dy}{y^3} [\, 8/3\, F_2(y,Q^2) + 4A(1-x/y)\, y\, G(y,Q^2)]$$

A = 10/9 in charged lepton scattering and 4 in neutrino interactions.

The longitudinal structure function is determined through a measurement of R' (or R): $R' = F_L / F_2$.

At small x ($x < 0.1$) the main contribution to F_L is from the gluon structure function $G(y,Q^2)$, whereas $F_2(y,Q^2)$ contributes mainly at large x. Thus both the value of α_s and the gluon structure function could be determined from a precise measurement of R'. The results of a recent measurement [307] of R integrated over x are plotted in Fig. 9.12 versus Q^2 and compared to the QCD prediction.

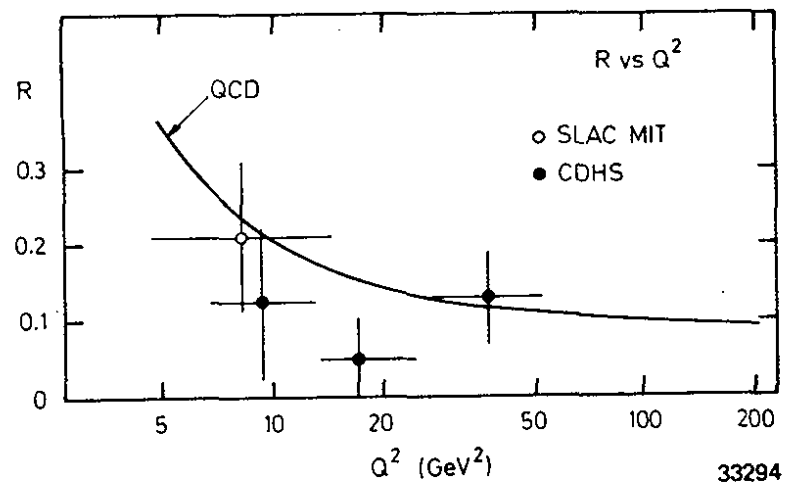

Fig. 9.12 - $R = \sigma_L/\sigma_T$ as a function of Q^2. The curve is the QCD prediction.

9.3.3 Moment analysis of $x F_3(x,Q^2)$

The data are in general analyzed in terms of the Nachtmann moments[323]. These moments project to definite spin N at all values of Q^2 and they take the finite target mass into account. Using this formalism the non-singlet moment can be written as:

$$9.33 \quad M_N^{(3)}(Q^2) = \int_0^1 \frac{dx}{x^3} \xi^{N+1} x F_3(x,Q^2) \cdot \left[\frac{1 + (N+1)\sqrt{1 + 4m^2 \cdot x^2/q^2}}{(N+2)} \right]$$

$$\text{with } \xi = \frac{2x}{1 + \sqrt{1 + 4m^2 x^2/Q^2}}$$

The moments at two different values of Q^2 are related in leading order of QCD as:

$$9.34 \quad \frac{M_N^{(3)}(Q^2)}{M_N^{(3)}(Q_0^2)} = \left(\frac{\ln (Q_0^2/\Lambda^2)}{\ln (Q^2/\Lambda^2)} \right)^{d_N}$$

d_{NS} is defined in eq. 9.30. The evolution of the valence quark distribution therefore depends on a single constant Λ.

This form suggests to plot the logarithm of the n-the moment of $2xF_3$ versus the logarithm of its m-th moment. Such a plot should yield a straight line with a slope d_N / d_M. The magnitude of the slope is an absolute prediction in QCD. This prediction has been verified by several groups. In Fig. 9.13 M_6^3 is plotted versus M_4^3 and M_5^3 is plotted versus M_3^3. Data from CDHS[328] and a combination of Gargamelle and BEBC results[291] are shown together with the QCD predictions. Obviously there is excellent agreement between the predicted and the measured value. For d_6/d_4 QCD predicts 1.29 compared to 1.29 ± 0.06 obtained

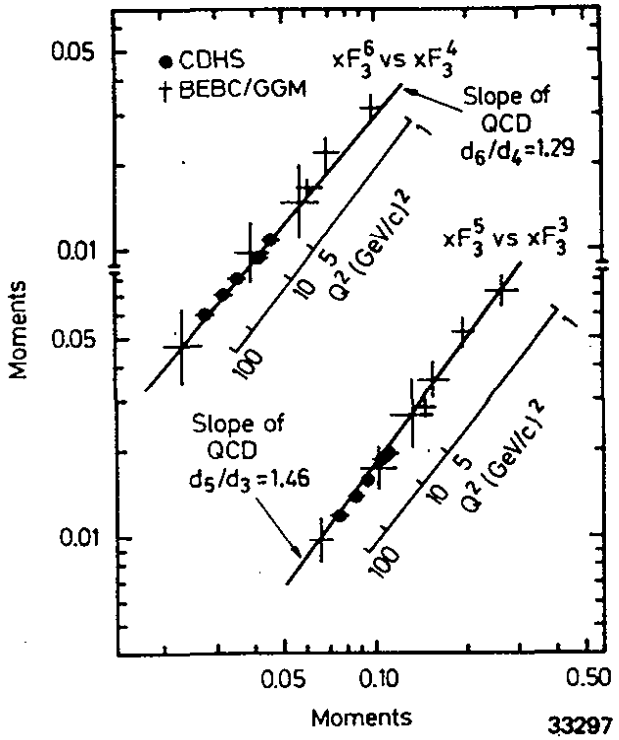

Fig.9.13
Moments of x F_3 on a double logarithmic plot. The data agree well with the first order QCD predictions

by BEBC/GGM and 1.18 ± 0.09 by CDHS. For d_5/d_3 QCD predicts 1.46 compared to 1.50 ± 0.08 by BEBC/GGM and 1.34 ± 0.12 obtained by CDHS. Note, however that this excellent agreement was obtained despite the fact that both groups treated these data quite differently. BEBC/GGM included elastic events whereas they were excluded by CDHS. BEBC/GGM included only non singlet data whereas CDHS include some electron data.

The Q^2 evolution of single moment can be written as:

$$2.35 \quad (M_n^{(3)}(Q^2))^{-1/dn} = C\,(\ln Q^2 - \ln \Lambda^2)$$

Fig. 9.14 shows the bubble chamber data from CERN PS[22] and SPS[291]. The data indeed fall on a straight line consistent with a logarithmic scaling violation. However, a power series in Q^2, as expected from higher twists can also mimic a logarithmic Q^2 dependence over the limited Q^2 range investigated.

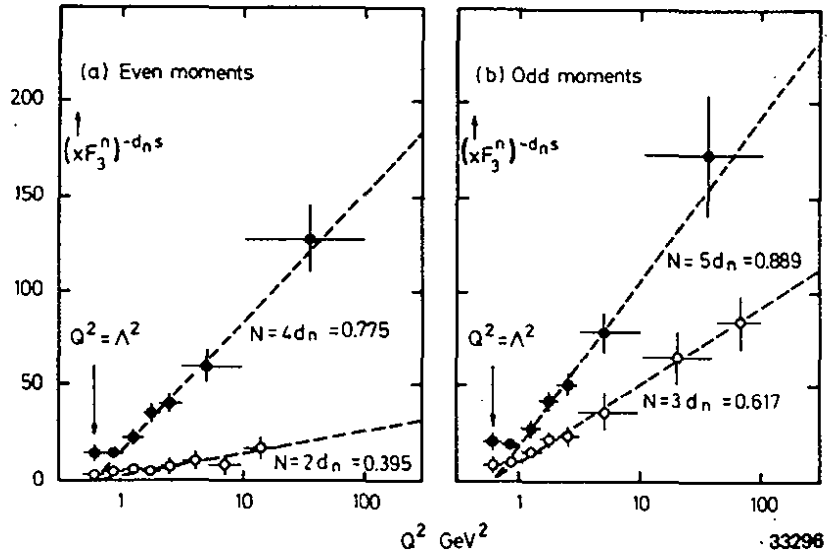

Fig. 9.14 - Comparison of the moments of xF_3 with the first order QCD prediction. According to QCD the datapoints are aligned on straight lines with respect to ln Q^2. The lines intercept all the same point $Q^2 = \Lambda^2$

In spite of the agreement with the predictions there are, however, serious experimental drawbacks in using the moment method. The evaluation of the moments requires the knowledge of the structure function at all x. But kinematical and experimental reasons allow a measurement only in a limited x domain and this domain is different for different values of Q^2 (see Fig. 9.3). Thus the data must be extrapolated into unknown regions and this introduces systematic uncertainties. A particularly serious problem arises from the fact, that all moments are derived from the same set of measurements: Different moments are obviously highly correlated. Furthermore target mass effects [324] play an important rôle. Finally, from the theoretical point of view the effects of higher twists could give the same ratios of anomalous dimensions and higher order predictions are missing. The direct solutions of the Altarelli Parisi equations avoid some of these problems.

9.3.4 Direct analysis of the formfactors

The Altarelli-Parisi equations hold at high Q^2, where "high" depends on the unknown parameter Λ and on yet unknown higher order terms in the perturbation expansion. The validita of the equations improves,with increasing values of Q^2, however, the bulk of the data is at relatively low Q^2 ($\sim$ 10 GeV^2/c^2). In addition, corrections due to the finite mass of the target nucleon are necessary. Several methods of solving (or approximately solving) the Altarelli-Parisi equations have been used in analyzing the data, the method of Buras and Gaemers[325], the method of Abbot and Barnett[326] and the method of Ganzales-Arroyo et al.[327].

The valence quark structure function xF_3 can be determined experimentally without assumptions on R or on the gluon structure function. However, target mass effects, the Fermi-motion inside the nuclear target, the limited resolutions in x and Q^2 and radiative corrections must be included in the analysis. An analysis of the F_2 structure function must in addition include effects due to R or the gluon structure function. The recent CHARM data [309,329] are shown in Fig. 9.15. The data are

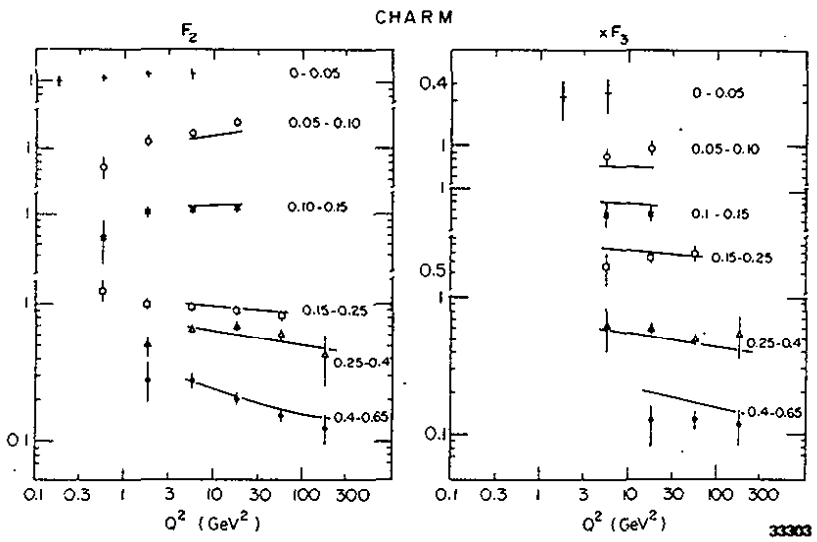

Fig. 9.15 - The structure functions F_2 and xF_3 as measured by the CHARM Collaboration

corrected for Fermi motion and radiative effects. The resolutions in x and Q^2 are unfolded. R = 0 was assumed for the analysis. $F_2(x,Q^2)$ and $xF_3(x,Q^2)$ are plotted versus ln Q^2 for fixed x bin. The data clearly show the scaling violations as expected in a field theory and the solid line represents the results of a Buras-Gaemers type QCD analysis.

Fig. 9.16 shows the recent GGM data [330]. The resolution of this experiment is in general superior to the counter experiments. The data are

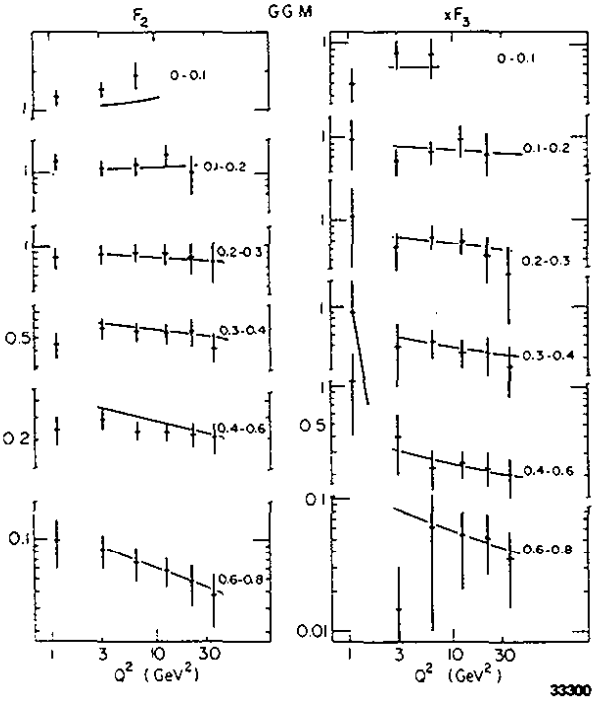

Fig. 9.16
The structure functions F_2 and xF_3 as measured by the GGM Collaboration. Curves correspond to a fit to the CHARM data.

corrected for Fermi motion but not for radiative effects and agree extremely well with the CHARM data.

The recent CDHS [311] data in Fig. 9.17 have by far the highest statistics of all neutrino experiments. The assumption R = 0.1

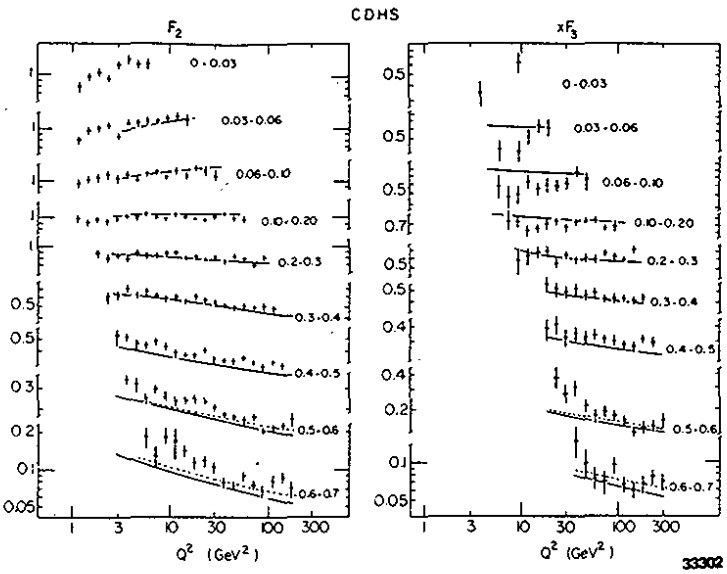

Fig. 9.17 - The structure functions F_2 and xF_3 as measured with high statistics by the CDHS Collaboration. Curves correspond to a fit to the CHARM data.

was made for the extraction of F_2. No Fermi motion correction was applied. While both experiments observed the same Q^2 dependence, differences show up in the x dependence. The CDHS structure functions are broader (extend to higher x). The same behaviour can be observed in the HPWFRO data [306] in Fig. 9.18 which were obtained assuming R = 0.1 and without Fermi motion correction. The resolution at high x is dominated by the measurement errors in the muon momentum. On the other hand, the Fermi motion correction is large at large x. It is therefore possible, that the discrepancies are due to the Fermi motion and the different unfolding of the resolution particularly at high x.

Recent measurements of the F_2 structure function in charged lepton scattering are shown in Fig. 9.19 and 9.20. The fully drawn curves correspond to a fit to the EMC [304] or BCDMS [29] data respectively. The

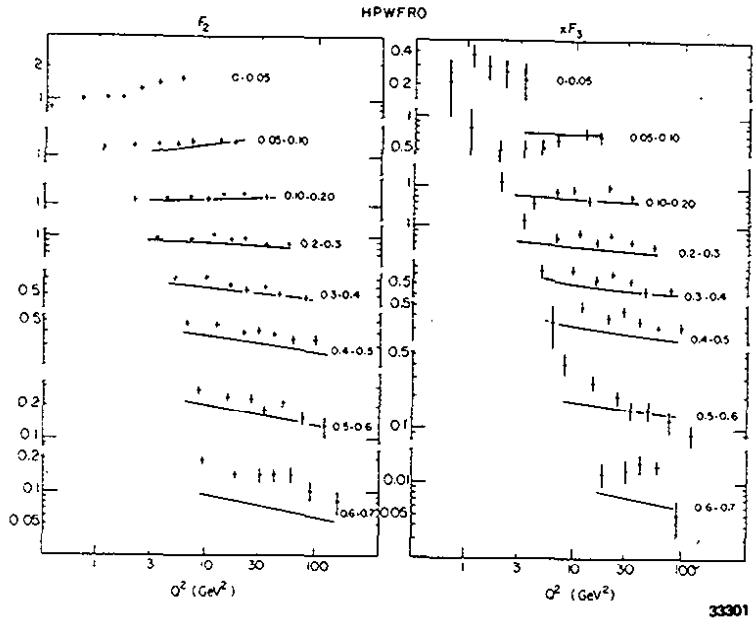

Fig. 9.18 - The structure functions F_2 and xF_3 as measured by the HPWFRO Collaboration. Curves correspond to a fit to the CHARM data.

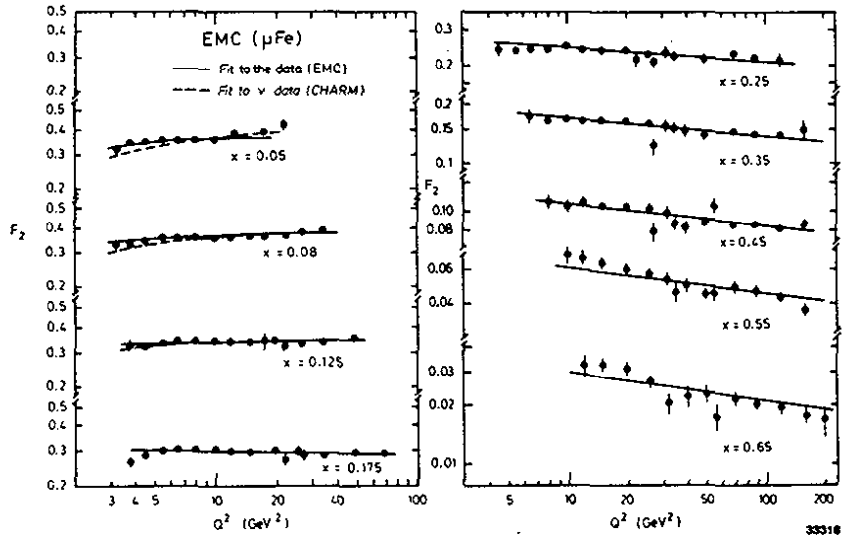

Fig. 9.19 - The structure function F_2 as measured by the EMC. The dashed curves correspond to a fit to the CHARM data only. Where the fit to the EMC data (full lines) agrees with the CHARM fit only a full line is drawn).

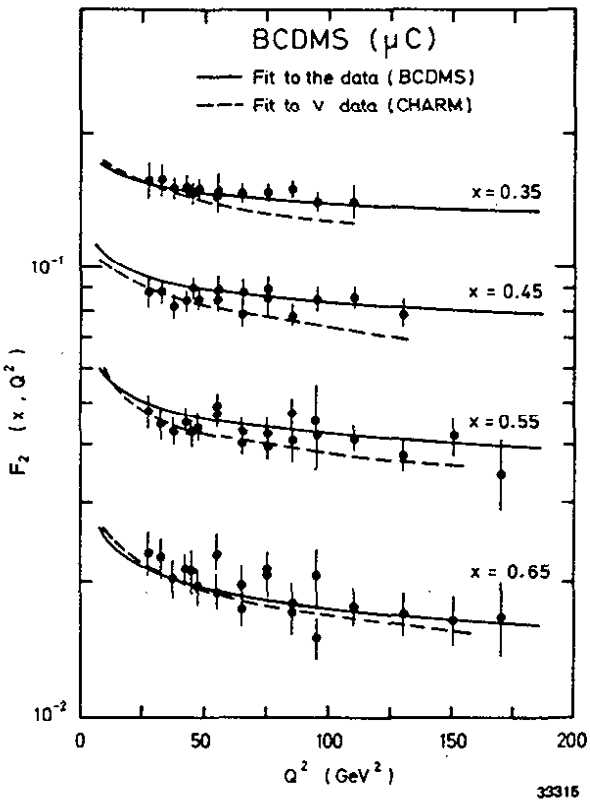

Fig. 9.20

The structure function F_2 as measured by the BCDMS Collaboration. The dashed curves correspond to a fit to the CHARM data.

dashed curves are the absolute predictions from the CHARM neutrino data. Where the dashed curve is missing the prediction is actually indistinguishable from the fits to the muon data. The agreement between neutrino data and BCDMS data (Fig. 9.20) (R = 0) is rather good taking the systematic errors into account. The agreement with the EMC data (R = 0) (Fig. 9.19) is extremely good.

From the fits mentioned above and those of other experiments values for Λ can be obtained. Unfortunately similar scale breaking effects can be simulated by the hadronization of the quark. It is difficult to discriminate between these higher twist effects and QCD effects in the limited Q^2 range presently available.

Higher twist effects are in general included in the analysis and they seem to account for roughly 10% of the cross section at high x.
The most recent results of Λ_{LO}, evaluated with and without higher twist effects included, are listed in Table 9.4.

Table 9.4 - Values for Λ_{LO}

Experiment	No Twist Λ_{LO}	Higher Twist Λ_{LO}(MeV)	μ^2(GeV^2)	Ref.
GGM	$190 \begin{smallmatrix}+160\\-120\end{smallmatrix}$	700	0.8 ... 0.7	330
BEBC	210 ± 95			299
CHARM	$290 \pm 120 \pm 100$	290 ± 120	0.09 ± 0.06	329
CDHS	$190 \begin{smallmatrix}+80\\-70\end{smallmatrix}$	200 ± 20	0.84 ± 0.1	311
EMC (Fe)	$122 \begin{smallmatrix}+22+114\\-20-70\end{smallmatrix}$		1.16 ± 0.07	303
EMC (H_2)	$110 \begin{smallmatrix}+58+124\\-46-69\end{smallmatrix}$		0.96 ± 0.15	304
BCDMS	$85 \begin{smallmatrix}+60+90\\-40-70\end{smallmatrix}$			29

All experiments agree on a rather low value of Λ despite the different methods used.

Up to now the structure functions F_2, xF_3 and $2xF_1$ have been discussed. It is however, possible to extract the gluon distribution function from the Q^2 variation of the momentum distributions of light antiquarks. The high statistics of the antineutrino wide band beam exposure made it possible for

the CDHS Collaboration [331] to extract the light antiquark momentum distribution as a function of Q^2

2.36
$$x\,\bar{q}\,(x,Q^2) = \frac{\pi}{G^2 ME}\left\{\frac{d^2\sigma^{\bar{\nu}N}}{dxdy} - (1-y)^2\,\frac{d^2\sigma^{\nu N}}{dxdy}\right\} + \text{corrections.}$$

The data are shown in Fig. 9.21. The distribution is strongly rising with Q^2

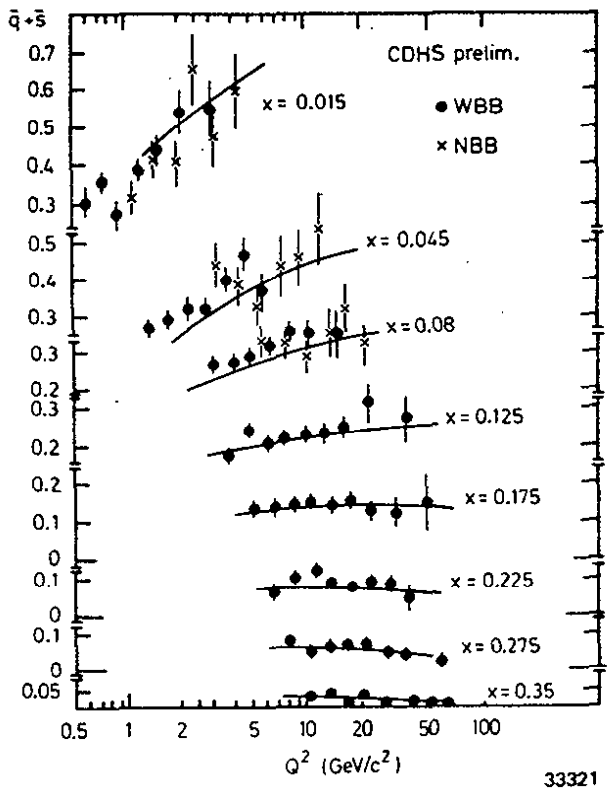

Fig. 9.21

The structure function of the light antiquarks. The curves correspond to a QCD fit to the data obtained by the CDHS Collaboration.

for small x and disappears for $x \geq 0.4$. The gluon distribution can be extracted, from the measured Q^2 evolution of quarks and antiquarks.

The CDHS group has performed [332] an analysis along this line. The gluon distribution at $Q^2 = Q_0^2 = 5\ \text{GeV}^2$ was parametrized as

$$x\,G(x) = a\,(1-x)^{p}\,(1 + c\,x)$$

with $a = 2.63$, $p = (5.9 \pm 0.5)$ and $c = (3.5 \pm 1.0)$. This analysis also confirms the value of Λ and the momentum fraction carried by gluons reported earlier.

10. The Search for New Particles

Electron-positron annihilation has become a favorite hunting ground for exotic particles as evidenced by a long list of unsuccessful searches[36,332]. In many cases, however, due to the well defined production mechanism and the high visibility a negative result can be used to exclude the eistence of new particles in the mass range investigated.

10.1 Limits on new sequential leptons

Leptons are pairproduced with the point cross section

$$\sigma = \frac{4\pi\,\alpha^2}{3\,s}\;\frac{\beta(3-\beta^2)}{2} \qquad \text{with } \beta = P_L/E. \tag{10.1}$$

The expected decay modes are shown in Fig. 10.1. The branching ratios, neglecting phase space factors, can be written as:

$$B(L \to \nu_L\, e\, \bar{\nu}_e) = B(L \to \nu_L \mu\, \bar{\nu}_\mu) = B(\tau \to \nu_L \to \tau\, \nu_\tau) \tag{10.2}$$

$$\approx \frac{1}{(e\nu) + (\mu\nu) + (\tau\nu) + 3(d\bar{u}) + 3(s\bar{c})} = 11\%$$

and $B(L^- \to \nu_L\, d\bar{u}) \approx B(L^- \to \nu_L\, s\bar{c}) \approx 3\, B(L^- \to \nu_L\, \ell\, \nu_e) \approx 33\%$.

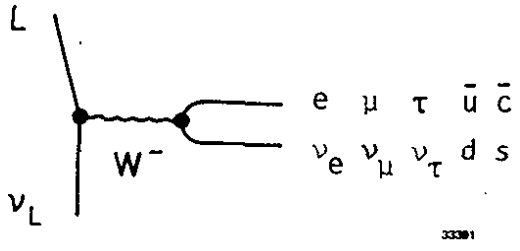

Fig. 10.1
Possible decay modes for a new sequential lepton.

These decays result in distinct final states:

a) Approximately 10% of all $L\bar{L}$ pairs result in a final state $e^+e^- \to e^\pm \mu^\mp$ + neutrinos. The muon and the electron are in general accolinear and the total energy visible in the event is less than the available center of mass energy.

b) $e^+e^- \to L\bar{L} \to e^\mp (\mu^\mp) + (\text{hadrons})^\pm$ + neutrinos. In this final state the electron (muon) is recoiling against a low multiplicity hadron jet. The electron (muon) and the jet axis are in general acollinear and some of the available energy is carried off by neutrinos. Roughly 40% of all new sequential lepton pairs will populate this final state. As an example, a tau pairproduction event observed by TASSO viewed along the beam direction is shown in Fig. 10.2.

c) $e^+e^- \to L\bar{L} \to (\text{hadrons})^+ + (\text{hadrons})^-$ + neutrinos. The two low multiplicity hadron jets will in general be acollinear and a fraction of the c.m. energy is carried off by neutrinos.

Groups at PETRA and PEP have used these topologies to search for sequential leptons beyond the tau. No evidence has been found and the resulting mass limits and the method used are listed in Table 10.1.

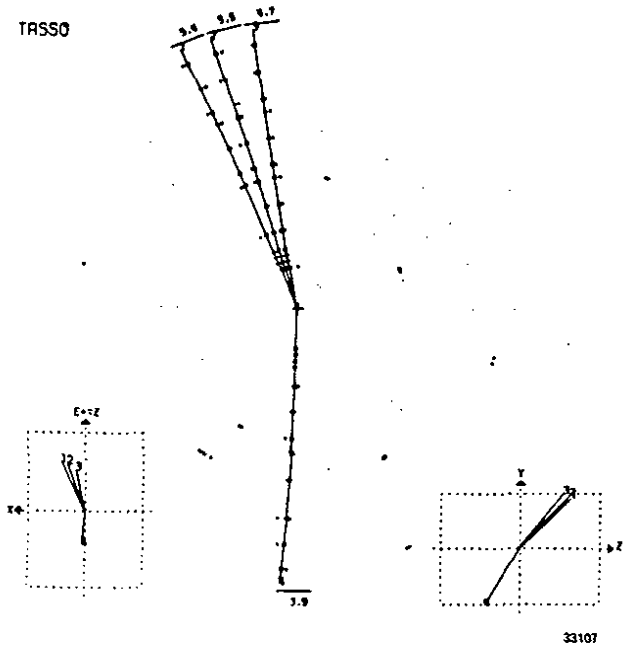

Fig. 10.2
A tau pairproduction event $e^+e^- \to \tau^+\tau^- \to \mu^-$ + hadrons + neutrinos observed by TASSO.

Table 10.1 - Mass limit on new sequential leptons

Group	Lower Limit 95% C.L.	Signature	Reference
JADE	18.1 GeV	Two acollinear jets	332
MARK J	16.0 GeV	Single muon recoiling against many hadrons	333
PLUTO	14.5 GeV	Single muon recoiling against many hadrons	334
TASSO	15.5 GeV	Single charged particle recoiling against many hadrons	335
MAC	14.0 GeV	Acollinear eμ events	37
MARK II	13.8 GeV	Acollinear eμ events	37

In SU(5) the charged lepton and the charged 1/3 quark within the same generation are degenerate in mass at the unification energy of 10^{15} GeV. This has been used to estimate[336] the mass of the s quark from the muon mass

and to predict the mass of the b quark from the tau mass. It seems reasonable to expect that the charged lepton in a new generation of elementary fermions is lighter than the quarks. Indeed, from the present lower limit on the mass of a new lepton, the charge 1/3 quark in a SU(5) model must have a mass above 50 GeV.

10.2 Search for neutral leptons with mass

Heavy neutral leptons[337-339] are not required in the standard theory, however, they are not excluded and indeed they became natural if the weak current should turn out to be a pure vector interaction at high energies. In such models a heavy neutral lepton E^0 is the partner of the electron in a right handed doublet i.e.

$$\begin{pmatrix} E_0 \\ e^- \end{pmatrix}_R$$

Possible production and decay mechanisms for an electronlike heavy neutral lepton are shown in Fig. 10.3 a,b,c. The E^0 can be pair-produced via the neutral weak current and singly produced via the charged weak current. Charged current production dominates at present energies provided the interaction has the usual weak strength. The decay modes $E^0 \rightarrow e^- W^+$ can lead to a pure leptonic final state or to a jet consisting of an electron and hadrons.

The production in e^+e^- annihilation of an electronlike heavy neutral lepton has a clean signature; the E^0 and the ν_e are produced back to back leading to an event with only a single large angle jet consisting of electrons and hadrons in one hemisphere and nothing visible in the other hemisphere to balance its transverse momentum.

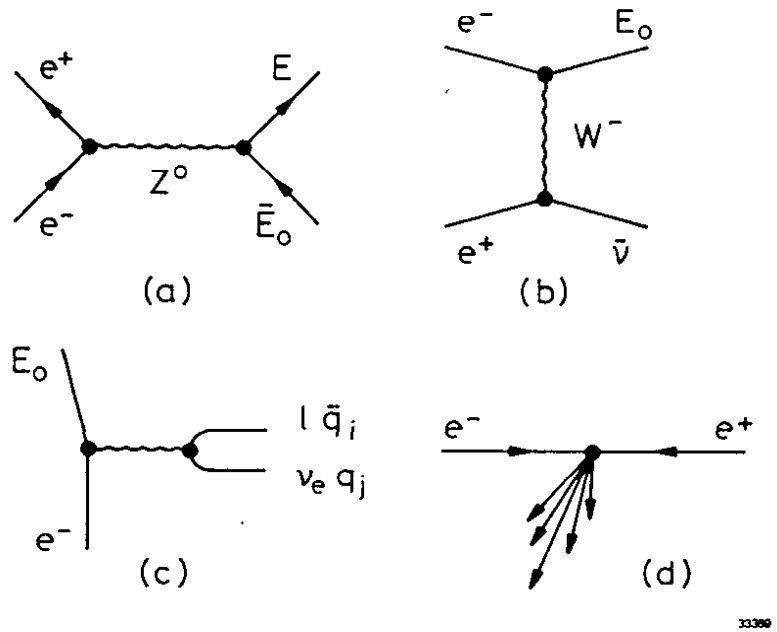

Fig. 10.3 - Heavy electronlike neutral lepton

a + b) Production mechanism via the neutral weak and the charged weak current

c) Decay modes

d) Final state in $e^+e^- \to E^0 \bar{\nu}$.

The JADE Collaboration has searched [332] for events with this topology: they select a group of hadrons containing at least one electron. These particles are constrained to be opposite to a cone with an opening angle of 50^0 which contains neither charged particles nor shower energy. None of the events satisfied the criteria. The expected number of such events resulting from $e^+e^- \to E^0\bar{\nu}_e$ is plotted in Fig.10.4 versus the mass of the heavy lepton. They conclude that electronlike heavy neutral leptons with the properties discussed above do not exist with a mass less than 20 GeV for V + A coupling and less than 17 GeV for a V - A coupling.

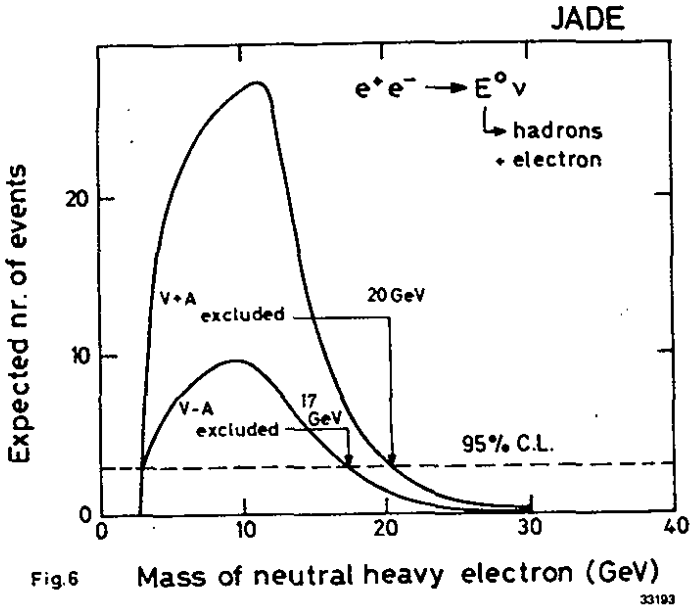

Fig. 10.4
The number of E^o events in the JADE experiment which satisfy the selection criteria versus the E^o mass.

10.3 Search for new quarks

All available data [100,146] are consistent with the assumption that the b-quark is member of a doublet with its 2/3 charge member, the t-quark, still missing. However, present theories are not able to constrain the mass of the t quark as evidenced by the flood of theoretical predictions. Production of a new quark has striking signatures: at threshold the normalized hadron cross section will have a step $\Delta R = 3e_i^2$ and the fragmentation of the $t\bar{t}$ quarks will lead to spherical events containing leptons with a high probability. Below threshold there will be narrow 1^{--} $t\bar{t}$-states.

10.3.1 Naked t quark production

The value of $R = \sigma(e^+e^- \rightarrow \text{hadrons}) / \sigma(e^+e^- \rightarrow \mu^+\mu^-)$ plotted in Fig. 6.2 versus the c.m. energy squared, does not show any steps and strongly disfavour the existence of new quarks with charge 2/3e.

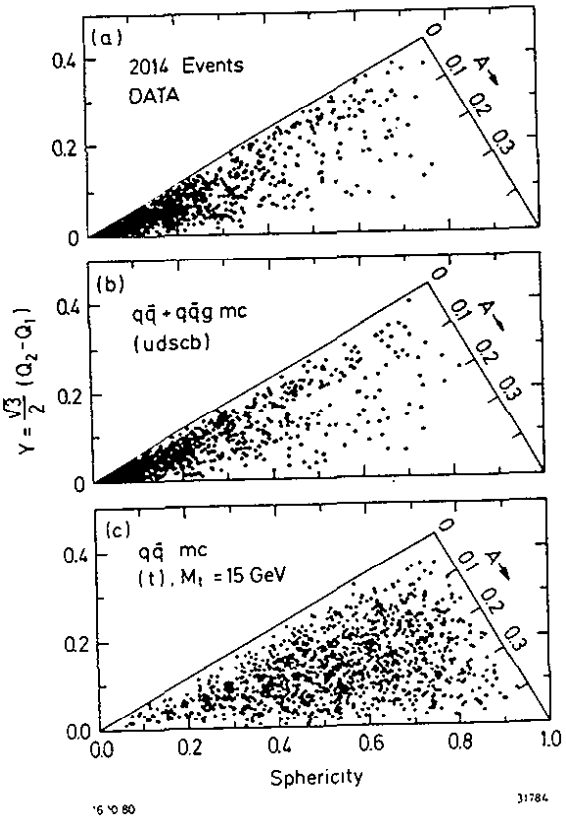

Fig.10.5
a) The event distribution in aplanarity and sphericity observed by the TASSO Collaboration between 27.4 GeV and 36.6 GeV in c.m. Monte Carlo created events in aplanarity and sphericity at 30 GeV in c.m. for
b) $e^+e^- \to q\bar{q}g$ with q = u,d,s,c and b
c) $e^+e^- \to t\bar{t}$ with m_t = 15 GeV
and a c.m. energy of 35 GeV.

A more sensitive limit on new quark production can be obtained by considering the event shape. Various methods used to determine the event shape have been discussed above. The distribution of events in aplanarity (A) and sphericity (S) as observed [175] by the TASSO Collaboration at c.m. energies between 27.4 GeV and 36.6 GeV is plotted in Fig. 10.5. In such a plot two jet events will cluster at small values of A and S, planar events resulting from gluon bremsstrahlung will have small values of A whereas both A and S will be large for spherical events. This is born out by the Monte Carlo results shown in Fig. 10.5 b,c. The data cluster at small values of S and A with a long tail of planar events as expected for light quark production including gluon bremsstrahlung. Similar results [332] have also been obtained by CELLO and JADE. The data are listed in Table 10.2

Table 10.2 - Number of aplanar (A > 0.15) multihadron events (Ref. 332)

Group	CELLO	TASSO
Number of events observed	9	12
Number of events expected (u,d,s,c,b and QCD)	5.2 ± 1.4	11 ± 1
Including a new quark with mass charge 2/3e	16.0 GeV	15.0 GeV
	96.3 ± 4.2	138
or charge 1/3e	31.8	43

Top quark production is expected to be a prolific source of prompt leptons. The MARK J group select[332] 352 events containing at least one muon. The thrust distribution of these events is plotted in Fig. 10.6 and compared with various models. The data are in agreement with the standard model with gluon bremsstrahlung and u, d, s, c and b quarks. New quarks would lead to a enhancement at low values of thrust which is not observed in the data. For $T \leq 0.75$ they find 14 events to be compared with 13.8 events predicted by the standard model with 5 quarks and the gluon radiation. A charge 1/3 respectively charge 2/3 quark would yield 60 respectively 163 events.

A similar analysis is made by the JADE Collaboration[332] for c.m. energies between 33 GeV and 36.7 GeV. They select events with one or more muons, in addition the muon must have at least 2 GeV transverse momentum with respect to the thrust axis and the event should have a sphericity $S \geq 0.5$. One event satisfies the selection criteria while they expect 104 such events from a charge 2/3 quark.

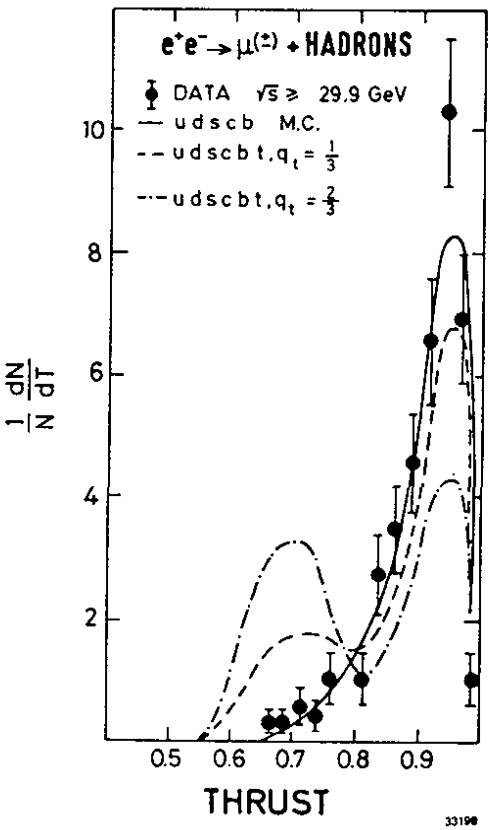

Fig. 10.6
Thrust distribution of multihadron events containing at least one muon compared with the thrust distribution expected for u, d, s, c, and b quarks and u, d, s, c, b and t quarks with the t quark charge 1/3e or 2/3e. The data were obtained by MARK J Collaboration.

The lack of a signal in any of these channels excludes the existence of a quark threshold in the mass range up to 36.7 GeV.

10.3.2 Search for narrow 1^{--} resonances

Narrow 1^{--} $t\bar{t}$ states are expected to occur some 1 GeV below $t\bar{t}$ threshold. To search for these narrow states the total cross section eas measured in steps of 20 MeV in the energy range of 27 GeV to 31.8 GeV and 33 GeV to 37 GeV. The normalized cross section[332)] obtained by combining the data from all groups (CELLO, JADE, MARK J and TASSO) is plotted in Fig.10.7 versus c.m. energy. No obvious structure is seen and an upper limit on the width of a resonance is obtained by fitting each measured cross section point to a Gaussian, radiatively correct, and a constant background term.

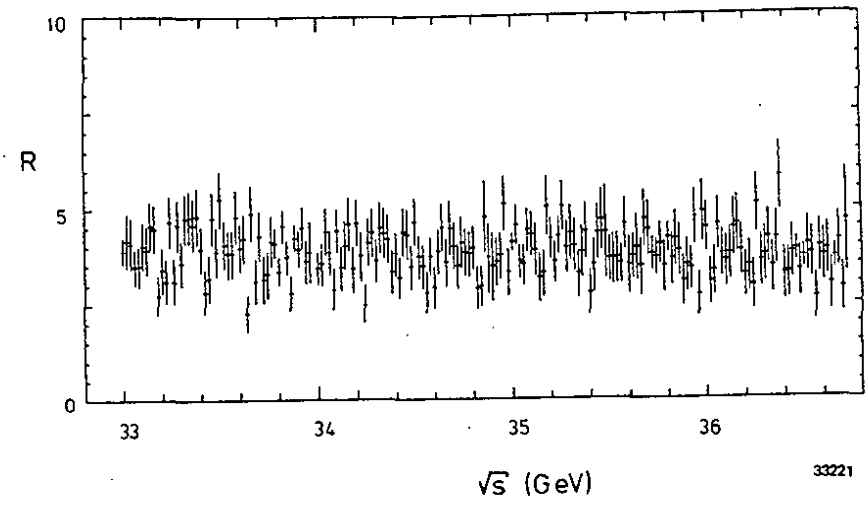

Fig. 10.7 - The normalized cross section R measured in steps of 20 MeV in c.m. The cross section shower was obtained by combining the results from CELLO, JADE, MARK J and TASSO.

The width of the Gaussian is determined by the energy resolution of PETRA. Since presumably the width of the resonance is much smaller than the energy resolution of PETRA the experiment determines only the area under the resonance

$$10.3 \qquad \int \sigma_{tot}(E)\, dE = \frac{6\pi^2}{M_R}\, \Gamma_{ee} \cdot B_h$$

Here M_R is the mass, Γ_{ee} the partial width into electrons and B_h the hadronic branching ratio of the resonance.

The upper limits obtained by each group are listed in Table 10.3 together with the value obtained by combining the data.

With $B_h = 0.7$ we expect $\Gamma_{ee} \cdot B_h = 3.08$ keV for a 1^{--} state made of charge 2/3 quarks and 0.77 keV for a 1^{--} state made of charge 1/3 quarks. Narrow resonances made of new charge 2/3 quarks are therefore excluded in the mass range investigated.

Table 10.3 - Upper limits on narrow states

Group	M_R (GeV)	$\Gamma_{ee} \cdot B_h$ (keV) (90% upper c.l.)
CELLO	33.52	1.79
JADE	33.34	1.22
MARK J	35.12	0.97
TASSO	33.34	1.33
Combined	33.34	< 0.61

10. 4 Search for free quarks

Free quarks are not in abundance although there is now little doubt that quarks indeed do exist forming colourless hadrons. Conflicting results [340,341] on the existence of free quarks have been reported from quark searches in bulk material whereas searches carried out using accelerator beams have not found any evidence of free quarks.

Since in e^+e^- annihilation the initial state consists of back to back quark pairs with large relative momenta one may expect that this reaction is particularly well suited to produce free qurks. Searches for both exclusive quark pair production and for inclusive hadron quark events have been made at PETRA, PEP and SPEAR. All searches have assumed that a free quark behaves like a pointlike strongly interacting particle with fractional charge.

The JADE Collaboration at PETRA have searched [332,342] both for inclusive and exclusive quark production using the information from their jet chamber. This detector provides tracking information and measures dE/dx at 48 points along a track. To measure the ionization tracks must be

separated by at least 7 mm. The overall efficiency in the inclusive channel range between 0.15 and 0.36 for charge 2/3 quarks and between 0.11 and 0.22 for charge 1/3 quarks as a function of quark mass. Due to triggering difficulties only charge 2/3 quarks can be measured in the exclusive channel. The mean energy loss dE/dx is plotted versus apparent momentum in Fig. 10.8. The entries cluster along the ionization curves of the known particles. The observed deuterons and tritons result from beam gas or particle beam pipe interactions. No quark candidate was found neither in the exclusive nor in the inclusive channel in an event sample corresponding to an integrated luminosity of 12000 nb^{-1} for the quark 2/3 search and 4500 nb^{-1} for the quark 1/3 search. The resulting upper limit cross sections normalized to the point cross section are plotted in Fig. 10.9 versus quark mass.

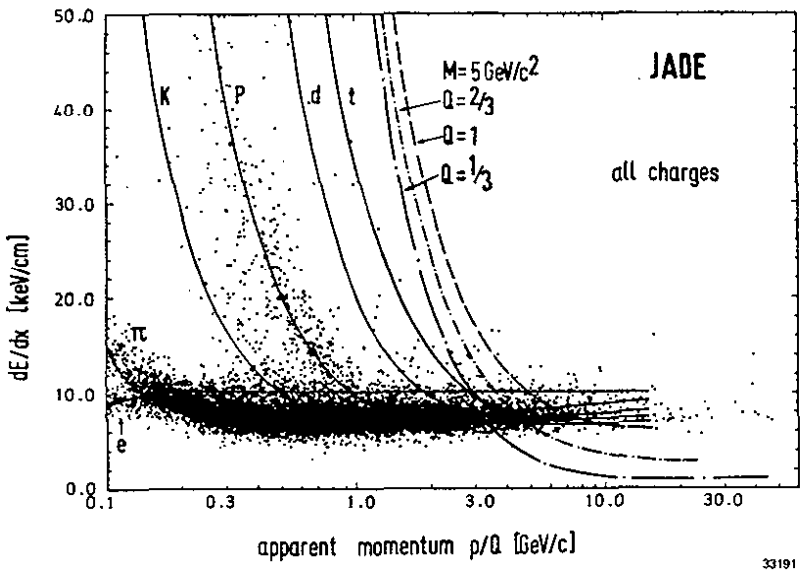

Fig. 10.8 - The energy loss dE/dx as a function of apparent momentum P/Q. The predicted energy loss curves for electrons, pions, kaons, protons, deterons and tritons are shown together with the curves for a hypothetical particle of mass 5 GeV and for quarks of charge 1/3, 2/3 and 1.

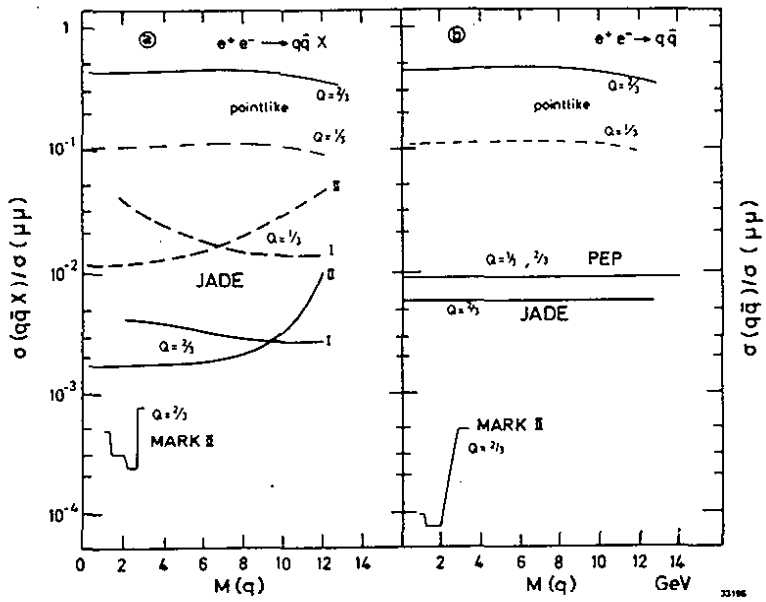

Fig. 10.9 - The 90% upper limit on the cross sections for
a) inclusive quark production $e^+e^- \to q\bar{q}$ X and
b) exclusive quark production $e^+e^- \to q\bar{q}$ plotted versus quark mass.
The curves marked I or II in a) show the limit obtained by JADE for two different assumptions or the momentum distributions of the quarks.

The quark mass limit in the inclusive search was extracted from these data for two different momentum distribution of the free quarks:

$$10.4 \qquad \frac{1}{\sigma(q\bar{q})} \cdot E \left(\frac{d^3\sigma}{dp^3} \right) = A \exp(-3.5\, E)$$

$$10.5 \qquad \frac{1}{\sigma(q\bar{q})} \cdot E \left(\frac{d^3\sigma}{dp^3} \right) = \text{constant.}$$

The resulting 90% C.L. cross sections for inclusive quark production is plotted in Fig. 10.9 versus quark mass.

The MARK II Collaboration at SPEAR has searched [342] for exclusive pair production of charge 2/3 quarks. They selected two prong events with a collinearity angle of less than 10^{o}, an apparent momentum p/q greater than half the beam energy. The energy loss normalized to that of a charge one particle should be between 0.2 and 0.65. The resulting upper limit is also plotted in Fig. 10.9.

To search for inclusively produced quarks they evaluated the apparent mass of each track

$$10.6 \qquad m_t^2 = p_e^2 / e^2 \, (1/\beta^2 - 1).$$

A quark candidate must have $m_t^2 > (1.6 \text{ GeV}/c^2)^2$ and an energy loss between 0.2 and 0.65 of that expected for a charge one particle. The resulting upper limit normalized cross section is plotted in Fig. 10.9

Recently the Northwestern University, Frascati, LBL, Stanford-University and the University of Hawaii Collaboration have reported [343] first results from a search at PEP for exclusively produced quarks. They used a non magnetic detector and the charge of a particle was determined from a measurement of energy loss and velocity. The cross section limit obtained by this experiment is also plotted in Fig. 10.9.

A CERN-Bologna-Frascati-Roma Collaboration has searched [344] for fractionally charged quarks in wide-band neutrino and antineutrino beams. The energy loss of the tracks is measured in an array of scintillation counters and in an streamer chamber. Charge 1/3 quarks can be measured for $\beta = \geq 0.4$ and charge 2/3 quarks for $\beta = \geq 0.8$. The acceptance

was 0.44 with the first and 0.28 with the last assumption. No candidate was found and the experimental limit expressed as the limit of quark candidate events normalized to the number of neutrino interactions is plotted in Fig. 10.10 as a function of $\Lambda_{quark} / \Lambda_{hadron}$ (Λ is the absorption length).

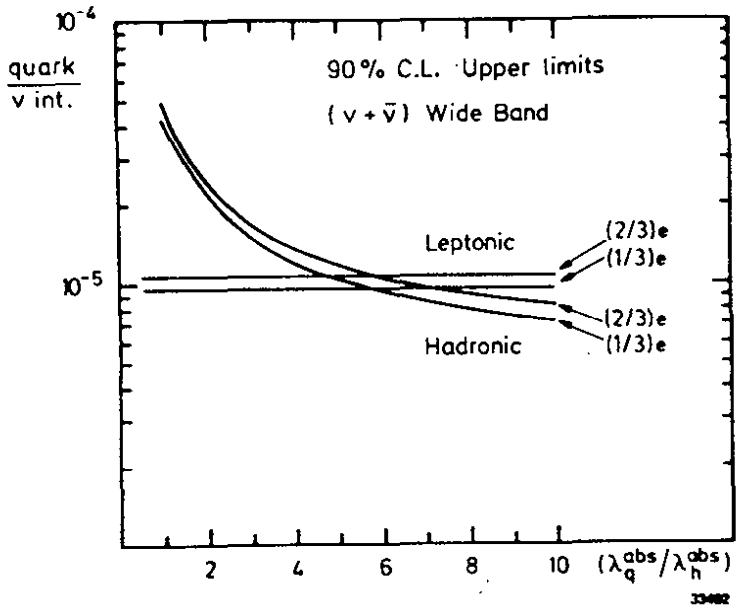

Fig. 10.10
Limit on quark candidate events normalized to the number of neutrino interactions as a function of the ratio of the absorption lengths $\Lambda_{quark} / \Lambda_{hadron}$

Note that the average Q^2 in neutrino interaction is much lower than the Q^2 investigated in e^+e^- interactions.

The fact that free quarks have not been observed in accelerator experiments does not necessarily exclude the existence of light free quarks. The colour force of a free quark is not shielded and this might cause a free quark to have a large size and "eat" normal hadrons. Such quarks could have large interaction cross sections but a small production cross section. It has even been suggested [347] that a quark has an indeterminate mass and expands to a size greater than that of an atom. It is easy to understand why quarks with such properties might have escaped detection.

10.5 Search for excited leptons

If a lepton has a finite size then it would naturally have excited states. Excited states of the leptons can be produced directly in e^+e^- annihilation. An excited electron state will also modify the cross section for $e^+e^- \to \gamma\gamma$.

10.5.1 Excited states of the muon

μ^*, the hypothetical excited state of the muon, can be pairproduced in e^+e^- annihilation with a known cross section. The μ^* decays into a muon and a photon leading to a final state consisting of two acollinear muons and two photons

10.7 $$e^+e^- \to \mu^{*+}\mu^{*-} \to \mu^+\mu^- \gamma\gamma \ .$$

The MARK J Collaboration select[36,332] events of the type $e^+e^- \to \mu^+\mu^-\gamma\gamma$ where each muon carried at least half of the beam energy and the acoplanarity angle was less than 20^0. The number of expected $e^+e^- \to \mu^{*+}\mu^{*-} \to \mu^+\mu^-\gamma\gamma$ events fullfilling the criteria above, is plotted in Fig. 10.11 versus the mass of the μ^*. The number of observed events is in agreement with the QED prediction [348] and the resulting upper limit is shown as the dotted line in Fig. 10.11. A μ^* with a mass of less than 10 GeV is ruled out.

In principle single μ^* can be produced in the reaction $e^+e^- \to \mu^{\mp}\mu^{\pm} \to \mu^{\mp}\mu^{\pm}\gamma\gamma$. The differential cross section for a μ^* with spin 1/2 and mass M can be written as:

10.8 $$\frac{d\sigma}{d\Omega} = \Lambda^2 \alpha^2 \frac{(s - M^2)^2}{s^3} \left((s+M^2) - (s-M^2) \cos^2\theta \right) .$$

The unknown coupling constant for the $\mu^*\mu\gamma$ vertex is written as $\sqrt{\alpha \cdot \Lambda}$.

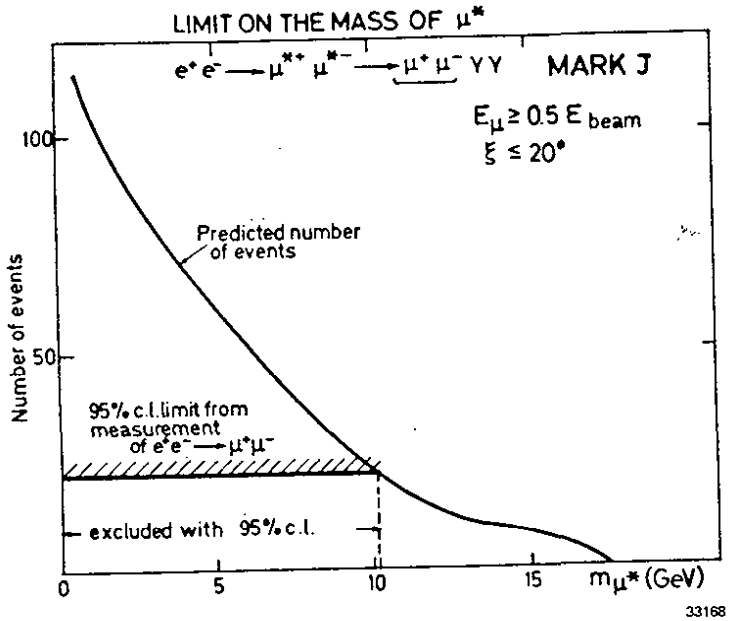

Fig. 10.11

Number of $e^+e^- \to \mu^{*+}\mu^{*-} \to \mu^+\mu^-\gamma\gamma$ events satisfying the selection criteria as a function of μ^* mass. The data were obtained by MARK J

The JADE Collaboration has searched [36,332] for events of the type $e^+e^- \to \mu^+\mu^-\gamma$ in an event sample representing an integrated luminosity of 10.6 p b^{-1} collected for c.m. energies between 22 GeV and 37 GeV. They select planar $\mu\,\mu\,\gamma$ events with an invariant $\mu^+\mu^-$ mass greater than 1 GeV. The photon should have an energy of at least 1 GeV and the opening angle between the direction of the photon and the direction of any of the muons should be at least 15^0. A total of 66 events satisfied the criteria compared to 68 events predicted by QED[349,350]. The effective $\mu\gamma$ mass distribution obtained by combining either muon in the event with the photon is plotted in Fig.10.12. There is no peak and the effective $\mu\gamma$ mass distribution is in good agreement with the QED prediction shown as the dotted line. From these data they extract an upper limit on Λ^2 as a function of μ^* mass. This limit is plotted in Fig. 10.13. The corresponding cross section limit is $\sigma(e^+e^- \to \mu\mu^*) \,/\, \sigma_{\mu\mu} < 0.0075$ for a μ^* mass of 16 GeV.

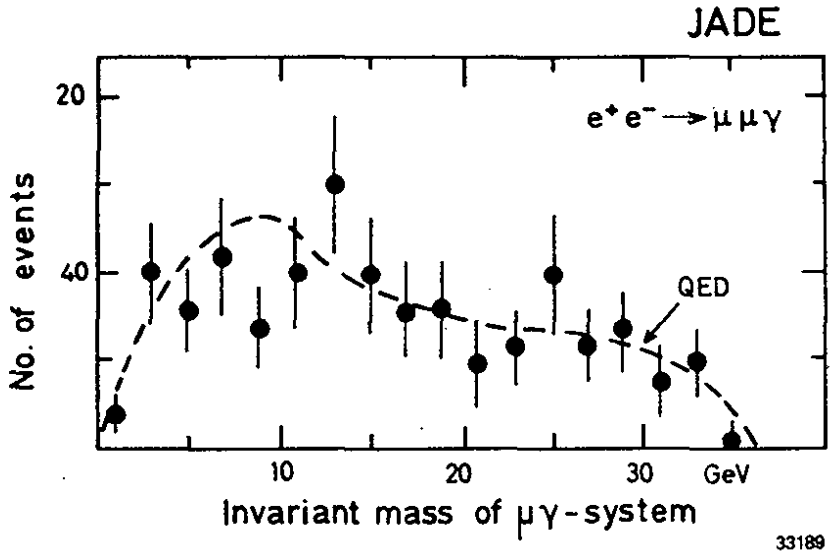

Fig. 10.12 - The effective ($\mu\gamma$) mass distribution observed by the JADE Collaboration in events of the type $e^+e^- \rightarrow \mu^+\mu^-\gamma$. Each event gives two entries. The dashed line represents the QED prediction.

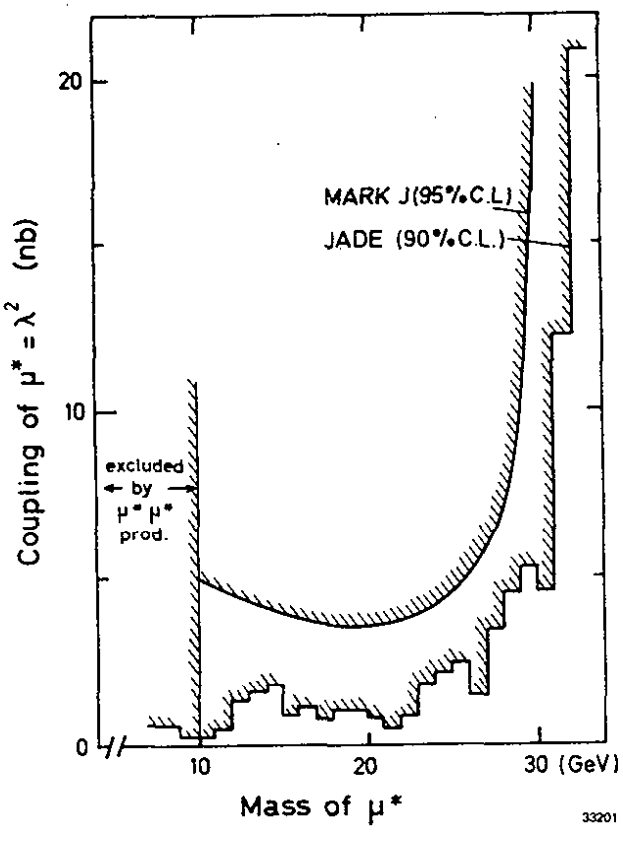

Fig. 10.13

Upper limits to the ($\mu^+\mu\gamma$) coupling constant ($\lambda\alpha$) plotted versus the μ^+ mass.

The MARK J Collaboration - in a similar analysis - found 11 $\mu\mu\gamma$ events compared to 12 events predicted for QED. The resulting 95% limit on Λ^2 is also plotted in Fig. 10.13 and corresponds to

$$\sigma(e^+e^- \to \mu\mu^*) \; / \; \sigma_{\mu\mu} < 0.035 \text{ (95\% C.L.) for a 16 GeV } \mu^* \; .$$

Similar searches[37] for excited muons have been carried out by the MAC and MARK II Collaborations at PEP. The data are in good agreement with the QED prediction resulting in similar mass limits on a hypothetical μ^* as listed above.

10.5.2 Excited state of the electron.

An excited state of the electron with a non vanishing coupling $e^*e\gamma$ will contribute as a t-channel exchange in $e^+e^- \to \gamma\gamma$ and modify the QED prediction. The data, discussed above in chapter 3, show that an excited lepton must have a mass greater than 50 GeV if $\alpha^* = \alpha$.

10.6 Search for Technipions

It is generally accepted that the gauge symmetry must be spontanously broken [351] to give mass to the intermediate vector bosons and make the theory renormalizable. However, there is no consensus how this symmetry breakdown is achieved. One mechanism is by introducing [32] I = 1/2 fundamental scalar Higgs fields. It has also been proposed [352] that the symmetry breakdown arises dynamically from the gauge interactions themselves. In this model a new set of unbroken non-Abelian gauge interactions with a mass scale on the order of 1 GeV/c^2 is introduced. The interaction gives the rise to a complicated spectrum [345] of technicolour less bound states with masses starting around 1 TeV/c^2. In addition, technicolour interactions will result in massless pseudoscalar mesons analogous to the pion in QCD. In the extended technicolour scheme which also gives mass to leptons and quarks there are more light pseudoscalars than can be eaten by the longitudinal polarization states of the gauge bosons. In particular we expect charged pointlike pseudoscalar particles with a mass perhaps between 5 and 14 GeV/c^2 and decay modes similar to those of the "normal" Higgs meson.

These particles p^+, p^- will be pairproduced in e^+e^- annihilation with cross section for a pointlike scalar particle

$$10.10 \quad \sigma(e^+e^- \to p^+p^-) = \frac{4\pi\alpha^2}{3s}\frac{\beta^3}{4} \qquad \text{with } \beta = p_p/E_B$$

Like the Higgs meson, they couple to mass and $BR(P \to \tau\nu) + BR(P \to \bar{c}s) \tilde{=} 1.0$. The relative importance of the two decay modes is model dependent, but it is unlikely that either of them is zero.

The production of technipions lead to distinct final states, however, the β^3 factor suppresses the cross section near threshold. It is therefore necessary to search at energies well above threshold such that the decays produce rather jetlike events and then the topology criteria for new thresholds are not very useful

The JADE group searched[332] for technipion pairproduction demanding that one of the technipions decays into $\tau\nu$ and the other into $c\bar{s}$. This lead to events where the thrust axis of the $c\bar{s}$ jet does not line up with the thrust axis defined by the τ decay due to the momentum carried off by the neutrinos. Specifically the JADE Collaboration select events with the thrust axis inside the full detector acceptance. The event was divided into two hemispheres by means of a plane normal to the thrust axis. The high energy hemisphere should contain at least 63% of the beam energy. In the low energy hemisphere there should be at least one charged particle and further charged particles should make an angle of at least 70^0 with respect to the thrust axes. The thrust axes, determined individually for each hemisphere, should be acoplanar with the beam axis to at least 70^0. Only one event satisfied the cuts in a sample of approximated 10000 nb^{-1}. The corresponding 90% C.L.mass limit on a technipion as a fraction of $BR(p \to \tau\nu)$ is plotted in Fig. 10.14.

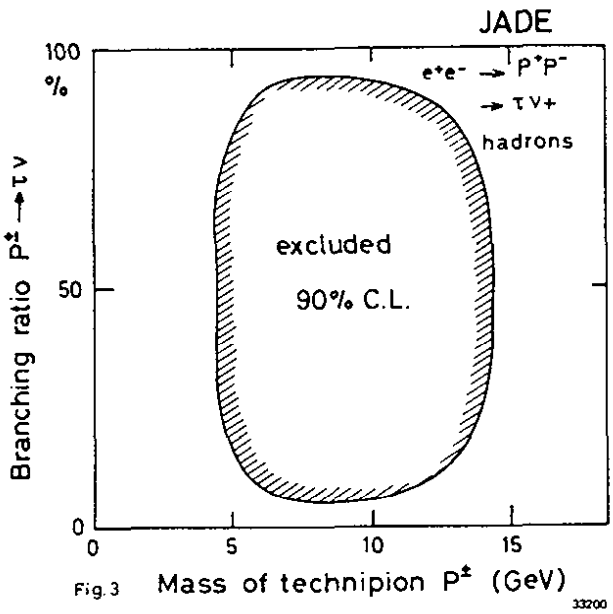

Fig.3

Fig. 10.14

The 90% C.L. mass limit boundary on charged technipions P is plotted for $B(P \to \tau\nu)$ versus the mass of the technipion

10.7 Search for supersymmetric particles

Gauging the isospin led to the successful unification of electromagnetic and weak interactions. In supersymmetric theories [353] the spin is gauged and this leads to a connection between fermions and bosons. Indeed the fundamental feature of supersymmetry is that it can generate fermions from bosons and vice versa. Thus for every particle with spin J there will be two new particles with spin $J \pm 1/2$. A partial list of such new particles based on the phenomenology proposed by Farrar and Fayet [354] is given below.

Electron-positron interactions are well suited [345] to search for supersymmetric heavy leptons, scalar-quarks and scalar leptons. So far, detailed searches have only been carried out for scalar leptons.

Table 10.5 - Possible supersymmetric particles

Type of conventional particles	s p i n 1	1/2	0
Matter		quark q leptons ℓ	scalar quarks s_q scalar leptons s_ℓ
Massive Gauge bosons	$W^\pm$	supersymmetric heavy leptons $\tilde{W}^\pm$, $\tilde{Z}^0$, $\tilde{H}$	Higgs scalar
Massless Gauge Bosons	g	photino $\tilde{\gamma}^2$ + other nuinos $\tilde{\nu}$ gluinos $\tilde{g}$	

The pair production of scalar leptons in e^+e^- annihilation lead to a distinct final state. According to the possible production graphs and decay modes shown in Fig. 10.15 we expect

$$e^+e^- \to \tilde{s}\,\bar{\tilde{s}} \to e^+e^- + \text{photinos}$$

$$e^+e^- \to \tilde{s}_\mu\,\bar{\tilde{s}}_\mu \to \mu^+\mu^- + \text{photinos}\ .$$

i.e. a final state with two leptons acoplanar with respect to the beam axis and with missing energy.

The CELLO group has carried out a search [355] for scalar leptons at an average c.m. energy of 34.6 GeV. They selected two prong events with an acoplanarity angle with respect to the beam axis of at least 30^o. After examining the surrounding shower counter they found that all such events have neutral energy deposited in the shower counters and could be explained as radiative QED events. The number of expected scalar lepton events satisfying their selection criteria is plotted in Fig. 10.16 ver-

sus the mass of the scalar lepton. The experimental limit is shown as the dashed line. The resulting mass limits are listed in Table 10.6 together with earlier results.

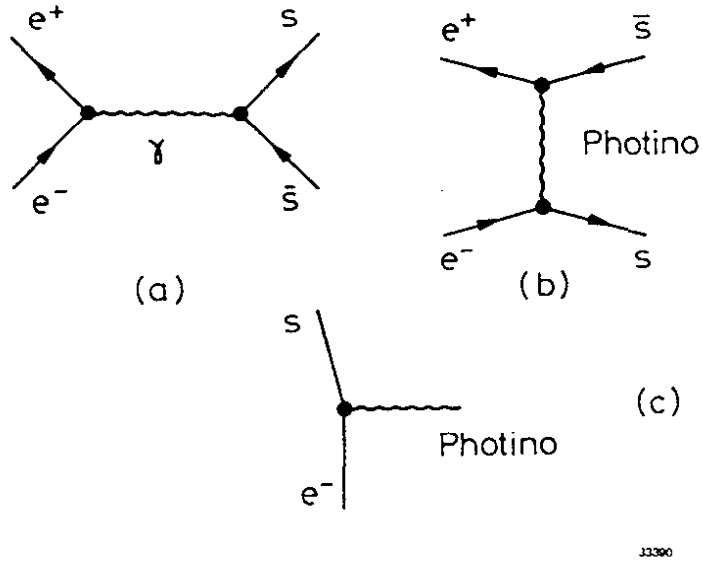

Fig. 10.15
Possible production and decay modes for scalar leptons

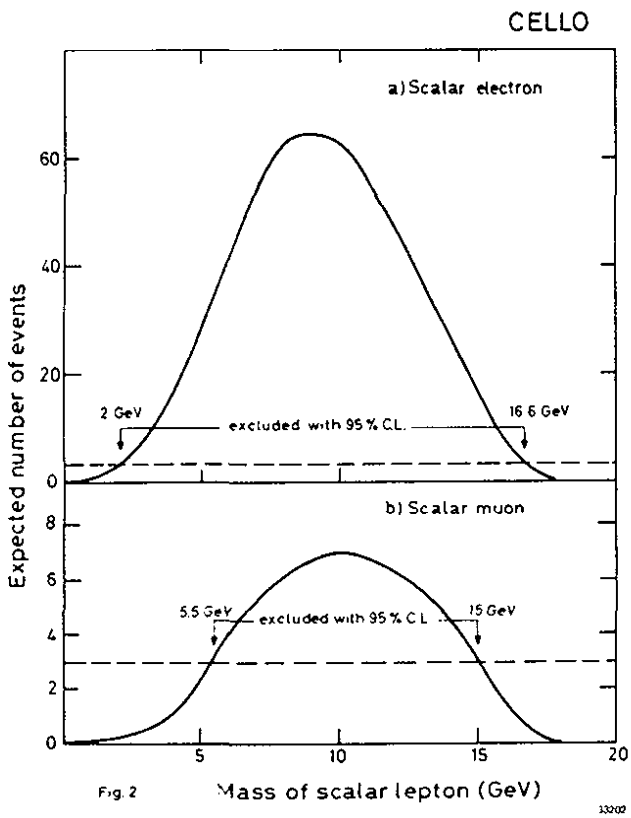

Fig. 10.16
Number of scalar leptons satisfying the selection criteria plotted versus lepton mass. The 95% C.L. are shown. The data were taken by the CELLO group.

Table 10.6 - Masslimits on scalar leptons

Collaboration	Mass limits in GeV		
	Electron	Muon	Reference
CELLO	5.5 < > 15	2 < > 16.6	355
JADE	> 16	-	175
MARK J		> 15	333
PLUTO	> 13		

10.8 Search for the axion

A possible mechanism to explain[357] the observed CP conservation in the strong interaction requires[358] the existence of a light boson, the axion.

Several beamdump experiments have searched[359] for axions with negative results. Recently, however, evidence for the existence of a light particle decaying into two photons has been presented[360].

The MARK II group at SPEAR has searched[122] for axions in the decay $J/\psi \to \gamma$ + axion. Since the axion a does not interact and is assumed to be light the signature for the decay $J/\psi \to \gamma$ + axion is simply a monoenergetic photon with an energy of about 1.5 GeV. In a sample of $1.43 \cdot 10^6$ J/ψ decays they found 5 candidates. These candidates could all be explained as cosmic ray events and they extracted the 90% upper confidence limit of $BR(J/\psi \to \gamma\, a) < 3 \cdot 10^{-5}$. Peccei[360] has estimated an upper limit on the branching ratio of $5 \cdot 10^{-5}$.

References

1) C.Bernardini, G.F.Corazza, G.Ghigo and B.Touschek,
Nuovo Cimento 18, 1293 (1960)

2) "Design Study of a 15 to 100 GeV e^+e^- Colliding Beam Machine"
CERN / ISR-LEP / 78-17 and later updates

3) PETRA proposal, DESY Report 1974 and later update

4) K.Robinson and G.A.Voss, CEA Report CEA-TM-149 (1965)
K.Steffen, Internal Report DESY M-79/07

5) For a very clear discussion on e^+e^- colliders and related references see:
M.Sands in: Physics with intersecting Storage Ring,
B.Touschek, ed. Academic Press, New York 1971, 257

6) For a more recent review see:
W.Schnell, CERN N-ISR-RF / 81-21

7) S.D.Drell, D.J.Levy, and T.M.Yan, Phys.Rev. 187, 2159 (1969) and
Phys.Rev. D1, 1617 (1970)

8) N.Cabibbo, G.Parisi, and M.Testa, Lett.Nuovo Cimento 4, 35 (1970)

9) J.D.Bjorken and S.J.Brodsky, Phys.Rev. D1, 1416 (1970)

10) R.P.Feynman, Photon-Hadron Interactions Benjamin, Reading Mass., 1972

11) The first quantitative discussion on the experimental implications
of gluon bremsstrahlung in e^+e^- annihilation was given by:
J.Ellis, M.K.Gaillard and G.G.Ross, Nucl.Phys. B 111, 253 (1976)
- erratum B 130, 516 (1977)
see also: T.A.DeGrand, Yee Jack Ng, and S.H.H.Tye,
Phys.Rev. D 16, 3251 (1977)

12) J.Kogut and L.Susskind, Phys.Rev. D9, 697, 3391 (1974)
A.M.Polyakov, Proceedings of the 1975 International Symposium on
Lepton and Photon Interactions at High Energies,
Standord, August 1975

13) T.Appelquist, H.D.Politzer, Phys.Rev.Lett 34, 43 (1975)

14) H.Fritzsch, M.Gell-Mann and H.Leutwyler, Phys.Lett. 47B, 365 (1973)
D.J.Gross and F.Wilczek, Phys.Rev.Lett. 30, 1343 (1973)
H.D.Politzer, Phys.Rev.Lett. 30, 1346 (1973)
S.Weinberg, Phys.Rev.Lett. 31, 31 (1973)
For recent reviews see: A.J.Buras, Rev.Mod.Phys. 52, 199 (1980)
E.Reya, Phys.Report 69, 195 (1981)

15) E.J.Williams, Kgl.Danske Videnskab.Selskab, Mat.Fys.Medd. 13 No. 4 (1934)
L.Landau and E.Lifshitz, Physik Z, Sovjetunion 6, 244 (1934)
A.Jaccarini, N.Arteaga-Romero, J.Parisi and P.Kessler, Compt.Rend. 269 B, 153, 1129 (1969)
Nuovo Cimento 4, 933 (1970)

16) For a review see: H.Terazawa, Rov.Mod. Phys. 45, 615 (1973)

17) S.M.Berman, J.D.Bjorken and J.B.Kogut, Phys.Rev.D4, 3388 (1971)

18) JADE: Proposal to construct a detector at PETRA by DESY, Hamburg, Heidelberg, Lancaster, Manchester, Rutherford and Tokyo

19) Crystal Ball Collaboration: Caltech, Harvard, Princeton, SLAC, Stanford, - E.D.Bloom, XIVth Recontre de Moriond, Les Arcs, France, March 11-23, 1979

20) J.Steinberger, Proc. of the 1976 CERN School of Physics CERN 76-20
F.W.Büßer, Proc. of the 19th Internationale Universitätswochen für Kernphysik, Schladming, Styria, Austria (1980)

R.Turlay, Lectures given at the XVI International School of Elementary Particle Physics, Kupari, Dubrovnik (1980)
and at the XX Cracow School of Theoretical Physics (1981)
Department de Physique des particules elementaires (DPh PE 81-02)

21) F.Sciulli - Hadron structure from lepton beams
XX International Conference on High Energy Physics
Madison, Wisconsin, 1980

22) P.C.Bosetti et al., Phys.Lett. 70B, 273 (1977)

23) CHDS Collaboration, M.Holder et al., Nucl.Instr. and Methods 148, 235 (1978) and ibid 151, 69 (1978)

24) CHARM Collaboration, A.N.Diddens et al., NIM 178, 27 (1980)

25) W.K.H.Panofsky, Proceedings of the XIV International Conference on High Energy Physics, Vienna, Austria, 1968

26) The SLED Scheme was first suggested by P.B.Wilson, SLAC

27) EMC Collaboration, O.C.Allkofer et al., Nucl.Instr. and Methods 79, 445 (1981)

28) CHIO Collaboration, B.A.Gordon et al., Phys.Rev. D 20, 2645 (1979)

29) BCDMS Collaboration, D.Bollini et al., Phys.Lett. 104B, 403 (1981)

30) S.L.Glashow, Nuclear Phys. 22, 579 (1961)
S.Weinberg, Phys.Rev.Lett. 19, 1264 (1967)
A.Salam, Elementary Particle Theory, ed. N.Svartholm (Almquist and Wiksell, Stockholm, 1968, p. 367

31) R.P.Feynman and M.Gell-Mann, Phys.Rev. 109, 193 (1958)
E.C.G.Sudarshan and R.E.Marshak, Phys.Rev. 104, 1860 (1958)
J.J.Sakurai, Nuovo Cimento 7, 647 (1958)

32) P.W.Higgs, Phys.Rev.Lett. 13, 508 (1964)

33) M.Kobayashi and T.Maskawa, Progr. Theoret.Phys. 49, 652 (1973)

34) J.E.Kim, P.Langacker, M.Levine and H.H.Williams, Rev. Mod. Phys. 53, 211 (1980)

35) For a recent review see:
P.Dittmann and V.Hepp, Zeit.Phys. C10, 283 (1981)

36) J.G.Branson, 1981 International Symposium on Lepton and Photon Interactions at High Energies, Bonn, August 1981

37) R.Hollebeek, 1981 International Symposium on Lepton and Photon Interactions at High Energies, Bonn, August, 1981

38) B.Kayser et al., Phys.Rev. D 15, 3407 (1977) and D 20, 87 (1979)

39) F.Reines et al., Phys.Rev.Lett. 37, 315 (1976)

40) F.J.Hasert et al., Phys.Lett. 46B, 121 (1973)

41) J.Blietschau et al., Nucl.Phys. B 114, 189 (1978)
and Phys.Lett. 73B, 232 (1978)

42) N.Armenise et al., Phys.Lett. 86B, 225 (1979)

43) D.Bertrand et al., PETHA preprint 79/07 (1979)

44) N.Armenise et al., Phys.Lett. 81B, 385 (1979)

45) A.M.Cnops et al., Phys.Rev.Lett. 41, 357 (1978)

46) J.P.Berge et al., Phys.Lett. 84B, 357 (1979)

47) H.Faissner et al., Phys.Rev.Lett. 41, 213 (1978)

48) R.H.Eisterberg et al., Phys.Rev.Lett. 44, 635 (1980)

49) M.Jonker et al., Phys.Lett. 105 B, 242 (1981)

50) R.Budny and A.McDonals, Phys.Lett. 48B, 423 (1974)
R.Budny, Phys.Lett. 55 B, 227, (1975)
J.Ellis and M.K.Gaillard, CERN 76/18

51) F.A.Berends, K.F.J.Gaemers and R.Gastmans,
Nucl.Phys. B 63, 381 (1973)
F.A.Berends, K.J.F.Gaemers and R.Gastmans,
Nucl.Phys. B 68, 541 (1974)
F.A.Berends and R.Kleiss, DESY-Report 80-66 (1980)

52) F.A.Berends and G.J.Komen, Phys.Lett. 63B, 432, 1980

53) JADE Collaboration, W.Bartel et al., DESY 81-072, 1981

54) H.Georgi and S.Weinberg, Phys.Rev. D17, 275 (1978)

55) J.D.Bjorken, Phys.Rev. D19, 335 (1979)

56) E.H.de Groot, G.J.Gounaris and D.Schildknecht, Phys.Lett. 85B,
399 (1979), Phys.Lett. 90B, 427 (1980) and Zeit. Phys. C 5, 127 (1980)
E.H.de Groot and D.Schildknecht, Phys.Lett. 95B, 149 (1980)

57) V.Barger, W.Y.Keung and E.Ma, Phys.Rev.Lett. 44, 1169 (1980)

58) P.A.Hung and J.J.Sakurai, preprint LBL-12364

59) F.W.Büsser, International Conference on Neutrino Physics and Astrophysics 1981, Wailea, Maui, Hawaii - USA

60) P.Q.Hung, and J.J.Sakurai, Phys.Lett. 63B, 295 (1976)

61) E.A.Paschos, L.Wolfenstein, Phys.Rev. D7, 91 (1973)

62) C.Geweniger, International Conference 1979, Bergen, Norway

63) M.Jonker et al., Phys.Lett. 99B, 265 (1981)

64) M.Shaevitz, International Conference on Neutrino Physics and Astrophysics 1981, Wailea, Maui, Hawaii-USA

65) Illinois-Maryland-Stony Brook-Tohoku-Tufts Collaboration, International Conference on Neutrino Physics and Astrophysics 1981 - Wailea, Maui, Hawaii, USA

66) J.Blietschau et al., Phys.Lett. 88 B, 381 (1979)

67) F.A.Harris et al., Phys.Rev.Letters 39, 437 (1977)

68) M.Derrick et al., Phys.Rev. D18, 7 (1978)

69) J.Marriner - LBL-6438 (1977) Thesis

70) V.I.Efremenko et al., Phys.Lett. 84B, 511 (1979)

71) Bari-Birmingham-Brussels-Ecole Polytechnique-Rutherford-Saclay-University College London Collaboration
International Conference on Neutrino Physics and Astrophysics 1981, Wailea, Maui, Hawaii, USA

72) J.Okada, S.Pakvasa, Nucl.Phys. B 112, 400 (1976)

73) P.W.Hung, Phys.Lett. 69B, 216 (1977)
L.M. Sehgal, Phys.Lett. 71B, 99 (1977)

74) H.Kluttig et al., Phys.Lett. 71B, 446 (1977)

75) L.M.Sehgal, Phys.Lett. 71B, 99 (1977)

76) GGM Collaboration, D.Haidt, Proc. of the 1977 International Symposium on Lepton and Photon Interactions at High Energies, Hamburg, 1977

77) E.Pasierb et al., Phys.Rev.Lett. 43, 96 (1979)

78) S.L.Glashow, J.Iliopoulos, L.Maiani, Phys.Rev. D2, 1285 (1970)

79) L.M.Seghal, Proc. Intern. Neutrino Conference 1978 (Purdue), p. 263

80) M.Jonker et al., Physics Lett. 102B, 67 (1981)

81) CDHS Collaboration, International Conference on Neutrino Physics and Astrophysics 1981, Wailea, Maui, Hawaii, USA

82) Y.B.Zel'dovich, JETP-9, 682 (1959)

83) M.A.Bouchiat and C.Bouchiat, Phys.Lett. 47B, 111 (1974)

84) L.M.Barkov and M.S.Zolotorev, Phys.Lett. 85B, 308 (1979)

85) P.E.G.Baird et al., Phys.Rev.Lett. 39, 798 (1977)

86) P.E.G.Baird, Proc.International Workshop on Neutral current interactions in atoms, Cargese p. 77

87) Y.V.Bogdanov et al., JETP Lett. 31, 214 (1977)

88) J.L.Lewis et al., Phys.Rev.Lett. 39, 795 (1977)

89) J.H.Hollister et al., Phys.Rev.Lett. 46, 643 (1981)

90) P.H.Bucksbaum et al., Phys.Rev. D24, 1134 (1981) and Phys.Rev.Lett. 46, 640 (1981)

91) V.N.Novikov, O.P.Sustkov and I.B.Khriplovich
JETP 46, 420 (1976)
P.G.H.Sandars, Physica Scripta 21, 289 (1980)
A.M.Märtenson, E.M.Henley, L.Wilets,
Univ. of Washington preprint, submitted to Phys.Rev. A

92) E.D.Commins, P.H.Bucksbaum, Ann.Rev.Nucl. Part. Sci. 30, 1 (1980)

93) C.Prescott et al., Phys.Lett. 77B, 347 (1978)
C.Prescott et al., Phys.Lett. 84B, 524 (1979)
C.Prescott et al., Phys.Lett. 72B, 489 (1980)

94) R.N.Cahn and F.J.Gilman, Phys.Rev. D17, 1313 (1978)

95) MARK J Collaboration, D.P.Barber et al., Phys.Rev.Lett. 64, 1663 (1981)

96) JADE Collaboration, W.Bartel et al., Phys.Lett. 101B, 361 (1981)

97) S.L.Glashow and S.Weinberg, Phys.Rev. D15, 1958 (1977)

98) G.Goldhaber et al., SLAC-PUB 1973, LBL 6467 (1977)

99) G.Feldman et al., Phys.Rev.Lett. 38, 1313 (1977)

100) A.Silverman, 1981 International Symposium on Lepton and Photon Interactions at High Energies, Bonn, August 1981

101) For a general review see: J.J.Sakurai, Neutrino-81, International Conference on Neutrino Physics and Astrophysics, Wailea, Maui, Hawaii 1981
J.Meyer, CERN EP, Internal Report 80-09

102) For a review see: F.Scheck, Phys.Rep. C 44, 187 (1978)

103) S.Shrock and L.L.Wang, Phys.Rev.Lett. 41, 1692 (1978)

104) M.Bourquin et al., Universitê Paris-Sud, LAL 81/18

105) R.L.Kingsley et al., Phys.Rev. D 10, 2216 (1974)

106) B.Kayser et al., Phys.Lett. 52B, 385 (1974)

107) M.Jonker et al., Phys.Lett. 86B, 229 (1979)

108) N.Armenise et al., Phys.Lett. 84B, 137 (1979)

109) M.Jonker et al., Phys.Lett. 93B, 203 (1980)

110) J.C.Pati and A.Salam, Phys.Rev. D8, 1240 (1973) and
Phys.Rev. D 10, 275 (1974)

111) G.Georgi and S.L.Glashow, Phys.Rev.Lett. 32, 438 (1974)

112) W.J.Marciano and A.Sirlin, Phys.Rev.Lett. 46, 163 (1981)

113) M.Perl et al., Phys.Rev.Lett. 35, 1489 (1975)

114) For a general review see: M.L.Perl, Ann.Rev.Nucl.Part.Sci. 30, 299 (1980)

115) DASP Collaboration, R.Brandelik et al., Phys.Lett.73B, 109 (1978)

116) W.Bacino et al., Phys.Rev.Lett. 41, 13 (1978)

117) W.Bacino et al., Phys.Rev.Lett. 42, 749 (1979)

118) H.B.Thacker, J.J.Sakurai, Phys.Lett. 36B, 103 (1971)
Y.S.Tsai, Phys.Rev. D4, 2821 (1971)
J.D.Bjorken, C.H.Llewellyn-Smith, Phys.Rev. D7, 887 (1973)
For a recent review see: Y.S.Tsai, SLAC-PUB-2105 (1978)

119) The most recent measurement of $\tau \to \nu_\tau \pi$ is by C.A.Blocker et al., SLAC-PUB-2785

120) G.S.Abrams et al., Phys.Rev.Lett. 43, 1555 (1979)

121) J.M.Dorfan et al., Phys.Rev.Lett. 46, 215 (1981)

122) F.C.Porter, SLAC-PUB-2785

123) G.J.Feldman et a., SLAC-PUB-2819 (1981)

124) For a recent review of $q\bar{q}$ spectroscopy and a complete set of references see: T.Appelquist, R.M.Barnett, and K.Lane, Ann.Rev.Nucl.Part.Sci.28, 387 and Ch.Quigg, Les Houches Lectures 1981

125) T.Appelquist and H.D.Politzer, Phys.Rev. D12, 1404 (1978)

126) R.Van Royen and V.F.Weisskopf, Nouvo Cimento 50A, 617 (1967)

127) L.B.Okun and M.Voloshin, Zh.Eksper.Theor.Fiz. 23, 369 (1976)
C.Rosenzweig, Phys.Rev.Lett. 36, 697 (1976)
M.Bander et al., Phys.Rev.Lett. 36, 695 (1976)
A.De Rujula et al., Phys.Rev.Lett. 38, 317 (1977)

128) R.C.Giles and S.H.H.Tye, Phys.Rev.Lett. 37, 1170 (1976)
W.Buchmüller and S.H.H.Tye, Phys.Rev.Lett. 44, 880 (1980)
P.Hasenfratz et al., CERN Preprint TH 2837

129) J.J.Aubert et al., Phys.Rev.Lett. 33, 1404 (1974)
J.E.Augustin et al., Phys.Rev.Lett. 33, 1406 (1979)
G.S.Abrams et al., Phys.Rev.Lett. 33, 1453 (1974)
P.A.Rapidis et al., Phys.Rev.Lett. 39, 526 (1977)
DASP Collaboration, R.Brandelik et al., Phys.Lett. 76B, 361 (1978)
J.Siegrist et al., Phys.Rev.Lett. 36, 700 (1976)
PLUTO Collaboration, J.Burmester et al., Phys.Lett. 66B, 395 (1977)
E.D.Bloom SLAC-PUB-2745. To be published in the Proceedings of the Sixteenth Rencontre de Moriond, Les Arcs, France, March 1981,
A.A.Zholentz et al., Phys.Lett. 96B, 214 (1980)

130) DASP Collaboration, W.Braunschweig et al., Phys.Lett. 57B, 407 (1975)
G.J.Feldman et al., Phys.Rev.Lett. 35, 821 (1975)

131) DASP Collaboration, W.Braunschweig et al., Phys.Lett. 67B, 243 (1977)

132) J.S.Whitaker et al., Phys.Rev.Lett. 37, 1596 (1976)

133) W.Bartel et al., Phys.Rev.Lett. 79B, 492 (1978)

134) D.L.Scharre, Proceedings of the 1981 International Symposium on Lepton and Photon Interactions at High Energies, Bonn, August 1981
D.L.Scharre, International Conference on Physics in Collisions, Blacksbury, Virginia, 1981 and SLAC-PUB-2761

135) For a review of the experimental data up to the end of 1978 see:
B.H.Wiik and G.Wolf, Electron-Postron Interactions,
Springer Tracts in Modern Physics, Vol. 86, 1979

136) D.L.Scharre, Stanford Linear Accelerator Center
Report SLAC-PUB-2761

137) E.Eichten, K.Gottfried, T.Kinoshita, K.D.Lane, and T.M.Yan
Phys.Rev. D 21, 203 (1980)

138) T.M.Himel et al., Phys.Rev.Lett. 34, 1357 (1979)

139) R.Partridge et al., Phys.Rev.Lett. 45, 1150 (1980)

140) T.M.Himel et al., Phys.Rev.Lett. 45, 1146 (1980)

141) S.W.Herb et al., Phys.Rev.Lett. 39, 252 (1977)

W.R.Innes et al., Phys.Rev.Lett. 39, 1240 (1977)

142) PLUTO Collaboration, Ch.Berger et al., Phys.Lett. 76B, 243 (1978)
DASP2 Collaboration, C.W.Darden et al., Phys.Lett. 76B, 246 (1970)

143) J.K.Bienlein et al., Phys.Lett. 78B, 360 (1979)
C.W.Darden et al., Phys.Lett. 78B, 364 (1979)

144) D.Andrews et al., Phys.Rev.Lett. 44, 1108 (1980) and 45, 219 (1980)
T.Böhringer et al., Phys.Rev.Lett. 44, 1111 (1980)
G.Finocchiaro et al., Phys.Rev.Lett. 45, 222 (1980)

145) J.L.Rosner, C.Quigg and H.B.Thacker, Phys.Lett. 74B, 350 (1978)

146) D.Schamberger: Proceedings of the 1981 International Symposium on Lepton and Photon Interactions at High Energies, Bonn, August 1981

147) W.Schmidt-Parzefall, Proceedings of the XX International Conference on High Energy Physics, Madison, Wisconsin, July 1980

148) J.K.Bienlein, Proceedings of the 1981 International Symposium on Lepton and Photon Interactions at High Energies, Bonn, August 1981 and DESY Report 81/076

149) G.Goldhaber and J.E.Wiss, Ann.Rev.Nucl.Part.Sci.28, 387 (1978)
R.H.Schindler et al., Phys.Rev. D21, 2716 (1980)

150) R.A.J.Lankford, Proceedings of the XX International Conference on High Energy Physics, Madison, Wisconsin, July 1980

151) A.Pais and S.B.Treiman, Phys.Rev. D15, 2529 (1977)

152) W.Bacino et al., Phys.Rev.Lett. 45, 329 (1980)

153) For a review the emulsion data see
J.Prentice, Proceedings of the EPS International Conference on High Energy Physics, Lisbon, 1981

154) F.Foa, Proceedings of the 1981 International Symposium on Lepton and Photon Interactions at High Energies, Bonn, August 1981

155) N.Cabibbo and L.Maiani, Phys.Lett. 79B, 109 (1978)
N.Cabibbo, G.Corbo, and L.Maiani, Nucl.Phys. B 155, 93 (1979)

156) H.Fritsch, Proceedings of the 1981 International Symposium on Lepton and Photon Interactions at High Energies, Bonn, August 1981

157) G.S.Abrams et al., Phys.Rev.Lett. 43, 481 (1979)

158) J.Knobloch, Neutrino-81, International Conference on Neutrino Physics and Astrophysics, Wailea, Maui, Hawaii, 1981
and J.Allaby ibid.

159) S.Pakraso, S.F.Tuan and J.J.Sakurai, Phys.Rev. D23, 2799 (1981)

160) DASP Collaboration, R.Brandelik et al., Phys.Lett. 70B, 132 (1977) and Phys.Lett. 80B, 412 (1979)

161) D.Aston et al., Phys.Lett. 100B, 91 (1981) and preprint CERN-EP / 81-47, 1981

162) J.Leveille, University of Michigan - U MHE 81-018 (1981)

163) V.Lüth, Proceedings of the International Symposium on Photon and Lepton Interactions at High Energy, Batavia, Illinois (1979)

164) T.Appelquist and H.Georgi, Phys.Rev. D8, 4000 (1973)
A.Zee, Phys.Rev. D8, 4038 (1973)
G.'t Hooft, Nucl.Phys. B 62, 444 (1973)
M.Dine and J.Sapirstein, Phys.Rev.Lett. 43, 668 (1979)
W.Celmaster and R.J.Gonsalves, Phys.Rev.Lett. 44, 560 (1979)
K.G.Chetyrkin, A.L.Kataev and F.V.Tkachov, Phys.Lett. 85B, 277 (1979)
USSR Academy of Sciences, Institute of Nuclear Research Preprint D-0178 (1980)

165) R.Felst, 1981 International Symposium on Lepton and Photon Interactions at High Energies, Bonn, August 1981

166) A.Quenzer, thesis, Orsay Report LAL 1299 (1977)
A.Cordier et al., Phys.Lett. 81B, 389 (1979)
V.A.Sidorov, Proceedings of the XVIII International Conference on High Energy Physics, Tbilisi, USSR, B13 (1976)
R.F.Schwitters, Proceedings of the XVIII International Conference on High Energy Physics, Tbilisi, USSR, July 1976
J.Perez-Y-Jorba, Proceedings of the XIX International Conference on High Energy Physics, Tokyo, 1978
PLUTO Collaboration, J.Burmester et al., Phys.Lett. 66B, 395 (1977)
DASP Collaboration, R.Brandelik et al., Phys.Lett. 76B, 361 (1978)

167) J.Siegrist, Report No. SLAC-225 (1979)

168) R.M.Barnett, M.Dine and J.McLerran, Phys.Rev. D 22, 594 (1980)

169) J.Jersak, E.Laermann, P.M.Zerwas, Phys.Lett. 98B, 363 (1981)

170) For a recent review and a complete set of references see:
M.E.Peskin, 1981 International Symposium on Lepton and Photon Interactions at High Energies, Bonn, August 1981

171) P.Söding and G.Wolf, DESY 81-013 and Ann.Rev.Nucl.Part. Sci. - Volume 31, 1981

172) J.D.Bjorken and S.J.Brodsky, Phys.Rev. D1, 1416 (1970)

173) E.Farhi, Phys.Rev.Lett. 39, 1587 (1979)
S.Brandt and H.D.Dahmen, Zeit. Phys. C 1, 61 (1979)

174) R.F.Schwitters et al., Phys.Rev.Lett. 35, 1320 (1975)

175) D.Cords, Proceedings XX International Conference on High Energy Physics, Madison, Wisconsin, 1980

176) T.F.Walsh and P.Zerwas, Nucl.Phys. B 77, 494 (1979)

177) TASSO Collaboration, R.Brandelik et al., Phys.Lett. 100B, 357 (1981)

178) R.D.Field and R.P.Feynman, Nucl.Phys. B 136, 1 (1978)

179) E.Bloom, Proceedings of the 1979 International Symposium on Lepton and Photon Interactions at High Energies, Fermilab (1979)

180) J.C.Pati and A.Salam, Nucl.Phys. B 144, 445 (1978)

181) TASSO Collaboration, R.Brandelik et al., Phys.Lett. 89B, 418 (1980)
PLUTO Collaboration, Ch.Berger et al., Phys.Lett. 95B, 313 (1980)

182) C.Bacci et al., Phys.Lett. 86B, 234 (1979)
Lena Collaboration, B.Niczyporuk et al., DESY 81-008
J.L.Siegrist, SLAC-225 (1979)

183) A.Bassetto, M.Ciafaloni and G.Marchesini, Phys.Lett. 83B, 207 (1978)
W.Furmanski, R.Petronzio and S.Pokorski, Nucl.Phys. B155, 253 (1979)
K.Konishi, Rutherford Preprint RL-79-035 T 241 (1979)
A.H.Mueller, CU-TP 197, Columbia University (1981)

184) E.Fermi, Prog. Theor.Phys. 5, 570 (1950)

185) TASSO Collaboration, R.Brandelik et al., DESY Report 81/69, 1981

186) TASSO Collaboration, R.Brandelik et al., Phys.Lett. 94B, 444 (1981)

187) PLUTO Collaboration, Ch.Berger et al., Phys.Lett. 104B, 79 (1981)

188) TASSO Collaboration, R.Brandelik et al., Phys.Lett. 94B, 91 (1981)

189) TASSO Collaboration, R.Brandelik et al., Phys.Lett. 105B, 75 (1981)

190) JADE Collaboration, W.Bartel et al., Phys.Lett. 104 B 325 (1981)

191) M.Holder, EPS International Conference on High Energy Physics, Lisbon 1981, University of Hamburg Preprint

192) B.Anderson et al., Lund University Preprint LU TP 81-03 (1981)
E.M.Ilgenfritz, J.Kripfganz, A.Schiller, Acta Phys.Pol. B9, 881 (1978)
A.Casher, H.Neuberger, S.Nussinov, Phys.Rev.D20, 179 (1979)
S.Ritter and J.Ranft, Acta Phys.Pol. B11, 259 (1980)
W.Hofmann, Z.Physik C10, 351 (1981)
G.Schierholz and M.Teper - DESY Report 81/41
M.Bowler, Oxford Univ. Report 76-81 (1981)

193) T.Meyer, DESY Report 81-046 (1981)

194) S.L.Wu - DESY Report 81/71 (1981)

195) S.D.Drell, D.J.Levy, and T.M.Yan, Phys.Rev. 187, 2159 (1969)
and Phys.Rev. D1, 1617 (1970)

196) K.Koller and T.F.Walsh, Nucl.Phys. B 140, 449 (1978)

197) PLUTO Collaboration, Ch.Berger et al., Phys.Lett. 78B, 176 (1978)
ibid 82B, 449 (1979)

198) S.Brandt and H.D.Dahmen, Zeit. Phys. C 1, 61 (1979)

199) T.F.Walsh and P.M.Zerwas, DESY 80/20

200) LENA Collaboration, B.Niczyporuk et al., Zeit. Phys. C 9, 1 (1981)
PLUTO Collaboration, Ch.Berger et al., Zeit. Phys. C 8, 101 (1981)

201) K.Koller and H.Krasemann, Phys.Lett. 88B, 119 (1979)

202) K.Gottfried, Phys.Rev. Lett. 40, 598 (1978)

203) K.Berkelman, Proceedings of the XXth International Conference
on High Energy Physics, Madison, Wisconsin, 1980

204) R.Barbieri et al., Phys.Lett. 57B, 455 (1978)
W.Celmaster, Phys.Rev. D19, 1517 (1979)

205) H.B.Thacker, C.Quigg, and J.L.Rosner, Phys.Rev. D18, 274 and 287 (1978)
C.Quigg and J.L.Rosner, Phys.Rev. D23, 2625 (1981)

206) H.Krasemann and S.Ono, Nucl.Phys. B 154, 282 (1979)

207) J.L.Richardson, Phys.Lett. 82B, 272 (1979)

208) A.Martin, Phys.Lett. 93B, 338 (1980)

209) W.Buchmüller, G.Grunberg, and S.H.H.Tye, Phys.Rev.Lett. 45, 103 (1980)

210) P.B.Mackenzie and G.P.Lepage
CLNS 81/498 (1981) submitted to Phys.Rev.Lett.

211) H.Fritzsch and M.Gell-Mann, Proceedings of the XVI International Conference on High Energy Physics, Chicago 1972

H.Fritzsch and P.Minkowski, Nuovo Cimento 30A, 343 (1975)

D.Robson, Nucl.Phys. B 130, 328 (1977)

K.Koller and T.Walsh, Nucl.Phys. B 140, 449 (1978)

212) G.S.Abrams et al., Phys.Rev.Lett. 44, 114 (1980)

212) D.L.Scharre et al., Phys.Lett. 97B, 329 (1980)

213) D.L.Scharre, in Experimental Meson Spectroscopy - 1980
edited by S.U.Chung and S.J.Lindenbaum (AIP, New York 1981)

214) Particle Data Group, Rev.Mod.Phys. 52, S 1 (1980)

215) C.Dionisi et al., Nucl.Phys. B 164, 1 (1980)

216) I.Cohen and H.J.Lipkin, Nucl.Phys. B 151, 16 (1979)

217) B.Berg, Phys. Lett. 97B, 401 (1980)

G.Bhanat and C.Rebbi, Nucl.Phys. B 189, 469 (1981)

J.Engels, F.Karsch, H.Satz and I.Montvay, Phys.Lett. 101B, 89 (1981) and 102 B, 332 (1981)

K.Ishikawa, M.Teper and G.Schierholtz, DESY Report 81-089

218) For an up to date review including references see:
A.J.Buras, Proceedings of the 1981 International Symposium on Lepton and Photon Interactions at High Energies, Bonn 1981

219) B.H.Wiik, Proceedings of the International Neutrino Conference, Bergen, Norway, June 1979

P.Söding, Proceedings EPS International Conference on High Energy Physics, Geneva, Switzerland, July 1979

220) TASSO Collaboration, R.Brandelik et al., Phys.Lett. 83B, 261 (1979)

221) MARK J Collaboration, D.P.Barber et al., Phys.Rev.Lett. 43, 830 (1979)

222) PLUTO Collaboration, Ch.Berger et al., Phys.Lett. 86 B, 418 (1979)

223) JADE Collaboration, W.Bartel et al., Phys.Lett. 91B, 142 (1980)

224) D.Fournier, Proceedings of the 1981 International Symposium on Lepton and Photon Interactions at High Energies, Bonn 1981

225) P.Hoyer, P.Osland, H.G.Sander, T.F.Walsh and P.M.Zerwas, Nucl.Phys. 161, 349 (1979)

226) A.Ali, E.Pietarinen, G.Kramer and J.Willrodt, Phys.Lett. 93B, 155 (1980)

227) B.Anderson, C.Gustafson and C.Peterson, Nucl.Phys. B135, 273 (1978)

B.Anderson and G.Gustafson, Z.Phys. C3, 223, 1980

B.Anderson, G.Gustafson and T.Sjöstrand - LU-TP-80-2

T.Sjöstrand, Lund Preprint, LU-TP-80-3

228) A.Casher, J.Kogut and L.Susskind, Phys.Rev.Lett. 31, 792 (1973)

229) G.Altarelli and G.Parisi, Nucl.Phys. B126, 298 (1977)

230) TASSO Collaboration, R.Brandelik et al., Phys.Lett. 94B, 437 (1980)

231) G.G.Hanson et al., Phys.Rev.Lett. 35, 1609 (1975)

232) Physics with High Energy Electron Positron Colliding Beams with MARK J Detector, Physics Report 63, 340 (19807

233) PLUTO Collaboration, Ch.Berger et al., Phys.Lett. 97B, 459 (1980)

H.J.Daum, H.Meyer and J.Bürger, DESY Report 80/101

234) J.Dorfan, Zeit. Phys. C 7, 349 (1981)

235) P.Söding, Particles and Fields Conference, Santa Cruz, 1981 DESY 81-070

236) W.Braunschweig, Proceedings of the 1981 International Symposium on Lepton and Hadron Interactions at High Energies, Bonn 1981

237) S.L.Wu and G.Zobernig, Z.Phys. C2, 207, 1979

238) H.Newman, Proceedings of the XX International Conference on High Energy Physics, Madison, Wisconsin, 1980

P.Duinker, DESY 81-012, submitted to Review of Modern Physics

239) S.Yamada, Proceedings of the XX International Conference on High Energy Interactions, Madison, Wisconsin 1980

R.Marshall, EPS International Conference on High Energy Physics, Lisbon 1981

240) JADE Collaboration, W.Bartel and A.Petersen, XV Rencontre de Moriond, Les Arces, March 9-21, 1980

241) J.Ellis and I.Karliner, Nucl.Phys.B 148, 141 (1979)

242) TASSO Collaboration, R.Brandelik et al., Phys.Lett. 94B, 437 (1980)

243) CELLO Collaboration, H.J.Behrend et al., 1981 DESY-Report 81/80

244) T.A.DeGrand, Y.J.Ng, and S.H.Tye, Phys.Rev. D 16, 3251 (1977)

J.F.Gunion, III International Warsaw Symposium on Elementary Particle Physics, UC Davies preprint 1981

245) PLUTO Collaboration, Ch.Berger et al., Phys.Lett. 97B, 459 (1980)

246) C.K.Chen, Phys.Rev. D 23, 712 (1981)

247) F.A.Berends and R.Kleiss, DESY Reports 80/66 and 80/73 (1980)

248) G.Sterman and S.Weinberg, Phys.Rev.Lett. 39, 1436 (1977)

249) K.Fabricius, I.Schmitt, G.Schierholtz and G.Kramer Phys.Rev.Lett. 97B, 431 (1980) and DESY Preprint 81-035 (1981)

250) R.K.Ellis, D.A.Ross and A.E.Terrano, Phys.Rev.Lett. 45, 1226 (1980) and Nucl.Phys. B 178, 421 (1981)

251) J.A.M.Vermaseren, K.J.F.Gaemers and S.J.Oldham, Nucl.Phys. B 187, 301 (1981)

252) T.D.Gottschalk, California Institute of Technology Report CALT 68-862

253) Z.Kunszt, Phys.Lett. 99B, 429 (1981)

254) CELLO Collaboration, H.-J.Behrend et al., DESY 81-080

255) PLUTO Collaboration, Ch.Berger et al., DESY 81-054

256) C.L.Basham, L.S.Brown, S.D.Ellis, and T.S.Love,
Phys.Rev.Lett. 41, 1581 (1978)
Phys.Rev. D 17, 2298 (1978) and Phys.Rev. D 19, 2018 (1979)

257) G.C.Fox and S.Wolfram, Nucl.Phys. B 149, 413 (1979)

258) PLUTO Collaboration, C.Berger et al., Phys.Lett. 99B, 292 (1981)

259) L.Clavelli and D.Wyler, preprint Univ. Bonn HE-81-3

260) A.Ali, DESY Report 81/59

261) K.Konishi, A.Ukawa, G.Veneziano, Nucl.Phys. B 157, 45 (1979)

262) A.Bassetto, M.Ciafaloni and G.Marchesini, Nucl.Phys. B 163, 477 (1980)

263) E.J.Williams, Kgl.Danski Videnskab Selskab.,
Mat.Fys. Medd. 13, No. 4 (1934)
L.Landau and E.Lifshitz, Phys. Z. Sov. 6, 244 (1934)

264) A.Jaccarini, N.Arteaga-Romero, J.Parisi and P.Kessler,
Compt. Rend. 269B, 153, 1129 (1969)
Nuovo Cimento 4, 933 (1970)
V.E.Balakin, V.M.Budnev, I.F.Ginzburg, JETP Lett. 11 388 (1970)
S.J.Brodsky, T.Kinoshita, H.Terazawa, Phys.Rev.Lett. 25, 972 (1970)
Phys.Rev. D4, 1532 (1971)

265) R.J.Wedemeyer, 1981 International Symposium on Lepton and Photon Interactions at High Energies, Bonn, August 1981

266) W.A.Bardeen, 1981 International Symposium on Lepton and Photon Interactions at High Energies, Bonn, August 1981

267) F.F.Low, Phys.Rev. 120, 582 (1960)

268) G.S.Abrams et al., Phys.Rev.Lett. 43, 477 (1979)

269) PLUTO Collaboration, Ch.Berger et al., Phys.Lett. 94B, 259 (1980)

270) TASSO Collaboration, R.Brandelik et al., DESY Report 81/020

271) A.Roussarie et al., Phys.Lett. 105B, 304 (1981)

272) CELLO Collaboration, contributed paper to the Lisbon Conference 1981

273) D.L.Burke, SLAC-PUB-2745 (1981)

274) J.A.M.Vermaseren, private communication
R.Bhattacharya, J.Smith and G.Gramm, Phys.Rev. D 15, 3267 (1977)

275) F.Calogero and C.Zemack, Phys.Rev. 120, 1860 (1960)
S.J.Brodsky and G.P.Lepage, SLAC PUB 2733

276) E.Hilger, XX International Conference on High Energy Physics, Madison, Wisconsin, 1980
TASSO Collaboration, R.Brandelik et al., Phys.Lett. 97B, 448 (1980)

277) D.L.Burke et al., Phys.Lett. 103 B, 153 (1981)

278) TASSO Collaboration, R.Brandelik et al., DESY 81/058

279) J.J.Sakurai, Ann.Phys. 11, 1 (1960)

280) S.M.Berman, J.D.Bjorken and J.B.Kogut, Phys.Rev. D4, 3388 (1971)
S.Brodsky, T. De Grant, J.Gunion and J.Weis, Phys.Rev. D19, 1418 (1979)

281) PLUTO Collaboration, Ch.Berger et al., Phys. Lett. 81B, 410 (1979) and Phys.Lett. 99B, 287 (1981)

282) W.Wagner, Proceedings of the XX International Conference on High Energy Physics, Madison, Wisconsin, 1980

283) TASSO Collaboration, R.Brandelik et al., Phys.Lett. 107B, 290 (1981)

284) D.Cords, 4th Int.Conf. on Photon-Photon Interactions, Paris 1981
DESY Report 81/033
H.Spitzer, XV Rencontre de Moriond, Les Arcs, France 1980

285) JADE Collaboration, W.Bartel et al., Report DESY 81/048

286) PLUTO Collaboration, Ch.Berger et al., DESY 81/051

287) T.F.Walsh, Phys.Lett. 36B, 121 (1971)
S.B.Brodsky, T.Kinoshita, and H.Terazawa, Phys.Rev.Lett. 27, 280 (1971)
E.Witten, Nucl.Phys. B 120, 189 (1972)
C.H.Llewellyn-Smith, Phys.Lett. 79B, 83 (1979)

288) W.A.Bardeen and A.J.Buras, Phys.Rev. D20, 166 (1979)
D.W.Duke and J.F.Owens, Phys.Rev. D22, 2280 (1980)

289) E.D.Bloom et a., Phys.Rev. Lett. 23, 930 (1969)
E.D.Bloom et al., Phys.Rev.Lett. 25, 1140 (1970)
and Phys.Rev. D4, 2901 (1971)

290) H.Deden et al., Nucl.Phys. B 85, 269 (1975)

291) P.C.Bosetti et al., Nucl.Phys. B 142, 1 (1978)

292) P.Musset et al., Phys.Report 39, 1 (1978)

293) J.G.H. De Groot et al., Zeit. Phys. C 1, 143 (1979)

294) J.Ellis, Les Houches Lectures 1976
C.T.Sachrajda, Les Houches Lectures 1981
D.H.Perkins, NSAI on Techniques and Concepts of High-Energy Physics,
ed. T.Febel - Plenum Press 1981

295) J.D.Bjorken, Phys.Rev. 179, 1547 (1969)

296) R.P.Feynman, Photon Hadron Interactions, (Frontiers in Physics)
W.A.Benjamin, Inc. (1972)

J.D.Bjorken and E.A.Paschos, Phys.Rev. 185, 1969 (1975)

297) J.Wotschack, 1981 International Symposium on Lepton and Photon
Interactions at High Energies, Bonn, August 1981

298) B.C.Barish et al., Phys.Rev.Lett. 39, 1595 (1977)

299) H.Deden et al., Contribution to the Neutrino 81, International Conference
on Neutrino Physics and Astrophysics, Wailea (Hawaii) presented
by P.Fritze

300) J.B.Morfin et al., Aachen, PITHA 81/14 (1981)

301) M.D.Mestayer (Thesis) SLAC 214 (1978)

302) A.Bodek et al., Phys.Rev. D 20, 1471 (1979)

303) J.J.Aubert et al., Phys.Lett. 105B, 315 (1981)

304) J.J.Aubert et al., Phys. Lett. 105 B, 322 (1981)

305) P.Musset et al., Phys. Report 39, 1 (1978)

306) S.M.Heagy et al., Phys.Rev. D 23, 1045 (1981)

307) Abramowicz et al., CERN-EP / 81-50 (1981 - submitted to Phys.Lett.)

308) V.V.Ammosov et al., Serpuchov, IHEP 81-66 (1981)

309) J.Panman (Thesis) NIKHEF (1981) to be published

310) C.Baltay et al., Phys. Rev. Lett. 44, 916 (1980)

311) H.Wahl et al., talk at the Rencontre de Moriond (1981) to be published

312) B.M.Heagy, Neutrino 79, International Conference on Neutrino Physics and Astrophysics, Bergen (1979)

313) R.D.Field, R.P.Feynman, Phys.Rev. D 15, 2590 (1977)

314) G.R.Farrar, D.R.Jackson, Phys.Rev. Lett. 35, 1416 (1975)

315) A.Donnachie, P.V.Landshoff, Phys.Lett. 95B, 437 (1980)

316) F.E.Close, R.G.Roberts, Rutherford Laboratory RL-80-058 (1980)

317) J.J.Aubert et al., to be published

318) P.Allen et al., Phys.Lett. 103 B, 71 (1981)

319) H.Deden et al., Nucl.Phys. B 149, 1 (1979)

320) F.S.Meritt et al., Phys.Rev. D 17, 2199 (1978)

321) G.Altarelli, Chromodynamics and Deep Inelastic Processes in New Phenomena in Lepton Hadron Physics (ed. E.E.C.Fries and J.Wess) Plenum Press

322) H.Georgi, H.D.Politzer, Phys.Rev. D14, 1829 (1976)

R.Barbieri, J.Ellis, M.K.Gaillard and G.G.Ross, Nucl.Phys. B 117, 50 (1976)

E.G.Floratos, D.A.Ross and C.T. Sachrajda, W.A.Bardeen, A.J.Buras, D.W.Duke, and T.Muta, Phys.Rev. D18, 3998 (1978)

A.F.Abott, R.M.Barnett, Ann.Phys. 125, 276 (1980)

323) J.M.Cornwall and R.E.Norton, Phys.Rev. 177, 2584 (1969)

O.Nachtmann, Nucl.Phys. B 63, 237 (1973) and Nucl.Phys. B 78, 455 (1974)

324) D.J.Gross and F.A.Wilczek, Phys.Rev. D8, 3633 (1973) and Phys.Rev. D 9, 980 (1974)

H.Georgi and H.Poltizer, Phys.Rev. D 9, 416 (1974)

325) A.J.Buras, K.F.Gaemers, Nucl.Phys. B 132, 249 (1978)

326) A.F.Abbott, R.M.Barnett, Annals of Phys. 125, 276 (1980)

327) A.Gonzales-Arroyo et al., Nucl.Phys. B 153, 161 (1979) and Nucl.Phys. B 159, 512 (1979) and Nucl.Phys. B 166, 429 (1980)

328) J.G.H.De Groot et al., Phys.Lett. 82B, 292 (1979) and Phys.Lett. 82B, 456 (1979)

329) M.Jonker et a., CERN EP/81-135 (1981)

330) J.G.Morfin et al., Phys.Lett. 104B, 235 (1981)

331) J.Steinberger - CERN EP/80-222
F.Eisele, Dortmund, DO-EXP 6/81

332) For a recent review see:
J.Bürger - Proceedings of the 1981 International Symposium on Lepton and Photon Interactions at High Energies, Bonn 1981

P.Duinker, EPS International Conference on High Energy Physics, Lisbon 1981

333) MARK J Collaboration, D.P.Barber et al., MIT Report LNS 113 (1980)

334) PLUTO Collaboration Ch.Berger et al., Phys.Lett. 99B, 489 (1981)

335) TASSO Collaboration, R.Brandelik et al., Phys.Lett. 99B, 163 (1981)

336) M.S.Chanowitz, J.Ellis and M.K.Gaillard, Nucl.Phys. B 128, 506 (1977
A.J.Buras, J.Ellis, M.K.Gaillard and D.V.Nonopoules, Nucl.Phys. B 135, 66 (1978)

337) J.D.Bjorken and C.Llewellyn Smith, Phys.Rev. D7, 887 (1973)

338) A.Ali, Phys.Rev. D 10, 2801 (1974)

339) F.Bletzacker and H.T.Nieh, Phys.Rev. D 16, 2115 (1977)

340) S. LaRue, D.Phillips and W.M.Fairbank, Phys.Rev.Lett. 46, 967 (1981)

341) M.Marinelli and G.Morpurgo, Phys.Lett. 94B, 427 and 433 (1980)

342) JADE Collaboration, W.Bartel et al., Zeit.Phys. C 6, 295 (1980)

343) J.M.Weiss et al., SLAC-PUB-2671, 1981
A.M.Litke, Proceedings of the 1981 International Symposium on Lepton and Photon Interactions at High Energies, Bonn 1981

344) G.Valente, Proceedings XX International Conference on High Energy Physics, Madison, Wisconsin 1980
A.Zichichi, private communication

345) For a review including a complete set of references see G.Barbiellini et al., to be published in Physics Reports

346) A.De Rujula, R.C.Giles and R.L.Jaffe, Phys.Rev. D 17, 285 (1978)

347) B.M.McCoy and T.T.Wu, Phys.Lett. 72B, 219 (1977)

348) F.A.Berends and R.Kleiss, Nucl.Phys. B 178, 141 (1981)

349) A.Litke, Harvard University thesis, 1970

350) F.A.Berends et al., Nucl.Phys. B 57, 381 (1973)

351) G.t'Hooft, Nucl.Phys. B 35, 167 (1971)

352) J.Schwinger, Phys.Rev. 125, 397 (1962)
and Phys.Rev. 128, 2425 (1969)

R.Jackiw and K.Johnson, Phys.Rev. D8, 2286 (1973)

J.M.Cornwall and R.E.Norton, Phys.Rev. D8, 3338 (1973)

M.A.B.Bég and A.Sirlin, Ann.Rev.Nucl.Sci. 24, 379 (1974)

S.Weinberg, Phys.Rev. D 13, 974 (1976) and
Phys. Rev. D 19, 1277 (1979)

L.Susskind, Phys.Rev. D 20, 2619 (1979)

353) Yu. A.Gol'fand and E.P.Likthman, JETP Letters 13, 323 (1971)

P.V.Volkov and V.P.Akulow, Phys.Lett. 46B, 109 (1973)

J.Wess and B.Zumino, Nucl.Phys. B 70, 39 (1974)

354) For reviews see: F.Fayet, Proceedings Orbis Scientiae (Coral Gables, Florida, US - Jan 1978) New Frontiers in High Energy Physics, Plenun, New York 1978

G.R.Farrar - Proceedings International School of Subnuclear Physics, Erice, Italy, 1978

355) CELLO Collaboration, H.J.Behrend et al., Contribution to the 1981 Bonn Conference

356) H.Spitzer, Proceedings of the 15 Rencontre de Moriond, Les Arces, 1980 and DESY 80/43

357) R.D.Peccei and H.R.Quinn, Phys.Rev.Lett. 38, 1440 (1970)

358) S.Weinberg, Phys.Rev.Lett. 40, 223 (1978)

F.Wilczek, Phys.Rev.Lett. 40, 279 (1978)

359) For a review on axions including references see:
J.Ellis, Les Houches Lectures 1981

360) A.Faissner, 1981 International Symposium on Lepton and Photon Interactions at High Energies, Bonn, August 1981